

Black hole simulations: from supercomputers to your laptop

Thesis by
Vijay Varma

In Partial Fulfillment of the Requirements for the
Degree of
Doctor of Philosophy

The logo for the California Institute of Technology (Caltech), featuring the word "Caltech" in a bold, orange, sans-serif font.

CALIFORNIA INSTITUTE OF TECHNOLOGY
Pasadena, California

2019
Defended May 07 2019

© 2019

Vijay Varma

ORCID: 0000-0002-9994-1761

All rights reserved

ACKNOWLEDGEMENTS

I am eternally grateful to my advisors Mark Scheel and Yanbei Chen for their mentorship and guidance throughout my PhD. Thanks Mark for putting up with me bothering you so much in the early days. I would like to also thank them, as well as Saul Teukolsky, Alan Weinstein, and Mark Wise for serving on my thesis committee and their advice.

I have gained immensely from various unofficial mentors, including but not limited to, Scott Field, Leo Stein, Davide Gerosa, Ajith Parameswaran, and Bala Iyer. Particular thanks to Ajith and Bala, for introducing me to gravitational waves and research in general. I thank Kip Thorne for inspiration, but more importantly, hosting amazing parties.

I am greatly indebted to my many peers at Caltech, for their company, friendship, and inspiration: Matt Giesler, Max Isi, Jonathan Blackman, Belinda Pang, Craig Cahillane, Masha Okounkova, Ron Tso, and Kevin Barkett. I cherish the trip trips, trivia, and poker nights. Thanks also to the various Tapir grads for much needed enlightenment.

I would like to acknowledge Mark Scheel, Larry Kidder, and Harald Pfeiffer, among others, for developing the greatest numerical relativity code in all the land. None of this would be possible without that.

Finally, special thanks to my parents for inventing me. Couldn't have done it without your encouragement and unwavering support. I thank my brother Rama for all the good times.

ABSTRACT

In this thesis, I will present various advancements in the modeling of binary black holes (BBHs): two black holes (BHs) that are in orbit around each other. The BHs lose energy to gravitational waves, causing them to spiral towards each other until they eventually merge and leave behind a single BH. BBHs are primary sources for ground based detectors such as the Laser Interferometer Gravitational-Wave Observatory (LIGO).

As the BHs are about to merge, they are moving at about half the speed of light and the spacetime is highly dynamical. All analytical methods break down at this stage, and numerical relativity (NR) simulations of the full Einstein's equations are necessary. These simulations, however, are very expensive, with each simulation taking a month on a supercomputer. For direct data analysis applications with LIGO, we need a model that can be evaluated in a fraction of a second. Therefore, several approximate but fast models that are calibrated to NR simulations have been developed over the years.

Surrogate modeling provides a more powerful alternative: trained directly against the NR simulations without added assumptions, these models can reproduce the simulations as accurately as the simulations themselves, while taking only a fraction of a second to evaluate on a laptop. In short, surrogate models take BBH NR simulations from supercomputers to your laptop, without a loss of accuracy.

In this thesis, I will present several state-of-the-art surrogate models including (i) the first NR based surrogate model to span the full range of frequencies for ground based detectors, (ii) the first surrogate model for the mass, spin, and kick velocity of the final black hole after merger, and (iii) extension of an existing precessing surrogate model to higher mass ratios. In addition, I will present some work in improving the BBH initial data used in NR simulations, as well as in understanding the systematic biases introduced by approximate waveform models in LIGO data analysis.

As we head into the imminent era of high-precision gravitational wave astronomy, accurate yet fast models such as surrogate models will play a crucial role in maximizing the science output of our detectors.

PUBLISHED CONTENT AND CONTRIBUTIONS

- [1] Vijay Varma, Leo C. Stein, and Davide Gerosa. “The binary black hole explorer: on-the-fly visualizations of precessing binary black holes”. In: *Class. Quant. Grav.* 36.9 (2019), p. 095007. DOI: [10.1088/1361-6382/ab0ee9](https://doi.org/10.1088/1361-6382/ab0ee9). arXiv: [1811.06552](https://arxiv.org/abs/1811.06552) [[astro-ph.HE](#)].
V.V. conceived the idea for the animations, built the Python package, produced the animations, and was the principal author of the manuscript.
- [2] Vijay Varma et al. “High-accuracy mass, spin, and recoil predictions of generic black-hole merger remnants”. In: *Phys. Rev. Lett.* 122.1 (2019), p. 011101. DOI: [10.1103/PhysRevLett.122.011101](https://doi.org/10.1103/PhysRevLett.122.011101). arXiv: [1809.09125](https://arxiv.org/abs/1809.09125) [[gr-qc](#)].
V.V. participated in the conception of the project, was involved in the implementation of the Gaussian process regression fitting method, constructed the fits, and was the principal author of the manuscript.
- [3] Vijay Varma et al. “Surrogate models for precessing binary black hole simulations with unequal masses”. In: (2019). arXiv: [1905.09300](https://arxiv.org/abs/1905.09300) [[gr-qc](#)].
V.V. participated in the conception of the project, determined optimal parameters for simulations, lead the planning of the supercomputer runs, constructed the surrogate model by extending existing methods, and was the principal author of the manuscript.
- [4] Vijay Varma and Mark A. Scheel. “Constructing a boosted, spinning black hole in the damped harmonic gauge”. In: *Phys. Rev. D* 98.8 (2018), p. 084032. DOI: [10.1103/PhysRevD.98.084032](https://doi.org/10.1103/PhysRevD.98.084032). arXiv: [1808.07490](https://arxiv.org/abs/1808.07490) [[gr-qc](#)].
V.V. participated in the conception of the project, derived the elliptic equations, solved them numerically, processed the results, and was the principal author of the manuscript.
- [5] Vijay Varma, Mark A. Scheel, and Harald P. Pfeiffer. “Comparison of binary black hole initial data sets”. In: *Phys. Rev. D* 98.10 (2018), p. 104011. DOI: [10.1103/PhysRevD.98.104011](https://doi.org/10.1103/PhysRevD.98.104011). arXiv: [1808.08228](https://arxiv.org/abs/1808.08228) [[gr-qc](#)].
V.V. participated in the conception of the project, implemented the new initial data methods, performed the simulations, processed the results, and was the principal author of the manuscript.
- [6] Vijay Varma et al. “Surrogate model of hybridized numerical relativity binary black hole waveforms”. In: (2018). DOI: [10.1103/PhysRevD.99.064045](https://doi.org/10.1103/PhysRevD.99.064045). arXiv: [1812.07865](https://arxiv.org/abs/1812.07865) [[gr-qc](#)].
V.V. participated in the conception of the project, determined optimal parameters for simulations, lead the planning of the supercomputer runs, developed the hybridization code, constructed the surrogate model, and was the principal author of the manuscript.

- [7] Vijay Varma and Parameswaran Ajith. “Effects of nonquadrupole modes in the detection and parameter estimation of black hole binaries with non-precessing spins”. In: *Phys. Rev. D* 96.12 (2017), p. 124024. DOI: [10.1103/PhysRevD.96.124024](https://doi.org/10.1103/PhysRevD.96.124024). arXiv: [1612.05608](https://arxiv.org/abs/1612.05608) [gr-qc].

V.V. participated in the conception of the project, performed the computations, processed the results, and was the principal author of the manuscript.

TABLE OF CONTENTS

Acknowledgements	iii
Abstract	iv
Published Content and Contributions	v
Table of Contents	vii
List of Illustrations	x
List of Tables	xiii
Chapter I: Introduction and summary	1
1.1 Setting the scene	1
1.2 General relativity	4
1.3 Gravitational waves	5
1.4 Binary black holes	6
1.5 Numerical relativity	8
1.6 Waveform models	9
1.7 Surrogate models	11
1.8 Extending the parameter space of surrogate models	15
1.9 Higher order modes of radiation	16
1.10 Testing general relativity	17
1.11 Remnant black hole surrogate models	18
1.12 Binary black holes on a laptop	19
1.13 Thesis outline	19
Chapter II: Constructing a boosted, spinning black hole in the damped harmonic gauge	24
2.1 Executive summary	24
2.2 Abstract	24
2.3 Introduction	25
2.4 Damped harmonic gauge	28
2.5 Boosted, spinning black hole in damped harmonic gauge	30
2.6 Validation against single black hole simulations	38
2.7 Conclusion	39
2.8 Acknowledgments	40
Chapter III: Comparison of binary black hole initial data sets	43
3.1 Executive summary	43
3.2 Abstract	43
3.3 Introduction	44
3.4 BBH initial data formalism	48
3.5 BBH initial data types	58
3.6 Convergence of initial data	60
3.7 BBH evolution with different initial data sets	62
3.8 Conclusion	73

3.9 Acknowledgments	77
Chapter IV: Effects of nonquadrupole modes in the detection and parameter estimation of black hole binaries with nonprecessing spins	82
4.1 Executive summary	82
4.2 Abstract	82
4.3 Introduction and summary	83
4.4 Methodology	88
4.5 Results and discussion	92
4.6 Conclusion	100
4.7 Acknowledgments	101
Appendices	102
4.A Comparison with Bayesian parameter estimation	102
Chapter V: Surrogate model of hybridized numerical relativity binary black hole waveforms	110
5.1 Executive summary	110
5.2 Abstract	110
5.3 Introduction	111
5.4 Training set generation	114
5.5 NR simulations	115
5.6 Early inspiral waveforms	117
5.7 Hybridization	119
5.8 Building the surrogate model	128
5.9 Results	134
5.10 Conclusion	145
5.11 Acknowledgments	146
Chapter VI: High-accuracy mass, spin, and recoil predictions of generic black-hole merger remnants	158
6.1 Executive summary	158
6.2 Abstract	158
6.3 Introduction	159
6.4 Fitting procedure	161
6.5 Aligned-spin model	162
6.6 Precessing model	163
6.7 Regime of validity	164
6.8 Conclusion	166
6.9 Acknowledgments	167
Appendices	168
6.A Gaussian process regression	168
6.B Input parameter space	169
6.C Extrapolation errors	171
6.D GPR error prediction	172
6.E Public Python implementation	173
Chapter VII: Surrogate models for precessing binary black hole simulations with unequal masses	183
7.1 Executive summary	183

7.2	Abstract	183
7.3	Introduction	184
7.4	Preliminaries and notation	185
7.5	NR simulations	188
7.6	Waveform surrogate	191
7.7	Remnant surrogate	196
7.8	Results	197
7.9	Conclusion	204
7.10	Acknowledgments	206
	Appendices	208
7.A	Evaluating surrogates at larger mass ratios	208
7.B	On the high mismatch tail in NR errors	210
Chapter VIII: The binary black hole explorer: on-the-fly visualizations of		
	precessing binary black holes	223
8.1	Executive summary	223
8.2	Abstract	223
8.3	Introduction	224
8.4	Methods	227
8.5	Explorations	235
8.6	Public Python implementation	242
8.7	Conclusion	243
8.8	Acknowledgments	243

LIST OF ILLUSTRATIONS

<i>Number</i>	<i>Page</i>
1.1 Artist’s impression showing two merging black	1
1.2 Depiction of Newton’s fixed space and	2
1.3 The LIGO Laboratory operates two detector	3
1.4 Warping of spacetime due to the Sun	4
1.5 Parameters of a quasicircular BBH system. Each	7
1.6 Schematic description of NR initial value problem.	9
1.7 Schematic description of reduced basis construction. At	11
1.8 Demo of surrogate model construction for nonspinning	12
1.9 Demo of surrogate model evaluation at a	14
1.10 Improved coverage of the BBH parameter	16
1.11 BBHs seen from a scattering view	17
2.1 Convergence test for solving the elliptic equations	36
2.2 Kruskal-Szekeres diagram showing constant time slices of	37
2.3 Snapshots during the evolution of a	39
3.1 Initial constraint violations on the equatorial	54
3.2 Convergence test for the spectral elliptic solver	61
3.3 Convergence test for constraints during evolution using	63
3.4 Damped harmonic constraint energy (Eq. 3.43) during evolution	65
3.5 Behavior of dimensionless spin along the angular	66
3.6 Comparison of the waveforms resulting from evolution	68
3.7 Median mismatches across the sky in	70
3.8 Computational efficiency. The top panel shows the	71
3.9 Eccentricity reduction iterations for different initial data	73
3.10 Apparent horizon surface for a single BH	76
4.1 These plots summarize the region in the	85
4.2 This plot shows the mass ratio (vertical	88
4.3 Example hybrid waveform constructed by matching NR	90
4.4 Optimal SNR (top panel) and fitting factor	93
4.5 Systematic bias in the estimation of total	94
4.6 “Ineffectualness” and effective parameter biases when using	95
4.7 Comparison of the frequency domain amplitudes of	96

4.8	Lowest SNR (orientation-averaged) at which the statistical	99
5.4.1	Largest mismatch of the surrogate (over the)	115
5.5.1	The parameter space covered by the 104	116
5.6.1	NR, PN (Sec. 5.6), and EOB-corrected PN	120
5.7.1	Top: The real part (top) and	126
5.7.2	An example hybrid waveform used in	127
5.9.1	Errors in NRHybSur3dq8 and SEOBNRv4HM when	135
5.9.2	The plus polarization of the waveforms for	137
5.9.3	Comparisons between the NRHybSur3dq8 surrogate model and . . .	139
5.9.4	Errors in the NRHybSur3dq8 surrogate model against	141
5.9.5	Errors in NRHybSur3dq8 when evaluated outside its	142
5.9.6	Mode mixing between spherical harmonic modes is	143
5.9.7	Evaluation cost for NRHybSur3dq8 including the cost	144
6.3.1	Quasi-circular binary BH merger problem viewed as	160
6.4.1	Errors in predicting remnant mass, spin, kick	162
6.6.1	Errors in predicting the remnant mass, spin	164
6.6.2	Left panel: Errors for <i>surfinBH7dq2</i> in predicting remnant	165
6.B.1	Errors in <i>surfinBH7dq2</i> when extrapolating to higher mass	170
6.C.1	Errors in predicting the remnant mass, spin,	171
6.D.1	Prediction errors for remnant mass, spin and	172
6.D.2	Comparison between out-of-sample (left), and 1σ GPR	174
7.4.1	The real part of the (2, 2) and	187
7.5.1	Parameters of the 1528 NR simulations used	189
7.6.1	The top panel shows the real part	192
7.8.1	Mismatches for NRSur7dq4 and SEOBNRv3 models, when compared	198
7.8.2	The plus polarization of the waveforms for	200
7.8.3	Same as the left panel of Fig. 7.8.1	201
7.8.4	Error histograms for <i>surfinBH7dq4</i> for the remnant	202
7.8.5	Errors for <i>surfinBH7dq4</i> in predicting remnant properties	203
7.9.1	The shaded region shows the regime of	205
7.A.1	Mismatch histogram when extrapolating the NRSur7dq4 waveform .	208
7.A.2	Error histograms of the remnant mass, spin	209
7.B.1	Dependence of the NR resolution error on	210
7.B.2	Mismatch histograms for NRSur7dq4 when compared against	211
7.B.3	NR resolution mismatches for the simulation leading	213
8.3.1	Snapshots during the inspiral (top-left), post-ringdown (top-right), . .	226

8.4.1	Example of the real part of the	228
8.4.2	Comparison of the coordinate trajectories of the	232
8.4.3	Visualization of a precessing binary black hole	236
8.5.1	Visualization of the orbital hang-up effect. We	238
8.5.2	Evolution of a super-kick configuration. Time flows	240
8.5.3	Sinusoidal dependence of the kick magnitude on	241

LIST OF TABLES

<i>Number</i>	<i>Page</i>
3.1 Types of initial data considered in this	57
4.1 Summary of the parameters of the NR	87
4.A.1 Comparison of systematic and statistical biases	102

Chapter 1

INTRODUCTION AND SUMMARY

1.1 Setting the scene

A long time ago in a galaxy far, far away, two black holes circled each other with vicious intent. The black holes were destined for a cataclysmic union that would unleash more power than is released in the form of light from the rest of the Universe combined! All of this power was in the form of gravitational waves, ripples in the very fabric of spacetime, that arrived on Earth on September 14, 2015 [1, 2]. The signal was received by the twin LIGO [3] (Laser Interferometer Gravitational-Wave Observatory) detectors, ushering in the era of gravitational wave astronomy.

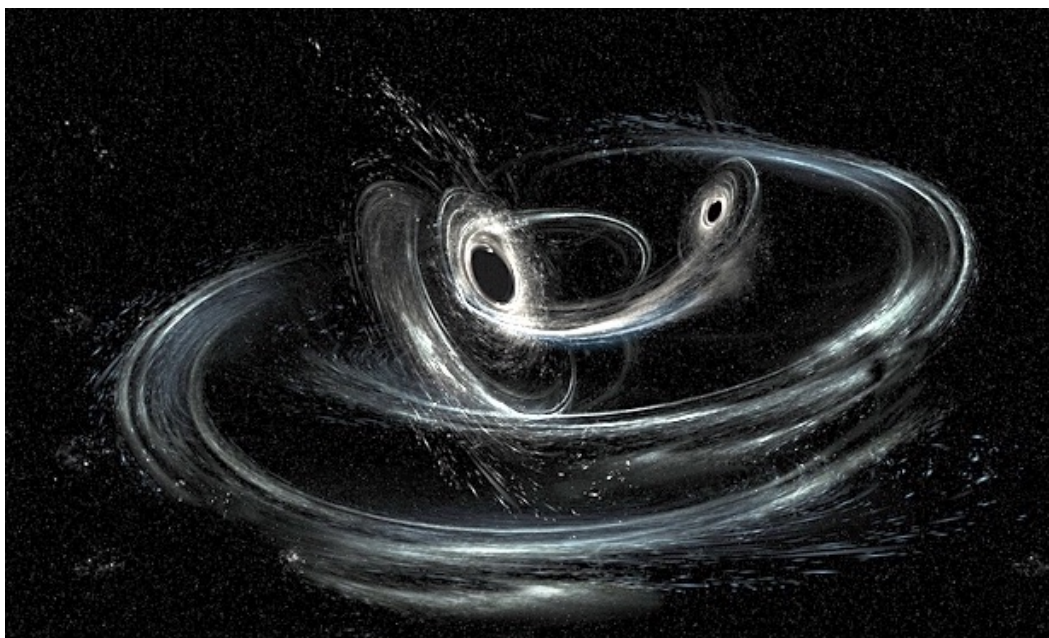


Figure 1.1: Artist's impression showing two merging black holes similar to those detected by LIGO. Credit: LIGO/Caltech/MIT/Sonoma State (Aurore Simonnet).

But what exactly are gravitational waves? Gravitational waves solve an old problem with Newton's law of gravitation. While this simple law describes nearly all gravitational effects we see in everyday life, it has a fundamental flaw: it describes gravity as an instantaneous force. In this framework, if the Sun were to suddenly vanish, the Earth would immediately stop orbiting and move in a straight line with its current velocity. Einstein realized that this would violate special relativity [4],

which says that no force can be transmitted faster than the speed of light. But according to Newtonian gravity, the Earth would instantaneously react to the Sun's disappearance.

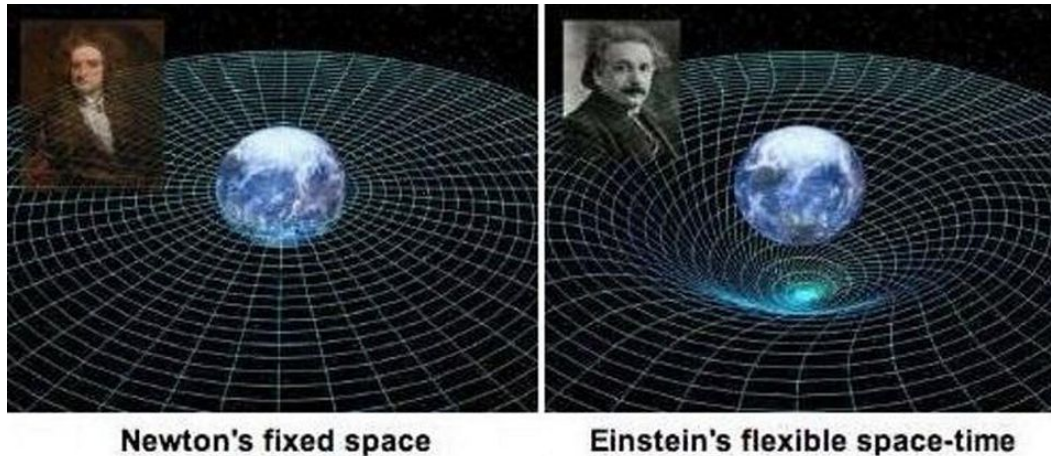


Figure 1.2: Depiction of Newton's fixed space and Einstein's flexible space-time. Credit: From the film "Testing Einstein's Universe" by Norbert Bartel.

This fundamental flaw is resolved by Einstein's general relativity [5], a geometric theory describing how gravity arises from the curvature of spacetime, the 4-dimensional fabric of the Universe. According to general relativity, if the Sun were to disappear, this information would be transmitted in the form of ripples in the curvature: gravitational waves. These waves travel at the same speed as light, thus keeping special relativity intact.

Einstein's theory also tells us that gravitational waves are incredibly tiny and interact weakly with matter. They cause distortions in the LIGO detector of about 10^{-18} meters [2], which is 10 trillion times smaller than the width of a human hair! This weakness is both a blessing and a curse. The weak interactions with matter allow the waves to travel through the Universe nearly unaffected, giving us clean information about their sources. In contrast, light, our primary source of information about objects in the Universe, gets scattered and contaminated by interstellar dust and our own atmosphere. But the weakness of gravitational waves also makes them very hard to observe. To be detectable on Earth, they need to be generated by extremely compact, massive objects moving at high velocities, such as two black holes orbiting each other.

Gravitational waves from such a binary black hole were detected for the first time by LIGO in 2015 [2], nearly a hundred years after Einstein's prediction [6, 7]. This

was the culmination of decades of experimental, theoretical, and computational advancements with important contributions from over a thousand scientists. Caltech's Kip Thorne and Barry Barish, along with MIT's Rai Weiss, were awarded the 2017 Nobel Prize in Physics for this monumental achievement [8]. LIGO's detection launched the field of gravitational wave astronomy and marked the opening of a never-before accessible window to the Universe.



Figure 1.3: The LIGO Laboratory operates two detector sites, one near Hanford in eastern Washington, and another near Livingston, Louisiana. This photo shows the Livingston detector site. Credit: Caltech/MIT/LIGO Lab.

LIGO, now joined by its sister detector Virgo [9], has been going strong since the first detection. The current number of detections stands at 11 [10]! In the future, detectors will become much more sensitive, and signals are expected to become routine. When Galileo turned his telescope to the sky, it marked the beginning of modern electromagnetic astronomy, a field which revealed a menagerie of unexpected cosmic wonders such as quasars, pulsars, cosmic microwave background, gamma-ray bursts, and much more. What new wonders does the field of gravitational wave astronomy hold for us?

1.2 General relativity

General relativity (GR) is our current prevailing description of gravity, formulated by Einstein in 1915 [5]. GR describes gravity as a geometric property of spacetime, the four-dimensional fabric of our Universe. The curvature of spacetime is dictated by the energy, momentum, and angular momentum of the matter present. And in response, the evolution of the matter is dictated by the curvature of spacetime. As John Wheeler eloquently put it: ‘Spacetime tells matter how to move; matter tells spacetime how to curve.’ For example, when the Earth orbits the Sun, according to GR it is not being pulled by a gravitational force, but instead is merely following the straightest possible path in the curved spacetime around the Sun (see Fig. 1.4). In this section I will very briefly mention the main equations of GR, but refer the reader to Refs. [11–14] for a more detailed study.

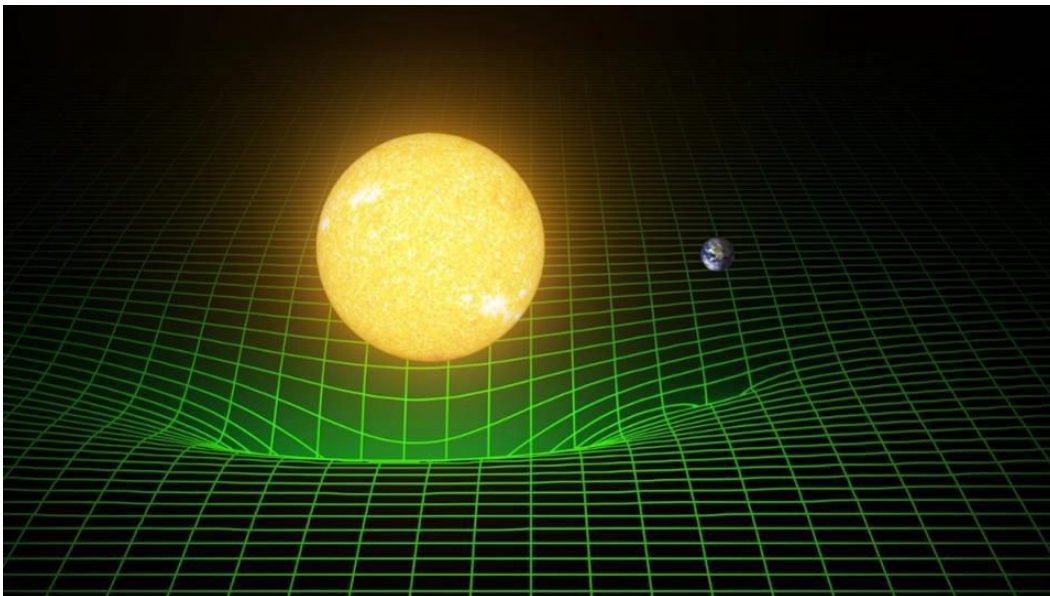


Figure 1.4: Warping of spacetime due to the Sun and Earth, represented with a grid. The spacetime around the Sun is warped due to its mass. The Earth then merely follows a geodesic, or a locally straight path, in this curved spacetime. However, since the spacetime itself is curved, this locally straight path becomes a curved path on a global scale; an ellipse in this instance. The Earth also warps the spacetime around itself, which causes the Moon to orbit it (not shown here). Credit: LIGO/T. Pyle.

In GR, the geometric structure of the spacetime is encoded in the spacetime metric, g_{ab} . For example, the infinitesimal line element is given by:

$$ds^2 = g_{ab} dx^a dx^b. \quad (1.1)$$

Here, I use the Einstein summation notation. I use Latin indices from the start of the alphabet ($a, b, c \dots$) for spacetime indices (which run from 0 to 3) and from the middle of the alphabet ($i, j, k \dots$) for space indices (which run from 1 to 3).

The Einstein field equations describe how the metric responds to the presence of matter:

$$G_{ab} = 8\pi T_{ab}, \quad (1.2)$$

where G_{ab} is the Einstein tensor which contains g_{ab} , and T_{ab} is the stress-energy tensor containing information about the density and flux of energy and momentum in the spacetime. Note that here, and throughout this thesis, I use geometric units with $G = c = 1$.

1.3 Gravitational waves

Gravitational waves (GWs) are an important prediction [6, 7] of GR. For a modern review see Refs. [15, 16]. Far away from the source, the waves can be described by perturbing about flat spacetime:

$$g_{ab} = \eta_{ab} + \bar{h}_{ab}, \quad (1.3)$$

where η_{ab} is the Minkowski metric for flat spacetime, and \bar{h}_{ab} is a small perturbation ($|\bar{h}_{ab}| \ll 1$). Under the Lorentz gauge, the linearized Einstein's equations become [11]:

$$\square h_{ab} = 0, \quad (1.4)$$

where $\square = \nabla_c \nabla^c$ is the d'Alembertian, $h_{ab} = \bar{h}_{ab} - \frac{1}{2} \eta_{ab} \bar{h}$ is the ‘‘trace reverse’’ of \bar{h}_{ab} , and $\bar{h} = \bar{h}_a^a$.

Eq. (1.4) admits solutions of the form [11]:

$$h_{ab} = A_{ab} \exp(ik^c x_c), \quad (1.5)$$

where A_{ab} is a (complex) constant tensor, and k^c is a (real) null vector. This means that Eq. (1.5) is a wavelike solution, whose propagation speed is the same as the speed of light [11]; we refer to these as GWs. As indicated in Eq. (1.3), GWs form part of the spacetime metric itself; hence they are often referred to as ‘‘ripples of curvature’’.

A spherically outgoing gravitational wave is typically converted into a spin-weight -2 complex scalar by contracting:

$$h \equiv h_{ab} \bar{m}^a \bar{m}^b, \quad (1.6)$$

where $m^a = (\hat{e}_\theta^a + i\hat{e}_\phi^a)/\sqrt{2}$ is an element of a complex null dyad [14] along with its conjugate \bar{m}^a , and $\hat{e}_\theta^a, \hat{e}_\phi^a$ are the standard unit vectors in the θ and ϕ directions, respectively. This quantity h is also equal to the fractional distortions caused in the arms of detectors such as LIGO/Virgo, hence h is typically referred to as the gravitational wave strain, or simply strain.

In many ways GWs are to gravity, what light is to electromagnetic theory (EMT). They are both transverse waves, with two independent polarizations, that carry information about changes in the field (g_{ab} for gravity, F_{ab} or \mathbf{E}/\mathbf{B} fields for EMT). Light waves are generated by time varying dipole (and higher) moments, while the monopole radiation is zero due to conservation of total charge. Similarly, GWs are generated by time varying quadrupole (and higher) moments, while the monopole and dipole radiation are zero due to conservation of total mass and total linear momentum, respectively.

Unlike light, however, the GWs we can observe on Earth are very weak. Following Ref. [17], we can use the quadrupole formula to make a rough estimate of the amplitude of gravitational waves emitted by two orbiting objects of equal mass:

$$h \sim 5 \times 10^{-20} \left(\frac{1 \text{ Mpc}}{R} \right) \left(\frac{m}{M_\odot} \right) \left(\frac{m}{r} \right), \quad (1.7)$$

where m is the mass of each object in solar masses (M_\odot), r is the distance between the two objects in units of m , and R is the distance to Earth in Megaparsecs. For a stellar mass compact object with $m = 10M_\odot$, at a binary separation of $r = 6m$, located in the Virgo cluster at $R = 20 \text{ Mpc}$, we get a strain of $h \sim 4 \times 10^{-21}$. This would distort the 4km arms of the LIGO detectors by about 10^{-17} meters; that is 100 times smaller than the size of a hydrogen nucleus!

This exercise also gives us useful insight into what constitutes a good source of GWs. For an astrophysical binary of a given component mass m to emit strong GWs, its m/r needs to be large. For this to happen, the mass of the component needs to be confined to a small region, so that the binary orbit can shrink to a small separation (r) before the two objects come into contact. Orbiting black holes and neutron stars have therefore long been identified as prime sources and have now been observed by LIGO and Virgo [10].

1.4 Binary black holes

In this thesis, I will focus mainly on orbiting black holes (BHs), referred to as binary black holes (BBH). These systems lose energy to GW radiation, causing them to

inspiral towards each other. This increases the amplitude of the GWs (see Eq. (1.7)), thus increasing the rate of energy loss. The result is a runaway process, where the BHs get closer and closer, until they eventually merge, leaving behind a highly distorted single BH. The distortions are then quickly radiated away as GWs at the characteristic quasi-normal mode frequencies of the final BH. GW150914 [1] was the first direct observation of such a signal, beginning the field of GW astronomy.

Despite their exotic nature, BHs are remarkably simple objects. An astrophysical BH is entirely characterized by its mass (m) and spin (χ) [18]. John Wheeler famously said, “Black holes have no hair.”, meaning that all other information — the “hair” — is forever lost behind the BH’s event horizon, and is inaccessible to external observers. Here, χ is the dimensionless spin vector (with magnitude $\chi \leq 1$), defined as $\chi = S/m^2 = \mathbf{a}/m$, where S is the spin angular momentum, and \mathbf{a} is the Kerr parameter.

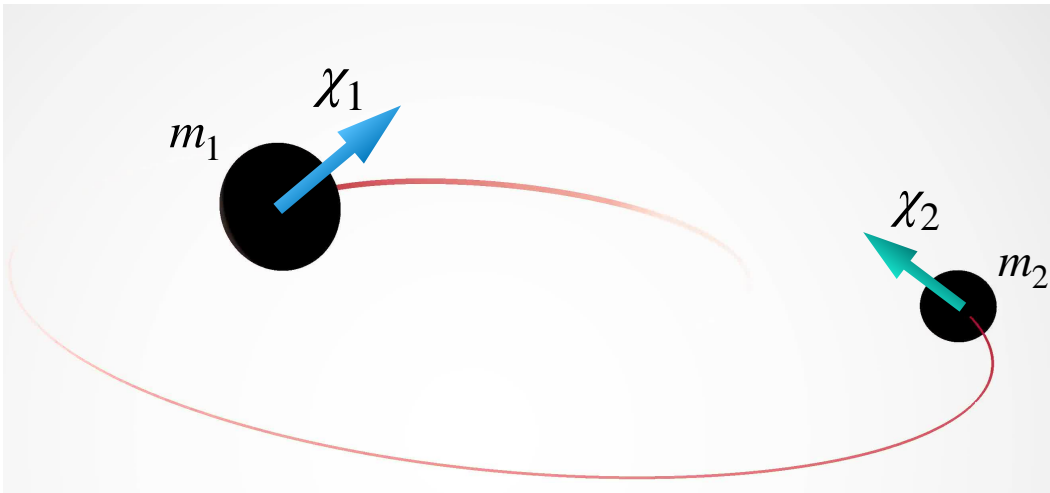


Figure 1.5: Parameters of a quasicircular BBH system. Each BH is characterized by a mass (m) and a spin vector (χ). Note, however, that the total mass scales out in GR, and the mass dependence is captured in a single parameter, the mass ratio $q = m_1/m_2$.

Similarly, a quasicircular BBH system is characterized by seven intrinsic parameters: mass ratio $q = m_1/m_2$, and two spin vectors χ_1, χ_2 (cf. Fig. 1.5). Here, subscript 1 (2) corresponds to the heavier (lighter) of the two BHs. The total mass of the system $M = m_1 + m_2$ can be scaled out and does not constitute an additional parameter.

If the BH spins are (anti-)aligned with respect to the orbital angular momentum, the emitted GWs have monotonically increasing amplitude and frequency. Instead, if the BH spins are misaligned with respect to the orbital angular momentum, relativistic

spin-spin and spin-orbit couplings cause the system to precess [19]. Much like a top whose spin axis is misaligned with the orbital angular momentum, the spins and the orbital angular momentum oscillate about the direction of the total angular momentum. This precession is imprinted on the gravitational waves as characteristic modulations of amplitude and frequency, making it possible to observe precessing BBHs with LIGO/Virgo. Precessing BBHs will be a major theme in Chapters 6, 7, and 8 of this thesis.

1.5 Numerical relativity

One needs to solve Einstein's equations (Eq. (1.2)) to obtain the spacetime metric g_{ab} for any system of interest. However, G_{ab} contains up to second derivatives of g_{ab} , and is nonlinear in g_{ab} . In other words, Einstein's equations are a system of coupled, nonlinear partial differential equations. This makes them notoriously difficult to solve. In fact, there are only a handful of exact, analytical solutions, and all of these correspond to simplified systems with a high degree of symmetry; for example, a stationary, axisymmetric, charged BH.

For more astrophysically relevant systems, such as BBHs, no exact analytical solutions are known. Post-Newtonian (PN) theory (cf. Ref. [20] for a review) provides a perturbative framework to compute approximate solutions. The expansion parameter in PN is the characteristic velocity of the BHs. However, as the BHs are about to merge, they are moving at about half the speed of light and the expansion parameter is no longer small. Similarly, BH perturbation theory can only be used to describe the settling down of the final BH after the merger (cf. Ref. [21] for a review). All perturbative methods break down near the BH merger, and full numerical simulation of Einstein's equations is the only avenue left.

This is the domain of numerical relativity (NR), where the Einstein field equations are reformulated as an initial value problem suitable for numerical solutions. I briefly describe NR here, but refer the reader to Ref. [17] for more details. The reformulation is as follows: The four-dimensional spacetime is broken up into a sequence of three-dimensional space-like hypersurfaces (cf. Fig. 1.6). Rather than work with the spacetime metric g_{ab} , we work with the induced metric g_{ij} on the spatial hypersurfaces, and the extrinsic curvature K_{ij} , which is related to the first time derivative of g_{ij} . The Einstein equations are decomposed into a set of constraint and evolution equations. The constraint equations do not contain any time derivatives of g_{ij} and K_{ij} , therefore they only need to be solved at the initial time slice. Solving

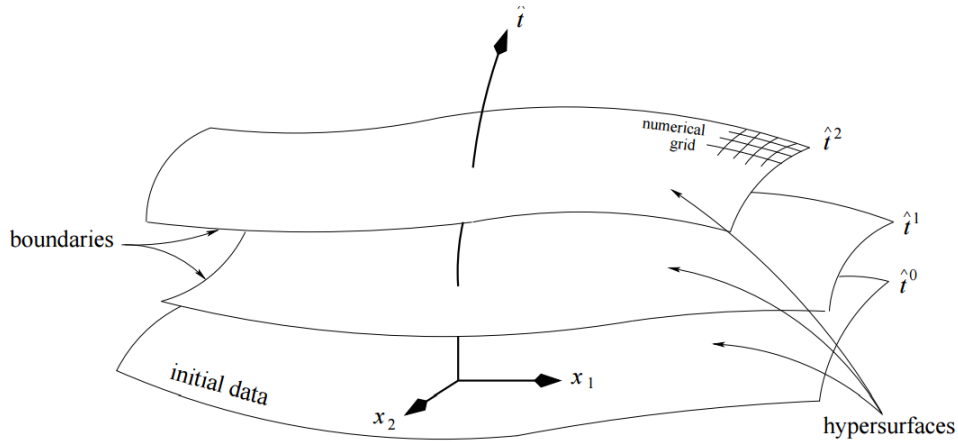


Figure 1.6: Schematic description of NR initial value problem. The constraint equations are solved on the initial hypersurfaces and the evolution equations are used to step forward in time. Credit: H. Dimmelmeier.

the constraint equations gives us initial values for g_{ij} and K_{ij} ; this is referred to as initial data. The evolution equations contain up to first time derivatives of g_{ij} and K_{ij} , and are used to step forward in time, to obtain g_{ij} and K_{ij} for the full spacetime.

The first successful NR simulation of a BH merger was achieved by Frans Pretorius in 2005 [22], after decades of development by various groups [23]. The Spectral Einstein Code (SpEC) [24], developed by the Simulating eXtreme Spacetimes [25] is the current state-of-the-art code for NR simulations. This work relies heavily on this code, as well as makes contributions to it. Chapters 2 and 3 present improvements to the initial data treatment in SpEC, while all other Chapters make use of the simulations performed using SpEC.

1.6 Waveform models

As discussed before, gravitational waves received by our detectors are very weak. This means that they are buried deep in the noise of the detectors. Matched filtering (see Ref. [15] for a review) is the optimal method to search for known signals in noisy data and is applied in LIGO/Virgo data analysis. This method, however, crucially depends on the accuracy of the model used in predicting the gravitational waves; these models are referred to as waveform models.

Apart from the detection of signals buried in noise, we also need waveform models to analyze the signal and identify the properties of the source of the signal; this is referred to as parameter estimation. Parameter estimation typically demands

higher accuracy in waveform models than detection. If the model has significant systematic biases, our understanding of the source properties will also be biased. As the detectors become more sensitive, the statistical biases due to noise become lower, placing higher accuracy requirements on the waveform models.

One of the most important promises of GW astronomy is to test GR in the highly dynamical, strong field regime. BBHs are prime candidates for this, as the gravitational fields are extreme and the BH speeds are relativistic as one approaches the merger. Tests of GR typically place the most stringent accuracy requirements on waveform models, as systematic biases in waveform models could lead to a bias being misidentified as a violation of GR.

Therefore, to maximize the science output of our detectors and to fulfill the promise of GW astronomy, it is vital to have an accurate waveform model. As mentioned in Sec. 1.5, perturbative schemes such as PN break down as one approaches the merger of a BBH, and NR is the only method that can accurately predict the outcome. NR simulations are very accurate, being limited mainly by the resolution of the grid used. However, these simulations are prohibitively expensive for most direct data analysis applications, with each simulation taking about a month on a supercomputer. To see why this is a problem, parameter estimation of a single event can require about 10^7 waveform evaluations in different regions of the 7-dimensional parameter space of BBHs.

Therefore, several approximate waveform models have been developed over the years. The two main approaches have been dubbed "Phenomenological" and "Effective-one-body" waveforms (see Ref. [26] for a review). These models typically make some assumptions about the phenomenology of the waveforms, based on good physical motivations. Then, any remaining free parameters are set by calibrating against NR simulations. These models are also quite fast and have been used in analyzing the signals seen by LIGO/Virgo. While these models have been shown to be accurate enough for current detector sensitivities [27, 28], they typically have a lower accuracy than NR simulations [29].

This raises the question: can we develop a model that can replicate the accuracy of NR, without introducing any additional assumptions, and yet is fast enough for direct data analysis applications? This is where surrogate modeling comes in.

1.7 Surrogate models

Surrogate modeling employs a data-driven approach to waveform modeling. Rather than make assumptions about the underlying phenomenology, one uses the NR waveforms themselves to implicitly reconstruct the phenomenology. Using clever interpolation techniques, the model learns from the NR simulations how the waveform depends on various parameters such as the masses and spins of the BHs.

In this section, I will demonstrate the steps involved in surrogate model construction and evaluation for the simple case of nonspinning BBHs. For these systems, the only free parameter is the mass ratio q . Note that this is a high-level description of the procedure, and I skip several important caveats in favor of simplicity. I refer the reader to Refs. [30, 31] for more details.

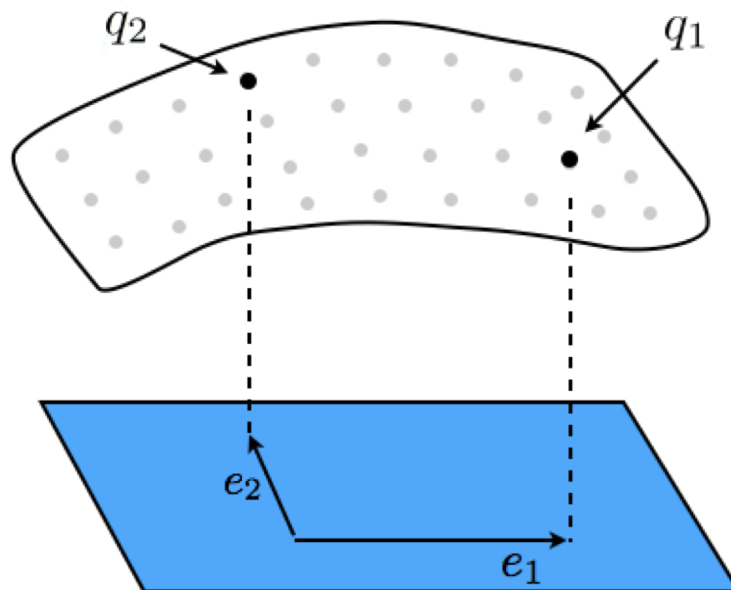


Figure 1.7: Schematic description of reduced basis construction. At the top, we have the dataset of waveforms, which sparsely populates the waveform space. At the bottom, we have the reduced basis, which is constructed using the most representative waveforms from the dataset. Credit: Chad Galley.

Reduced basis

To build a surrogate model, we begin with a dataset of waveforms. This dataset is usually expensive to generate, and only sparsely covers the parameter space of interest (cf. Fig. 1.7); for example, an NR waveform catalog. Our goal is to build a much faster yet accurate interpolant that covers the parameter space of the dataset. In this example, the dataset is comprised of nonspinning NR waveforms with mass

ratio q between 1 and 10. Rather than work with the waveforms directly, which is highly oscillatory, it is typically easier to work with slowly varying functions of time such as the amplitude and phase. So, in this example we will build a surrogate model for the waveform amplitude.

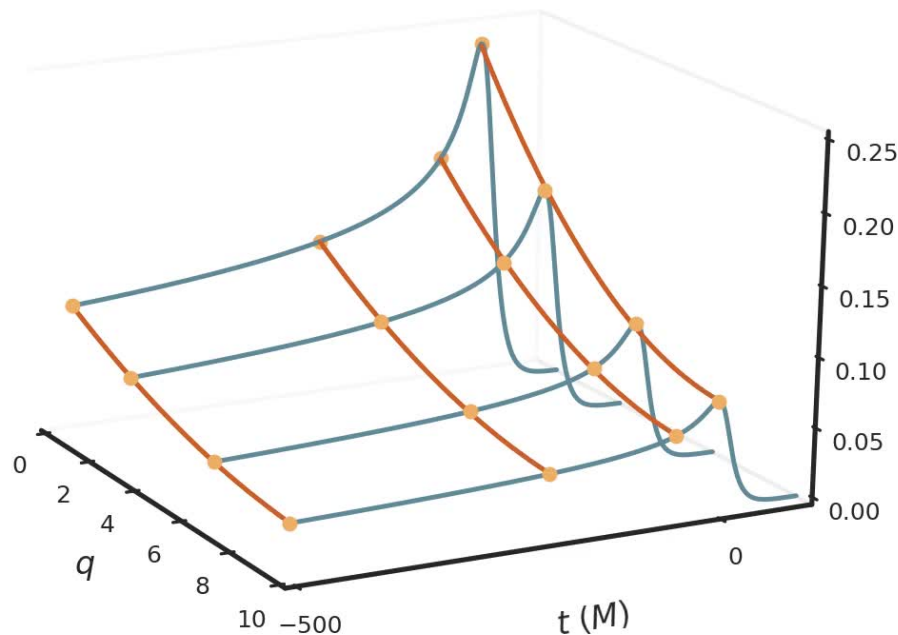


Figure 1.8: Demo of surrogate model construction for nonspinning BBHs. The mass ratio (q) and time are shown on the horizontal axes, while the waveform amplitude is shown on the vertical axis. The blue lines show the reduced basis. The yellow-orange circular markers indicate the empirical time nodes. The red lines indicate the fits across parameter space. A visualization of this procedure is available at vijayvarma392.github.io/SurrogateMovie/#demo.

The first step in the surrogate modeling procedure is to construct an accurate basis that represents our space of waveforms (see Fig. 1.7 for a schematic description). This is done using the very waveforms we are trying to model. The basis functions are picked in an iterative manner such that the most representative waveforms get picked. At each iteration, the waveform that has the largest projection error onto the current basis gets added to the basis for the next iteration. This is done until the largest projection error falls below a certain threshold. Typically, one only requires a handful ($\lesssim 10$) of waveforms to bring the basis projection error down to the resolution error of current NR simulations. At the end of this procedure, we have reduced our large dataset of waveforms down to a small set of basis functions,

without a loss of accuracy. Therefore, the final basis set is called a reduced basis. This is represented by the blue lines in Fig. 1.8.

Empirical interpolation

Given an orthogonal basis, one can easily compute the basis coefficients for any given waveform by basis decomposition. Therefore, we orthonormalize the reduced basis using a modified Gram-Schmidt procedure [30]. Now, if we compute and store the basis coefficients for all waveforms in the dataset, this gives us all the information we need to reproduce the dataset at the required accuracy level. To reproduce any given waveform, one just sums up the basis functions weighted by the basis coefficients.

Unfortunately, this restricts us to the sparse set of waveforms already in the dataset. We cannot generate the waveform at a generic point in parameter space, where we do not *a priori* know the basis coefficients. We could overcome this problem by constructing fits across parameter space for each of the basis coefficients. We instead take a different approach called empirical interpolation, which lets us construct fits for the amplitude directly, which is physically more meaningful.

Empirical interpolation makes use of the reduced basis to construct an effective interpolant in time using only a small set of time values [30]. These time values, called the empirical time nodes, are once again picked iteratively such that the most representative time values are picked. These are represented by the yellow-orange circular markers in Fig. 1.8. The number of empirical time nodes is the same as the number of basis function. Given the amplitude values at each of the empirical time nodes, one can compute the basis coefficients by solving a linear system of equations [30].

Parametric fits

At this point we have reduced our dataset in both parameter space and time directions. To evaluate the waveform at a generic point, the empirical interpolant needs the amplitude values at the empirical time nodes. Therefore, we construct fits across parameter space for the amplitude, at each of the empirical time nodes. This is indicated by the red lines in Fig. 1.8.

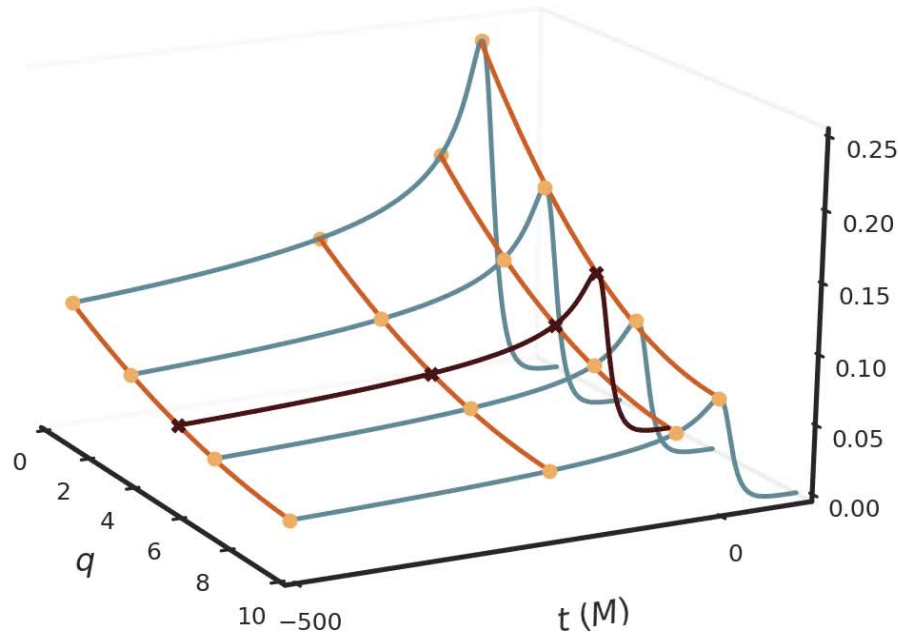


Figure 1.9: Demo of surrogate model evaluation at a generic q . We first evaluate the fits at each empirical time node, as indicated by the brown cross markers. This gives us the basis coefficients. To evaluate the waveform (brown line) at the given q , we just sum up the basis functions weighted by the basis coefficients. A visualization of this procedure is available at vijayvarma392.github.io/SurrogateMovie/#demo.

Evaluation

Finally, to evaluate the waveform at a generic parameter space point: We first evaluate the amplitude fits at that point for each empirical time node. This is indicated by the brown cross markers in Fig. 1.9. As mentioned above, the amplitude values at the empirical time nodes can be used to obtain the basis coefficients. Now, all we need to do is sum up the basis functions with these coefficients as weights, to get the amplitude evaluation at the given point. This is indicated by the brown line in Fig. 1.9.

The basis functions are already chosen such that the projection errors are comparable to the intrinsic NR resolution error. If the fits across parameter space can be done accurately enough, we do not introduce additional errors in the estimation of the basis coefficients. Therefore, the surrogate model accuracy can be comparable to the error in the NR simulations themselves, while taking only a fraction of a second to evaluate. In Chapters 5 and 7, I will present the current state-of-the-art surrogate models for aligned-spin and precessing BBHs, respectively.

1.8 Extending the parameter space of surrogate models

Hybridization

While NR surrogate models are very accurate and fast, they still have one important limitation: they are restricted to the same number of orbits as the NR simulations. Because of the computational expense of these simulations, they are typically restricted to only 20 orbits before merger. Therefore, the surrogate models [29, 31, 32] constructed previously have been rather short, and cover only the late-time, high frequency stage close to the merger. The frequency of the GWs scales as $1/M$, where M is the total mass of the system. This means that low-mass signals enter the LIGO/Virgo detector band early in the inspiral and have a lot of orbits before merger. Therefore, the previous surrogate models have been restricted to $M \gtrsim 57M_{\odot}$. This means that they do not cover the full range of masses for stellar mass BBHs in ground based detectors, which can go down to $M \sim 5M_{\odot}$. See for example, the mass range of the yellow patch in the left panel of Fig. 1.10 corresponding to the NRSur7dq2 model of Ref. [29].

While NR simulations are currently too expensive to include enough orbits to cover low-mass BBHs (although see Ref. [33]), fortunately, PN is accurate when the BHs are far from each other. We can build a “hybrid” of NR and PN, where the early evolution is modeled by PN, and the late time evolution including the merger is modeled by NR. In Chapter 5, I will present NRHybSur3dq8, the first surrogate model based on NR-PN hybrid waveforms.

Generic mass ratios

Another limitation of surrogate models is that they are restricted to the bounds of parameter space set by the NR simulations. NR simulations become very expensive for large mass ratios (q) and large spin magnitudes (χ). For large q , the length scale of the smaller BH demands larger spatial and temporal resolution requirements. For large χ , the BH horizons require significantly more resolution. Therefore, NR simulations have typically been restricted to comparable masses ($q \lesssim 10$) and moderate spins ($\chi \lesssim 0.8$) (although see Refs. [34, 35]).

In addition, the vast 7-dimensional parameter space of precessing BBHs requires a large number of simulations to populate. Therefore, previous surrogate models have been restricted to nearly equal masses ($q \leq 2$), apart from the nonspinning model of Ref. [32]. For aligned-spin BBHs, the parameter space is only 3-dimensional and

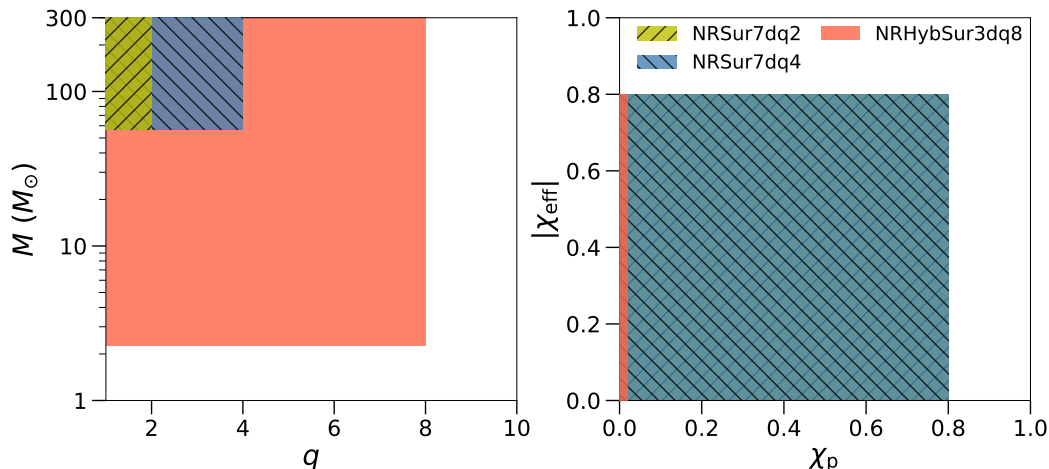


Figure 1.10: Improved coverage of the BBH parameter space over NRSur7dq2 [29] due to the models presented in Chapter 5 (NRHybSur3dq8) and Chapter 7 (NRSur7dq4). **Left:** Coverage of total mass M and mass ratio q . NRHybSur3dq8 covers the full range of total masses relevant for ground based detectors, and extends to $q = 8$. NRSur7dq4 is still limited to high masses, but greatly extends the mass ratio coverage over NRSur7dq2. **Right:** Coverage of spin space. χ_{eff} is the “effective spin” along the orbital angular momentum direction, and χ_p is the effective in-plane spin. Roughly speaking, the larger the χ_p , the larger the effects of precession. NRHybSur3dq8 is an aligned-spin model, therefore it is restricted to $\chi_p = 0$. Note that NRSur7dq2 and NRSur7dq4 are on top of each other here; they are both generically precessing with spin magnitude $\chi \leq 0.8$.

is much easier to populate with simulations, therefore the NRHybSur3dq8 model of Chapter 5 extends to $q = 8$ for aligned-spin BBHs. In addition, the NRSur7dq4 model of Chapter 7 extends to $q = 4$ for precessing BBHs, while still being restricted to pure NR simulations without hybridization. A hybridized, precessing, surrogate model is still in development and will be made available in the future. Figure 1.10 shows the improved coverage of the BBH parameter space due to the NRHybSur3dq8 and NRSur7dq4 models.

1.9 Higher order modes of radiation

The gravitational-wave strain h on a sphere can be conveniently decomposed as

$$h(t, r, \theta, \phi) = \sum_{\ell=2}^{\infty} \sum_{m=-\ell}^{\ell} {}_{-2}Y_{\ell m}(\theta, \phi) h_{\ell m}(t, r), \quad (1.8)$$

where ${}_{-2}Y_{\ell m}$ are the $s = -2$ spin-weighted spherical harmonics [36], t is the time, and (r, θ, ϕ) are the standard spherical polar coordinates. The functions $h_{\ell m}$ are

referred to as the *modes* of the GWs.

The quadrupole modes ($\ell = 2, m \pm 2$) typically dominate the sum in Eq. (1.8), and the other subdominant modes are often ignored for the sake of simplicity. This assumption, however, does not always hold, and the subdominant modes can become important at high mass ratios (q) and when the binary orbit is inclined with respect to the plane of the detector. For these cases, neglecting these modes of radiation can lead to systematic biases in data analysis.

In Chapter 4, I investigate the effects of subdominant modes for LIGO and identify regions of parameter space where these modes are important for detection and parameter estimation. In addition, the waveform models presented in Chapters 5 and 7 include the effects of subdominant modes, along with the quadrupole modes.

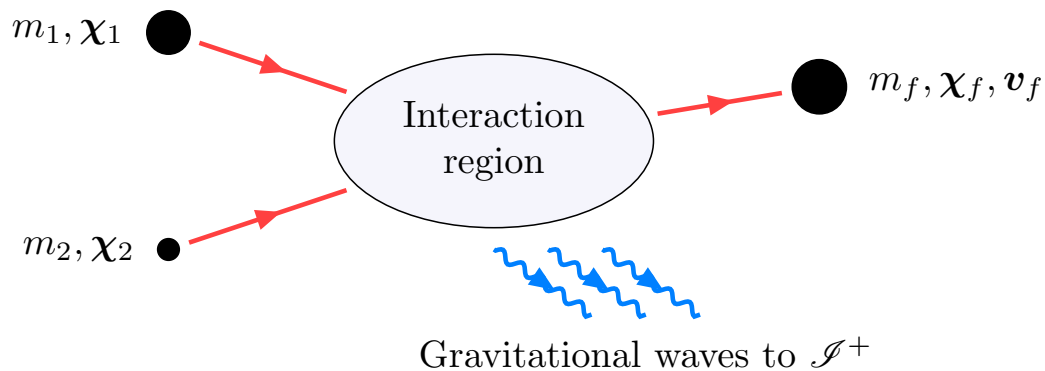


Figure 1.11: BBHs seen from a scattering view point through a “Feynman diagram”. Time flows to the right in this picture. On the left, we have the initial state: the component BHs, characterized by their masses and spins. On the right, we have the final state at the end of the merger: the gravitational waves escaping to future null-infinity, and the final BH characterized entirely by its mass, spin, and a recoil velocity imparted during the merger process. In this picture, the messy merger process is hidden behind the interaction region.

1.10 Testing general relativity

While GR is the current best description of gravity, it is likely an incomplete theory, as it is incompatible with quantum mechanics. Therefore, one might expect GR to break down in certain extreme conditions. Just before the BHs collide, they are moving at about half the speed of light, and the gravity is extreme. This is the most curved that spacetime gets throughout all the Universe, except for during the Big

Bang. Therefore, gravitational waves from a BH merger provide the most stringent tests of GR.

Here, I will discuss one particular test of GR with GWs from BBH systems [37, 38], but see Ref. [39] for a review of tests of GR with GWs. As described in Sec. 1.4, both BHs and BBH systems are characterized by a small set of parameters. We can take advantage of this and use Nature as our particle accelerator to test GR. As seen from a high-energy physics scattering view point (see Fig. 1.11), two accelerated BHs smash into each other and a single final BH emerges along with the GWs. The masses and spins of the initial BHs can be inferred from the GWs: as mentioned in Sec. 1.6, this involves parameter estimation with an accurate waveform model. In addition, due to the no-hair theorem, the GW signal after the final BH has formed has specific characteristic frequencies that depend only on the mass and spin of the final BH. This can be used to infer the final BH's mass and spin. We can also get the final BH's mass and spin in an independent manner: by performing an NR simulation starting from the initial BHs and evolving the spacetime through merger. If GR agrees with the observed signal, both estimates of the final BH's mass and spin should agree with each other.

1.11 Remnant black hole surrogate models

The key ingredient in the above test is the map from the initial BHs to the final BH provided by NR. Therefore, apart from the waveform, the final BH properties are the most widely used outputs from NR simulations. Again, because the NR simulations are too expensive for direct use in data analysis, several approximate models have been developed that predict the final BH's mass and spin (see Ref. [40] for a review). These models, however, are all phenomenological in nature; one first comes up with an ansatz based on perturbation theory and physical intuition, and then calibrates any free parameters to NR simulations.

This problem, however, is ideally suited to the data-driven approach of surrogate modeling. In Chapter 6, I will present the first surrogate model for the final BH's mass, spin, and recoil kick velocity. With this in place, surrogate models are now capable of reproducing all of the important outputs of NR simulations, cheaply and without a loss of accuracy.

1.12 Binary black holes on a laptop

Only 16 years ago, it was considered a remarkable achievement to numerically simulate a single orbit of a BBH close to merger [41]. However, we have come a long way since Pretorius's 2005 breakthrough [22]. The SXS collaboration recently published a catalog [42] of 2,018 BBH NR waveforms, with a median length of ~ 20 orbits. Perhaps in the future, NR will become advanced enough to generate simulations on one's personal laptop or even a mobile phone, rather than a supercomputer.

In the meantime, surrogate models provide an excellent alternative to a full NR simulation, by accurately yet cheaply reproducing the main outputs of the simulation: the waveform and the final BH properties. To demonstrate this in practice, Chapter 8 presents a visualization package based on the surrogate models of Chapters 6 and 7. Previously, visualizations of BBH systems required a supercomputer NR simulation that lasted for a month, followed by expensive rendering. With this package, you can generate a visualization that is just as accurate, in a few seconds on your laptop. This demonstrates the power of surrogate models: from supercomputers to your laptop!

1.13 Thesis outline

The rest of the thesis is organized as follows.

Chapter 2 presents work towards constructing BBH initial data in the preferred gauge of SpEC, the damped harmonic gauge. This work was published as Physical Review D., 98, 084032 (2018), [arxiv:1808.07490](https://arxiv.org/abs/1808.07490).

Chapter 3 presents various improvements to the initial data in SpEC, including better boundary conditions, reduced unwanted initial transients, and more computationally efficient evolution. This work was published as Physical Review D., 98, 104011 (2018), [arxiv:1808.08228](https://arxiv.org/abs/1808.08228).

Chapter 4 presents work in identifying regions in the parameter space of BBH systems where gravitational wave models must include the effects of the subdominant modes. This work was published as Physical Review D., 96, 124024 (2017), [arxiv:1612.05608](https://arxiv.org/abs/1612.05608).

Chapter 5 presents the first surrogate model based on hybrid waveforms for aligned-spin BBH, and therefore covers the full range of frequencies relevant for ground

based detectors. This work was published as *Physical Review D.*, 99, 064045 (2019), [arxiv:1812.07865](https://arxiv.org/abs/1812.07865).

Chapter 6 presents the first surrogate model for the mass, spin, and recoil kick velocity of the final BH left behind after a BBH merger. This work was published as *Physical Review Letters*, 122, 011101 (2019), [arxiv:1809.09125](https://arxiv.org/abs/1809.09125).

Chapter 7 presents an extension of existing precessing BBH surrogate models to larger mass ratios. A manuscript based on this work is in preparation.

Chapter 8 presents a Python visualization package based on surrogate models for precessing BBH. This work was published as *Classical and Quantum Gravity*, 36, 095007 (2019), [arxiv:1811.06552](https://arxiv.org/abs/1811.06552).

References

- [1] B. P. Abbott et al. “Observation of Gravitational Waves from a Binary Black Hole Merger”. In: *Phys. Rev. Lett.* 116 (6 Feb. 2016), p. 061102. DOI: [10.1103/PhysRevLett.116.061102](https://doi.org/10.1103/PhysRevLett.116.061102). URL: <http://link.aps.org/doi/10.1103/PhysRevLett.116.061102>.
- [2] Benjamin P. Abbott et al. “The basic physics of the binary black hole merger GW150914”. In: *Annalen Phys.* 529.1-2 (2017), p. 1600209. DOI: [10.1002/andp.201600209](https://doi.org/10.1002/andp.201600209). arXiv: [1608.01940](https://arxiv.org/abs/1608.01940) [gr-qc].
- [3] J. Aasi et al. “Advanced LIGO”. In: 32 (2015), p. 074001. DOI: [10.1088/0264-9381/32/7/074001](https://doi.org/10.1088/0264-9381/32/7/074001). arXiv: [1411.4547](https://arxiv.org/abs/1411.4547) [gr-qc].
- [4] A. Einstein. “Zur Elektrodynamik bewegter Körper”. In: *Annalen der Physik* 17: 891. (1905). URL: https://web.archive.org/web/20050220050316/http://www.pro-physik.de/Phy/pdfs/ger_890_921.pdf.
- [5] A. Einstein. “Die Feldgleichungen der Gravitation”. In: *Sitzungsberichte der Preussischen Akademie der Wissenschaften zu Berlin*: 844–847. (1915). URL: <http://digilib.mpiwg-berlin.mpg.de/digitallibrary/jquery/digilib.html?fn=/permanent/einstein/sitzungsberichte/6E3MAXK4/pageimg>.
- [6] A. Einstein. “Näherungsweise Integration der Feldgleichungen der Gravitation”. In: *Sitzungsberichte der Königlich Preussischen Akademie der Wissenschaften (Berlin)*, Seite 688-696. (1916).
- [7] A. Einstein. “Über Gravitationswellen”. In: *Sitzungsberichte der Königlich Preussischen Akademie der Wissenschaften (Berlin)*, Seite 154-167. (1918).
- [8] nobelprize.org/prizes/physics/2017.

- [9] F. Acernese et al. “Advanced Virgo: a second-generation interferometric gravitational wave detector”. In: 32.2 (2015), p. 024001. doi: [10.1088/0264-9381/32/2/024001](https://doi.org/10.1088/0264-9381/32/2/024001). arXiv: [1408.3978](https://arxiv.org/abs/1408.3978) [gr-qc].
- [10] B. P. Abbott et al. “GWTC-1: A Gravitational-Wave Transient Catalog of Compact Binary Mergers Observed by LIGO and Virgo during the First and Second Observing Runs”. In: (2018). arXiv: [1811.12907](https://arxiv.org/abs/1811.12907) [astro-ph.HE].
- [11] Bernard F. Schutz. *A First Course in General Relativity*. 2nd. New York: Cambridge University Press, 2009.
- [12] James B. Hartle. *Gravity: An Introduction to Einstein’s General Relativity*. New York: Addison-Wesley, 2003.
- [13] Sean Carroll. *Spacetime and Geometry: An Introduction to General Relativity*. New York: Addison Wesley, 2003.
- [14] Charles W. Misner, Kip S. Thorne, and John Archibald Wheeler. *Gravitation*. New York, New York: Freeman, 1973. doi: [10.1002/asna.19752960110](https://doi.org/10.1002/asna.19752960110).
- [15] B.S. Sathyaprakash and Bernard F. Schutz. “Physics, Astrophysics and Cosmology with Gravitational Waves”. In: *Living Reviews in Relativity* 12.2 (2009). doi: [10.1007/lrr-2009-2](https://doi.org/10.1007/lrr-2009-2). URL: <http://www.livingreviews.org/lrr-2009-2>.
- [16] M Maggiore. *Gravitational Waves - Volume 1*. First. New York, NY: Oxford University Press, 2008.
- [17] Thomas W. Baumgarte and Stuart L. Shapiro. *Numerical Relativity: Solving Einstein’s Equations on the Computer*. New York: Cambridge University Press, 2010. doi: [10.1080/00107514.2011.586052](https://doi.org/10.1080/00107514.2011.586052).
- [18] B. Carter. “Axisymmetric Black Hole Has Only Two Degrees of Freedom”. In: *Phys. Rev. Lett.* 26 (6 Feb. 1971), pp. 331–333. doi: [10.1103/PhysRevLett.26.331](https://doi.org/10.1103/PhysRevLett.26.331). URL: <https://link.aps.org/doi/10.1103/PhysRevLett.26.331>.
- [19] Theocharis A. Apostolatos et al. “Spin induced orbital precession and its modulation of the gravitational wave forms from merging binaries”. In: *Phys. Rev. D* 49 (1994), pp. 6274–6297. doi: [10.1103/PhysRevD.49.6274](https://doi.org/10.1103/PhysRevD.49.6274).
- [20] Luc Blanchet. “Gravitational Radiation from Post-Newtonian Sources and Inspiralling Compact Binaries”. In: *Living Rev. Rel.* 17 (2014), p. 2. doi: [10.12942/lrr-2014-2](https://doi.org/10.12942/lrr-2014-2). arXiv: [1310.1528](https://arxiv.org/abs/1310.1528) [gr-qc].
- [21] Emanuele Berti, Vitor Cardoso, and Andrei O. Starinets. “Quasinormal modes of black holes and black branes”. In: *Class. Quant. Grav.* 26 (2009), p. 163001. doi: [10.1088/0264-9381/26/16/163001](https://doi.org/10.1088/0264-9381/26/16/163001). arXiv: [0905.2975](https://arxiv.org/abs/0905.2975) [gr-qc].

- [22] Frans Pretorius. “Evolution of binary black hole spacetimes”. In: 95 (2005), p. 121101. DOI: [10.1103/PhysRevLett.95.121101](https://doi.org/10.1103/PhysRevLett.95.121101). arXiv: [gr-qc/0507014](https://arxiv.org/abs/gr-qc/0507014) [gr-qc].
- [23] Ulrich Sperhake. “The numerical relativity breakthrough for binary black holes”. In: *Class. Quant. Grav.* 32.12 (2015), p. 124011. DOI: [10.1088/0264-9381/32/12/124011](https://doi.org/10.1088/0264-9381/32/12/124011). arXiv: [1411.3997](https://arxiv.org/abs/1411.3997) [gr-qc].
- [24] *The Spectral Einstein Code*. <http://www.black-holes.org/SpEC.html>.
- [25] *Simulating eXtreme Spacetimes*. <http://www.black-holes.org/>.
- [26] Frank Ohme. “Analytical meets numerical relativity - status of complete gravitational waveform models for binary black holes”. In: *Class. Quant. Grav.* 29 (2012), p. 124002. DOI: [10.1088/0264-9381/29/12/124002](https://doi.org/10.1088/0264-9381/29/12/124002). arXiv: [1111.3737](https://arxiv.org/abs/1111.3737) [gr-qc].
- [27] B. P. Abbott et al. “Effects of waveform model systematics on the interpretation of GW150914”. In: (2016). arXiv: [1611.07531](https://arxiv.org/abs/1611.07531) [gr-qc].
- [28] B. P. Abbott et al. “Directly comparing GW150914 with numerical solutions of Einstein’s equations for binary black hole coalescence”. In: *Phys. Rev. D* 94 (6 Sept. 2016), p. 064035. DOI: [10.1103/PhysRevD.94.064035](https://doi.org/10.1103/PhysRevD.94.064035). URL: <http://link.aps.org/doi/10.1103/PhysRevD.94.064035>.
- [29] Jonathan Blackman et al. “Numerical relativity waveform surrogate model for generically precessing binary black hole mergers”. In: *Phys. Rev. D* 96.2 (2017), p. 024058. DOI: [10.1103/PhysRevD.96.024058](https://doi.org/10.1103/PhysRevD.96.024058). arXiv: [1705.07089](https://arxiv.org/abs/1705.07089) [gr-qc].
- [30] S. E. Field et al. “Fast Prediction and Evaluation of Gravitational Waveforms Using Surrogate Models”. In: 4.3, 031006 (July 2014), p. 031006. DOI: [10.1103/PhysRevX.4.031006](https://doi.org/10.1103/PhysRevX.4.031006). arXiv: [1308.3565](https://arxiv.org/abs/1308.3565) [gr-qc].
- [31] Jonathan Blackman et al. “A Surrogate Model of Gravitational Waveforms from Numerical Relativity Simulations of Precessing Binary Black Hole Mergers”. In: *Phys. Rev. D* 95.10 (2017), p. 104023. DOI: [10.1103/PhysRevD.95.104023](https://doi.org/10.1103/PhysRevD.95.104023). arXiv: [1701.00550](https://arxiv.org/abs/1701.00550) [gr-qc].
- [32] Jonathan Blackman et al. “Fast and Accurate Prediction of Numerical Relativity Waveforms from Binary Black Hole Coalescences Using Surrogate Models”. In: *Phys. Rev. Lett.* 115.12 (2015), p. 121102. DOI: [10.1103/PhysRevLett.115.121102](https://doi.org/10.1103/PhysRevLett.115.121102). arXiv: [1502.07758](https://arxiv.org/abs/1502.07758) [gr-qc].
- [33] B. Szilágyi et al. “Approaching the Post-Newtonian Regime with Numerical Relativity: A Compact-Object Binary Simulation Spanning 350 Gravitational-Wave Cycles”. In: 115 (2015), p. 031102. DOI: [10.1103/PhysRevLett.115.031102](https://doi.org/10.1103/PhysRevLett.115.031102). arXiv: [1502.04953](https://arxiv.org/abs/1502.04953) [gr-qc].

- [34] M. A. Scheel et al. “Improved methods for simulating nearly extremal binary black holes”. In: 32.10, 105009 (May 2015), p. 105009. DOI: [10.1088/0264-9381/32/10/105009](https://doi.org/10.1088/0264-9381/32/10/105009). arXiv: [1412.1803](https://arxiv.org/abs/1412.1803) [gr-qc].
- [35] Carlos O. Lousto and Yosef Zlochower. “Orbital Evolution of Extreme-Mass-Ratio Black-Hole Binaries with Numerical Relativity”. In: *Phys. Rev. Lett.* 106 (2011), p. 041101. DOI: [10.1103/PhysRevLett.106.041101](https://doi.org/10.1103/PhysRevLett.106.041101). arXiv: [1009.0292](https://arxiv.org/abs/1009.0292) [gr-qc].
- [36] J. N. Goldberg et al. “Spin- s Spherical Harmonics and δ ”. In: *Journal of Mathematical Physics* 8.11 (1967), pp. 2155–2161. DOI: [10.1063/1.1705135](https://doi.org/10.1063/1.1705135). URL: <http://link.aip.org/link/?JMP/8/2155/1>.
- [37] B. P. Abbott et al. “Tests of General Relativity with GW150914”. In: *Phys. Rev. Lett.* 116 (22 May 2016), p. 221101. DOI: [10.1103/PhysRevLett.116.221101](https://doi.org/10.1103/PhysRevLett.116.221101). URL: <http://link.aps.org/doi/10.1103/PhysRevLett.116.221101>.
- [38] A. Ghosh et al. “Testing general relativity using gravitational wave signals from the inspiral, merger and ringdown of binary black holes”. In: *CQG* 35.1, 014002 (Jan. 2018), p. 014002. DOI: [10.1088/1361-6382/aa972e](https://doi.org/10.1088/1361-6382/aa972e). arXiv: [1704.06784](https://arxiv.org/abs/1704.06784) [gr-qc].
- [39] Nicolás Yunes and Xavier Siemens. “Gravitational-Wave Tests of General Relativity with Ground-Based Detectors and Pulsar Timing-Arrays”. In: *Living Rev. Rel.* 16 (2013), p. 9. DOI: [10.12942/lrr-2013-9](https://doi.org/10.12942/lrr-2013-9). arXiv: [1304.3473](https://arxiv.org/abs/1304.3473) [gr-qc].
- [40] D. Gerosa and M. Kesden. “precession: Dynamics of spinning black-hole binaries with python”. In: *PRD* 93.12, 124066 (June 2016), p. 124066. DOI: [10.1103/PhysRevD.93.124066](https://doi.org/10.1103/PhysRevD.93.124066). arXiv: [1605.01067](https://arxiv.org/abs/1605.01067) [astro-ph.HE].
- [41] Bernd Bruegmann, Wolfgang Tichy, and Nina Jansen. “Numerical simulation of orbiting black holes”. In: *Phys. Rev. Lett.* 92 (2004), p. 211101. DOI: [10.1103/PhysRevLett.92.211101](https://doi.org/10.1103/PhysRevLett.92.211101). arXiv: [gr-qc/0312112](https://arxiv.org/abs/gr-qc/0312112) [gr-qc].
- [42] Michael Boyle et al. “The SXS Collaboration catalog of binary black hole simulations”. In: (2019). arXiv: [1904.04831](https://arxiv.org/abs/1904.04831) [gr-qc].

*Chapter 2***CONSTRUCTING A BOOSTED, SPINNING BLACK HOLE IN
THE DAMPED HARMONIC GAUGE**

Vijay Varma and Mark A. Scheel, *Physical Review D.*, 98, 084032 (2018),
[arxiv:1808.07490](https://arxiv.org/abs/1808.07490).

2.1 Executive summary

NR simulations begin with a solution of the Einstein constraint equations at the initial time; this is referred to as initial data. The initial data formalism used in SpEC allows some quantities such as the conformal 3-metric to be specified freely; these quantities are referred to as free data. Despite this freedom, the choice of free data is important, particularly to control unwanted initial transients. Another important choice one makes in NR is the gauge choice; a bad gauge choice can lead to coordinate singularities. This Chapter presents work towards constructing initial data in SpEC in the preferred gauge choice in SpEC, the damped harmonic gauge. We construct a numerical solution for a single black hole in this gauge, which will be used to construct initial data in this gauge in Chapter 3.

2.2 Abstract

The damped harmonic gauge is important for numerical relativity computations based on the generalized harmonic formulation of Einstein's equations, and is used to reduce coordinate distortions near binary black hole mergers. However, currently there is no prescription to construct quasiequilibrium binary black hole initial data in this gauge. Instead, initial data are typically constructed using a superposition of two boosted analytic single black hole solutions as free data in the solution of the constraint equations. Then, a smooth time-dependent gauge transformation is done early in the evolution to move into the damped harmonic gauge. Using this strategy to produce initial data in damped harmonic gauge would require the solution of a single black hole in this gauge, which is not known analytically. In this work we construct a single boosted, spinning, equilibrium black hole in damped harmonic coordinates as a regular time-independent coordinate transformation from Kerr-Schild coordinates. To do this, we derive and solve a set of four coupled, nonlinear,

elliptic equations for this transformation, with appropriate boundary conditions. This solution can now be used in the construction of damped harmonic initial data for binary black holes.

2.3 Introduction

Gauge freedom is one of the most elegant features of general relativity. Numerical relativity, however, inherently breaks this freedom, since one picks a particular set of coordinates to represent the solution on the computer. Gauge choices are particularly important in numerical relativity, since a poor gauge choice can lead to coordinate singularities.

Here we consider numerical relativity simulations that use the generalized harmonic formulation of the Einstein equations [1–4]. In this formalism, the coordinates x^a obey

$$\nabla^c \nabla_c x^a = H^a, \quad (2.1)$$

where the gauge source function H^a is an arbitrarily chosen function of the coordinates and of the 4-metric ψ_{ab} , but not of the derivatives of the 4-metric. Here ∇_a is the covariant derivative operator compatible with ψ_{ab} . The coordinates x^a are treated as four scalars in Eq. (2.1), so that one can write $\nabla^c \nabla_c x^a = -\psi^{bc} {}^{(4)}\Gamma^a{}_{bc}$, where ${}^{(4)}\Gamma^a{}_{bc}$ are the Christoffel symbols associated with ψ_{ab} . Despite the considerable freedom allowed in the choice of H^a , in practice it is not straightforward to choose an H^a that leads to coordinates without singularities or large distortions.

One gauge choice that has been particularly successful in the numerical evolution of binary black hole (BBH) mergers is to choose H^a to satisfy the damped harmonic gauge [5–7], given by Eqs. (2.6) below. In damped harmonic gauge, the spatial coordinates and the lapse function obey damped wave equations, and the damping terms suppress spatial and temporal coordinate distortions that grow large near merging black hole horizons when using simpler gauge choices. Damped harmonic gauge is a key ingredient in BBH simulations that use the generalized harmonic formulation of Einstein’s equations [8].

In this paper we are interested in combining damped harmonic gauge with another property that is often desirable in BBH simulations: initial data that is as close to equilibrium (in a co-rotating frame) as possible. If the initial data, including the gauge degrees of freedom, are close to stationary in a co-rotating frame, then the

subsequent evolution will be slowly-varying in this frame (at least during the inspiral phase), leading to higher accuracy and lower computational cost. However, there is currently no good prescription for constructing BBH initial data that satisfy both the properties of quasiequilibrium and of damped harmonic gauge.

To further motivate the desire for BBH simulations that share both of these properties, consider in more detail the construction of initial data for BBH simulations using the code SpEC [9], which we use as an example in this paper. Initial data are constructed [10] using the Extended Conformal Thin Sandwich (XCTS) [11, 12] formalism, which is a reformulation of the Einstein constraint equations. The free data in this formalism are the conformal 3-metric \tilde{g}_{ij} , the trace of the extrinsic curvature K , and the initial time derivatives of these quantities $\partial_t \tilde{g}_{ij}$ and $\partial_t K$. These time derivatives are customarily set to zero in a co-rotating frame; this is meant as a quasi-equilibrium condition. The other free data, \tilde{g}_{ij} and K , are constructed by superposing the analytic expressions for the (non-conformal) three-metric g_{ij} and K of two single black holes (BHs) in Kerr-Schild [13, 14] coordinates. With this choice of free data, the XCTS equations are solved to yield a constraint satisfying initial data set.

The generalized harmonic evolution equations require as initial data the initial values and time derivatives of all components of the 4-metric. The solution of the XCTS equations determines all of these except for the initial time derivatives $\partial_t N$ and $\partial_t N^i$ of the lapse N and shift N^i . These initial time derivatives are customarily chosen to be zero in a co-rotating frame at $t = 0$; these are additional quasi-equilibrium conditions meant to reduce initial gauge dynamics. By rewriting the Christoffel symbols in Eq. (2.1) in terms of time derivatives of the lapse and shift, these quasi-equilibrium conditions can be written as conditions on H^0 and H^i :

$$0 = \partial_t N = N^j \partial_j N - N^2 K + N^3 H^0, \quad (2.2)$$

$$0 = \partial_t N^i = N^j \partial_j N^i - N^2 g^{ij} \partial_j (\log N) + N^2 \Gamma^i + N^2 (H^i + N^i H^0). \quad (2.3)$$

Here g_{ij} is the spatial metric, and Γ^i is the Christoffel symbol associated with g_{ij} . Note that H^a thus constructed does not necessarily satisfy the damped harmonic gauge condition.

The quasi-equilibrium initial H^a constructed above is typically used only during the very early inspiral of the BBH system. Once the black holes approach each other, this choice of H^a leads to coordinate singularities. So early in the evolution

a time-dependent gauge transformation is done to gradually change H^a from its initial quasiequilibrium value into damped harmonic gauge. Unfortunately, this gauge transformation can lead to several complications: (1) The early evolution of the BBH initial data described above is typically discarded as it is contaminated by spurious transients generally referred to as *junk radiation* [15, 16]. The junk radiation is caused by several physical effects, such as the initial ringdown of each BH to its correct equilibrium shape. The transformation to damped harmonic gauge that begins near the start of the evolution introduces gauge dynamics, making it difficult to separate the physical junk radiation from gauge effects. (2) In full general relativity there is no analytic expression for the orbital parameters of two compact objects that yields a quasi-circular orbit. So to produce initial data describing a quasi-circular binary, we use an iterative procedure [17] in which we guess orbital parameters, evolve the binary for a few orbits, measure the eccentricity from the (coordinate) trajectories of the BHs, and then compute new lower-eccentricity orbital parameters for the next iteration. This procedure occurs at early times while the gauge transformation (which affects BH trajectories) is active, and this might make it difficult to achieve a desired eccentricity. (3) Typically, the evolution becomes more computationally expensive during the gauge transition, because of additional gauge dynamics that must be resolved. (4) It is difficult to start simulations at close separations, because merger occurs so quickly that there is not enough time to transition smoothly to damped harmonic gauge before merger.

Therefore, there are several possible benefits in constructing BBH initial data that satisfy the damped harmonic gauge condition and are in quasi-equilibrium. If one could construct a time-independent representation of a *single black hole* in damped harmonic coordinates, then one could construct quasi-equilibrium damped harmonic BBH data by using a superposition of two single BHs in these coordinates, rather than in Kerr-Schild coordinates, as free data in the XCTS system. This would produce quasi-equilibrium BBH data that are nearly in damped harmonic gauge near each of the two black holes. We know that a time-independent solution for a single BH in damped harmonic coordinates exists, because this is the final state of the merged black hole in BBH simulations done in the damped harmonic gauge. Unfortunately, the form of such a single-BH solution is not known analytically.

In this work, we construct a numerical solution for a boosted, spinning single BH in damped harmonic coordinates. This is done as a regular, time independent, coordinate transformation from Kerr-Schild coordinates. We show that one needs to

solve a set of four coupled, nonlinear, elliptic equations for this transformation. After imposing appropriate boundary conditions, we solve these equations numerically. Finally, we test our solution using a single BH evolution: We evolve a single BH that starts in Kerr-Schild coordinates and then transitions into the damped harmonic gauge. We show that the final steady state of this evolution agrees with our solution for a single BH in damped harmonic coordinates.

Given the single-BH coordinate representation presented here, one can construct initial data for a binary BH in damped harmonic gauge by superposing two such single BHs. We discuss the binary case in a separate work [18], in which we construct, evolve, and compare several BBH initial data sets (including those initially in harmonic gauge and in damped harmonic gauge), and in which we also introduce new boundary conditions for the XCTS equations.

The rest of the paper is organized as follows. Section 2.4 describes the damped harmonic gauge. In Sec 2.5, we develop a method to construct a boosted, spinning single BH in the damped harmonic gauge. In Sec 2.6 we validate our solution using a single BH evolution. Finally, in Sec 2.7 we provide some concluding remarks. Throughout this paper we use geometric units with $G = c = 1$. We use Latin letters from the start of the alphabet (a, b, c, \dots) for spacetime indices and from the middle of the alphabet (i, j, k, \dots) for spatial indices. We use ψ_{ab} for the spacetime metric, g_{ab} for the spatial metric, N for the lapse and N^i for the shift of the constant- t hypersurfaces.

2.4 Damped harmonic gauge

In this section we describe the damped harmonic gauge in more detail. But instead of immediately discussing the damped harmonic gauge, we start first with the simpler case of the harmonic gauge, which is defined by the condition that each coordinate satisfies the covariant scalar wave equation:

$$\nabla^c \nabla_c x^a = 0. \tag{2.4}$$

Harmonic coordinates are not unique: different coordinates can satisfy Eq. (2.4) but have different initial conditions and boundary values.

Harmonic coordinates have proven to be extremely useful in analytic studies in general relativity [19–23], but numerical simulations of BBH in this gauge tend to fail as they approach the merger stage. One reason for these failures might be

that Eq. (2.4) does not sufficiently constrain the coordinates; for example it admits dynamical wavelike solutions. Since all physical fields in numerical relativity are expressed in terms of the coordinates, an ideal gauge condition would eliminate these unwanted gauge dynamics.

The dynamical range available to harmonic coordinates can be reduced by adding a damping term, resulting in the damped harmonic gauge [6]:

$$\nabla^c \nabla_c x^a = H_{DH}^a, \quad (2.5)$$

$$H_{DH}^a = \mu_L \log\left(\frac{\sqrt{g}}{N}\right) t^a - \mu_S N^{-1} g_i^a N^i. \quad (2.6)$$

Here t^a is the future directed unit normal to constant- t hypersurfaces, $g_{ab} = \psi_{ab} + t_a t_b$ is the spatial metric of the constant- t hypersurfaces, g is the determinant of this metric, N is the lapse, N^i is the shift, and μ_L and μ_S are positive damping factors chosen as follows:

$$\mu_S = \mu_L = \mu_0 \left[\log\left(\frac{\sqrt{g}}{N}\right) \right]^2, \quad (2.7)$$

where

$$\mu_0 = f_0(t) \exp\left(-a \frac{R^2}{w^2}\right). \quad (2.8)$$

Equation (2.7) describes the dependence of the damping factors on metric components, and Eq. (2.8) describes rolloff factors that are used to reduce damped harmonic gauge to harmonic gauge far from the origin or at early times. In Eq. (2.8), R is the Euclidean distance from the origin and w is a length scale which we choose to be $100M$, where M is the total mass of the system. The dimensionless constant a is chosen to be 34.54, so that the Gaussian factor reaches a value of 10^{-15} at $R = w$. Finally, $f_0(t)$ is an optional smooth function of time that we include if the evolution is meant to transition from a different gauge into damped harmonic gauge; this function is zero before the transition and unity afterwards. The precise values of the constants w and a are not important for the success of damped harmonic gauge in BBH simulations; any choice that results in $\mu_0 \sim 1$ near the black holes and $\mu_0 = 0$ near the outer boundary should suffice.

This choice of the gauge source function H_{DH}^a has the following benefits [6]: (1) The spatial coordinates x^i satisfy a damped wave equation and are driven towards solutions of the covariant spatial Laplace equation on a timescale of $1/\mu_S$. This tends to reduce extraneous gauge dynamics when $1/\mu_S$ is chosen to be smaller than

the characteristic physical timescale. (2) Similarly, the lapse satisfies a damped wave equation with damping factor μ_L [5]. (3) This gauge condition controls the growth of \sqrt{g}/N , which tends to blow up near black hole horizons near merger in simpler gauges like the harmonic gauge. (4) The gauge source function H_{DH}^a depends only on the coordinates and the spacetime metric, but not on the derivatives of the metric. This means that this gauge condition preserves the principal part of the Einstein equations in the generalized harmonic formalism [24], and hence preserves symmetric hyperbolicity. Like harmonic coordinates, damped harmonic coordinates are not unique: any initial coordinate choice can be evolved using Eq. (2.5) and will satisfy the damped harmonic condition.

2.5 Boosted, spinning black hole in damped harmonic gauge

First consider harmonic (not damped harmonic) coordinates. Although harmonic coordinates are not unique, there is a unique coordinate representation of a single boosted, charged, spinning black hole that satisfies the harmonic coordinate condition Eq. (2.4), is time-independent, and is regular at the event horizon. This coordinate representation can be determined analytically [23] by considering a regular coordinate transformation from Kerr-Schild coordinates.

The situation is similar for damped harmonic coordinates. In this section, we construct the unique coordinate representation of a boosted, spinning single black hole that satisfies the damped harmonic condition, Eqs. (2.5)–(2.6), is time-independent, and is regular at the event horizon. Following Ref. [23], we construct this solution by considering a coordinate transformation from Kerr-Schild coordinates. But unlike the case of harmonic coordinates, for damped harmonic coordinates we will obtain a numerical rather than an analytical solution.

Starting with Kerr-Schild coordinates (denoted by $x^{\bar{a}}$), we try to find a transformation to new coordinates x^a that satisfy the damped harmonic condition,

$$\nabla^c \nabla_c x^a = \frac{\partial_b (\sqrt{-\psi} \psi^{ab})}{\sqrt{-\psi}} = H_{DH}^a, \quad (2.9)$$

where ψ is the determinant of the spacetime metric ψ_{ab} .

For simplicity, we start with Kerr-Schild coordinates that represent an unboosted black hole. However, we desire our damped harmonic coordinates to represent a boosted black hole, so that we can use them in BBH initial data where the two BHs are in orbit. To obtain a boosted BH we can apply a Lorentz transformation. For fully

harmonic coordinates (as opposed to damped harmonic coordinates), adding a boost is not difficult, because applying a Lorentz transformation to harmonic coordinates results in boosted coordinates that still satisfy the harmonic gauge condition [23]. However, this is not true for damped harmonic gauge. To see this, consider a set of coordinates $x^{\hat{a}}$, related to x^a by a Lorentz transformation:

$$x^a = \Lambda^a_{\hat{b}} x^{\hat{b}}. \quad (2.10)$$

Because $\Lambda^a_{\hat{a}}$ has only constant components and its determinant is unity, Eq. (2.9) is transformed into:

$$\frac{\partial_{\hat{b}} \left(\sqrt{-\hat{\psi}} \psi^{\hat{a}\hat{b}} \right)}{\sqrt{-\hat{\psi}}} = \nabla^{\hat{c}} \nabla_{\hat{c}} x^{\hat{a}} = \Lambda^{\hat{a}}_{\ a} H^a_{DH}. \quad (2.11)$$

As H^a_{DH} is not a tensor, $H^{\hat{a}}_{DH} \neq \Lambda^{\hat{a}}_{\ a} H^a_{DH}$, so the transformed coordinates $x^{\hat{a}}$ do not satisfy the damped harmonic condition. Therefore instead of constructing unboosted damped harmonic coordinates and boosting the coordinates afterwards, we must build the boost into the coordinate construction, by demanding that the transformed coordinates $x^{\hat{a}}$ satisfy Eq. (2.11).

Similarly, we desire a BH solution with an arbitrary spin direction, but it is most straightforward to work with Kerr-Schild coordinates with spin along the z-axis. In order to construct damped harmonic coordinates with generic spins, we can apply an additional rotation transformation $R^{\tilde{b}}_{\hat{b}}$ to Eq. (2.11).

Combining the boost and the rotation, the equation that must be satisfied for the coordinates x^a to obey the damped harmonic condition and to have the desired boost and spin direction is

$$\frac{\partial_{\hat{b}} \left(\sqrt{-\hat{\psi}} \psi^{\hat{a}\hat{b}} \right)}{\sqrt{-\hat{\psi}}} = \nabla^{\hat{c}} \nabla_{\hat{c}} x^{\hat{a}} = T^{\hat{a}}_{\ a} H^a_{DH}, \quad (2.12)$$

where

$$x^a = T^a_{\hat{b}} x^{\hat{b}}, \quad (2.13)$$

$$T^a_{\hat{b}} = \Lambda^a_{\tilde{b}} R^{\tilde{b}}_{\hat{b}}. \quad (2.14)$$

We proceed as follows: we start with unboosted Kerr-Schild coordinates $x^{\bar{a}}$ with spin in the z-direction and find a transformation to intermediate coordinates $x^{\hat{a}}$ such

that $x^{\hat{a}}$ satisfies the condition Eq. (2.12). This means that x^a , related to $x^{\hat{a}}$ by Eq. (2.13), satisfies the damped harmonic condition (Eq. (2.5)), while having the desired spin direction and boost with respect to $x^{\bar{a}}$.

Transformation to damped harmonic gauge

We define a time-independent transformation from the Kerr-Schild coordinates $x^{\bar{a}}$ to intermediate coordinates $x^{\hat{a}}$ as follows:

$$\begin{aligned} x^{\hat{0}} &= x^{\bar{0}} + 2M \log \left(\frac{2M}{r - r_-} \right) + U^{\hat{0}}(x^{\bar{i}}), \\ x^{\hat{1}} &= x^{\bar{1}} - M \sin \theta \cos \phi + U^{\hat{1}}(x^{\bar{i}}), \\ x^{\hat{2}} &= x^{\bar{2}} - M \sin \theta \sin \phi + U^{\hat{2}}(x^{\bar{i}}), \\ x^{\hat{3}} &= x^{\bar{3}} - M \cos \theta + U^{\hat{3}}(x^{\bar{i}}), \end{aligned} \quad (2.15)$$

where M is the mass of the black hole, $r_- = M - \sqrt{M^2 - a^2}$ is the radius of the Cauchy horizon, a is the Kerr spin parameter and (r, θ, ϕ) are the spatial coordinates of the spherical coordinate version of the standard Kerr-Schild coordinates [13]:

$$r^2 = \frac{\sum_{\bar{i}=1}^3 (x^{\bar{i}})^2 - a^2}{2} + \sqrt{\frac{\left(\sum_{\bar{i}=1}^3 (x^{\bar{i}})^2 - a^2\right)^2}{4} + (ax^{\bar{3}})^2} \quad (2.16)$$

$$\cos \theta = \frac{x^{\bar{3}}}{r} \quad (2.17)$$

$$\cos \phi = \frac{rx^{\bar{1}} + ax^{\bar{2}}}{(r^2 + a^2) \sin \theta} \quad (2.18)$$

Using Eq. (2.15), the left hand side of Eq. (2.12) can be written in terms of the Jacobian of the transformation $J^{\hat{a}}_{\bar{a}} = \partial x^{\hat{a}} / \partial x^{\bar{a}}$:

$$\frac{\partial_{\bar{b}} \left(\sqrt{-\hat{\psi}} \psi^{\hat{a}\hat{b}} \right)}{\sqrt{-\hat{\psi}}} = \partial_{\bar{b}} \left(J^{\hat{a}}_{\bar{a}} \psi^{\bar{a}\bar{b}} \right). \quad (2.19)$$

Note that the Jacobian depends on first derivatives of $U^{\hat{a}}$, so this is a second-order elliptic equation for $U^{\hat{a}}$.

Elliptic equations

After substituting the explicit form of the Kerr-Schild metric [13] $\psi^{\bar{a}\bar{b}}$ into Eq. (2.12), and using Eq. (2.19), a lengthy but straightforward computation yields:

$$\mathcal{L}U^{\hat{a}} = T^{\hat{a}}_a H^a_{DH}, \quad (2.20)$$

$$\mathcal{L} = \frac{\partial_r(\Delta\partial_r)}{\rho^2} + \frac{\partial_\theta(\sin\theta\partial_\theta)}{\rho^2 \sin\theta} + \frac{\partial_\phi^2}{\rho^2 \sin^2\theta} + \frac{2a\partial_r\partial_\phi}{\rho^2}, \quad (2.21)$$

where \mathcal{L} is a linear differential operator, $\Delta = r^2 - 2Mr + a^2$, and $\rho^2 = r^2 + a^2 \cos^2\theta$.

On the right hand side of these equations, H^a_{DH} is obtained from Eq. (2.6):

$$H^0_{DH} = \frac{\mu_0}{N} \left[\log \left(\frac{\sqrt{-\psi}}{N^2} \right) \right]^3, \quad (2.22)$$

$$H^i_{DH} = \frac{-\mu_0 N^i}{N} \left[\log \left(\frac{\sqrt{-\psi}}{N^2} \right) \right]^2 \left[1 + \log \left(\frac{\sqrt{-\psi}}{N^2} \right) \right], \quad (2.23)$$

where

$$N = \sqrt{\frac{1}{-\psi^{00}}}, \quad (2.24)$$

$$N^i = N^2 \psi^{0i}, \quad (2.25)$$

$$\psi^{ab} = T^a_{\hat{a}} T^b_{\hat{b}} J^{\hat{a}}_{\hat{a}} J^{\hat{b}}_{\hat{b}} \psi^{\bar{a}\bar{b}}, \quad (2.26)$$

and ψ is the determinant of ψ_{ab} .

Finally, following Eq. (2.8), we get

$$\mu_0 = \exp \left(-a \frac{\sum_i x^i x^i}{w^2} \right), \quad (2.27)$$

$$x^i = T^i_{\hat{a}} J^{\hat{a}}_{\hat{a}} x^{\bar{a}}. \quad (2.28)$$

Eqs. 2.20 are a set of four coupled, nonlinear elliptic equations with three independent variables (r, θ, ϕ) . Note that the left hand side of Eq. (2.20) is linear in the functions $U^{\hat{a}}$ and all the nonlinearities come from the source function H^a_{DH} as seen in Eqs. (2.22) and (2.23) (the functions $U^{\hat{a}}$ appear in the Jacobians $J^{\hat{a}}_{\hat{a}}$). For harmonic coordinates, as the gauge source function is zero, the four equations are decoupled, linear, and separable in the radial and polar coordinates [23]. In the more general case of damped harmonic coordinates, obtaining an analytical solution is

very challenging because the equations are coupled and nonlinear. Therefore, we solve these elliptic equations numerically, using a spectral elliptic solver [25].

It is interesting to note that the principal part of the elliptic equations is entirely on the left hand side, as H_{DH}^a has only up to first derivatives of the functions $U^{\hat{a}}$ (in the form of the Jacobians). Hence, the principal part is the same as that for harmonic coordinates, derived in Ref. [23].

Boundary conditions

Before we can solve the elliptic equations derived above, we need to impose suitable boundary conditions. The elliptic equations have three independent variables (r, θ, ϕ) . We do not need to specify a boundary condition for θ and ϕ as we use spherical harmonic basis functions for the angular part in the elliptic solver. For the radial outer boundary condition, we impose asymptotic flatness. Note that Eq. (2.15) is equivalent to writing $x^{\hat{a}} = x_h^a + U^{\hat{a}}$, where x_h^a are the fully harmonic coordinates of Ref. [23]. Because x_h^a are already asymptotically flat, our boundary condition is

$$U^{\hat{a}} \Big|_{r \rightarrow \infty} = 0. \quad (2.29)$$

For the boundary condition at the inner radial boundary, consider the elliptic equations, Eqs. (2.20) and (2.21), with the radial derivatives expanded,

$$\begin{aligned} \frac{\Delta \partial_r^2 U^{\hat{a}}}{\rho^2} + \frac{2(r-M) \partial_r U^{\hat{a}}}{\rho^2} + \frac{\partial_\theta (\sin \theta \partial_\theta U^{\hat{a}})}{\rho^2 \sin \theta} \\ + \frac{2a \partial_r \partial_\phi U^{\hat{a}}}{\rho^2} + \frac{\partial_\phi^2 U^{\hat{a}}}{\rho^2 \sin^2 \theta} = T_a^{\hat{a}} H_{DH}^a. \end{aligned} \quad (2.30)$$

Now, $\Delta = 0$ at $r = r_+ = M + \sqrt{M^2 - a^2}$, the event horizon. Therefore, at $r = r_+$ the first term of Eq. (2.30) goes to zero and the nature of the principal part changes. In order to ensure regularity of coordinates at the event horizon we restrict the domain to $[r_+, \infty)$ and impose a regularity boundary condition at r_+ :

$$\begin{aligned} \frac{2(r-M) \partial_r U^{\hat{a}}}{\rho^2} + \frac{\partial_\theta (\sin \theta \partial_\theta U^{\hat{a}})}{\rho^2 \sin \theta} + \frac{\partial_\phi^2 U^{\hat{a}}}{\rho^2 \sin^2 \theta} \\ + \frac{2a \partial_r \partial_\phi U^{\hat{a}}}{\rho^2} = T_a^{\hat{a}} H_{DH}^a \quad \text{at } r \rightarrow r_+. \end{aligned} \quad (2.31)$$

¹In practice, the outer boundary is set at a radius $\sim 10^{15}$ times the mass of the BH.

Convergence tests

Having chosen suitable boundary conditions for the elliptic equations, we solve them numerically using a spectral elliptic solver [25]. Our domain consists of 12 concentric spherical shells extending from the horizon r_+ to $10^{15}M$, distributed roughly exponentially in radius. Each shell has the same number of angular collocation points and approximately the same number of radial points. The number of collocation points in each subdomain is set by specifying an error tolerance to our adaptive mesh refinement (AMR) algorithm [26, 27].

The elliptic solver yields a solution for the intermediate coordinates $x^{\hat{a}}$, from which we obtain the damped harmonic coordinates x^a using Eq. (2.13). To quantify how well the final coordinates x^a actually satisfy the damped harmonic gauge condition (Eq. (2.5)), we define normalized damped harmonic constraints and constraint energy²:

$$C_{DH}^a = \frac{\|\psi^{bc} {}^{(4)}\Gamma^a{}_{bc} + H_{DH}^a\|}{\left\| \sqrt{\sum_{a,b,c=0}^3 [(\psi^{bc} {}^{(4)}\Gamma^a{}_{bc})^2 + (H_{DH}^a)^2]} \right\|}, \quad (2.32)$$

$$C_{DH} = \sqrt{\sum_{a=0}^3 C_{DH}^a C_{DH}^a}, \quad (2.33)$$

where $\|\cdot\|$ is the L^2 norm over the domain. The numerator of Eq. (2.32) is zero if Eq. (2.5) is exactly satisfied, and the denominator of Eq. (2.32) is chosen so that a solution very far from damped harmonic gauge has C_{DH}^a of order unity.

Figure 2.1 shows the values of the damped harmonic constraints as a function of numerical resolution, where higher resolution is achieved by setting a lower AMR error tolerance. We note that the constraints decrease exponentially with resolution, as expected for a spectral method.

Choosing a time slice

The solution of the elliptic equations along with Eq. (2.13) gives us a transformation from Kerr-Schild coordinates ($x^{\hat{a}}$) to damped harmonic coordinates (x^a). But the

²Notice that for the denominator of Eq. (2.32) below, repeated indices are summed over *after* squaring the quantities, unlike the standard summation notation.

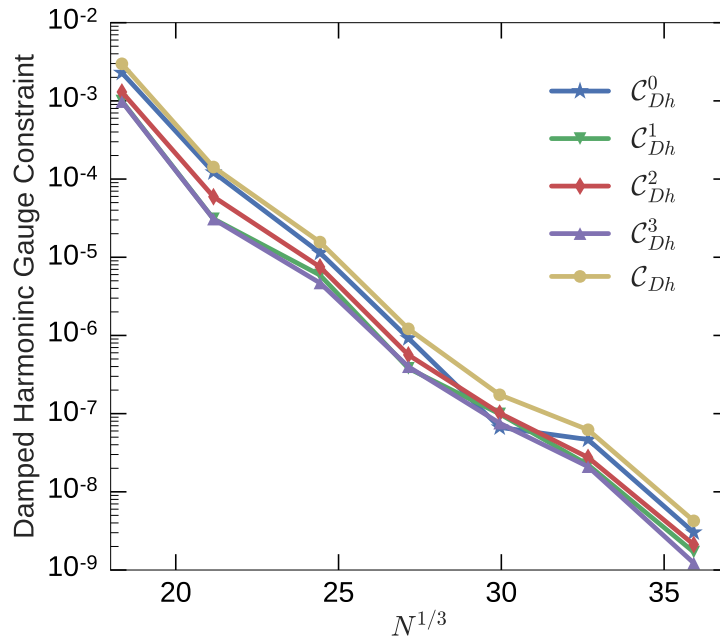


Figure 2.1: Convergence test for solving the elliptic equations (Eq. (2.20)) to construct a single BH in the damped harmonic gauge. Plotted are the damped harmonic constraints (cf. Eqs. (2.32) and (2.33)) as a function of the number of collocation points per dimension in the domain. As expected for spectral methods, the constraints converge exponentially.

desired initial data requires computing the metric and its derivatives on a slice of constant time in the new coordinates x^a , so it is necessary to construct such a slice as a function of the Kerr-Schild coordinates. Using Eq. (2.13), we can construct a $x^0 = 0$ slice as follows:

$$x^0 = 0 = T^0_{\hat{a}} x^{\hat{a}}, \quad (2.34)$$

$$x^{\hat{0}} = \frac{-T^0_{\hat{i}}}{T^0_{\hat{0}}} x^{\hat{i}}, \quad (2.35)$$

$$x^i = T^i_{\hat{a}} x^{\hat{a}} = \frac{-T^i_{\hat{0}} T^0_{\hat{i}}}{T^0_{\hat{0}}} x^{\hat{i}} + T^i_{\hat{j}} x^{\hat{j}}. \quad (2.36)$$

This gives us a constant-time slice of damped harmonic coordinates ($x^0 = 0$, x^i) in terms of the intermediate coordinates ($x^{\hat{a}}$), which in turn are expressed as a transformation from Kerr-Schild coordinates (Eqs. (2.15)).

The final step in constructing single-BH initial data is to compute the metric and its derivatives on a slice of constant $x^0 = 0$. This is done by choosing a set of points in the new coordinates ($x^0 = 0$, x^i), computing the corresponding $x^{\hat{a}}$ using

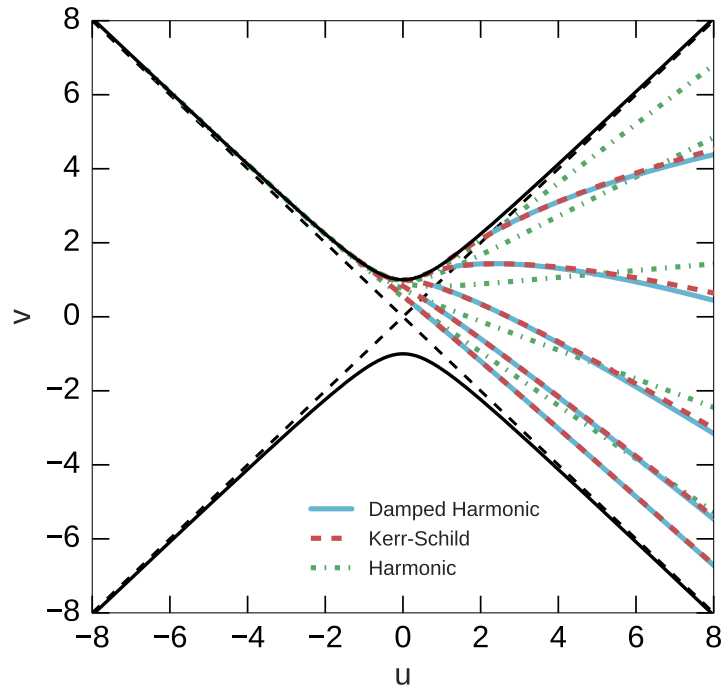


Figure 2.2: Kruskal-Szekeres diagram showing constant time slices of the unique horizon-penetrating time-independent slicings of Schwarzschild spacetime in damped harmonic and harmonic coordinates, and constant time slices in Kerr-Schild coordinates. The solid black curves represent the curvature singularity while the dashed black lines represent the event horizon. Note that the damped harmonic slices only extend up to the event horizon because we restrict our numerical solution to this region; nevertheless, the damped harmonic slices are horizon-penetrating. Interestingly, we see that the damped harmonic slices are quite close to the Kerr-Schild slices.

Eqs. (2.35) and (2.36), computing the corresponding Kerr-Schild coordinates $x^{\bar{a}}$ using Eqs. (2.15), and evaluating the metric and its derivatives analytically at those values of $x^{\bar{a}}$ using the Kerr-Schild expressions. The components of the metric and its derivatives are then transformed using the Jacobians (and Hessians for the metric derivatives) that relate $x^{\bar{a}}$ and x^a .

To visualize the embedding of these damped harmonic slices in spacetime, we restrict ourselves to a nonspinning BH with zero boost. In this spherically symmetric case, we can use the Kruskal-Szekeres coordinates to display the time slices on a spacetime diagram. These are shown in Fig 2.2, along with constant Kerr-Schild time slices and constant time slices of the unique time-independent horizon-penetrating harmonic slicing of Schwarzschild spacetime [23]. We note that constant time

slices of damped harmonic coordinates lie nearly on top of the constant time slices of Kerr-Schild coordinates, indicating that the extrinsic curvature of the two slicings are quite similar.

2.6 Validation against single black hole simulations

In this section, we check whether the solution we constructed in Sec. 2.5 agrees with the time-independent final state of a single BH that begins in some different gauge and is evolved numerically using damped harmonic gauge conditions.

We start with a single BH on a $t = 0$ slice of Kerr-Schild coordinates, and we evolve it using the following time-dependent gauge source function:

$$H^a(t) = \widehat{H}^a e^{-t^4/\sigma^4} + H_{DH}^a. \quad (2.37)$$

Here \widehat{H}^a is the equilibrium gauge source function satisfying Eqs. (2.2) and (2.3) for a single Kerr black hole in Kerr-Schild coordinates. It is computed analytically as a known function of t and x^i during the evolution. H_{DH}^a is the damped harmonic gauge source function given by Eq. (2.6) and Eq. (2.7), where we set $f_0(t) = 1 - e^{-t^4/\sigma^4}$. During the evolution, H_a is computed numerically using live values of the metric and its derivatives. We choose the time scale of the gauge transformation, σ , to be $50M$. At early times, the BH remains time-independent in Kerr-Schild coordinates, then there is a transition on a timescale of $50M$ in which the solution is dominated by gauge dynamics, and at late times the solution obeys the damped harmonic gauge condition and settles down to a time-independent state.

Figure 2.3 shows the evolution of certain components of the metric as the evolution progresses. These are compared against the single BH damped harmonic solution of Sec. 2.5. The final steady state solution of the simulation agrees with our solution for the time-independent single BH in damped harmonic coordinates. We note that the extrinsic curvature, lapse and shift of the initial state, which is a black hole in Kerr-Schild coordinates, are quite close to the corresponding quantities in the final state; these are all quantities that depend on the embedding of the constant time hypersurfaces in spacetime. We have already seen from Fig. 2.2 that for zero spin, this embedding is very similar for Kerr-Schild and damped harmonic slicings; Fig. 2.3 suggests that this embedding is also similar for nonzero spin.

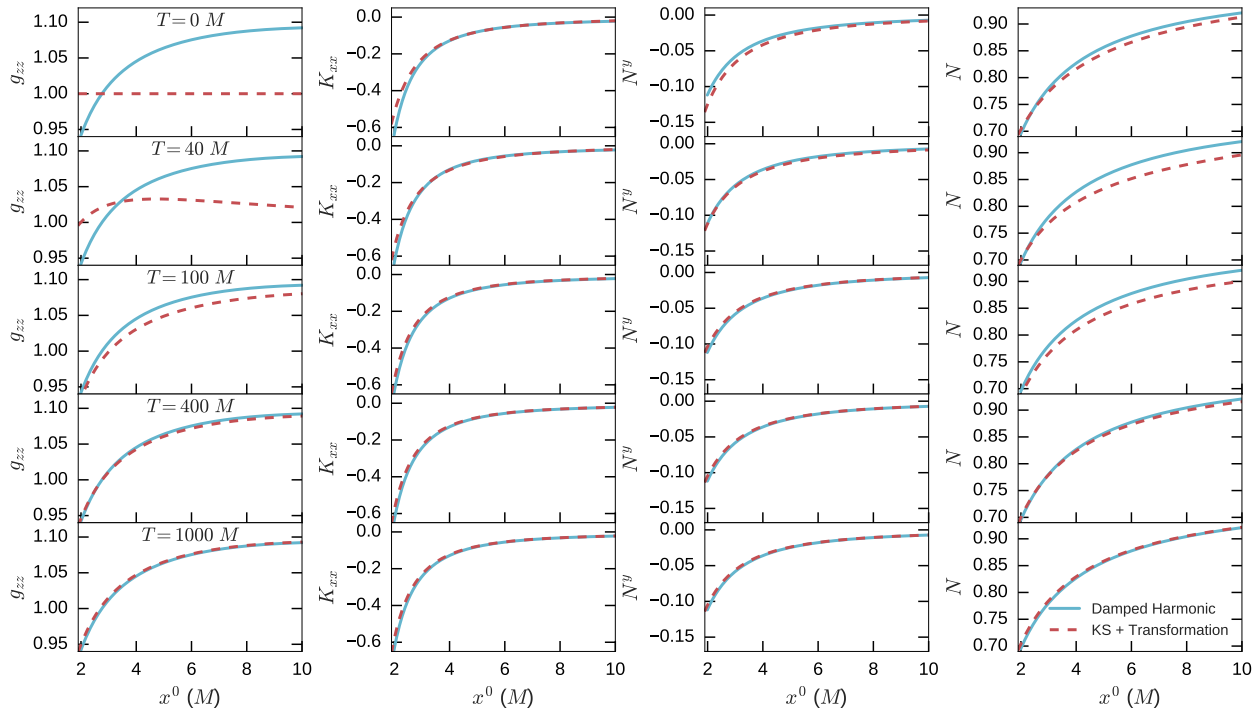


Figure 2.3: Snapshots during the evolution of a single BH with mass, $M = 1$ and dimensionless spin, $\chi_z = 0.5$, starting in Kerr-Schild coordinates and moving into damped harmonic coordinates over a time scale of $50M$. Certain components of the spatial metric g_{ij} , extrinsic curvature K_{ij} , shift N^i and lapse N along the x -axis are shown as dashed red lines as the evolution progresses. The horizontal axis shows the x coordinate. For each column, time flows downwards and is shown in the left most column. The solid blue lines show our solution for a single time-independent BH in damped harmonic gauge, as described in Sec. 2.5. This solution agrees with the final state of the evolution.

2.7 Conclusion

The damped harmonic gauge has been useful for simulations of binary black hole spacetimes, and is a key ingredient for handling mergers in simulations that use the generalized harmonic formalism. However, currently there is no prescription to construct quasi-equilibrium binary black hole initial data in this gauge; until now, there has been no prescription to construct even a time-independent *single* black hole in this gauge.

In this work we have developed a method to construct a time-independent boosted, spinning single black hole in damped harmonic gauge. We start with a black hole in Kerr-Schild coordinates, and we construct a coordinate transformation to damped harmonic coordinates. This transformation involves the numerical solution of four

coupled, nonlinear elliptic equations with appropriate boundary conditions. We solve these equations with a spectral elliptic solver, and we verify that the solution agrees with the final time-independent state of a single black hole that begins in Kerr-Schild coordinates and is evolved using the damped harmonic gauge.

Our procedure to construct a time-independent boosted, spinning, single BH in damped harmonic coordinates can now be used to construct equilibrium BBH initial data that satisfies the damped harmonic gauge. This is done by superposing two time-independent damped-harmonic BH solutions, in the same way that BBH initial data is currently built by superposing two time-independent Kerr-Schild BH solutions.

The next step is to use the solutions here to construct a BBH initial data set in damped harmonic gauge, evolve it, and compare with evolutions of BBH initial data sets in harmonic gauge and in superposed Kerr-Schild coordinates. This is done in a separate work, Ref. [18].

2.8 Acknowledgments

This work was supported in part by the Sherman Fairchild Foundation and NSF grants PHY-1404569, PHY-1708212, and PHY-1708213 at Caltech. The simulations were performed on the Wheeler cluster at Caltech, which is supported by the Sherman Fairchild Foundation and Caltech.

References

- [1] Helmut Friedrich. “On the hyperbolicity of Einstein’s and other gauge field equations”. In: 100.4 (1985), pp. 525–543. DOI: [10.1007/BF01217728](https://doi.org/10.1007/BF01217728). URL: <http://www.springerlink.com/content/w602g633428x8365>.
- [2] David Garfinkle. “Harmonic coordinate method for simulating generic singularities”. In: 65.4 (2002), p. 044029.
- [3] Frans Pretorius. “Evolution of binary black hole spacetimes”. In: 95 (2005), p. 121101. DOI: [10.1103/PhysRevLett.95.121101](https://doi.org/10.1103/PhysRevLett.95.121101). arXiv: [gr-qc/0507014](https://arxiv.org/abs/gr-qc/0507014) [gr-qc].
- [4] Lee Lindblom et al. “A New Generalized Harmonic Evolution System”. In: 23 (2006), S447. DOI: [10.1088/0264-9381/23/16/S09](https://doi.org/10.1088/0264-9381/23/16/S09). arXiv: [gr-qc/0512093v3](https://arxiv.org/abs/gr-qc/0512093v3) [gr-qc].
- [5] Lee Lindblom and Béla Szilágyi. “An Improved Gauge Driver for the GH Einstein System”. In: 80 (2009), p. 084019. eprint: [arXiv:0904.4873](https://arxiv.org/abs/0904.4873).

- [6] Bela Szilagyi, Lee Lindblom, and Mark A. Scheel. “Simulations of Binary Black Hole Mergers Using Spectral Methods”. In: *Phys.Rev. D*80 (2009), p. 124010. DOI: [10.1103/PhysRevD.80.124010](https://doi.org/10.1103/PhysRevD.80.124010). arXiv: [0909.3557](https://arxiv.org/abs/0909.3557) [gr-qc].
- [7] Matthew W. Choptuik and Frans Pretorius. “Ultra Relativistic Particle Collisions”. In: 104 (2010), p. 111101. DOI: [10.1103/PhysRevLett.104.111101](https://doi.org/10.1103/PhysRevLett.104.111101). arXiv: [0908.1780](https://arxiv.org/abs/0908.1780) [gr-qc].
- [8] A. H. Mroué et al. “A Catalog of 174 Binary Black Hole Simulations for Gravitational Wave Astronomy”. In: 111 (2013), p. 241104. arXiv: [1304.6077](https://arxiv.org/abs/1304.6077) [gr-qc].
- [9] The Spectral Einstein Code. URL: <http://www.black-holes.org/SpEC.html>.
- [10] Geoffrey Lovelace et al. “Binary-black-hole initial data with nearly-extremal spins”. In: *Phys. Rev. D*78 (2008), p. 084017. DOI: [10.1103/PhysRevD.78.084017](https://doi.org/10.1103/PhysRevD.78.084017). arXiv: [0805.4192](https://arxiv.org/abs/0805.4192) [gr-qc].
- [11] James W. York. “Conformal “Thin-Sandwich” Data for the Initial-Value Problem of General Relativity”. In: 82.7 (Feb. 1999), pp. 1350–1353. DOI: [10.1103/PhysRevLett.82.1350](https://doi.org/10.1103/PhysRevLett.82.1350).
- [12] Harald P. Pfeiffer and James W. York. “Extrinsic curvature and the Einstein constraints”. In: 67.4 (Feb. 2003), p. 044022. DOI: [10.1103/PhysRevD.67.044022](https://doi.org/10.1103/PhysRevD.67.044022).
- [13] Charles W. Misner, Kip S. Thorne, and John Archibald Wheeler. *Gravitation*. New York, New York: Freeman, 1973. DOI: [10.1002/asna.19752960110](https://doi.org/10.1002/asna.19752960110).
- [14] Matt Visser. “The Kerr spacetime: A Brief introduction”. In: *Kerr Fest: Black Holes in Astrophysics, General Relativity and Quantum Gravity Christchurch, New Zealand, August 26-28, 2004*. 2007. arXiv: [0706.0622](https://arxiv.org/abs/0706.0622) [gr-qc]. URL: <https://inspirehep.net/record/752316/files/arXiv:0706.0622.pdf>.
- [15] Fan Zhang and Béla Szilágyi. “Joint approach for reducing eccentricity and spurious gravitational radiation in binary black hole initial data construction”. In: 88 (8 Oct. 2013). arXiv:1309.1141, p. 084033. DOI: [10.1103/PhysRevD.88.084033](https://doi.org/10.1103/PhysRevD.88.084033). arXiv: [1309.1141](https://arxiv.org/abs/1309.1141) [gr-qc]. URL: <http://link.aps.org/doi/10.1103/PhysRevD.88.084033>.
- [16] Geoffrey Lovelace. “Reducing spurious gravitational radiation in binary-black-hole simulations by using conformally curved initial data”. In: *Class. Quant. Grav.* 26 (2009), p. 114002. DOI: [10.1088/0264-9381/26/11/114002](https://doi.org/10.1088/0264-9381/26/11/114002). arXiv: [0812.3132](https://arxiv.org/abs/0812.3132) [gr-qc].

- [17] A. Buonanno et al. “Reducing orbital eccentricity of precessing black-hole binaries”. In: 83.10 (May 2011), p. 104034. DOI: [10.1103/PhysRevD.83.104034](https://doi.org/10.1103/PhysRevD.83.104034).
- [18] Vijay Varma, Mark A. Scheel, and Harald P. Pfeiffer. “Comparison of binary black hole initial data sets”. In: *Phys. Rev. D* 98.10 (2018), p. 104011. DOI: [10.1103/PhysRevD.98.104011](https://doi.org/10.1103/PhysRevD.98.104011). arXiv: [1808.08228](https://arxiv.org/abs/1808.08228) [gr-qc].
- [19] T. DeDonder. *La Gravifique Einsteinienne*. Paris: Gunthier-Villars, 1921.
- [20] C. Lanczos. “Ein vereinfachtes Koordinatensystem für die Einsteinschen Gravitationsgleichungen”. In: *Phys. Z.* 23 (1922), pp. 537–539.
- [21] Y. Fourès-Bruhat. “Théorème d’existence pour certains systèmes d’équations aux dérivées partielles non linéaires”. In: *Acta Math.* 88 (1952), pp. 141–225.
- [22] A. E. Fischer and J. E. Marsden. “The Einstein evolution equations as a first-order quasi-linear symmetric hyperbolic system”. In: 28 (1972), pp. 1–38.
- [23] Gregory B. Cook and Mark A. Scheel. “Well-behaved harmonic time slices of a charged, rotating, boosted black hole”. In: 56.8 (1997), p. 4775.
- [24] L. Lindblom et al. “A new generalized harmonic evolution system”. In: 23 (Aug. 2006), S447. DOI: [10.1088/0264-9381/23/16/S09](https://doi.org/10.1088/0264-9381/23/16/S09). eprint: [gr-qc/0512093](https://arxiv.org/abs/gr-qc/0512093).
- [25] H. P. Pfeiffer et al. “A multidomain spectral method for solving elliptic equations”. In: 152 (May 2003), pp. 253–273. DOI: [10.1016/S0010-4655\(02\)00847-0](https://doi.org/10.1016/S0010-4655(02)00847-0). eprint: [gr-qc/0202096](https://arxiv.org/abs/gr-qc/0202096).
- [26] S. Ossokine et al. “Improvements to the construction of binary black hole initial data”. In: 32.24, 245010 (Dec. 2015), p. 245010. DOI: [10.1088/0264-9381/32/24/245010](https://doi.org/10.1088/0264-9381/32/24/245010). arXiv: [1506.01689](https://arxiv.org/abs/1506.01689) [gr-qc].
- [27] B. Szilágyi. “Key elements of robustness in binary black hole evolutions using spectral methods”. In: *Int. J. Mod. Phys. D* 23, 1430014 (May 2014), p. 1430014. DOI: [10.1142/S0218271814300146](https://doi.org/10.1142/S0218271814300146). arXiv: [1405.3693](https://arxiv.org/abs/1405.3693) [gr-qc].

COMPARISON OF BINARY BLACK HOLE INITIAL DATA SETS

Vijay Varma, Mark A. Scheel, and Harald P. Pfeiffer, *Physical Review D.*, 98, 104011 (2018), [arxiv:1808.08228](https://arxiv.org/abs/1808.08228).

3.1 Executive summary

NR simulations begin with a solution of the Einstein constraint equations at the initial time; this is referred to as initial data. The Einstein evolution equations are then used to step forward in time. This Chapter presents various improvements to the initial data in SpEC, including better boundary conditions, reduced unwanted initial transients, and more computationally efficient evolution.

3.2 Abstract

We present improvements to construction of binary black hole initial data used in SpEC (the Spectral Einstein Code). We introduce new boundary conditions for the extended conformal thin sandwich elliptic equations that enforce the excision surfaces to be slightly inside rather than on the apparent horizons, thus avoiding extrapolation into the black holes at the last stage of initial data construction. We find that this improves initial data constraint violations near and inside the apparent horizons by about 3 orders of magnitude. We construct several initial data sets that are intended to be astrophysically equivalent but use different free data, boundary conditions, and initial gauge conditions. These include free data chosen as a superposition of two black holes in time-independent horizon-penetrating harmonic and damped harmonic coordinates. We also implement initial data for which the initial gauge satisfies the harmonic and damped harmonic gauge conditions; this can be done independently of the free data, since this amounts to a choice of the time derivatives of the lapse and shift. We compare these initial data sets by evolving them. We show that the gravitational waveforms extracted during the evolution of these different initial data sets agree very well after excluding initial transients. However, we do find small differences between these waveforms, which we attribute to small differences in initial orbital eccentricity, and in initial BH masses and spins, resulting from the different choices of free data. Among the cases considered, we

find that superposed harmonic initial data leads to significantly smaller transients, smaller variation in BH spins and masses during these transients, smaller constraint violations, and more computationally efficient evolutions. Finally, we study the impact of initial data choices on the construction of zero-eccentricity initial data.

3.3 Introduction

Numerical simulations of binary black holes (BBH) have been crucial for our understanding of BBH systems. For example, these simulations are important for the construction of accurate waveform models that cover the inspiral-merger-ringdown phases of a BBH system [1–5]; these models were used in successful detections [6–10] of gravitational waves by LIGO [11]. Accurate waveform models are necessary not only for the detection of gravitational wave signals but also for making inferences about the astrophysical properties of the sources [12] and for conducting strong field tests of general relativity [13].

A numerical BBH simulation begins with the construction of initial data that describes the state of the system on some three-dimensional initial surface labeled $t = 0$. Constructing initial data requires not only solving the Einstein constraint equations, but also freely choosing the initial spatial coordinates, the embedding of the three-dimensional initial surface in the four-dimensional spacetime, and some physical degrees of freedom; these choices are encoded in freely-specifiable functions and boundary conditions that are used in the solution of the constraint equations. The subset of these choices that amount to choosing coordinates should not, of course, affect the physics [14], but they may affect the robustness and accuracy of the subsequent evolution. This is because they influence the gauge degrees of freedom that evolve along with, and are intermixed with, the physical degrees of freedom.

In this paper we study how binary black hole simulations are affected by different choices of free data, gauge, and boundary conditions that are made when constructing initial data sets that are meant to be physically identical. We consider simulations performed with one particular numerical relativity code, the Spectral Einstein Code (SpEC) [15].

Summary of initial data for SpEC simulations

Before discussing how to improve the treatment of initial data, we first outline the current procedure used to construct initial data for binary black hole simulations using SpEC; this procedure is described in more detail in Sec. 3.4. We adopt the Extended Conformal Thin Sandwich (XCTS) formalism [16, 17], and the free data supplied to the XCTS equations are chosen to be constructed from a superposition of two single black holes (BHs) in Kerr-Schild coordinates [18]. The region inside each of the BHs is excised from the computational domain, and boundary conditions are chosen that enforce the boundaries of these excision regions to be apparent horizons [19].

After the XCTS system of equations is solved, yielding a constraint-satisfying initial data set, the metric quantities are interpolated (and extrapolated) onto a new numerical grid that extends slightly inside the original excision boundaries. This new grid is used for the evolution. On the new grid the apparent horizons lie inside the computational domain rather than on its boundary, and this allows the subsequent evolution to track the apparent horizons as they dynamically change in shape and size. Unfortunately, the small extrapolation to points inside the apparent horizons introduces some constraint violations in the vicinity of the excision boundaries.

Binary black hole initial data described above represent a physical solution to Einstein’s equations but do not result in an exact snapshot of a quasi-equilibrium inspiral: the solution contains near-zone transient dynamics and does not include the correct initial gravitational radiation in the far zone. During evolution the system relaxes into a quasi-equilibrium state with the mismatch radiating away as a pulse of spurious radiation, which is generally referred to as *junk radiation*. The initial transients typically contain high spatial and temporal frequencies, so that resolving them is computationally expensive. For this reason, we typically choose not to fully resolve them at all, and we instead simply discard the initial part of the gravitational waveforms that are affected by these transients.

In addition to initial data, evolution also requires an initial choice of gauge. SpEC employs the generalized harmonic formulation of the Einstein equations [20–23], where gauge conditions are imposed through gauge source functions H_a (see 3.4). At the beginning of a binary black hole simulation, H_a is currently chosen such that the time derivatives of lapse and shift vanish at $t = 0$ in a frame co-rotating with the binary; this quasi-equilibrium condition is intended to minimize gauge dynamics at the beginning of the evolution [24]. However, a different choice of

H_a , the *damped harmonic* gauge [25–27], is usually necessary later in the evolution when the black holes merge. The choice of H_a cannot be discontinuous in time because time derivatives of H_a appear in the evolution equations. Hence, a smooth gauge transformation is applied in the early stages of evolution to move into damped harmonic gauge.

Improvements in initial data treatment

In this paper we present several improvements to BBH initial data construction. First, we introduce new boundary conditions for the XCTS elliptic equations that enforce the excision surfaces to have a negative expansion. This means that the excision surfaces are already inside the apparent horizons, eliminating the need to extrapolate inside the horizons during the initial data construction. We find that this improves constraint violations in initial data near and inside the apparent horizon surfaces by about 3 orders of magnitude.

Next, we construct several initial data sets that implement different free data in the XCTS equations as well as different initial gauge conditions. The new free data choices include superpositions of two single BHs in time-independent horizon-penetrating harmonic [28] and damped harmonic [29] coordinates rather than in Kerr-Schild coordinates. The new initial gauge choices include imposing (to numerical truncation error) the harmonic and damped harmonic gauge conditions at $t = 0$, instead of setting the initial time derivatives of the lapse and shift to zero.

We evolve all these initial data sets. Among all the initial data constructions considered here, we find that superposed harmonic initial data exhibits the most favorable behavior in subsequent evolutions. Superposed harmonic initial data exhibits the smallest amount of junk radiation, and the smallest variation in the measured masses and spins of the BHs during the initial relaxation. Furthermore, the constraint violations during the initial relaxation are smaller by about an order of magnitude. Remarkably, evolution of superposed harmonic initial data also shows a speed-up of about 33% compared to superposed Kerr-Schild data for the case considered, reducing the runtime and computational cost of BBH simulations. The speed-up can be traced to the adaptive mesh refinement (AMR) choosing fewer grid points to achieve the same accuracy. We also find that during the initial relaxation, when we intentionally do not attempt to resolve initial transients, the constraint violations converge to zero with increasing resolution only for superposed harmonic initial data.

These positive findings suggest that simulations in the future should use superposed harmonic initial data; however, it is known that a single BH in time-independent horizon-penetrating harmonic coordinates becomes very distorted in the direction of spin for large spins (cf. Fig. 3.10). These distortions are inherited by the superposed harmonic BBH initial data sets, so that the black hole horizons become so deformed to render evolutions of nearly extremal spins impractical. We find that superposed harmonic initial data works well when both BH dimensionless spin magnitudes are below 0.7.

We also find that superposed damped harmonic initial data does not perform as well as superposed Kerr-Schild initial data in the above respects. However, we find that we can construct superposed Kerr-Schild initial data that is initially in damped harmonic gauge (so as to avoid a subsequent gauge transformation during the evolution), and that this initial data set performs as well as superposed Kerr-Schild with the current quasiequilibrium initial gauge, in the above respects. Therefore, we recommend that superposed harmonic initial data be used for spin magnitudes ≤ 0.7 . For higher spins, we recommend superposed Kerr-Schild initial data with damped harmonic initial gauge, since this performs no worse than the current choice of superposed Kerr-Schild with quasi-equilibrium initial gauge, and it is simpler because it requires no gauge transition during evolution.

The rest of the paper is organized as follows. Section 3.4 provides a brief overview of the initial data formalism, including the new negative-expansion boundary conditions and new choices of free data and initial gauge. In Sec. 3.5 we summarize the particular choices of initial data that we choose to construct and compare in this work. In Sec. 3.6 we test convergence of constraints in each of these initial data sets. In Sec. 3.7 we evolve these different initial data sets and compare the results of these evolutions. Finally, in Sec. 3.8 we provide a conclusion and recommendations for the construction of initial data in future BBH simulations. Throughout this paper we use geometric units with $G = c = 1$. We use Latin letters from the start of the alphabet (a, b, c, \dots) for spacetime indices and from the middle of the alphabet (i, j, k, \dots) for spatial indices. We use ψ_{ab} for the space-time metric. We use g_{ij} for the spatial metric, N for the lapse and N^i for the shift of the constant- t hypersurfaces.

We note that this paper focuses entirely on improvements to the initial data treatment adopted by codes [15, 23] that use the generalized harmonic formulation [20–23] of the evolution equations. NR codes [30–36] that use moving-puncture initial data [37] (since they do not employ BH excision) and/or the BSSNOK formulation [30, 38,

39] of the evolution equations (since the gauge is set directly by setting a lapse and a shift, rather than a gauge source function) would not benefit from these improvements.

3.4 BBH initial data formalism

In this section we provide a brief overview of binary black hole initial data formalism, and we suggest improved boundary conditions and gauge choices. We start by discussing the Extended Conformal Thin Sandwich (XCTS) system of elliptic equations in Sec. 3.4. Next, in Sec. 3.4 we cover the boundary conditions for the elliptic equations, including the new negative expansion boundary conditions that lets us avoid spatial extrapolation of the initial data quantities. Finally, in Sec. 3.4 we discuss different gauge choices that we use in initial data. In the next section, Sec. 3.5, we summarize the different initial data sets constructed for this study.

Extended conformal thin sandwich equations

XCTS [16, 17] is a formulation of the Einstein constraint equations well-suited for numerical solution. The “extended” part of XCTS refers to an additional equation that is added to the system: the evolution equation for the trace of the extrinsic curvature, converted into an elliptic equation. This extra equation is useful in producing initial data in quasi-equilibrium. For a more detailed review of initial data construction, see [40–42].

The XCTS construction starts with a conformal decomposition of the 3-metric into a conformal factor ψ and a conformal metric \bar{g}_{ij}

$$g_{ij} = \psi^4 \bar{g}_{ij}. \quad (3.1)$$

Using the definition of extrinsic curvature in terms of the time derivative of the spatial metric, the extrinsic curvature K_{ij} takes the form

$$K_{ij} = \frac{1}{3} g_{ij} K + A_{ij}, \quad (3.2)$$

where

$$A_{ij} = \psi^{-2} \bar{A}_{ij}, \quad \bar{A}^{ij} = \frac{\psi^6}{2N} \left((\bar{\mathbb{L}}N)^{ij} - \bar{u}^{ij} \right). \quad (3.3)$$

Here N is the lapse, N^i is the shift, $(\bar{\mathbb{L}}N)^{ij}$ represents the conformal Killing operator in conformal space, and $\bar{u}_{ij} = \partial_t \bar{g}_{ij}$ ¹. K and A_{ij} are the trace and trace-free part of K_{ij} .

¹Note that one also needs to set $\bar{g}^{ij} \bar{u}_{ij} = 0$ to uniquely specify \bar{u}_{ij} .

In the XCTS formalism, one can freely specify the conformal metric \bar{g}_{ij} , trace of extrinsic curvature K , and their time derivatives \bar{u}_{ij} and $\partial_t K$. For quasi-equilibrium situations, these time derivatives are typically set to zero. The system of of elliptic equations to be solved becomes:

$$\bar{\nabla}^2 \psi - \frac{1}{8} \bar{R} \psi - \frac{1}{12} K^2 \psi^5 + \frac{1}{8} \psi^{-7} \bar{A}^{ij} \bar{A}_{ij} = 0, \quad (3.4)$$

$$\bar{\nabla}_j \left(\frac{\psi^6}{2N} (\bar{\mathbb{L}}N)^{ij} \right) - \frac{2}{3} \psi^6 \bar{\nabla}^i K - \bar{\nabla}_j \left(\frac{\psi^6}{2N} \bar{u}^{ij} \right) = 0, \quad (3.5)$$

$$\begin{aligned} \bar{\nabla}^2(N\psi) - N\psi \left(\frac{\bar{R}}{8} + \frac{5}{12} K^4 \psi^4 + \frac{7}{8} \psi^{-8} \bar{A}^{ij} \bar{A}_{ij} \right) \\ + \psi^5 (\partial_t K - N^k \partial_k K) = 0, \end{aligned} \quad (3.6)$$

where \bar{R} and $\bar{\nabla}_i$ are the Ricci scalar and the spatial covariant derivative operator associated with \bar{g}_{ij} . Once these equations are solved for ψ , $N\psi$ and N^i , the physical solution (g_{ij}, K_{ij}) is constructed from Eqs. (3.1-3.3) and the free data $(\bar{g}_{ij}, \bar{u}_{ij}, K$ and $\partial_t K)$.

Choosing freely specifiable data

If the lapse N and shift N^i computed from XCTS are used in the evolution of the initial data, the time derivative of K will initially be equal to the specified $\partial_t K$ and the trace-free part of $\partial_t g_{ij}$ will be initially proportional to the specified \bar{u}_{ij} . In order to generate quasi-equilibrium initial data, the natural choice for these freely specifiable quantities is:

$$\bar{u}_{ij} = 0, \quad \partial_t K = 0. \quad (3.7)$$

Following Ref. [18], we construct the free data based on a superposition of two single-BH solutions. Let g_{ij}^α and K^α be the 3-metric and the trace of extrinsic curvature of a single boosted, spinning black hole, with $\alpha = 1, 2$ labeling the two black holes. We then choose the conformal 3-metric \bar{g}_{ij} and the trace of the extrinsic curvature K to be

$$\bar{g}_{ij} = f_{ij} + \sum_{\alpha=1}^2 e^{-r_\alpha^2/w_\alpha^2} (g_{ij}^\alpha - f_{ij}), \quad (3.8)$$

$$K = \sum_{\alpha=1}^2 e^{-r_\alpha^2/w_\alpha^2} K^\alpha, \quad (3.9)$$

where f_{ij} is the flat 3-metric. Far from the holes, the conformal metric is very nearly flat and the trace of extrinsic curvature is very nearly zero. This is achieved through a Gaussian weight around each hole, with a width w_α that determines how fast the conformal metric approaches the flat metric with increasing Euclidean distance r_α from the center of each hole. The widths of the Gaussians w_α are chosen to be

$$w_\alpha = 0.6 d_\alpha^{L_1}, \quad (3.10)$$

where $d_\alpha^{L_1}$ is the Euclidean distance to the Newtonian L_1 Lagrange point from the center of hole α . This is identical to the choice made in Ref. [18]. This ensures that the widths are larger than the size scale of the hole ($\sim M_\alpha$, the mass of the hole) but smaller than the distance to the other hole. This also ensures that near each black hole, the contributions of the other black hole are attenuated by several orders of magnitude. The Gaussians are also needed so that at large distances the solution does not develop a logarithmic singularity [43].

The single-BH quantities g_{ij}^α and K^α above are determined by the Kerr metric, by a choice of how to slice the Kerr metric into a foliation of three-dimensional hypersurfaces, and by a choice of spatial coordinates on these hypersurfaces. These choices are largely arbitrary, but they must satisfy certain conditions to produce a viable initial data set; for example, the slices must contain an apparent horizon and be regular there.

Exploring new choices of free data

A key goal of this paper is to investigate the effect of the choice of g_{ij}^α and K^α on the resulting initial data set and subsequent evolution. Here we consider three choices, explained in more detail in Sec. 3.5. The first is the choice made in the current implementation of SpEC, which was introduced in Ref. [18]: g_{ij}^α and K^α are taken to be in Kerr-Schild coordinates centered about each BH. The second is to specify g_{ij}^α and K^α in harmonic coordinates, using the unique harmonic time slicing that is both time-independent (for a single BH) and that penetrates the horizon as derived in Ref. [28]. Finally, we also consider the case in which g_{ij}^α and K^α are chosen in the unique coordinate system that obeys the damped harmonic condition [25–27] and for which the time slices are time-independent and horizon-penetrating [29]. For all of these cases, we use the same Gaussian weights in Eqs. (3.8) and (3.9).

Boundary conditions

Equations (3.4), (3.5), and (3.6) require appropriate boundary conditions in order to solve for initial data.

The outer boundary (denoted by \mathcal{B}_∞) conditions are obtained by requiring the initial data to be asymptotically flat. Note that in practice, we do not actually place the boundary \mathcal{B}_∞ at spatial infinity, but at a coordinate sphere of radius $\sim 10^9 M$. Because the conformal metric and trace of extrinsic curvature, as given by Eqs. (3.8) and (3.9), are already asymptotically flat, the outer boundary conditions are

$$\psi = 1 \quad \text{at } \mathcal{B}_\infty, \quad (3.11)$$

$$N\psi = 1 \quad \text{at } \mathcal{B}_\infty, \quad (3.12)$$

$$\tilde{N}^i = (\mathbf{\Omega}_0 \times \mathbf{r})^i + \dot{a}_0 r^i \quad \text{at } \mathcal{B}_\infty. \quad (3.13)$$

Here, \tilde{N}^i is the shift in a frame that co-rotates with the binary, r^i is the coordinate position vector, $\mathbf{\Omega}_0$ is the orbital angular velocity and \dot{a}_0 is an expansion parameter. The shift boundary condition consists of a rotation and an expansion term. The rotation term (parametrized by $\mathbf{\Omega}_0$) ensures that the time coordinate is helical and tracks the rotation of the system, and the expansion term (parametrized by \dot{a}) sets a non-zero radial velocity, to account for the initial decrease in the orbit due to radiation reaction. These boundary conditions are identical to those in [44], which presents a more detailed exposition.

The inner boundary conditions are imposed on the excision surfaces, denoted by \mathcal{B}_E . These are chosen to be surfaces of constant radial coordinate in the single BH coordinates used in Eq. 3.8. We choose our single BH coordinates such that the apparent horizon has a constant radial coordinate² but the excision boundary may or may not be an apparent horizon, as explained below. Here we consider two types of inner boundary conditions.

Horizon boundary conditions

The standard practice in SpEC has been to choose quasi-equilibrium apparent/isolated horizon boundary conditions on the inner excision surfaces [19, 45]. We refer the reader to [40, 46, 47] for a review of the properties of apparent and isolated horizons.

²For superposed Kerr-Schild and superposed harmonic, this is the Boyer-Lindquist radius; for superposed damped harmonic, this coordinate is determined numerically [29].

We require boundary conditions on the conformal factor, the shift vector, and the lapse function.

The boundary condition for the conformal factor is obtained by setting the expansion scalar on the excision surface to zero, ensuring that it is an apparent horizon. To see how this results in a boundary condition, we first write out the expansion of \mathcal{B}_E as

$$\Theta = \frac{4}{\psi^3} \left[\bar{s}^k \partial_k \psi + \frac{\psi^3}{8N} \bar{s}^i \bar{s}^j ((\bar{\mathbb{L}}N)_{ij} - \bar{u}_{ij}) + \frac{\psi}{4} \bar{h}^{ij} \bar{\nabla}_i \bar{s}_j - \frac{1}{6} K \psi^3 \right], \quad (3.14)$$

where $\bar{s}^i = \psi^2 s^i$, s^i is the spatial unit normal to \mathcal{B}_E , and $\bar{h}_{ij} = \bar{g}_{ij} - \bar{s}_i \bar{s}_j$ is the induced conformal 2-metric on \mathcal{B}_E . \bar{h}_{ij} is related to the induced 2-metric on \mathcal{B}_E by $h_{ij} = \psi^4 \bar{h}_{ij}$. Enforcing the excision surfaces to be apparent horizons (setting $\Theta = 0$) gives us a boundary condition on the conformal factor at \mathcal{B}_E :

$$\bar{s}^k \partial_k \psi = - \frac{\psi^3}{8N} \bar{s}^i \bar{s}^j ((\bar{\mathbb{L}}N)_{ij} - \bar{u}_{ij}) - \frac{\psi}{4} \bar{h}^{ij} \bar{\nabla}_i \bar{s}_j + \frac{1}{6} K \psi^3. \quad (3.15)$$

The boundary condition on the shift is obtained by requiring that: (1) The coordinate location of the apparent horizons do not change (in a co-rotating frame) as the initial data begin to evolve. (2) The shear tensor vanishes on the excision surface; this is a property of isolated horizons [46]. We impose these two conditions only approximately, as described below. To obtain the shift boundary condition, we first decompose the shift into parts normal and tangential to the surface \mathcal{B}_E ,

$$N^i = N_{\parallel}^i + N_{\perp} s^i, \quad (3.16)$$

where

$$N_{\parallel}^i \equiv h_j^i N^j, \quad (3.17)$$

$$N_{\perp} \equiv N^i s_i. \quad (3.18)$$

The inner boundary condition (at \mathcal{B}_E) for the shift is

$$N_{\perp} = N, \quad (3.19)$$

$$N_{\parallel}^i = -\Omega_r^{(k)} \xi_{(k)}^i, \quad (3.20)$$

where

$$\vec{\xi}_{(0)} = y\hat{z} - z\hat{y}, \quad (3.21)$$

$$\vec{\xi}_{(1)} = z\hat{x} - x\hat{z}, \quad (3.22)$$

$$\vec{\xi}_{(2)} = x\hat{y} - y\hat{x} \quad (3.23)$$

are three linearly independent conformal Killing vectors of a coordinate sphere, and $\Omega_r^{(k)}$ are three arbitrarily specifiable free parameters that will be discussed below. The first condition, Eq. (3.19), ensures the apparent horizons are initially at rest in the coordinates. The second condition, Eq. (3.20), sets the spin of the black hole [19, 45]. If the excision surface is a coordinate sphere, then $\vec{\xi}_{(k)}$ are conformal Killing vectors associated with \bar{h}_{ij} , $\vec{\xi}_{(k)}$ are orthogonal to s_i , and the shear tensor vanishes on the excision surface [19]. For the initial data choices compared here, the excision boundary is not a coordinate sphere, so neither the shear-free condition nor the stationary-horizon condition that motivated the shift boundary conditions are satisfied. Nevertheless, we find that the boundary conditions above are adequate for binary black hole initial data.

In practice, it is not possible to *a priori* choose values of $\Omega_r^{(k)}$ that will yield a desired black hole spin; instead one must use an iterative procedure [48, 49], where at each iteration $\Omega_r^{(k)}$ is updated until the spin converges to the desired value. For each iteration, the spin parameter in the single-black-hole solutions \bar{g}_{ij}^α and K^α (cf. Eqs. (3.8) and (3.9)) is unchanged, and is set to the desired black hole spin.

Finally, the boundary condition at \mathcal{B}_E for the lapse (which can be chosen freely [19]) is chosen such that its value in the vicinity of each black hole approaches that of the corresponding single black hole lapse,

$$N\psi = 1 + \sum_{\alpha=1}^2 e^{-r_\alpha^2/w_\alpha^2} (N_\alpha - 1), \quad (3.24)$$

where N_α is the lapse corresponding to single black hole α and the Gaussian weights are the same as in Eq. (3.8).

Negative expansion boundary conditions

The horizon boundary conditions discussed above enforce the excision surfaces to be apparent horizons. However, BBH evolutions require an inner boundary that is slightly *inside* the apparent horizons, for the following reasons: (1) The apparent

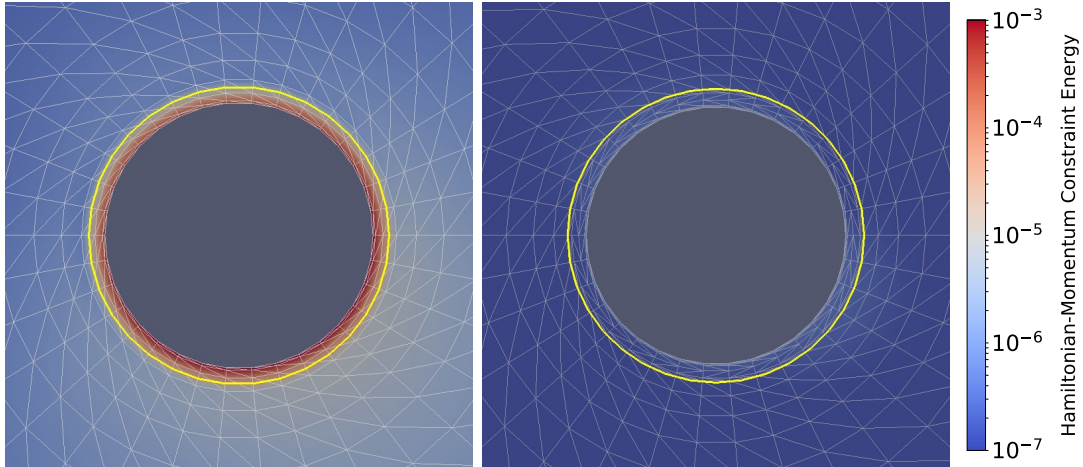


Figure 3.1: Initial constraint violations on the equatorial plane near the larger hole of a BBH system, for horizon boundary conditions (left) and negative expansion boundary conditions (right). Colors show the magnitude of the Hamiltonian-momentum constraint energy (cf. Eq. 3.42), the yellow circle is the apparent horizon, and the large black area inside the horizon is the excision region. Here superposed Kerr-Schild free data are used to construct a BBH with mass ratio $q = 1.1$ and spins $\chi_{1z} = -0.3$ and $\chi_{2z} = -0.4$ along the direction of orbital angular momentum. Unlike the horizon boundary conditions, the negative expansion boundary conditions require no extrapolation inside the horizon, and thus yield constraints near and inside the apparent horizon that are about 3 orders of magnitude smaller.

horizons dynamically change shape and size during evolution, so if the excision surfaces are *at* the apparent horizons, the horizons can fall off the numerical grid during evolution. (2) Our method of finding apparent horizons during the evolution needs to explore regions just inside and just outside of the horizon in order to converge onto the correct surface. (3) During the evolution, no boundary conditions need to be imposed at the inner boundary, because all characteristic fields are ingoing (into the black hole) there. To maintain this ingoing-characteristic-fields condition, the inner boundary is adjusted to closely track the apparent horizon to within a small but nonzero error tolerance.

This means that after solving for initial data using horizon boundary conditions, the initial data must be extrapolated spatially to a new grid that has smaller excision surfaces. This extrapolation introduces constraint violations (cf. left panel of Fig. 3.1), and therefore we propose new boundary conditions that are similar to the horizon boundary conditions discussed above but are set on a surface inside the horizon and thus avoid extrapolation altogether.

The idea behind the new boundary conditions is to set the expansion not to zero, but to some nonzero value that ensures that the excision boundary is inside an apparent horizon rather than on one. We use Eq. (3.14) to modify the conformal factor boundary condition at \mathcal{B}_E to:

$$\begin{aligned} \bar{s}^k \partial_k \psi &= -\frac{\psi^3}{8N} \bar{s}^i \bar{s}^j ((\bar{\mathbb{L}}N)_{ij} - \bar{u}_{ij}) \\ &\quad -\frac{\psi}{4} \bar{h}^{ij} \bar{\nabla}_i \bar{s}_j + \frac{1}{6} K \psi^3 + \frac{\psi^3}{4} \Theta_\alpha, \end{aligned} \quad (3.25)$$

where α denotes the particular BH and Θ_α is computed from the single BH metrics used in Eq. 3.8. As we choose the excision surface to be slightly inside the single BH horizons, Θ_α is negative on the surface. Henceforth we refer to this boundary condition as a negative expansion boundary condition.

When imposing the negative expansion condition, we also need to modify the shift boundary condition, as Eq. (3.19) holds only on a horizon. Noting that for a single BH, $\epsilon = N_\perp - N$ is positive inside the horizon and negative outside, we modify the boundary condition at \mathcal{B}_E for the normal component of shift to:

$$N_\perp = N + \epsilon_\alpha, \quad (3.26)$$

where $\epsilon_\alpha = N_{\perp\alpha} - N_\alpha$ are again obtained from the single BH solutions of the individual holes.

For negative expansion boundary conditions, we continue to use Eq. (3.20) for the tangential part of the shift. We also continue to use Eq. (3.24) for the boundary condition on the lapse, with N_α evaluated at the new location of the inner boundary. We find that the procedure for setting the spin via iteration over $\Omega_r^{(k)}$, as described in Sec. 3.4, works just as well in the case of a negative expansion BC as it does for a horizon BC.

Figure 3.1 demonstrates the efficacy of these new boundary conditions; shown are the constraints near the larger black hole when using horizon boundary conditions and the new negative expansion boundary conditions. When using negative expansion boundary conditions, the constraints improve by about 3 orders of magnitude inside and near the apparent horizon. Note, however, that once the evolution begins, most of this constraint violation propagates inwards into the excision surfaces and out of the computational domain. This is because in the generalized harmonic formalism the evolution of constraint violations is governed by a wave equation [20], which ensures that constraint violations propagate causally. Hence, we do not expect the

new boundary conditions to reduce constraint violations during the evolution nearly as much as they improve initial constraint violations.

Gauge choices

SpEC uses the generalized harmonic evolution system [20–23] to evolve the initial data. In this formalism, the gauge choice is set by requiring the coordinates to satisfy an inhomogeneous wave equation,

$$- {}^{(4)}\Gamma^a = \nabla^c \nabla_c x^a = H^a, \quad (3.27)$$

where ${}^{(4)}\Gamma^a = \psi^{bc} {}^{(4)}\Gamma_{bc}^a$, ψ_{ab} is the spacetime metric, ${}^{(4)}\Gamma_{bc}^a$ are the Christoffel symbols associated with ψ_{ab} , ∇_a is the covariant derivative operator compatible with ψ_{ab} , and H^a (called the gauge source function) is a function of the coordinates x^a and the metric ψ_{ab} (but not the derivatives of the metric).

The simplest choice for the gauge source function is to set it to zero, which yields the harmonic gauge:

$$\nabla^c \nabla_c x^a = H^a = 0. \quad (3.28)$$

Harmonic coordinates have proven to be extremely useful in analytic studies in GR [28, 50–53]. However, this gauge does not work well for simulations of black hole mergers. One common reason for the failure is growth in \sqrt{g}/N , which tends to blow up as the black holes approach each other [27].

SpEC evolutions are done instead in the damped harmonic gauge [27] given by:

$$\nabla^c \nabla_c x^a = H_{DH}^a, \quad (3.29)$$

$$H_{DH}^a \equiv \mu_L \log \left(\frac{\sqrt{g}}{N} \right) t^a - \mu_S \frac{N^i}{N} g^a{}_i, \quad (3.30)$$

where t^a is the future directed unit normal to constant- t hypersurfaces, g_{ab} is the spatial metric of the constant- t hypersurfaces and g its determinant, and μ_L and μ_S are positive damping factors that can be chosen arbitrarily. The spatial coordinates and lapse satisfy a damped wave equation with damping factors μ_S and μ_L , and are driven towards solutions of the covariant spatial Laplace equation on timescales of $1/\mu_S$ and $1/\mu_L$, respectively. Damped harmonic gauge tends to reduce extraneous gauge dynamics present in the harmonic gauge.

The damping factors are chosen as follows:

$$\mu_S = \mu_L = \mu_0 \left[\log \left(\frac{\sqrt{g}}{N} \right) \right]^2, \quad (3.31)$$

Type	Initial Data		Evolution	
	XCTS free data (\bar{g}_{ij}, K)	Inner BC	Initial Gauge	Final Gauge
SKS-Eq- θ_0	Superposed Kerr-Schild	Horizon BC	Quasi-equilibrium	Damped Harmonic
SKS-Eq	Superposed Kerr-Schild	Negative expansion BC	Quasi-equilibrium	Damped Harmonic
SH-H	Superposed Harmonic	Negative expansion BC	Harmonic	Damped Harmonic
SDH-DH	Superposed Damped Harmonic	Negative expansion BC	Damped Harmonic	Damped Harmonic
SKS-DH	Superposed Kerr-Schild	Negative expansion BC	Damped Harmonic	Damped Harmonic

Table 3.1: Types of initial data considered in this study. The initial data formalism is described in Sec. 3.4. See Sec. 3.4 for the XCTS system of equations and Sec. 3.4 for the freely specifiable data in XCTS. We describe the horizon boundary conditions in Sec. 3.4 and negative expansion boundary conditions in Sec. 3.4. The gauge choices are described in Sec. 3.4. The initial gauge is chosen by setting $\partial_t N$ and $\partial_t N^i$ according to Sec. 3.4.

where $M\mu_0$ is chosen to be of order unity, and μ_0 is a function of time (to accommodate starting an evolution from initial data satisfying a different gauge condition). This choice of the damping factors ensures that \sqrt{g}/N is driven faster than exponentially towards an asymptotic state [27], so that \sqrt{g}/N does not grow rapidly near mergers as often happens with harmonic gauge.

Setting the initial gauge

The generalized harmonic evolution system requires the metric ψ_{ab} and its time derivative $\partial_t \psi_{ab}$ to be specified on the initial time slice. Most of these quantities are determined by the solution of the XCTS equations and the free data that are used in solving these equations. However, $\partial_t \psi_{ab}$ also includes the time derivatives of the lapse and shift, which are independent of the XCTS equations. Instead, they are equivalent to the initial choice of the gauge source function H^a . To see this, we expand the generalized harmonic gauge condition, Eq. (3.27), and rewrite it in terms of the time derivatives of lapse and shift:

$$\partial_t N = N^j \partial_j N - N^2 K + N^3 H^0, \quad (3.32)$$

$$\begin{aligned} \partial_t N^i &= N^j \partial_j N^i - N^2 g^{ij} \partial_j (\log N) + N^2 \Gamma^i \\ &\quad + N^2 (H^i + N^i H^0). \end{aligned} \quad (3.33)$$

Here $\Gamma^i = g^{jk} \Gamma_{jk}^i$ and Γ_{jk}^i are the Christoffel symbols associated with g_{ij} . Note that N^2 and N^3 indicates powers of the lapse function, whereas N^i , H^0 and H^i are components of the shift-vector N^i and the gauge-source function H^a .

The default choice in SpEC simulations has been to set $\partial_t N = \partial_t N^i = 0$ in a frame co-rotating with the binary; this is meant to be a quasiequilibrium condition that reduces initial gauge dynamics. Given this choice, Eqs. (3.32) and (3.33) determine the initial values of H^a , which are kept time-independent in this co-rotating frame during the initial stages of the evolution. However, the damped harmonic gauge works best for mergers, so SpEC simulations customarily move from co-rotating gauge to damped harmonic gauge via a smooth gauge transformation during the first $\sim 50M$ of the evolution. However, this gauge transformation introduces additional complications: (1) The gauge change causes additional gauge dynamics in the evolution. (2) The gauge change happens at the same time as the junk radiation leaves the system, making it difficult to distinguish junk radiation from gauge dynamics. (3) The gauge change impacts the ability to achieve configurations with zero orbital eccentricity. To understand this last point, we note that SpEC evolutions customarily employ iterative eccentricity reduction [54]: Starting with orbital parameters predicted by post-Newtonian theory, we evolve the binary for ~ 2 orbits, compute the eccentricity, adjust the initial parameters and repeat until the desired eccentricity is achieved. This involves an extrapolation back in time to compute adjusted parameters and this extrapolation happens at the same time as the gauge transformation.

New choices of initial gauge

With the aim of addressing these issues, as part of this work we have also explored setting the initial gauge to satisfy the harmonic or damped harmonic condition, as explained in more detail in Sec. 3.5. In order to set the initial gauge to the harmonic or damped harmonic gauge, we set $\partial_t N$ and $\partial_t N^i$ according to Eqs. (3.32) and (3.33) at $t = 0$, with $H^a = 0$ for harmonic gauge and $H^a = H_{DH}^a$ for damped harmonic gauge.

3.5 BBH initial data types

Having introduced the BBH initial data formalism, in this section we discuss the different initial data sets considered in this study; these are also listed in Table 3.1. Our naming convention for the initial data sets indicates the choice of free data, initial gauge condition and boundary conditions at excision surfaces. For example, SKS-Eq- θ_0 stands for superposed Kerr-Schild free data, quasi-equilibrium initial gauge condition, and horizon boundary conditions at excision surfaces. Unless

explicitly specified, we use the new negative expansion boundary conditions at excision surfaces.

Superposed Kerr-Schild with horizon boundary conditions (SKS-Eq- θ_0)

This is the type of initial data currently implemented in SpEC [18]. Initial data are constructed by solving the XCTS system of equations, with horizon boundary conditions imposed on the excision surfaces. The free data for XCTS equations are obtained using a superposition of two single BHs in the Kerr-Schild gauge. Once the XCTS equations are solved, the initial data are extrapolated slightly inside the apparent horizon surfaces. The initial gauge is set by imposing $\partial_t N = \partial_t N^i = 0$ in a co-rotating frame. During the initial stages of the evolution a smooth gauge transformation moves into the damped harmonic gauge over a time scale of $50M$. We refer to this initial data set as SKS-Eq- θ_0 .

Superposed Kerr-Schild with negative expansion boundary conditions (SKS-Eq)

This is the same as SKS-Eq- θ_0 above but with a negative expansion boundary condition (Sec. 3.4) on the excision surfaces. We choose the excision surfaces to be slightly inside the apparent horizons and thus avoid the need for extrapolation in initial data. We refer to this as SKS-Eq.

Superposed Harmonic-Kerr (SH-H)

The free data are obtained by superposing two single BHs in the harmonic coordinates of Ref. [28]. The time derivatives $\partial_t N$ and $\partial_t N^i$ at $t = 0$ are set according to the Harmonic gauge condition (cf. Eqs. 3.28, 3.32 and 3.33):

$$\partial_t N = N^j \partial_j N - N^2 K, \quad (3.34)$$

$$\partial_t N^i = N^j \partial_j N^i - N^2 g^{ij} \partial_j (\log N) + N^2 \Gamma^i. \quad (3.35)$$

Therefore, the initial data is in the harmonic gauge at $t = 0$. As in the case of SKS-Eq, during the initial stages of the evolution we do a smooth gauge transformation to the damped harmonic gauge over a time scale of $50M$. A negative expansion boundary condition (Sec. 3.4) is used on the excision surfaces. We refer to this initial data as SH-H. We find that SH-H initial data works well for dimensionless

spin magnitudes $\chi \leq 0.7$; for higher spins the single BHs in harmonic coordinates are highly compressed in the direction of spin (see Fig. 3.10).

Superposed Damped Harmonic (SDH-DH)

The free data are obtained by superposing two single BHs in the damped harmonic gauge of Ref. [29], and a negative expansion boundary condition (Sec. 3.4) is used on the excision surfaces. $\partial_t N$ and $\partial_t N^i$ at $t = 0$ are set according to the damped harmonic gauge condition, Eqs. (3.30), (3.32) and (3.33):

$$\partial_t N = N^j \partial_j N - N^2 K + N^3 H_{DH}^0, \quad (3.36)$$

$$\begin{aligned} \partial_t N^i = & N^j \partial_j N^i - N^2 g^{ij} \partial_j (\log N) + N^2 \Gamma^i \\ & + N^2 (H_{DH}^i + N^i H_{DH}^0). \end{aligned} \quad (3.37)$$

Because the initial data are already in the damped harmonic gauge at $t = 0$, no gauge transformation is necessary during the evolution. We refer to this initial data set as SDH-DH.

Superposed Kerr-Schild with Damped Harmonic Gauge (SKS-DH)

This is the same as SKS-Eq, except the initial gauge is set to the damped harmonic gauge using Eqs. (3.36) and (3.37). Because the damped harmonic gauge condition is satisfied at $t = 0$, no gauge transformation is needed during evolution. We refer to these initial data as SKS-DH. Although the motivation for SKS-DH is to avoid the smooth gauge transformation during the evolution, for SKS-DH the gauge is not in quasi-equilibrium at $t = 0$ even if the BHs are far apart; this could potentially lead to more gauge dynamics at the start of the evolution.

3.6 Convergence of initial data

In this section, we perform a convergence test of the different initial data sets we construct. We use the spectral elliptic solver described in Refs. [48, 55] to solve the XCTS equations. We compare the Hamiltonian and momentum constraint violations at different resolutions, for the case of a nonprecessing BBH system with mass ratio $q = 1.1$ and dimensionless spins $\chi_{1z} = -0.3$, $\chi_{2z} = -0.4$ along the orbital angular momentum direction. The Hamiltonian and momentum constraints in vacuum are

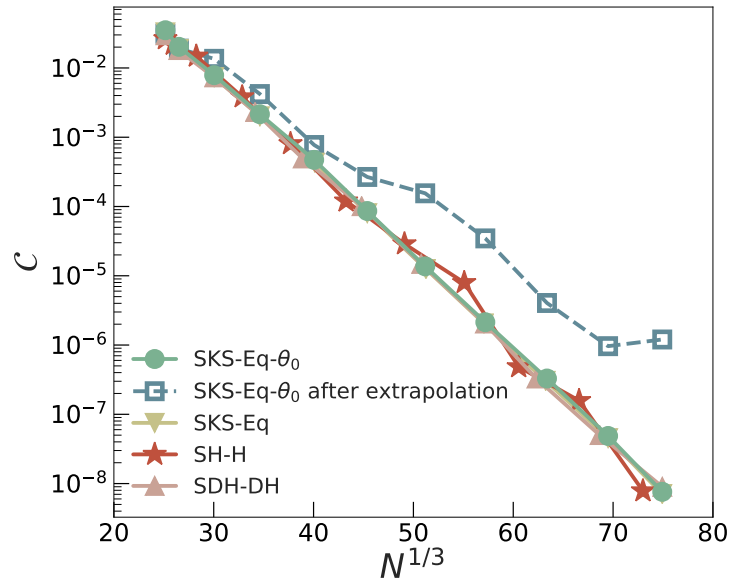


Figure 3.2: Convergence test for the spectral elliptic solver in solving the XCTS equations for the different initial data types listed in Table. 3.1. Shown is the Hamiltonian-momentum constraint energy (Eq. 3.42) vs. the number of collocation points per dimension in the domain. As expected for spectral methods, the constraints decrease exponentially. Also shown are the constraints for SKS-Eq- θ_0 after extrapolation of initial data, where, at high resolution, the constraint violation from extrapolation dominates (cf. Fig. 3.1). There is no extrapolation for SKS-Eq, SH-H, and SDH-DH, as we use negative expansion boundary conditions for these. Note that SKS-DH is not shown here because its solution of the XCTS equations is identical to SKS-Eq; the cases SKS-Eq and SKS-DH differ only in the initial gauge condition.

given by:

$$R + K^2 - K_{ij}K^{ij} = 0, \quad (3.38)$$

$$g^{jk}(\nabla_j K_{ki} - \nabla_i K_{jk}) = 0, \quad (3.39)$$

where R and ∇_i are the Ricci scalar and the spatial covariant derivative operator associated with g_{ij} . We quantify these constraint violations by computing their L^2 norms over the initial data domain. We also normalize them to obtain dimensionless

quantities ³,

$$\mathcal{H} = \frac{\|R + K^2 - K_{ij}K^{ij}\|}{\left\| \sqrt{\sum_{i,j,k} [(R_{ij}g^{ij})^2 + (K_{ij}K_{kl}g^{ik}g^{jl})^2 + (K_{ij}K_{kl}g^{ij}g^{kl})^2]} \right\|}, \quad (3.40)$$

$$\mathcal{M}_i = \frac{\|g^{jk}(\nabla_j K_{ki} - \nabla_i K_{jk})\|}{\left\| \sqrt{\sum_{i,j,k} [(g^{jk})^2((\nabla_j K_{ki})^2 + (\nabla_i K_{jk})^2)]} \right\|}, \quad (3.41)$$

where $\|\cdot\|$ denotes the L^2 norm over the domain. Finally, we define a Hamiltonian-Momentum constraint energy:

$$C = \sqrt{\mathcal{H}^2 + \sum_{i=0}^2 \mathcal{M}_i^2}. \quad (3.42)$$

Figure 3.2 shows a convergence test for the different initial data sets considered in this study. We see exponential convergence in all cases, as is expected with spectral methods. For SKS-Eq- θ_0 , while we see exponential convergence for the constraints before extrapolation, the constraints after extrapolation are significantly higher. This is why we introduced the new negative expansion boundary condition, which avoids extrapolation by placing the excision surface inside rather than at the apparent horizons.

3.7 BBH evolution with different initial data sets

In this section we evolve the different initial data sets discussed above and compare them for a nonprecessing BBH system with mass ratio $q = 1.1$ and dimensionless spins $\chi_{1z} = -0.3$, $\chi_{2z} = -0.4$ along the orbital angular momentum direction. In particular we look at the constraint violations, gauge evolution, component parameters, extracted waveforms, junk radiation, simulation expense, and ease of constructing zero-eccentricity initial data.

We performed each of these simulations for 5 different resolutions in order to do a convergence study. Each resolution is determined by specifying an error tolerance to our adaptive mesh refinement (AMR) algorithm [56]. In order to match this error tolerance as the evolution proceeds, AMR adds or removes collocation points from

³Notice that for the denominator of Eqs. (3.40) and (3.41) as well as Eq. (3.44) below, repeated indices are summed over *after* squaring the quantities, unlike the standard summation notation.

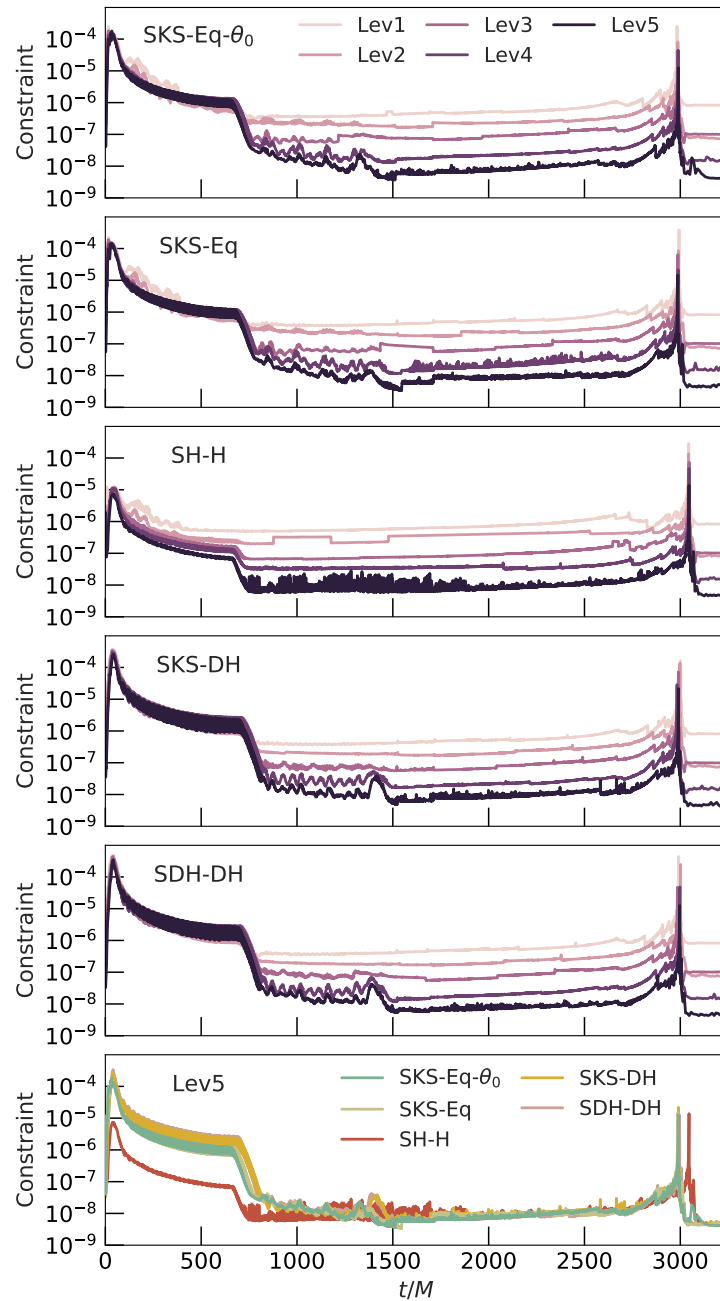


Figure 3.3: Convergence test for constraints during evolution using different initial data sets. The top panels show the constraints for different resolutions for each case: Lev1 corresponds to the lowest resolution and Lev5 corresponds to the highest resolution. After the junk radiation leaves the system, we see convergence in all cases. However, we get good convergence during junk radiation stages only for SH-H. The bottom panel shows the constraints for the highest resolution for each case. We see that for SH-H, the constraints during junk radiation are smaller by about an order of magnitude.

each subdomain (p-type refinement) and also splits a single subdomain into two or joins two neighboring subdomains as needed (h-type refinement). We use the labels “Lev1” through “Lev5” to indicate decreasing values of AMR error tolerance. During the junk radiation stage, we intentionally prevent the AMR algorithm [56] from resolving the high-frequency features present in the initial transients. This is done because attempting to resolve these features slows down the evolution considerably, and for most purposes (such as comparing with LIGO data) the junk-containing part of the waveforms is removed anyway.

Constraint violations

Figure 3.3 shows the generalized harmonic constraint energy (defined in Eq.(53) of Ref. [20]) during the evolution of the initial data sets for different resolutions. As expected, we see convergence for all the cases after the junk radiation has left the system. Because we intentionally prevent the AMR algorithm from resolving the high-frequency junk-radiation features, it is no surprise that we lose exponential convergence during the junk stage ($t \lesssim 700M$) for most of the cases considered. However, for SH-H initial data, we still retain exponential convergence for most of the junk stage, i.e. for $100M \lesssim t \lesssim 700M$, although with a shallower slope than at later times. This indicates that there are less prominent high-frequency features present during the junk for SH-H initial data. The bottom panel of Fig. 3.3 shows the constraints for the highest resolution for different initial data sets. We see that during the initial junk radiation stage, the constraints are lower for SH-H by about an order of magnitude compared to SKS-Eq- θ_0 . SDH-DH and SKS-DH initial data sets result in slightly higher constraint violations during junk radiation than SKS-Eq- θ_0 , but not by much.

Approach to damped harmonic gauge

The evolution of each initial data set discussed above eventually settles into damped harmonic gauge (Eq. 3.27). For SDH-DH and SKS-DH, the initial data should already be in damped harmonic gauge, and for the other cases damped harmonic gauge is achieved via an explicit gauge transformation. Here we quantify to what extent the evolutions of these initial data sets actually satisfy the damped harmonic gauge condition. Using Eqs. (3.27) and (3.29), we define a normalized damped

harmonic constraint energy,

$$C_{DH} = \sqrt{\sum_{a=0}^3 C_{DH}^a C_{DH}^a}, \quad (3.43)$$

$$C_{DH}^a = \frac{\|({}^{(4)}\Gamma^a + H_{DH}^a)\|}{\left\| \sqrt{\sum_{a,b,c=0}^3 \left[(\psi^{bc} {}^{(4)}\Gamma_{bc}^a)^2 + (H_{DH}^a)^2 \right]} \right\|}, \quad (3.44)$$

where $\|\cdot\|$ denotes the L^2 norm over the domain. We call this quantity an “energy” because it represents one piece of the constraint energy defined in Eq. (53) of Ref. [20].

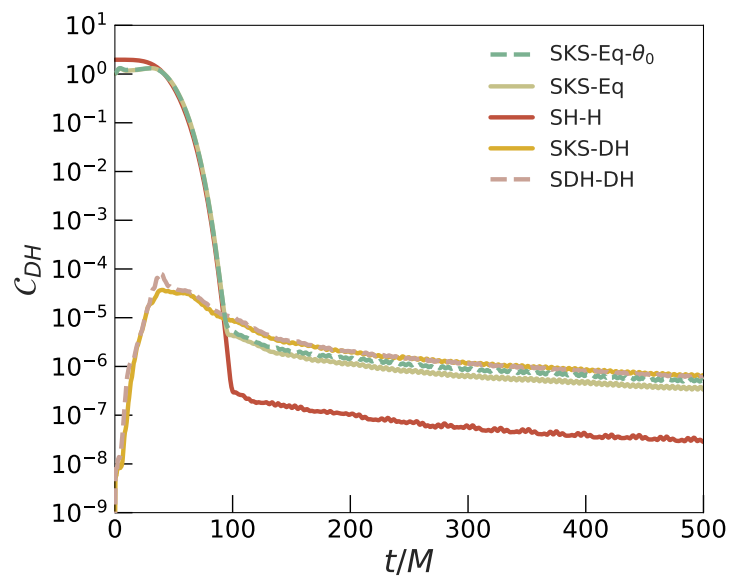


Figure 3.4: Damped harmonic constraint energy (Eq. 3.43) during evolution of different initial data sets. The damped harmonic constraint energy quantifies to what extent the gauge satisfies the damped harmonic condition. For SDH-DH and SKS-DH initial data sets, the initial data are already in the damped harmonic gauge. For the other cases, a smooth gauge transformation is done during early evolution, on a time scale of about $50M$, to move into the damped harmonic gauge. The curves for SKS-Eq- θ_0 and SKS-Eq lie nearly on top of each other.

Figure 3.4 shows the damped harmonic constraint energy during evolution of different initial data sets. For SDH-DH and SKS-DH, since initial data are already in the damped harmonic gauge, C_{DH} starts at about 10^{-8} , and rises during the junk radiation stage. However, C_{DH} always stays below about 10^{-4} . Furthermore, the two

methods to generate damped harmonic initial data give rise to comparable C_{DH} . We find that this peak value of 10^{-4} does not change significantly with resolution. This is understandable, as this is caused by junk radiation, which we intentionally do not fully resolve. SKS-Eq- θ_0 , SKS-Eq, and SH-H start in a different gauge, and there is no reason to expect small C_{DH} at $t = 0$. C_{DH} falls as the evolution transitions to damped harmonic gauge around $t \sim 50M$. The damped harmonic constraint values after the gauge transformation are lower for SH-H than for all the other cases because of smaller junk radiation content, as we will see in Sec.3.7 below.

Component parameters

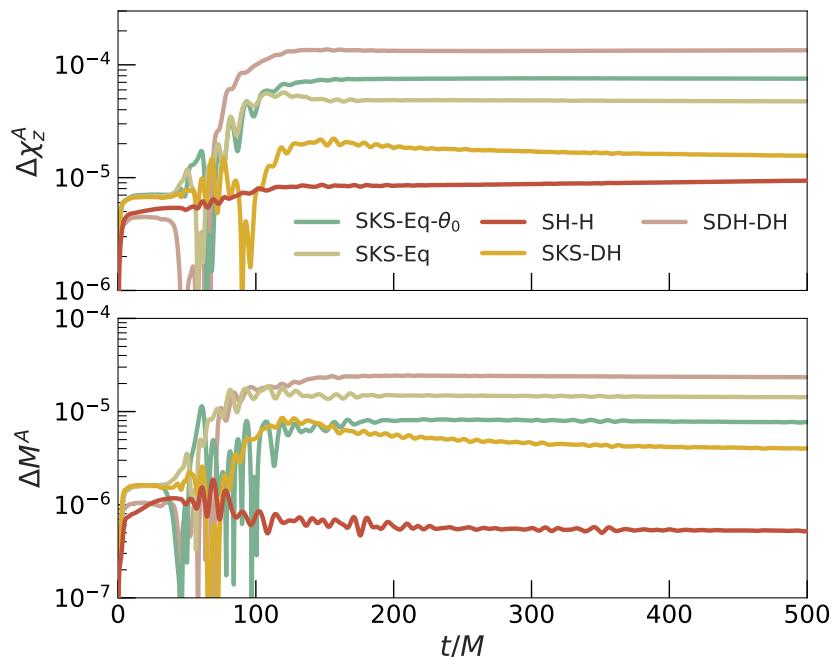


Figure 3.5: Behavior of dimensionless spin along the angular momentum direction (top panel) and mass (bottom panel) of the larger black hole during the initial stages of the evolution. Here, $\Delta M^A = |M^A(t) - M^A(t = 0)|$ and $\Delta \chi_z^A = |\chi_z^A(t) - \chi_z^A(t = 0)|$. The mass and spin are much more stable for SH-H than for the other cases. We attribute this to the small amount of junk radiation in this case; see Sec. 3.7 below.

At the start of the evolution, the component spins and masses change slightly with time. This typically results in slightly lower spins than what we start with. These changes occur as a result of initial transients such as junk radiation leaving the system. Note also that in our initial data we do not tidally deform the BHs. Hence, the initial component parameters can change as the BHs settle down into their

equilibrium shapes.

Figure 3.5 shows the change in mass and spin of the larger black hole (with respect to the simulation input parameters), as the simulation progresses. We see that the component parameters are more stable by about an order of magnitude for the SH-H initial data compared to SKS-Eq- θ_0 . SDH-DH initial data results in the largest changes while SKS-DH does better than SKS-Eq- θ_0 . In Sec. 3.7 we will see that this can be attributed to the amount of junk radiation for each of these initial data sets. Note that Fig. 3.5 corresponds to the highest resolution (Lev=5) used for this study. Repeating Fig. 3.5 with a lower resolution results in changes on the order of 10^{-4} in spin and 10^{-5} in mass for all cases except SH-H, and changes on the order of 10^{-5} in spin and 10^{-6} in mass for SH-H. Since the changes with resolution are on the same order as the variations shown in the figure, the curves in Fig. 3.5 should be regarded only as order of magnitude estimates. For all resolutions, the variations in mass and spin for SH-H are smaller than for the other cases.

Waveform comparison

Figure 3.6 shows the gravitational waveforms obtained by the evolution of the different initial data sets. The waveforms are extracted at different extraction radii up to $600M$ from the origin and extrapolated to spatial infinity [57]. The left column shows different spin weighted spherical harmonic modes of the waveform (we only show the real parts of the modes here; the imaginary parts have very similar features). As expected, after the initial junk radiation stage the waveforms between the different initial data sets agree very well.

The right panels of Fig. 3.6 show the amplitudes of different modes during the junk radiation stage. Among all the initial data sets considered here, the junk radiation is the least in the case of SH-H initial data. Compared to the current implementation in SpEC (SKS-Eq- θ_0), the junk radiation decreases by a significant amount for SH-H initial data. The junk radiation also leaves the system much faster in this case.

As noted before, when evolving most initial data sets we perform a smooth time-dependent gauge transformation so that the system settles into damped harmonic gauge on a time scale of $50M$ after the start of the evolution. The SDH-DH and SKS-DH initial data sets already satisfy the damped harmonic condition at $t = 0$, so there is no need for such a gauge transformation. We see that, among the cases considered, the junk radiation is largest in the case of SDH-DH initial data. For SKS-DH initial data, the junk radiation is at a comparable level to SKS-Eq- θ_0 . This

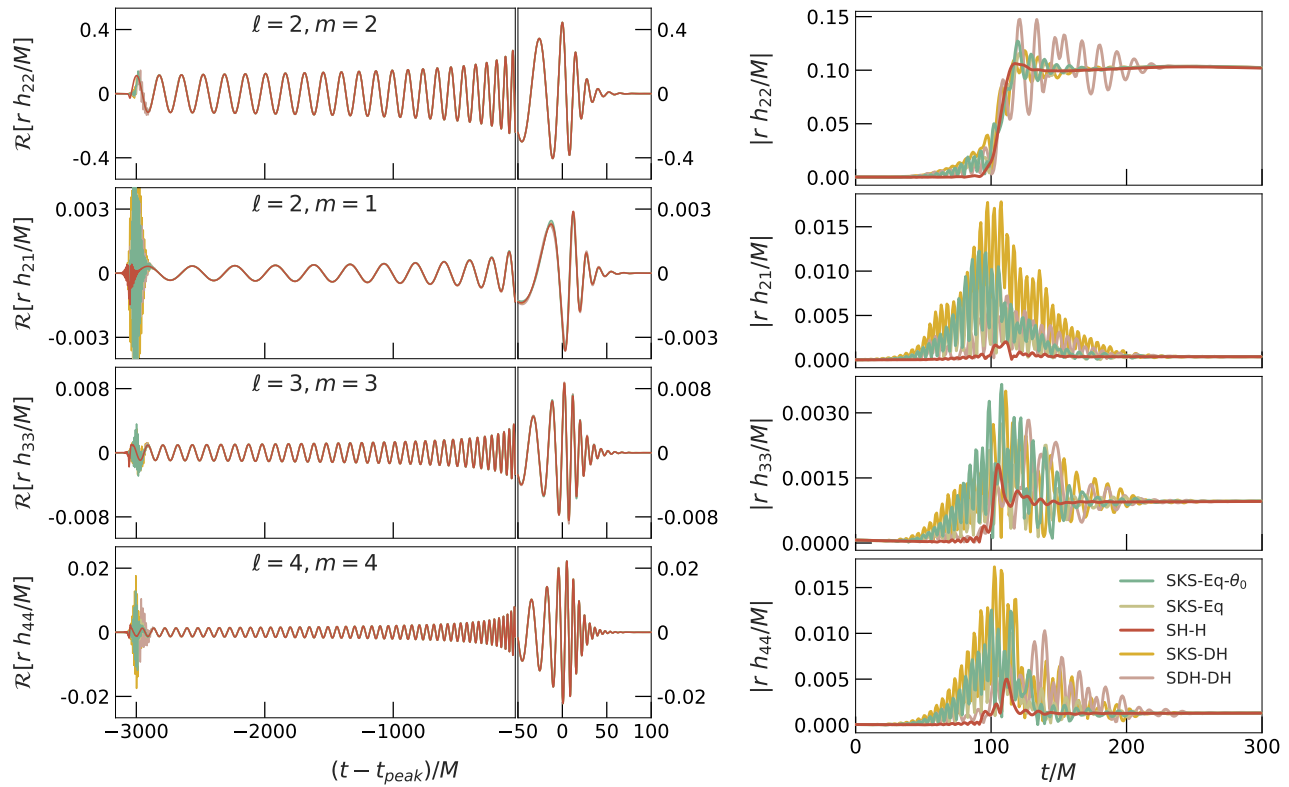


Figure 3.6: Comparison of the waveforms resulting from evolution of different initial data sets. The left column shows the real parts of different spin-weighted spherical harmonic modes. The waveforms are aligned by time-shifting them so that the peak amplitude occurs at $t = 0$, and phase-shifting them so that the orbital phase is zero at $t = 0$. Once the junk radiation leaves the domain, the waveforms agree very well between the different initial data sets. The right panels show the amplitudes of the different modes (without any time-shifting) during the junk radiation stage. We see that SH-H initial data results in the least amount of junk radiation. SDH-DH initial data, on the other hand, leads to the most junk radiation. Note however, that junk radiation is not well resolved for all cases except SH-H (cf. Fig 3.3), hence the amount of junk radiation changes significantly with resolution.

suggests that we lose nothing by choosing the simpler SKS-DH initial data over the standard choice of SKS-Eq- θ_0 . We also confirm that, as expected, the amount of junk radiation is roughly independent of initial gauge, but depends on the free data.

We can quantify the agreement between any pair of waveforms by the mismatch⁴ between them:

$$\mathcal{MM} = 1 - \frac{\langle h_1, h_2 \rangle}{\sqrt{\langle h_1, h_1 \rangle \langle h_2, h_2 \rangle}}, \quad (3.45)$$

$$\langle h_1, h_2 \rangle = 4\mathcal{R} \left[\int_{f_{min}}^{f_{max}} \tilde{h}_1(f) \tilde{h}_2^*(f) df \right], \quad (3.46)$$

where $\tilde{h}_1(f)$ is the Fourier transform of $h_1(t)$, $\mathcal{R}[\cdot]$ denotes the real part, $*$ denotes a complex conjugation, and f_{min} and f_{max} denote the relevant frequency range. f_{min} is chosen to be the GW frequency at a time $500M$ from the start (to exclude junk radiation) and f_{max} is chosen to be 8 times the merger frequency of the $\ell = m = 2$ mode.

We compute the mismatches as outlined in Appendix D of Ref. [58], where both polarizations are treated on an equal footing and the mismatch is minimized over shifts in time, initial binary phase, and polarization angle. We include all available modes ($\ell \leq 8, |m| \leq \ell$), when computing the strain

$$h(\theta, \phi, t) = \sum_{\ell, m} {}_{-2}Y_{\ell m}(\theta, \phi) h_{\ell m}(t), \quad (3.47)$$

where ${}_{-2}Y_{\ell m}(\theta, \phi)$ are the spin-weighted spherical harmonics, θ is the polar angle defined with respect to the initial orbital angular momentum direction and ϕ is the azimuthal angle in the source frame. We compute the mismatch for several different values of (θ, ϕ) (uniformly distributed in $\cos \theta$ and ϕ) and compare the median mismatches between different cases.

Figure 3.7 compares the median mismatches between waveforms from different initial data sets to the median mismatch between waveforms computed at different numerical resolutions. First, we note that the numerical resolution errors show reasonable convergence, as expected. Interestingly, we find that the differences between different initial data sets does not change significantly with resolution. We understand this as follows: Different initial data sets correspond to slightly different

⁴We choose to use a flat noise curve so that our statements are independent of the choice of GW detector.

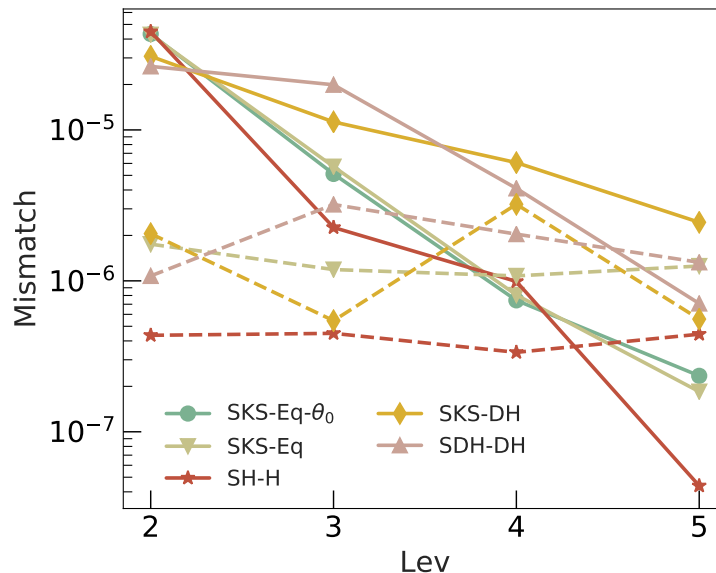


Figure 3.7: Median mismatches across the sky in the source frame between waveforms generated from different initial data sets, as a function of numerical resolution. The horizontal axis shows the numerical resolution; we ran at five different numerical resolutions labeled from lowest (Lev=1) to highest (Lev=5). The solid lines represent numerical resolution error: they compare the waveform at the labeled Lev to that of Lev-1. Dashed lines show the differences between the waveform generated from evolving the labeled initial data set to that generated from evolving SKS-Eq- θ_0 . The numerical resolution errors show reasonable convergence, as expected. Interestingly, the mismatch between different initial data sets does not change significantly with resolution. For sufficiently high resolution, the resolution errors become smaller than initial data differences. See discussion in Sec. 3.7 for more details.

physical systems (i.e. they have different junk radiation and therefore slightly different orbital eccentricities and BH masses and spins, cf. Fig. 3.5 and Fig. 3.9) and this difference is independent of resolution. At low resolution, the differences due to different initial data sets are within the numerical resolution errors, as was found in Ref. [14]. However, contrary to the findings⁵ of Ref. [14], as we go towards high resolution, the numerical resolution errors eventually go below the initial data differences. This suggests that the resolution is now high enough to differentiate between the initial data sets. These results also suggest that when very high accuracy

⁵Note that Ref. [14] compares the phase and amplitude of the quadrupole mode ($\ell = 2, m = \pm 2$) to evaluate the errors between waveforms. Instead, we use the mismatch between the waveforms, including all available modes, to evaluate the errors. Also, Ref. [14] compares SKS-Eq- θ_0 initial data to CFMS (Conformally Flat Maximally Sliced) initial data, for an equal mass non-spinning BBH.

is required, one should be concerned with how well the initial data set represents the desired astrophysical system. Specifically, it is important to measure masses and spins after the junk radiation, and one must consider tuning initial data parameters to achieve desired “post-junk” parameters.

Simulation expense

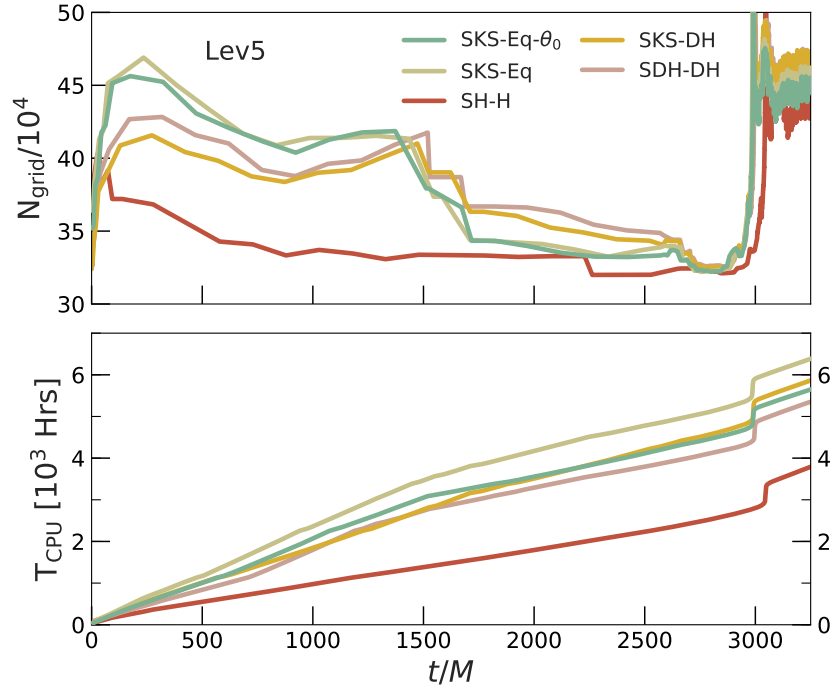


Figure 3.8: Computational efficiency. The top panel shows the total number of collocation points versus time for several simulations running with the same AMR tolerance. The bottom panel shows the total CPU time as a function of the evolution time. Using SH-H initial data speeds up the evolution by about 33% compared to SKS-Eq- θ_0 . All simulations are performed on the same machine with the same number of CPUs.

As discussed at the beginning of Sec. 3.7, the resolution of a simulation is determined by specifying an AMR error tolerance. For different simulations, the same AMR tolerance may result in a different number of collocation points and a different computational expense, since AMR chooses the number of collocation points based on the properties of the solution. Figure 3.8 shows the number of collocation points in the domain (top panel) and the total CPU time (bottom panel) for the different cases we consider, for a fixed AMR tolerance. For SH-H initial data, not only is the constraint violation during the junk radiation stage lower by an order

of magnitude, this is achieved using 15% fewer collocation points and with a 33% speed-up compared to SKS-Eq- θ_0 . This is another indication that evolutions of SH-H data contain fewer or smaller high-frequency features than for other initial data sets, so that AMR needs fewer collocation points to meet its error tolerance. These features can possibly be physical high-frequency oscillations associated with junk radiation, gauge oscillations, or gauge features that might manifest as sharper features in quasi-stationary metric functions near the horizons. We do not see significant differences in simulation expense between SKS-Eq- θ_0 and SDH-DH or SKS-DH initial data sets. While this speedup is shown for the specific case of $q = 1.1$, $\chi_{1z} = -0.3$, and $\chi_{2z} = -0.4$, we find similar improvements for more generic cases as well. However, since this improvement is largely due to lesser junk content, we expect speed-ups only in the initial stages of the evolution. For example, at times ⁶ $t > 1600M$ in Fig. 3.8, the number of grid points and the CPU-time per simulation time are comparable for SH-H and SKS-Eq- θ_0 . This also implies that the speed advantage of SH-H will be less for longer simulations.

Constructing zero-eccentricity initial data

Unlike the Newtonian or post-Newtonian (PN) case, in full general relativity there is no analytic expression for the orbital parameters of two compact objects that yield a zero-eccentricity orbit. In order to achieve quasi-circular initial data, we adopt an iterative procedure as follows [54]: Start with an initial guess for orbital parameters $\mathbf{\Omega}_0$ and \dot{a}_0 (defined in Eq. 3.13), typically taken from PN. Construct initial data with these initial orbital parameters and evolve for ~ 2 orbits, compute the eccentricity from the binary orbit and update the initial orbital parameters. Repeat until the desired eccentricity is achieved.

Note that the eccentricity is measured over a few orbits of evolution, so that updating the initial orbital parameters effectively involves an extrapolation back in time to $t = 0$. When there is also a gauge transformation happening before or during the eccentricity measurement (cf. Sec. 3.4), this extrapolation can in principle be erroneous. Therefore, it is interesting to compare the eccentricity reduction procedure for the different initial data sets we construct. Particularly for SKS-DH and SDH-DH initial data sets, where there is no initial gauge transformation, we might expect improvements in eccentricity reduction. Figure 3.9 shows the

⁶The outer boundary for these simulations is placed at a Euclidean radius of $800M$, so $1600M$ is approximately the light crossing time for the domain, at which point the junk radiation will have moved out of the domain.

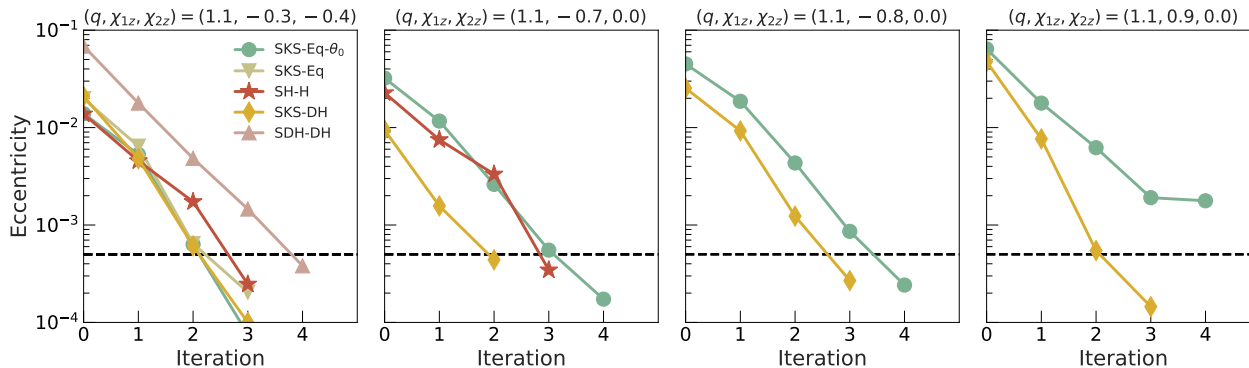


Figure 3.9: Eccentricity reduction iterations for different initial data sets considered in this study. The parameters of the binary are shown in the text above each plot. We stop the iterations once the eccentricity reaches 5×10^{-4} ; this cutoff is shown as a black dashed line.

eccentricity reduction iterations for different initial data sets. While we see that SKS-DH reaches the desired eccentricity in fewer iterations than SKS-Eq- θ_0 , we note that the initial guess from PN theory produces lower starting eccentricity for this case. In general, as the slopes of the curves do not differ significantly, we cannot conclusively say that the eccentricity reduction procedure improves when there is no gauge transformation. However, we find that SKS-DH is either better or the same as SKS-Eq- θ_0 for eccentricity reduction, for the cases we tested. Apart from SDH-DH initial data, all other initial data sets seem to perform at the same level as SKS-Eq- θ_0 . For SDH-DH, while the rate of eccentricity reduction is the same, the initial guess from post-Newtonian theory produces higher eccentricity initial data. These results suggest that other approximations made in our eccentricity-reduction procedure have a larger influence than the effect of a time-dependent gauge transformation.

3.8 Conclusion

In this paper, we introduce new ways to choose free data and new boundary conditions at excision surfaces, when constructing BBH initial data. Furthermore, we experiment with several initial gauge choices. We evolve these initial data sets and compare the waveforms, junk radiation, evolution of component parameters, constraint violations, simulation expense, and ease of constructing zero-eccentricity initial data for the different cases.

The initial data cases we compare include the following new features compared to the traditional “SKS” initial data (here called SKS-Eq- θ_0) used in past BBH

simulations performed by the SpEC code:

- We introduce new boundary conditions that allow the initial-data numerical grid to extend inside (as opposed to on) the apparent horizons. Because the numerical grid for *evolution* must extend inside the apparent horizon, these new boundary conditions allow us to eliminate an extrapolation from the initial-data grid to the evolution grid. This reduces the initial constraint violations near the individual BH horizons by about 3 orders of magnitude. We denote the current implementation (SKS-Eq- θ_0) with only this change by SKS-Eq.
- We construct BBH initial data with free data given by a superposition of two Harmonic-Kerr single BHs as derived in Ref. [28]. The initial gauge is imposed by setting $\partial_t N$ and $\partial_t N^i$ according to the harmonic gauge condition. We denote this by SH-H.
- We construct BBH initial data with free data given by a superposition of two Damped-Harmonic single BHs as derived in Ref. [29]. The initial gauge is imposed by setting $\partial_t N$ and $\partial_t N^i$ according to the damped harmonic gauge condition. We denote this by SDH-DH.
- We also construct initial data identical to SKS-Eq above, except $\partial_t N$ and $\partial_t N^i$ are chosen according to the damped harmonic gauge condition as opposed to a quasiequilibrium condition. We denote this by SKS-DH.

Note that among these cases, we use the negative expansion boundary condition for all except SKS-Eq- θ_0 and we do a gauge transformation into the damped harmonic gauge over a time scale of $50M$ at the start of evolution for all except SDH-DH and SKS-DH (which already satisfy this gauge condition).

We compare these initial data sets by evolving a nonprecessing BBH system with mass ratio $q = 1.1$ and dimensionless spins $\chi_{1z} = -0.3$, $\chi_{2z} = -0.4$ along the orbital angular momentum direction. We compare the gravitational waves (extrapolated to spatial infinity) generated using the different initial data sets by computing the mismatches between them. We also compare these mismatches to the mismatches between waveforms evolved at different numerical resolution. As expected, the numerical resolution errors decrease as we go towards higher resolutions. However, we find that the mismatches between different initial data sets are approximately

independent of resolution; we attribute this to the small physical differences between different initial data sets. These differences correspond to different amounts of junk radiation, and different parameters such as masses, spins, and orbital eccentricity. At low resolution, the initial data differences are below the numerical resolution errors. However, at high resolutions the numerical truncation error eventually drops below the initial data differences. Therefore, one must be careful to associate the waveform with the parameters (masses, spins, orbital eccentricity) measured after the junk radiation stage of the evolution rather than the parameters used to construct initial data.

The case for using SH-H initial data

By comparing the different initial data sets we conclude that SH-H initial data has the following benefits over the current implementation in SpEC (SKS-Eq- θ_0):

- The initial spurious junk radiation is much smaller.
- The junk radiation leaves the system sooner.
- The constraint violations during the junk radiation stage decrease by about an order of magnitude.
- The constraints have good convergence even during junk radiation. This suggests that the junk radiation is being resolved properly.
- The time variation in masses and spins during junk radiation is smaller by an order of magnitude.
- This improvement in constraints during junk radiation is achieved using 15% less collocation points in the domain. This leads to a remarkable 33% speed up in the total evolution time.

Because of these benefits, we recommend SH-H as the preferred choice for initial data, when possible. Unfortunately, we are currently able to construct SH-H initial data only for dimensionless spin magnitudes $\chi \leq 0.7$. At higher spins the single BH harmonic coordinates used for the construction of the free data in XCTS are too distorted (see Fig. 3.10), and the elliptic solver fails to converge. Therefore,

we recommend that SH-H initial data be used for $\chi \leq 0.7$; otherwise, SKS-DH is our recommendation, since SKS-DH eliminates the need for extrapolation and for dynamical gauge changes, and it performs no worse than SKS-Eq- θ_0 .

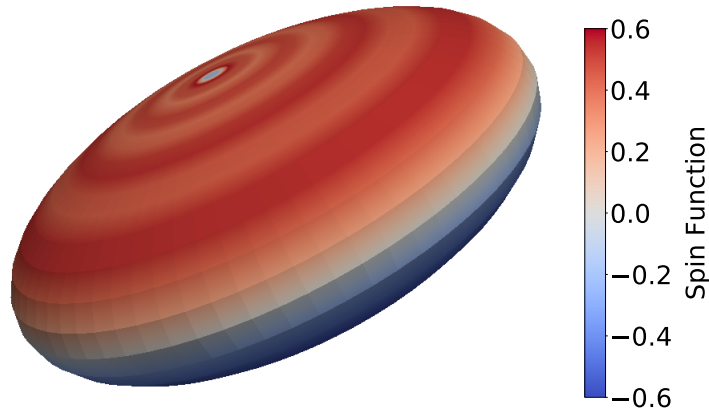


Figure 3.10: Apparent horizon surface for a single BH with dimensionless spin, $\chi = 0.9$ in the harmonic coordinates of Ref. [28]. The colors show the imaginary part of complex scalar curvature of the 2D horizon surface [59, 60]. The spin direction is along the poles. We note that the shape of the surface is compressed in the spin direction (much like a pancake), making it difficult to construct initial data. The ratio of the extents of the horizon between the spin direction and an orthogonal direction goes as $\sqrt{1 - \chi^2}$, so this issue becomes more prominent at high spins. We currently can construct superposed harmonic initial data only for spins $\chi \leq 0.7$.

Outlook and future work

Having seen that SH-H initial data is superior to the current implementation in SpEC, it would be worthwhile to extend it to spins higher than $\chi = 0.7$. To overcome the problem with highly distorted horizons, one could use a coordinate map to make the horizons more spherical; this may violate the harmonic spatial gauge condition but will preserve harmonic time slicing. It would be interesting to see if such a map preserves the benefits of SH-H initial data.

Our tests on SH-H initial data suggest that even the junk radiation stage is convergent when using this initial data. Therefore, SH-H initial data allows us to study properties of junk radiation transients, such as their frequency content or how long they remain in the computational domain. For other initial data sets, the main obstacle for such a study is the prohibitively high resolution needed to fully resolve junk radiation.

3.9 Acknowledgments

We thank Geoffrey Lovelace, Saul Teukolsky and Leo Stein for useful discussions. This work was supported in part by the Sherman Fairchild Foundation and NSF grants PHY-1404569, PHY-170212, and PHY-1708213 at Caltech. The simulations were performed on the Wheeler cluster at Caltech, which is supported by the Sherman Fairchild Foundation and Caltech.

References

- [1] Sebastian Khan et al. “Frequency-domain gravitational waves from non-precessing black-hole binaries. II. A phenomenological model for the advanced detector era”. In: *Phys. Rev. D* 93.4 (2016), p. 044007. doi: [10.1103/PhysRevD.93.044007](https://doi.org/10.1103/PhysRevD.93.044007). arXiv: [1508.07253](https://arxiv.org/abs/1508.07253) [gr-qc].
- [2] Mark Hannam et al. “A simple model of complete precessing black-hole-binary gravitational waveforms”. In: *Phys. Rev. Lett.* 113 (2014), p. 151101. doi: [10.1103/PhysRevLett.113.151101](https://doi.org/10.1103/PhysRevLett.113.151101). arXiv: [1308.3271](https://arxiv.org/abs/1308.3271) [gr-qc].
- [3] Alejandro Bohé et al. “Improved effective-one-body model of spinning, non-precessing binary black holes for the era of gravitational-wave astrophysics with advanced detectors”. In: *Phys. Rev. D* 95 (4 Feb. 2017), p. 044028. doi: [10.1103/PhysRevD.95.044028](https://doi.org/10.1103/PhysRevD.95.044028). arXiv: [1611.03703](https://arxiv.org/abs/1611.03703) [gr-qc]. URL: <https://link.aps.org/doi/10.1103/PhysRevD.95.044028>.
- [4] Yi Pan et al. “Inspiral-merger-ringdown waveforms of spinning, precessing black-hole binaries in the effective-one-body formalism”. In: *Phys. Rev. D* 89.8 (2014), p. 084006. doi: [10.1103/PhysRevD.89.084006](https://doi.org/10.1103/PhysRevD.89.084006). arXiv: [1307.6232](https://arxiv.org/abs/1307.6232) [gr-qc].
- [5] Andrea Taracchini et al. “Effective-one-body model for black-hole binaries with generic mass ratios and spins”. In: *Phys. Rev. D* 89.6 (2014), p. 061502. doi: [10.1103/PhysRevD.89.061502](https://doi.org/10.1103/PhysRevD.89.061502). arXiv: [1311.2544](https://arxiv.org/abs/1311.2544) [gr-qc].
- [6] B. P. Abbott et al. “Observation of Gravitational Waves from a Binary Black Hole Merger”. In: *Phys. Rev. Lett.* 116 (6 Feb. 2016), p. 061102. doi: [10.1103/PhysRevLett.116.061102](https://doi.org/10.1103/PhysRevLett.116.061102). arXiv: [1602.03837](https://arxiv.org/abs/1602.03837) [gr-qc]. URL: <http://link.aps.org/doi/10.1103/PhysRevLett.116.061102>.
- [7] B. P. Abbott et al. “GW151226: Observation of Gravitational Waves from a 22-Solar-Mass Binary Black Hole Coalescence”. In: *Phys. Rev. Lett.* 116.24 (2016), p. 241103. doi: [10.1103/PhysRevLett.116.241103](https://doi.org/10.1103/PhysRevLett.116.241103). arXiv: [1606.04855](https://arxiv.org/abs/1606.04855) [gr-qc].
- [8] B. P. Abbott et al. “GW170608: Observation of a 19-solar-mass Binary Black Hole Coalescence”. In: *Astrophys. J.* 851.2 (2017), p. L35. doi: [10.3847/2041-8213/aa9f0c](https://doi.org/10.3847/2041-8213/aa9f0c). arXiv: [1711.05578](https://arxiv.org/abs/1711.05578) [astro-ph.HE].

- [9] B. P. Abbott et al. “GW170814: A Three-Detector Observation of Gravitational Waves from a Binary Black Hole Coalescence”. In: *Phys. Rev. Lett.* 119.14 (2017), p. 141101. doi: [10.1103/PhysRevLett.119.141101](https://doi.org/10.1103/PhysRevLett.119.141101). arXiv: [1709.09660](https://arxiv.org/abs/1709.09660) [gr-qc].
- [10] Benjamin P. Abbott et al. “GW170104: Observation of a 50-Solar-Mass Binary Black Hole Coalescence at Redshift 0.2”. In: *Phys. Rev. Lett.* 118.22 (2017), p. 221101. doi: [10.1103/PhysRevLett.118.221101](https://doi.org/10.1103/PhysRevLett.118.221101). arXiv: [1706.01812](https://arxiv.org/abs/1706.01812) [gr-qc].
- [11] J. Aasi et al. “Advanced LIGO”. In: 32 (2015), p. 074001. doi: [10.1088/0264-9381/32/7/074001](https://doi.org/10.1088/0264-9381/32/7/074001). arXiv: [1411.4547](https://arxiv.org/abs/1411.4547) [gr-qc].
- [12] B. P. Abbott et al. “Properties of the binary black hole merger GW150914”. In: *Phys. Rev. Lett.* 116 (2016), p. 241102. doi: [10.1103/PhysRevLett.116.241102](https://doi.org/10.1103/PhysRevLett.116.241102). arXiv: [1602.03840](https://arxiv.org/abs/1602.03840) [gr-qc].
- [13] B. P. Abbott et al. “Tests of general relativity with GW150914”. In: *Phys. Rev. Lett.* 116 (2016), p. 221101. arXiv: [1602.03841](https://arxiv.org/abs/1602.03841) [gr-qc].
- [14] B. Garcia et al. “Are different approaches to constructing initial data for binary black hole simulations of the same astrophysical situation equivalent?” In: 86.8, 084054 (Oct. 2012), p. 084054. doi: [10.1103/PhysRevD.86.084054](https://doi.org/10.1103/PhysRevD.86.084054). arXiv: [1206.2943](https://arxiv.org/abs/1206.2943) [gr-qc].
- [15] The Spectral Einstein Code. URL: <http://www.black-holes.org/SpEC.html>.
- [16] James W. York. “Conformal “Thin-Sandwich” Data for the Initial-Value Problem of General Relativity”. In: 82.7 (Feb. 1999), pp. 1350–1353. doi: [10.1103/PhysRevLett.82.1350](https://doi.org/10.1103/PhysRevLett.82.1350).
- [17] Harald P. Pfeiffer and James W. York. “Extrinsic curvature and the Einstein constraints”. In: 67.4 (Feb. 2003), p. 044022. doi: [10.1103/PhysRevD.67.044022](https://doi.org/10.1103/PhysRevD.67.044022).
- [18] Geoffrey Lovelace et al. “Binary-black-hole initial data with nearly-extremal spins”. In: *Phys. Rev. D* 78 (2008), p. 084017. doi: [10.1103/PhysRevD.78.084017](https://doi.org/10.1103/PhysRevD.78.084017). arXiv: [0805.4192](https://arxiv.org/abs/0805.4192) [gr-qc].
- [19] Gregory B. Cook and Harald P. Pfeiffer. “Excision boundary conditions for black-hole initial data”. In: 70.10 (Nov. 2004), p. 104016. doi: [10.1103/PhysRevD.70.104016](https://doi.org/10.1103/PhysRevD.70.104016).
- [20] Lee Lindblom et al. “A New Generalized Harmonic Evolution System”. In: 23 (2006), S447. doi: [10.1088/0264-9381/23/16/S09](https://doi.org/10.1088/0264-9381/23/16/S09). arXiv: [gr-qc/0512093v3](https://arxiv.org/abs/gr-qc/0512093v3) [gr-qc].
- [21] Helmut Friedrich. “On the hyperbolicity of Einstein’s and other gauge field equations”. In: 100.4 (1985), pp. 525–543. doi: [10.1007/BF01217728](https://doi.org/10.1007/BF01217728). URL: <http://www.springerlink.com/content/w602g633428x8365>.

- [22] David Garfinkle. “Harmonic coordinate method for simulating generic singularities”. In: 65.4 (2002), p. 044029.
- [23] F. Pretorius. “Numerical relativity using a generalized harmonic decomposition”. In: 22 (Jan. 2005), p. 425. DOI: [10.1088/0264-9381/22/2/014](https://doi.org/10.1088/0264-9381/22/2/014). eprint: [gr-qc/0407110](https://arxiv.org/abs/gr-qc/0407110).
- [24] Mark A. Scheel et al. “High-accuracy waveforms for binary black hole inspiral, merger, and ringdown”. In: *Phys. Rev. D* 79 (2009), p. 024003. DOI: [10.1103/PhysRevD.79.024003](https://doi.org/10.1103/PhysRevD.79.024003). arXiv: [0810.1767](https://arxiv.org/abs/0810.1767) [gr-qc].
- [25] Lee Lindblom and Béla Szilágyi. “An Improved Gauge Driver for the GH Einstein System”. In: 80 (2009), p. 084019. eprint: [arXiv:0904.4873](https://arxiv.org/abs/0904.4873).
- [26] Matthew W. Choptuik and Frans Pretorius. “Ultra Relativistic Particle Collisions”. In: 104 (2010), p. 111101. DOI: [10.1103/PhysRevLett.104.111101](https://doi.org/10.1103/PhysRevLett.104.111101). arXiv: [0908.1780](https://arxiv.org/abs/0908.1780) [gr-qc].
- [27] Bela Szilagy, Lee Lindblom, and Mark A. Scheel. “Simulations of Binary Black Hole Mergers Using Spectral Methods”. In: *Phys.Rev. D* 80 (2009), p. 124010. DOI: [10.1103/PhysRevD.80.124010](https://doi.org/10.1103/PhysRevD.80.124010). arXiv: [0909.3557](https://arxiv.org/abs/0909.3557) [gr-qc].
- [28] Gregory B. Cook and Mark A. Scheel. “Well-behaved harmonic time slices of a charged, rotating, boosted black hole”. In: 56.8 (1997), p. 4775.
- [29] Vijay Varma and Mark A. Scheel. “Constructing a boosted, spinning black hole in the damped harmonic gauge”. In: *Phys. Rev. D* 98.8 (2018), p. 084032. DOI: [10.1103/PhysRevD.98.084032](https://doi.org/10.1103/PhysRevD.98.084032). arXiv: [1808.07490](https://arxiv.org/abs/1808.07490) [gr-qc].
- [30] T. W. Baumgarte and S. L. Shapiro. “On the Numerical Integration of Einstein’s Field Equations”. In: 59 (1999). gr-qc/9810065, p. 024007.
- [31] Bernd Brügmann et al. “Calibration of moving puncture simulations”. In: 77.2, 024027 (2008), p. 024027. DOI: [10.1103/PhysRevD.77.024027](https://doi.org/10.1103/PhysRevD.77.024027). eprint: [gr-qc/0610128](https://arxiv.org/abs/gr-qc/0610128). URL: <http://link.aps.org/abstract/PRD/v77/e024027>.
- [32] Y. Zlochower et al. “Accurate black hole evolutions by fourth-order numerical relativity”. In: 72 (2005), p. 024021. DOI: [10.1103/PhysRevD.72.024021](https://doi.org/10.1103/PhysRevD.72.024021). arXiv: [gr-qc/0505055](https://arxiv.org/abs/gr-qc/0505055) [gr-qc].
- [33] Ulrich Sperhake. “Binary black-hole evolutions of excision and puncture data”. In: 76 (2007), p. 104015. eprint: [gr-qc/0606079](https://arxiv.org/abs/gr-qc/0606079).
- [34] Denis Pollney et al. “High accuracy binary black hole simulations with an extended wave zone”. In: 83.4 (Feb. 2011), p. 044045. DOI: [10.1103/PhysRevD.83.044045](https://doi.org/10.1103/PhysRevD.83.044045).
- [35] F. Herrmann et al. “Unequal Mass Binary Black Hole Plunges and Gravitational Recoil”. In: 24 (2007), S33–S42. eprint: [gr-qc/0601026](https://arxiv.org/abs/gr-qc/0601026).

- [36] Larne Pekowsky et al. “Comparing gravitational waves from nonprecessing and precessing black hole binaries in the corotating frame”. In: 88 (2013), p. 024040. arXiv: [1304.3176 \[gr-qc\]](#).
- [37] Steve Brandt and Bernd Brügmann. “A Simple Construction of Initial Data for Multiple Black Holes”. In: 78.19 (1997), pp. 3606–3609.
- [38] Masaru Shibata and Takashi Nakamura. “Evolution of three-dimensional gravitational waves: Harmonic slicing case”. In: 52 (1995), p. 5428.
- [39] T. Nakamura, K. Oohara, and Y. Kojima. “General Relativistic Collapse to Black Holes and Gravitational Waves from Black Holes”. In: *Prog. Theor. Phys. Suppl.* 90 (1987), pp. 1–218. doi: [10.1143/PTPS.90.1](#).
- [40] Thomas W. Baumgarte and Stuart L. Shapiro. *Numerical Relativity: Solving Einstein’s Equations on the Computer*. New York: Cambridge University Press, 2010. doi: [10.1080/00107514.2011.586052](#).
- [41] Harald P. Pfeiffer. “The initial value problem in numerical relativity”. In: 2.2 (2005), pp. 497–520. eprint: [gr-qc/0412002](#).
- [42] Greg Cook. “Initial Data for Numerical Relativity”. In: 3 (Nov. 2000). 5. URL: <http://www.livingreviews.org/lrr-2000-5>.
- [43] Geoffrey Lovelace. “Reducing spurious gravitational radiation in binary-black-hole simulations by using conformally curved initial data”. In: *Class. Quant. Grav.* 26 (2009), p. 114002. doi: [10.1088/0264-9381/26/11/114002](#). arXiv: [0812.3132 \[gr-qc\]](#).
- [44] Harald P. Pfeiffer et al. “Reducing orbital eccentricity in binary black hole simulations”. In: 24.12 (2007), S59–S81. eprint: [gr-qc/0702106](#).
- [45] Gregory B. Cook. “Corotating and irrotational binary black holes in quasi-circular orbits”. In: 65.8 (Mar. 2002), p. 084003. doi: [10.1103/PhysRevD.65.084003](#).
- [46] Abhay Ashtekar and Badri Krishnan. “Isolated and dynamical horizons and their applications”. In: 7 (Dec. 2004). 10. URL: <http://www.livingreviews.org/lrr-2004-10>.
- [47] Olaf Dreyer et al. “Introduction to isolated horizons in numerical relativity”. In: 67.2 (Jan. 2003), p. 024018. doi: [10.1103/PhysRevD.67.024018](#).
- [48] S. Ossokine et al. “Improvements to the construction of binary black hole initial data”. In: 32.24, 245010 (Dec. 2015), p. 245010. doi: [10.1088/0264-9381/32/24/245010](#). arXiv: [1506.01689 \[gr-qc\]](#).
- [49] Luisa T. Buchman et al. “Simulations of non-equal mass black hole binaries with spectral methods”. In: *Phys.Rev.* D86 (2012), p. 084033. doi: [10.1103/PhysRevD.86.084033](#). arXiv: [1206.3015 \[gr-qc\]](#).
- [50] T. DeDonder. *La Gravifique Einsteinienne*. Paris: Gunthier-Villars, 1921.

- [51] C. Lanczos. “Ein vereinfachtes Koordinatensystem für die Einsteinschen Gravitationsgleichungen”. In: *Phys. Z.* 23 (1922), pp. 537–539.
- [52] Y. Fourès-Bruhat. “Théorème d’existence pour certains systèmes d’équations aux dérivées partielles non linéaires”. In: *Acta Math.* 88 (1952), pp. 141–225.
- [53] A. E. Fischer and J. E. Marsden. “The Einstein evolution equations as a first-order quasi-linear symmetric hyperbolic system”. In: 28 (1972), pp. 1–38.
- [54] Alessandra Buonanno et al. “Reducing orbital eccentricity of precessing black-hole binaries”. In: 83 (2011), p. 104034. DOI: [10.1103/PhysRevD.83.104034](https://doi.org/10.1103/PhysRevD.83.104034). arXiv: [1012.1549](https://arxiv.org/abs/1012.1549) [gr-qc].
- [55] H. P. Pfeiffer et al. “A multidomain spectral method for solving elliptic equations”. In: 152 (May 2003), pp. 253–273. DOI: [10.1016/S0010-4655\(02\)00847-0](https://doi.org/10.1016/S0010-4655(02)00847-0). eprint: [gr-qc/0202096](https://arxiv.org/abs/gr-qc/0202096).
- [56] B. Szilágyi. “Key elements of robustness in binary black hole evolutions using spectral methods”. In: *Int. J. Mod. Phys. D* 23, 1430014 (May 2014), p. 1430014. DOI: [10.1142/S0218271814300146](https://doi.org/10.1142/S0218271814300146). arXiv: [1405.3693](https://arxiv.org/abs/1405.3693) [gr-qc].
- [57] Michael Boyle and Abdul H. Mroué. “Extrapolating gravitational-wave data from numerical simulations”. In: 80.12 (Dec. 2009), pp. 124045–14. DOI: [10.1103/PhysRevD.80.124045](https://doi.org/10.1103/PhysRevD.80.124045). arXiv: [0905.3177](https://arxiv.org/abs/0905.3177) [gr-qc]. URL: <http://link.aps.org/abstract/PRD/v80/e124045>.
- [58] Jonathan Blackman et al. “A Surrogate Model of Gravitational Waveforms from Numerical Relativity Simulations of Precessing Binary Black Hole Mergers”. In: *Phys. Rev. D* 95.10 (2017), p. 104023. DOI: [10.1103/PhysRevD.95.104023](https://doi.org/10.1103/PhysRevD.95.104023). arXiv: [1701.00550](https://arxiv.org/abs/1701.00550) [gr-qc].
- [59] R. Owen. “Final remnant of binary black hole mergers: Multipolar analysis”. In: 80 (8 Oct. 2009), p. 084012. DOI: [10.1103/PhysRevD.80.084012](https://doi.org/10.1103/PhysRevD.80.084012).
- [60] Robert Owen et al. “Frame-Dragging Vortexes and Tidal Tendexes Attached to Colliding Black Holes: Visualizing the Curvature of Spacetime”. In: 106 (2011), p. 151101.

*Chapter 4***EFFECTS OF NONQUADRUPOLE MODES IN THE
DETECTION AND PARAMETER ESTIMATION OF BLACK
HOLE BINARIES WITH NONPRECESSING SPINS**

Vijay Varma and P. Ajith, Physical Review D., 96, 124024 (2017), [arxiv:1612.05608](https://arxiv.org/abs/1612.05608).

4.1 Executive summary

Gravitational radiation on a sphere can be decomposed into a sum of spin-weighted spherical harmonic modes. The quadrupole modes ($\ell = 2, m = \pm 2$) typically dominate this sum, and the other subdominant modes are often ignored in LIGO data analysis. This assumption, however, does not always hold, particularly when the two black holes have significantly unequal masses. In this Chapter, we study the importance of these subdominant modes for detection and parameter estimation with LIGO. We identify regions in the parameter space of binary black hole systems where gravitational wave models must include the effects of the subdominant modes.

4.2 Abstract

We study the effect of nonquadrupolar modes in the detection and parameter estimation of gravitational waves (GWs) from black hole binaries with nonprecessing spins, using Advanced LIGO. We evaluate the loss of the signal-to-noise ratio (SNR) and the systematic errors in the estimated parameters when a quadrupole-mode template family is used to detect GW signals with all the relevant modes. Target signals including nonquadrupole modes are constructed by matching numerical-relativity simulations of nonprecessing black hole binaries describing the late inspiral, merger and ringdown with post-Newtonian/effective-one-body waveforms describing the early inspiral. We find that neglecting nonquadrupole modes will, in general, cause unacceptable loss in the detection rate and unacceptably large systematic errors in the estimated parameters, for the case of massive binaries with large mass ratios. For a given mass ratio, neglecting subdominant modes will result in a larger loss in the detection rate for binaries with aligned spins. For binaries with antialigned spins, quadrupole-mode templates are more effectual in detection, at the cost of introducing a larger systematic bias in the parameter estimation. We provide a sum-

mary of the regions in the parameter space where neglecting nonquadrupole modes will cause an unacceptable loss of detection rates and unacceptably large systematic biases in the estimated parameters.

4.3 Introduction and summary

We are firmly in the era of gravitational wave (GW) astronomy, with LIGO having made two confident detections of binary black holes [1, 2] and many more expected in upcoming observing runs [3, 4]. Indeed, these first observations have already given us a glimpse of the unique capabilities of GW astronomy. Apart from providing the first direct evidence of the existence of GWs, these observations confirmed the existence of stellar mass black holes that are much more massive than commonly thought by astronomers [5, 6]. They also provided the first evidence of black hole binaries that inspiral under GW emission and merge within the age of the Universe. These observations also enabled us to perform the first tests of GR in the highly relativistic and nonlinear regime of gravity – a regime inaccessible by other astronomical observations and laboratory tests [7].

The first LIGO event, termed GW150914, was produced by the merger of two massive black holes. The resultant signal in the detectors contained imprints of the late inspiral and merger of the two holes and the subsequent ringdown of the remnant black hole. The signal was first detected by two low-latency searches for generic transient signals that are coherent in multiple detectors [8–11]. The signal was later confirmed with higher confidence by matched filter-based searches that use relativistic models of expected signals from coalescing compact binaries [12–15]. The second signal was produced by the coalescence of two less massive black holes, and the resultant signal in the detector predominantly consisted of the long inspiral. Hence matched filter-based searches were essential for its detection [2].

Matched-filtering is the most sensitive search method for extracting signals of known signal shape from noisy data, such as the GW signals from the coalescence (inspiral, merger and ringdown) of binary black holes. The source parameters are then extracted by comparing the data against theoretical templates by means of Bayesian inference [5, 16]. Our ability to optimally detect the signal using matched-filtering and to estimate the source parameters using Bayesian inference depends crucially on how faithfully the theoretical templates model the signal present in the data. If the template is a poor representation of the true signal, this can reduce the matched-filtering signal-to-noise ratio (SNR), potentially causing nondetection and/or caus-

ing unacceptable systematic biases in the estimated parameters. Good waveform templates should be not only *effectual* in the detection (small loss in the SNR) but also *faithful* in parameter estimation (small systematic biases) [17].

Matched filter-based searches for GWs performed to date, including the ones that resulted in detections, have employed templates that model only the leading (quadrupole, or $\ell = 2$, $m = \pm 2$) spherical harmonic modes of the GWs radiated from the binary. The parameter estimation exercise also has largely employed quadrupole mode templates (with the notable exception of one that directly employed numerical-relativity (NR) waveforms [18]). This choice is partly dictated by the unavailability of fast-to-evaluate, semianalytical waveform templates describing the inspiral, merger and ringdown of binary black holes that model the subdominant (nonquadrupole) modes over a sufficiently wide region in the parameter space (e.g., spinning binaries). More importantly, several studies in the past have suggested that the contribution from subdominant modes are appreciable only for very massive binaries with large mass ratios [19–22]. The effect of subdominant modes was thoroughly investigated in the context of GW150914, and the study concluded that the effect of subdominant modes is negligible in the detection and parameter estimation of this event [23, 24].

In a previous study [22], we investigated the effect of subdominant modes in the detection and parameter estimation of a population of nonspinning black hole binaries. Here, we extend our previous study to the case of black hole binaries with nonprecessing spins ¹. We construct target GW signals that include subdominant modes ($\ell \leq 4$, $m \neq 0$) by matching nonprecessing numerical-relativity simulations describing the late inspiral, merger and ringdown with post-Newtonian/effective-one-body waveforms describing the early inspiral. We then compute the reduction in the detectable volume (for a fixed SNR threshold) and systematic bias in the estimated parameters when nonprecessing quadrupole-mode only templates are employed in the detection and parameter estimation of these target waveforms.

Figure 4.1 summarizes the main results from this study. The left plot shows the region in the parameter space where neglecting subdominant modes will cause an unacceptable (more than 10%) loss in the detectable volume (appropriately averaged

¹We note that, in a recent paper, Calderon-Bustillo *et al* [25] extended our previous study of nonspinning binaries to the case of spinning binaries with equal component spins. Our new study covers a larger region in the parameter space, by employing numerical-relativity waveforms with larger mass ratios and spins. The template family that we use also can span a large spin range ($\chi_{1z,2z} \in [-1, 1]$ as opposed to $\chi \in [-1, 0.6]$ employed in [25]); hence we see better fitting factors at the cost of a larger parameter bias.

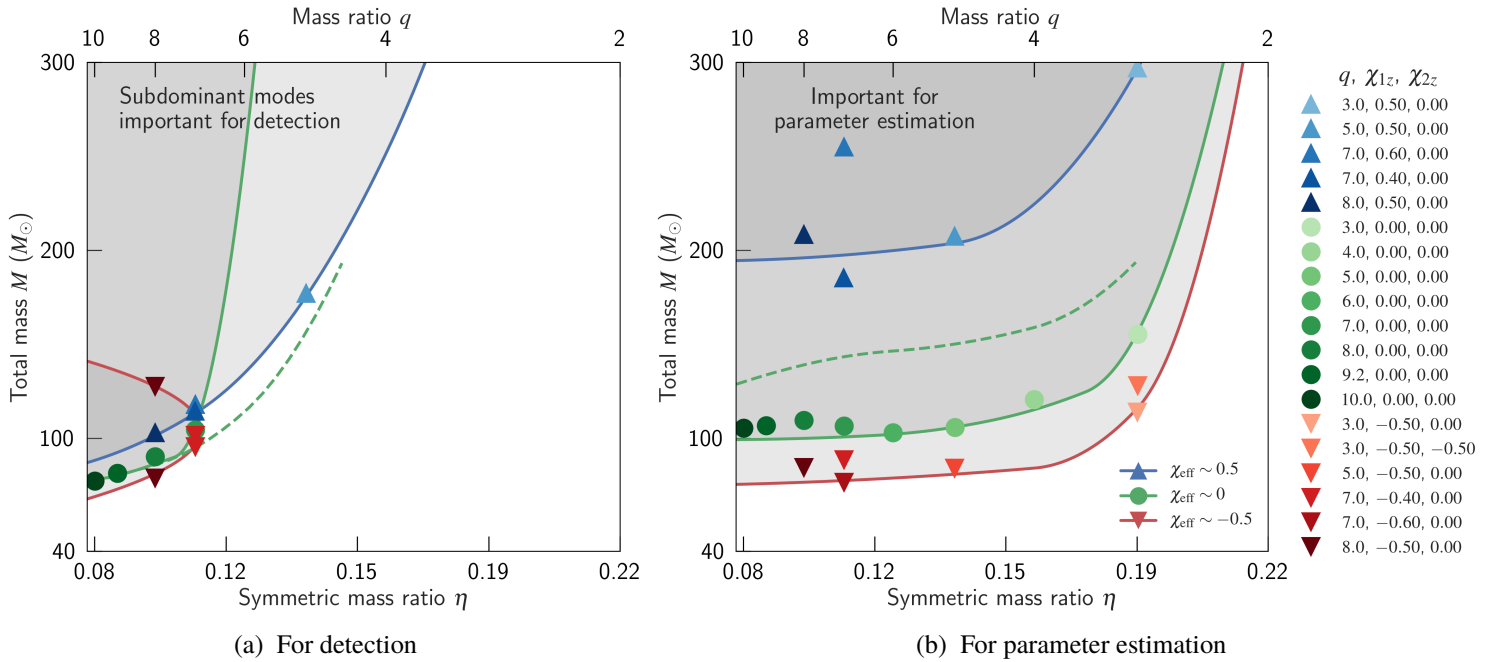


Figure 4.1: These plots summarize the region in the parameter space of nonprecessing black-hole binaries where contributions from subdominant modes are important for detection and parameter estimation. In the left panel, the shaded areas show the regions in the parameter space where the loss of detection volume due to neglecting subdominant modes is larger than 10%. In the right panel, shaded areas show the regions in the parameter space where the systematic errors in any of the estimated parameters [M , η and χ_{eff}] are larger than the expected statistical errors for a sky and orientation-averaged SNR of 8. In each plot the three solid curves correspond to different effective spin values: blue for $\chi_{\text{eff}} \sim 0.5$, green for $\chi_{\text{eff}} \sim 0$ and red for $\chi_{\text{eff}} \sim -0.5$. The left panel was made by computing the fitting factors of dominant-mode templates including nonprecessing spins with hybrid waveforms including all the relevant modes, and the right panel was made making use of averaged systematic biases. The markers (triangles pointing up/down denoting binaries with aligned/antialigned spins and circles denoting nonspinning binaries) indicate the data points that are used to construct the shaded regions and curves. The legend shows the mass ratios and spins of the target signals featured in these plots. See Sec. 4.3 for a summary and Sec. 4.5 for a detailed discussion. For comparison, the dashed green lines show the same results for nonspinning binaries using a nonspinning template family from our previous work [22].

over all orientation and sky location angles) for a fixed SNR threshold. The right plot shows the region in the parameter space where neglecting subdominant modes will cause unacceptably large systematic bias in the parameter estimation (i.e., systematic errors larger than the expected statistical errors for a sky and orientation-averaged SNR of 8). Comparing these results with our previous study employing nonspinning

templates (i.e., by comparing the dashed green curve with the solid green curve in the left plot of Fig. 4.1), we see that including spin effects in the dominant-mode templates enhances their effectualness, thus reducing the region in the parameter space where subdominant mode templates are required for detection. However, this is achieved at the cost of introducing larger systematic errors in the estimated parameters, thus increasing the volume of the parameter space where subdominant mode templates should be used in the parameter estimation. This effect (better effectualness at the cost of larger systematic errors) is more pronounced in the case of binaries with spins *antialigned* with the orbital angular momentum. Thus, subdominant-mode templates are required for detection of binaries with antialigned spins only over a small region in the parameter space; but they are required for parameter estimation over a large region. This effect is reversed in the case of *aligned* spins.

The rest of this paper is organized as follows: Section 4.4 provides details of the methodology and figures of merit for this study. Section 4.5 discusses our results including how we arrive at Fig. 4.1. Finally, Sec. 4.6 has some concluding remarks, limitations of this work and targets for future work. Appendix 4.A presents a comparison of our estimates of the statistical and systematic errors with the same estimated from fully Bayesian parameter estimation for one sample case. Please note our notation for the rest of this article: M refers to the total mass of the binary, m_1 and m_2 ($m_1 \geq m_2$) refer to the component masses, and χ_1 and χ_2 refer to the dimensionless spin parameters; $\chi_{1,2} = S_{1,2}/m_{1,2}^2$ where $S_{1,2}$ are the spin angular momenta of the components. All masses are detector frame (redshifted) masses. We only consider spins aligned/antialigned with the orbital angular momentum. The mass ratio is denoted by $q = m_1/m_2$ while $\eta = m_1 m_2 / M^2$ denotes the symmetric mass ratio. We also define the effective spin parameters $\chi_{\text{eff}} = (m_1 \chi_1 + m_2 \chi_2) / M$ and $\tilde{\chi}_{\text{eff}} = (m_1 \chi_1 - m_2 \chi_2) / M$. We refer to waveforms that include contributions from sub-dominant modes ($\ell \leq 4, m \neq 0$) as “full” waveforms and waveforms that include only quadrupole modes ($\ell = 2, m = \pm 2$) as “quadrupole” waveforms. We refer to the SNR averaged over orientation and inclination angles as the orientation-averaged SNR; note that SNR along optimal orientation is ~ 2.5 times the orientation-averaged SNR [26].

Simulation ID	q	χ_{1z}	χ_{2z}	$M\omega_{\text{orb}}$	Number of orbits
SXS:BBH:0172	1	0.98	0.98	0.015	25.4
SXS:BBH:0160	1	0.90	0.90	0.015	24.8
SXS:BBH:0155	1	0.80	0.80	0.015	24.1
SXS:BBH:0152	1	0.60	0.60	0.016	22.6
SXS:BBH:0090	1	0.00	0.00	0.011	32.4
SXS:BBH:0151	1	-0.60	-0.60	0.016	14.5
SXS:BBH:0154	1	-0.80	-0.80	0.016	13.2
SXS:BBH:0159	1	-0.90	-0.90	0.016	12.7
SXS:BBH:0156	1	-0.95	-0.95	0.016	12.4
SXS:BBH:0253	2	0.50	0.50	0.014	28.8
SXS:BBH:0047	3	0.50	0.50	0.017	22.7
SXS:BBH:0174	3	0.50	0.00	0.013	35.5
SXS:BBH:0110	5	0.50	0.00	0.019	24.2
SXS:BBH:0202	7	0.60	0.00	0.013	62.1
SXS:BBH:0203	7	0.40	0.00	0.013	58.5
SXS:BBH:0065	8	0.50	0.00	0.019	34.0
SXS:BBH:0184	2	0.00	0.00	0.018	15.6
SXS:BBH:0183	3	0.00	0.00	0.020	15.6
SXS:BBH:0167	4	0.00	0.00	0.021	15.6
SXS:BBH:0056	5	0.00	0.00	0.016	28.8
SXS:BBH:0181	6	0.00	0.00	0.018	26.5
SXS:BBH:0298	7	0.00	0.00	0.021	19.7
SXS:BBH:0063	8	0.00	0.00	0.019	25.8
SXS:BBH:0189	9.2	0.00	0.00	0.021	25.2
SXS:BBH:0185	10	0.00	0.00	0.021	24.9
SXS:BBH:0238	2	-0.50	-0.50	0.011	32.0
SXS:BBH:0036	3	-0.50	0.00	0.012	31.7
SXS:BBH:0046	3	-0.50	-0.50	0.018	14.4
SXS:BBH:0109	5	-0.50	0.00	0.020	14.7
SXS:BBH:0205	7	-0.40	0.00	0.013	44.9
SXS:BBH:0207	7	-0.60	0.00	0.014	36.1
SXS:BBH:0064	8	-0.50	0.00	0.020	19.2

Table 4.1: Summary of the parameters of the NR waveforms used in this paper: $q \equiv m_1/m_2$ is the mass ratio of the binary, χ_{1z} and χ_{2z} are the dimensionless spins of the larger and smaller black holes respectively, and $M\omega_{\text{orb}}$ is the orbital frequency after the junk radiation. All of these waveforms have residual eccentricity, $e < 4 \times 10^{-3}$ (typically significantly smaller).

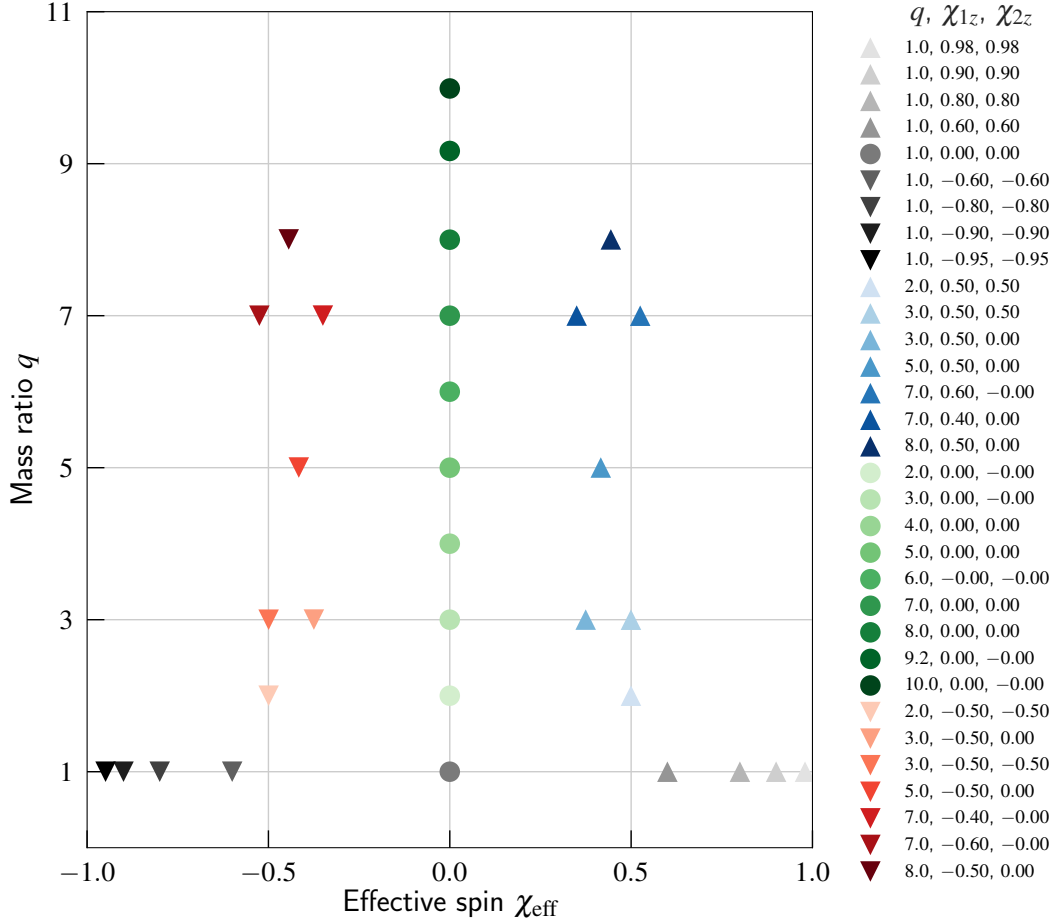


Figure 4.2: This plot shows the mass ratio (vertical axis) and effective spin (horizontal axis) of the NR waveforms used in this study. The color scheme of the markers is same as that in Figs. 4.1, 4.6 and 4.8, enabling direct comparison.

4.4 Methodology

In a past study [22], we investigated the effects of nonquadrupole modes in the detection and parameter estimation of nonspinning binaries. Here we extend the earlier work to the case of nonprecessing binaries, covering a wide range of total masses ($40M_{\odot} \leq M \leq 300M_{\odot}$), mass ratios ($q \leq 10$) and spins ($-0.5 \lesssim \chi_{\text{eff}} \lesssim 0.5$ for $q \geq 2$ and $-0.95 \leq \chi_{\text{eff}} \leq 0.98$ for $q = 1$). For our target signals, we use hybrid waveforms constructed by matching NR waveforms that describe the late inspiral, merger and ringdown of binary black holes with post-Newtonian (PN) / effective-one-body (EOB) waveforms modeling the early inspiral. These hybrids contain several nonquadrupolar modes ($h_{\ell m}(t)$ with $\ell \leq 4, |m| \leq \ell, m \neq 0$) of GW signals from binary black holes. The PN waveforms were generated using the 3PN

amplitude given by [27–29], but using the phase evolution given by the SEOBNRv2 waveform family² [30]. We match them with NR waveforms produced by the SpEC [31–47] code by the SXS Collaboration that are available at the public SXS catalog of NR waveforms [31]. The parameters of the NR waveforms used in this study are shown in Table 4.1 and Fig. 4.2. Note that the $(\ell, m) = (4, 1)$ mode in several of the NR waveforms has significant numerical noise. However, as the amplitude of this mode is several orders of magnitude smaller than that of the dominant mode, we do not expect this to impact our results.

As described in detail in our past study [22], to construct hybrids, we match the PN modes $\hat{h}_{\ell m}^{\text{PN}}(t)$ with NR modes $\hat{h}_{\ell m}^{\text{NR}}(t)$ by a least square fit over two rotations (φ_0, ψ) on the NR mode and the time difference between NR and PN modes:

$$\Delta = \min_{t_0, \varphi_0, \psi} \int_{t_1}^{t_2} dt \sum_{\ell, m} \left| \hat{h}_{\ell m}^{\text{NR}}(t - t_0) e^{i(m\varphi_0 + \psi)} - \hat{h}_{\ell m}^{\text{PN}}(t) \right|. \quad (4.1)$$

The hybrid modes are constructed by combining the NR modes with the “best-matched” PN modes:

$$\hat{h}_{\ell m}^{\text{hyb}}(t) \equiv \tau(t) \hat{h}_{\ell m}^{\text{NR}}(t - t'_0) e^{i(m\varphi'_0 + \psi')} + (1 - \tau(t)) \hat{h}_{\ell m}^{\text{PN}}(t), \quad (4.2)$$

where t'_0, φ'_0 and ψ' are the values of t_0, φ_0 and ψ that minimizes the difference Δ between PN and NR modes and $\tau(t)$ is a suitable weighting function that smoothly goes from 0 to 1 during the interval $t_1 \leq t \leq t_2$. We refer the reader to Ref. [22] for details about the construction of hybrid waveforms. An example of hybrid waveform modes is shown in Fig. 4.3. It can be seen that higher modes are excited only during the very late inspiral, merger and ringdown. The effect of higher modes will be appreciable only in the mass range where the SNR contributed by the merger-ringdown is a significant fraction of the total SNR. This is the reason we restrict our study to the mass range $40M_\odot \leq M \leq 300M_\odot$; we do not see any evidence of a significant impact of higher modes for binaries with lower masses. Since the NR waveforms we use include tens of cycles in the inspiral, we do not expect hybridization errors to impact our results, particularly for high masses. For a detailed study on hybridization errors, we refer the reader to Refs. [48–52].

The template family used is IMRPhenomD [53, 54], which is a quadrupole-only ($\ell = 2, m = \pm 2$) inspiral, merger and ringdown waveform family described by two

²This was done in order to make the phase evolution of the hybrids very similar to that of the templates, so that a mismatch between the hybrid and the template due to the different phase evolution will not be mistaken as due to the effect of subdominant modes.

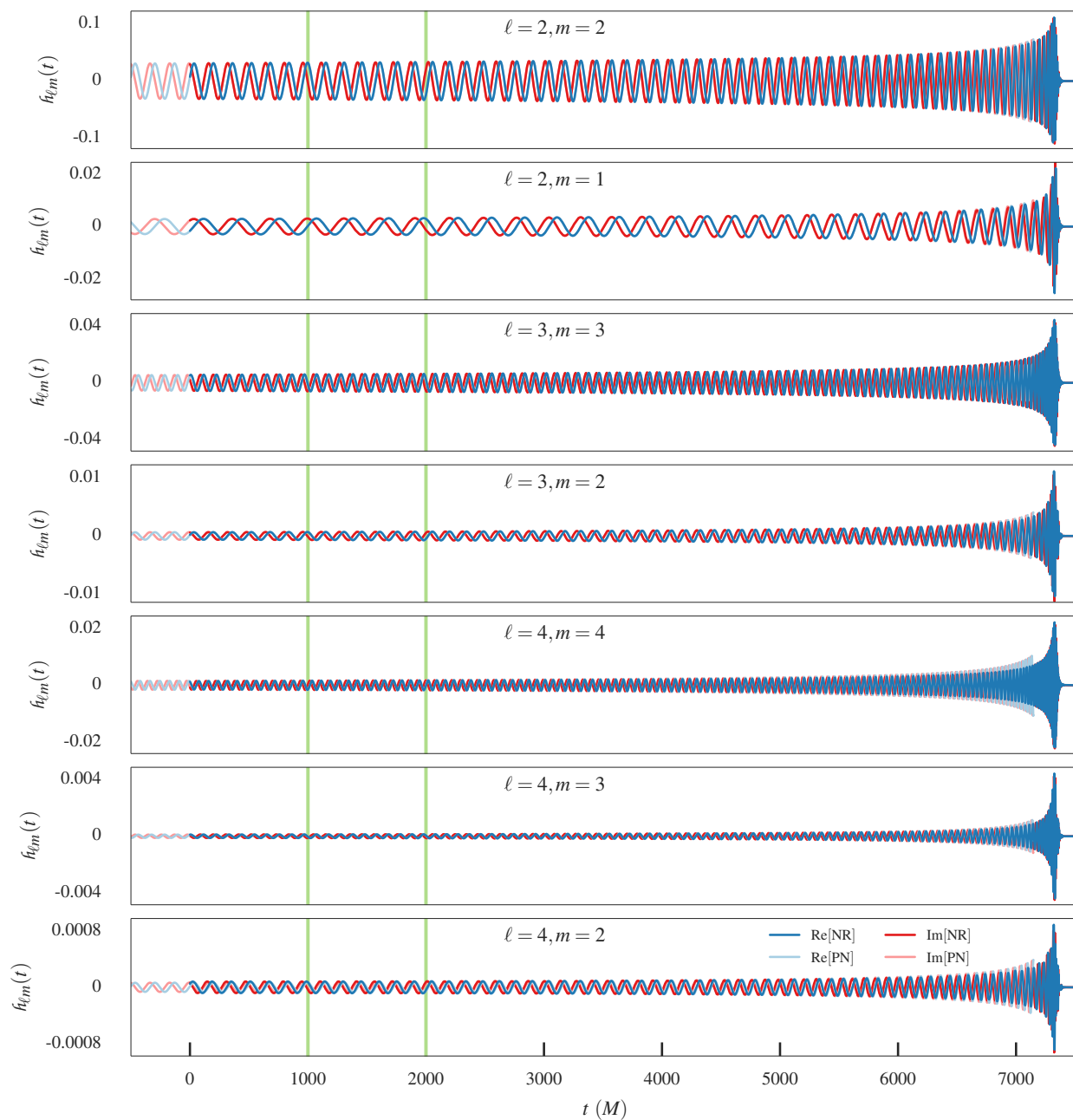


Figure 4.3: Example hybrid waveform constructed by matching NR and PN, for $q = 8$, $\chi_{1z} = 0.5$, $\chi_{2z} = 0$. The matching region ($1000M, 2000M$) is marked by vertical green lines.

mass parameters and two nonprecessing spin parameters. These waveforms are calibrated to NR waveforms with $q \leq 18$, $|\chi_{1z,2z}| \lesssim 0.85$ (0.98 for $q = 1$) and we find that they have a very good agreement with the quadrupole modes of the hybrid waveforms discussed above (cf. the dashed lines in Fig. 4.6). The waveforms are generated in the Fourier-domain using the LALSimulation [55] software package.

We compute fitting factors [56] by maximizing the overlap (noise weighted inner product) of the template family against the target hybrid signals and infer the systematic errors by comparing the best-match parameters with the true parameters. The overlaps are maximized over the extrinsic parameters (time of arrival t_0 and the reference phase φ_0) using the standard techniques in GW data analysis (see, e.g., Ref. [57]), while the overlaps are maximized over the intrinsic parameters (M , η , χ_{1z} and χ_{2z}) of the templates using a Nelder-Mead downhill simplex algorithm [58], with additional enhancements described in Ref. [22]. For the model of the noise power spectrum, we use the “zero-detuned, high-power” design noise power spectral density (PSD) [59] of Advanced LIGO with a low frequency cut-off of 20 Hz.

The contribution of subdominant modes in the observed signal depends on the relative orientation of the binary and the detector. The SNR (and hence the volume in the local Universe where the binary can be confidently detected) is also a strong function of this relative orientation. For, e.g., binaries that are face-on produce the largest SNR in the detector; however, the contribution from subdominant modes is minimal for this orientation. This effect is reversed for the case of edge-on orientations. Thus, if we want to calculate the effect of subdominant modes on detection and parameter estimation of a population of binary black holes, the effect has to be averaged over all orientations after appropriately weighting each orientation.

We evaluate the *effective volume* [22] of a search, defined as the fraction of the volume that is accessible by an optimal search (corresponding to a fixed SNR threshold), by averaging over all the relative orientations in the following way:

$$V_{\text{eff}}(m_1, m_2, \chi_{1z}, \chi_{2z}) = \frac{\overline{\rho_{\text{opt}}^3 \text{FF}^3}}{\overline{\rho_{\text{opt}}^3}}, \quad (4.3)$$

where ρ_{opt} is the optimal SNR of the full signal, FF is the fitting factor of the dominant mode template, and the bars indicate averages over all (isotropically distributed) orientations³. The dominant-mode template family is deemed effectual

³This corresponds to uniform distributions in the phase angle $\varphi_0 \in [0, 2\pi)$, polarization angle

for detection when the effective volume is greater than 90%; or when the *effective fitting factor* $\text{FF}_{\text{eff}} := V_{\text{eff}}^{1/3}$ is greater than 0.965.

Similarly, we define the *effective bias* [22] in estimating an intrinsic parameter λ as

$$\Delta\lambda_{\text{eff}}(m_1, m_2, \chi_{1z}, \chi_{2z}) = \frac{\overline{|\Delta\lambda| \rho_{\text{opt}}^3 \text{FF}^3}}{\overline{\rho_{\text{opt}}^3 \text{FF}^3}}, \quad (4.4)$$

where $\Delta\lambda$ is the systematic bias in estimating the parameter λ for one orientation, FF is the corresponding fitting factor, and ρ_{opt} the corresponding optimal SNR. Here, also, the bars indicate averages over all orientations. The effective bias provides an estimate of the bias averaged over a population of detectable binaries with isotropic orientations. We compare them against the sky and orientation averaged statistical errors. Statistical errors are computed using the Fisher matrix formalism employing quadrupole-only templates. The quadrupole-mode template family is deemed faithful for parameter estimation when the effective biases in all of the three intrinsic parameters $M, \eta, \chi_{\text{eff}}$ are smaller than the 1σ statistical errors in measuring the same parameter for an orientation-averaged SNR of 8.

4.5 Results and discussion

In this section, we evaluate the performance of the quadrupole-mode inspiral-merger-ringdown template family IMRPhenomD, against the “full” hybrid waveforms by computing the fitting factor of the template and inferring the parameter biases from the best-matched parameters.

Figure 4.4 shows the optimal SNR of the hybrid waveforms and fitting factor of the quadrupole-mode templates at different values of ι and φ_0 (averaged over the polarization angle ψ). Figure 4.5 shows the systematic bias in estimating parameters total mass M , symmetric mass ratio η , and effective spin χ_{eff} , using the quadrupole-mode template family. It is clear that for the $q = 1$ case (left column) the fitting factor is close to 1, and the systematic errors are negligible for all orientations, indicating the weak contribution of subdominant modes. For mass ratio 8, the fitting factor can be as low as ~ 0.84 for binaries that are highly inclined ($\iota \simeq \pi/2$) with the detector, where the contribution from nonquadrupole modes is the highest. However, these

$\psi \in [0, 2\pi)$, and the cosine of the inclination angle $\cos \iota \in [-1, 1]$. Note that we assume that the binaries are optimally located (i.e., the angles θ, ϕ describing the location of the binary in the detector frame on the sky are set to zero). The error introduced by this restriction is very small ($\sim 0.1\%$) due to the weak dependence of the matches on (θ, ϕ) and the strong selection bias towards binaries with $\theta \simeq 0, \pi$, where the antenna pattern function peaks [22].

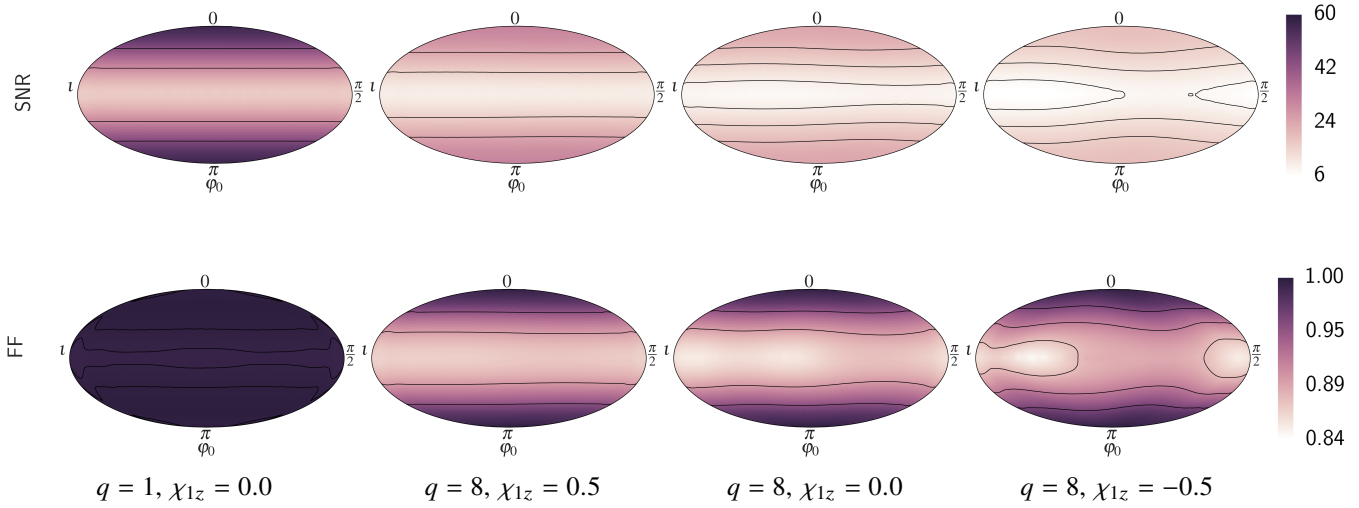


Figure 4.4: Optimal SNR (top panel) and fitting factor of quadrupole templates (bottom panel), averaged over polarization angle ψ for binaries with total mass $M = 100 M_{\odot}$, located at 1 Gpc. The y-axis shows the inclination angle ι in radians and the x-axis shows the initial phase of the binary φ_0 in radians. The equator ($\iota = \pi/2$) corresponds to “edge-on” orientation while the poles ($\iota = 0, \pi$) correspond to “face-on” orientation. Different columns correspond to different mass ratios and spins of the larger black hole (the spin on the smaller black hole is 0 in all three cases). It may be noted that the fitting factor as well as the intrinsic luminosity are smallest (largest) at $\iota = \pi/2$ ($\iota = 0, \pi$) where contribution from the nonquadrupole modes is the largest (smallest), illustrating the selection bias toward configurations where nonquadrupole modes are less important.

are the orientations where the SNR is the minimum (see Fig. 4.4). Similarly, the systematic biases are typically the largest (smallest) for the edge-on (face-on) configurations where the SNR is the smallest (largest). Hence GW observations are intrinsically biased toward orientations where the effect of nonquadrupole modes is minimum. This effect, in general, reduces the importance of nonquadrupole modes for a population of binaries that are oriented isotropically [19–22] ⁴.

Figure 4.6 shows the *ineffectualness* ($1 - \text{FF}_{\text{eff}}$) and effective biases in estimated parameters as a function of the total mass of the binary for different mass ratios and spins. For total mass M and symmetric mass ratio η , fractional biases are shown while for χ_{eff} absolute biases are shown⁵. Solid (dashed) lines correspond

⁴Note that this is an artifact of the limited horizon distance of the second-generation GW detectors. For the case of third generation GW detectors, binaries with practically all orientations will be detected, thus eliminating this selection bias; see, e.g., [60]

⁵In the case of anti-symmetric spin parameter $\tilde{\chi}_{\text{eff}}$, the biases are dominated by the bias in the

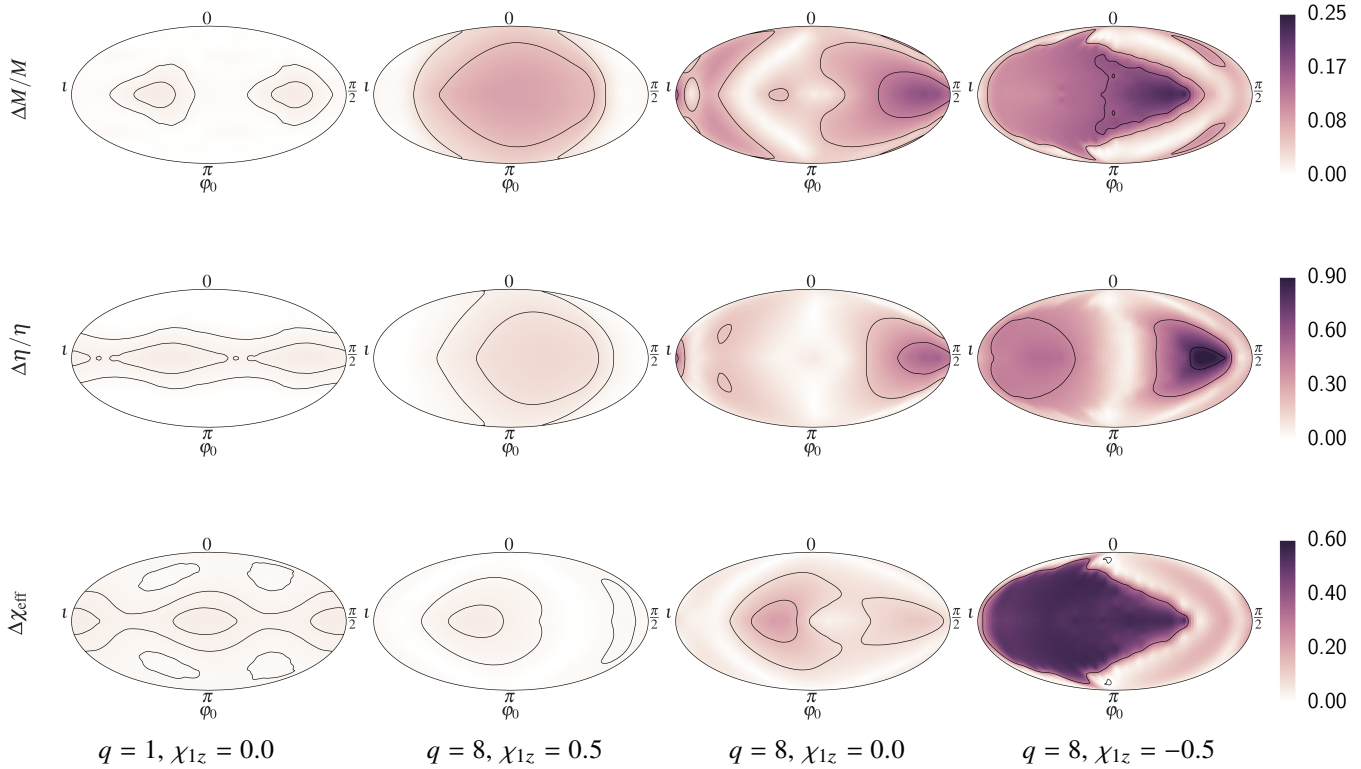


Figure 4.5: Systematic bias in the estimation of total mass (top panel), symmetric mass ratio (middle panel), and effective spin (bottom panel), averaged over polarization angle ψ for binaries with total mass $M = 100 M_{\odot}$. For M and η , relative biases are shown, while for χ_{eff} absolute biases are shown. The y-axis shows the inclination angle ι in radians and the x-axis shows the initial phase of the binary φ_0 in radians. Different columns correspond to different mass ratios and spins of the larger black hole (the spin on the smaller black hole is 0 in all three cases).

to the case where “full” (quadrupole-only) hybrid waveforms are used as target waveforms. The template family in both cases contains only the quadrupole mode. The difference between the solid and dashed lines indicates the effect of ignoring sub-dominant modes for detection and parameter estimation. Note that many of the dashed lines lie below the scale of these plots and are not displayed.

Previous studies [19–22, 25] have shown that the effects of subdominant modes become important for binaries with high masses and large mass ratios. At large mass ratios, subdominant modes are excited by a larger extent due to higher asymmetry. For high masses, the observed signal is dominated by the merger, during which quadrupole mode itself. This is expected as previous studies have shown that LIGO can only estimate χ_{eff} to a good accuracy. Therefore we do not consider biases in $\tilde{\chi}_{\text{eff}}$ in this study.

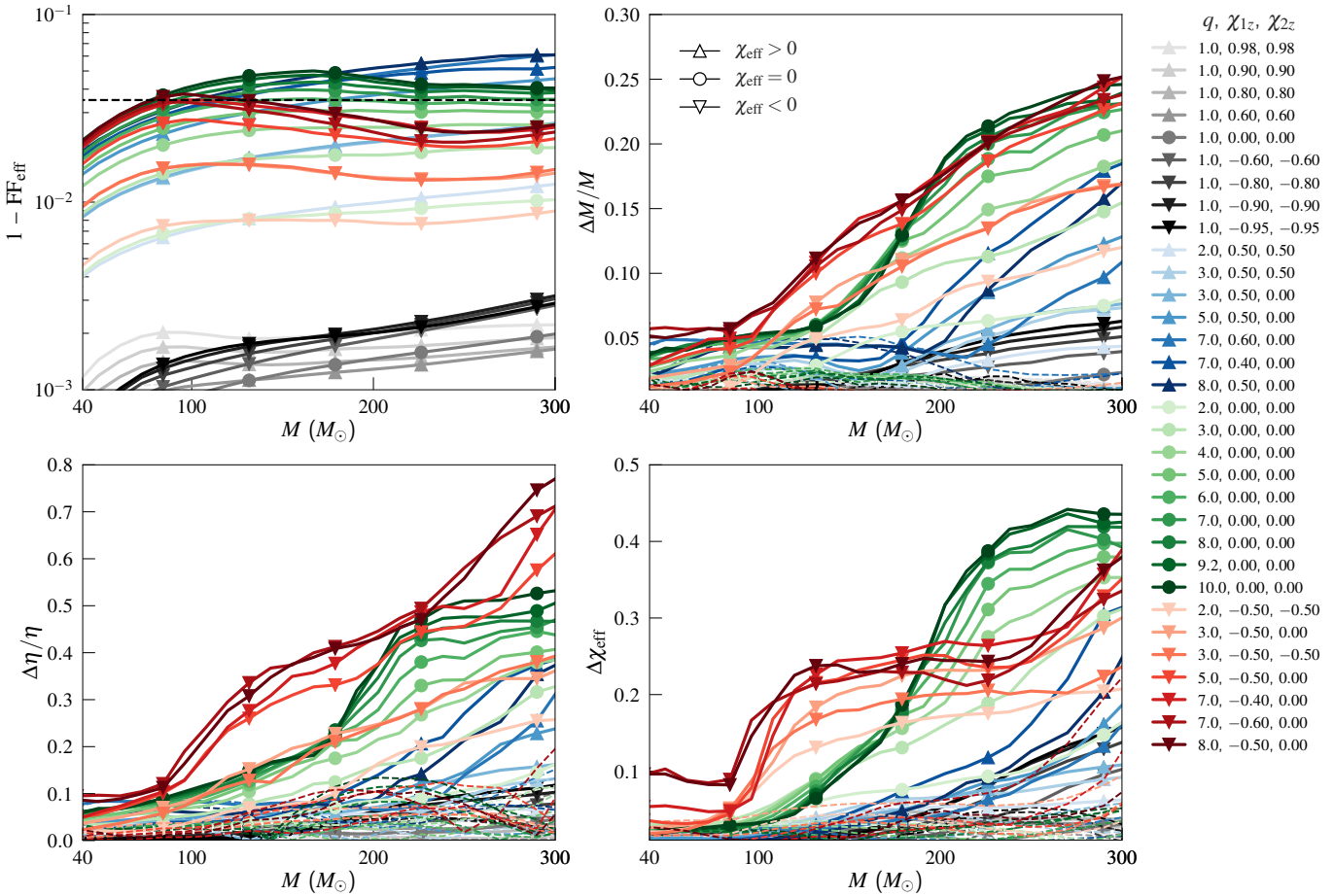


Figure 4.6: “Ineffectualness” and effective parameter biases when using quadrupole-mode templates against hybrid waveforms including all modes. Dashed lines correspond to the same but against quadrupole-only hybrid waveforms, so that the difference between the dashed and solid lines gives an indication of the effect of nonquadrupole modes. Fractional biases are shown for total mass M and symmetric mass ratio η , while absolute biases are shown for effective spins χ_{eff} . FF_{eff} and effective parameter biases are obtained by averaging over all relevant orientations of the binary using Eqs. (4.3) and (4.4). The horizontal axis reports the total mass of the binary while the mass ratio and spins are shown in the legend. The markers indicate the spin types: triangles pointing up/down denoting binaries with aligned/antialigned spins and circles denoting nonspinning binaries. The horizontal dashed black line corresponds to $1 - \text{FF}_{\text{eff}}^3 = 0.1$. Note that most of the dashed lines in the top-left subplot lie below 10^{-3} . We see that as the total mass increases, the ineffectualness and effective biases in M , η and χ_{eff} increase and are dominated by the effects of subdominant modes; see Sec. 4.5 for further discussion.

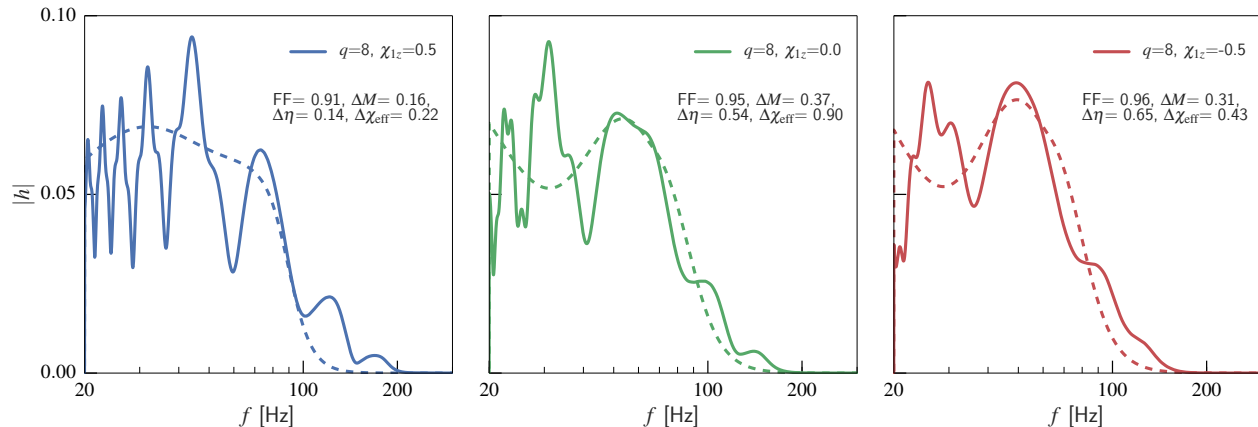


Figure 4.7: Comparison of the frequency domain amplitudes of the “full” hybrid waveform containing subdominant modes (solid lines) and the best-match template waveforms containing only the quadrupole modes (dashed lines). The waveforms have been “whitened” according to the PSD used for match calculation and normalized such that the match with itself is unity. The orientation angles are chosen to be $\iota = \pi/4$, $\varphi_0 = \pi$, $\psi = \pi/3$. The total mass is $M = 200 M_\odot$, and the mass ratio is $q = 8$. The legends show the spin of the larger black hole. The spin on the smaller black hole is zero in all three cases. The inset text shows the fitting factor, fractional biases in parameters M and η and absolute bias in parameter χ_{eff} , at the best-match point. Particularly in the case of negative spin, where the observed signal is dominated by the ringdown, we see that the template is able to mimic the target, producing a reasonably good fitting factor. But this comes at the expense of larger parameter biases.

sub-dominant modes are excited prominently. Consistent with our expectation, in Fig. 4.6, the solid lines show that, in general, the ineffectualness and effective biases increase with increasing mass ratio and with increasing mass. We also see a clear separation of the solid and dashed lines for large mass ratios and high masses, illustrating the effect of neglecting nonquadrupole modes.

Figure 4.6 also reveals an interesting dependence of the effect of nonquadrupole modes on the spins. For binaries with aligned, zero, and antialigned spins, the ineffectualness peaks at total masses of $M \sim 300M_\odot$, $M \sim 150M_\odot$, $M \sim 100M_\odot$, respectively⁶. This is roughly the mass range where the observed signal is dominated by the late inspiral and merger – the phase where the higher modes are excited most prominently. For binaries with antialigned spins, merger happens at relatively lower frequencies, while, for the case of aligned spins, merger happens at relatively higher

⁶Note that this is not true for the $q \approx 1$ cases. For these, since the mismatches are quite small $\sim 10^{-3}$, several competing effects are playing out.

frequencies, owing to the “orbital hangup” [61, 62] effect. Since frequencies are scaled inversely to the total mass of the system, this creates the mass dependence of the ineffectualness that we describe above. For very high masses, the observed signal will contain only the ringdown phase. Due to the smaller bandwidth and the relatively simpler structure of the ringdown signal, the quadrupole-only templates are likely to be able to mimic the full ringdown signal relatively well, at the cost of considerable systematic errors (see Fig. 4.7 for an example). Hence, we anticipate the effectualness of the quadrupole-mode templates to go up at very high masses. This effect should start dominating the effectualness patterns at relatively lower masses for binaries with antialigned spins. Consistent with our expectation, we see in Fig. 4.6 (top left panel) that for a given mass ratio, at low masses, binaries with negative spins have higher ineffectualness but as the mass increases there is a crossover point beyond which binaries with positive spins have higher ineffectualness. While for positive spins, the ineffectualness continues to increase with total mass, for zero spins the ineffectualness plateaus and for negative spins it reaches a maximum value and starts decreasing beyond that point. We see from Fig. 4.6 that this trend of larger (smaller) effectualness for negative (positive) spins at high masses ($M \gtrsim 100M_{\odot}$) is achieved at the cost of larger (smaller) systematic biases in the estimated parameters.

We set $FF_{\text{eff}} \geq 0.965$ (which corresponds to a $\sim 10\%$ loss in detection volume for a fixed SNR threshold) as the benchmark for the relative importance of nonquadrupole modes in detection. This is shown by the dashed black line in the top-left panel of Fig. 4.6. Figure 4.1a summarizes the region in the parameter space where the loss of detectable volume (at a fixed SNR threshold) due to neglecting nonquadrupole modes is greater than 10%. For the case of negative spins, even at large mass ratios, we see that subdominant modes are important for detection only over a range of masses ($M \sim 75 - 150M_{\odot}$). For binaries with positive and zero spins, we anticipate that the upper limit of total mass where the higher modes are important is above $300M_{\odot}$, the highest mass that we consider in this study. Based on Fig. 4.1a, we expect the quadrupole mode templates to be fully effectual for detection either when $q \lesssim 4$ or when $M \lesssim 70M_{\odot}$ (irrespective of spins), considering a population of binaries distributed with isotropic orientations. We note that the region in which subdominant modes become important for detection is the smallest (largest) for negative (positive) spins.

Figure 4.1a also shows the region in the parameter space (marked by the green dashed line) where subdominant modes are important for the detection of nonspinning

binaries when nonspinning quadrupole mode templates are used, obtained in our previous study [22]. We see that the use of quadrupole mode templates with nonprecessing spins has helped us to reduce the region in the parameter space where subdominant modes cause unacceptable loss in the detection volume. This is consistent with our expectation, as two additional parameters (spins) in the templates allow them to achieve higher fitting factors with the target signals, at the cost of a larger bias in the best-matched template parameters.

In order to gauge the relative importance of the systematic errors shown in Fig. 4.6, we compare them against the expected statistical errors from the quadrupole-mode template family IMRPhenomD (computed using Fisher matrix formalism). Figure 4.8 shows the minimum SNR (orientation-averaged) at which the 1σ statistical errors become low enough to equal the systematic errors. (Note that statistical errors are inversely proportional to the SNR.) We see that, at high masses, the systematic errors start to dominate the error budget for orientation-averaged SNRs as low as 3. In this study, whenever the systematic errors are less than the statistical error for an orientation-averaged SNR of 8 (horizontal black dashed line in Fig. 4.8), we regard the quadrupole-mode templates to be faithful for parameter estimation ⁷.

Figure 4.1b summarizes the region in the parameter space where this minimum orientation-averaged SNR is less than or equal to 8 for estimation of any of M , η or χ_{eff} . We exclude any cases where the systematic biases are dominated by the biases in the quadrupole mode itself. We note that the region in which subdominant modes become important for parameter estimation is smallest (largest) for positive (negative) spins. This trend is opposite to what we see in Fig. 4.1a for detection. This is because, at high masses negative spin binaries have higher effectualness than positive spin binaries, which is achieved at the cost of higher systematic biases. We remind the reader that, for spins of higher magnitude than considered in this study (i.e. $|\chi_{\text{eff}}| > 0.5$ for $q \geq 2$), we expect the shaded regions in Fig. 4.1 to expand or reduce depending on the spin; the contours that we draw are indicative demarcations only. For greater aligned spins, the shaded region for detection should expand and the shaded region for parameter estimation should reduce. The opposite trend is expected for greater antialigned spins. Figure 4.1b also compares these results with the results obtained in our previous study [22] (dashed green line) using nonspinning quadrupole-only templates against nonspinning “full” target waveforms. We see that

⁷Note that, when full mode templates are employed in the parameter estimation, the statistical errors are expected to go down in general, due to the increased amount of information in the waveform (see, e.g., [63]). We do not consider this effect here.

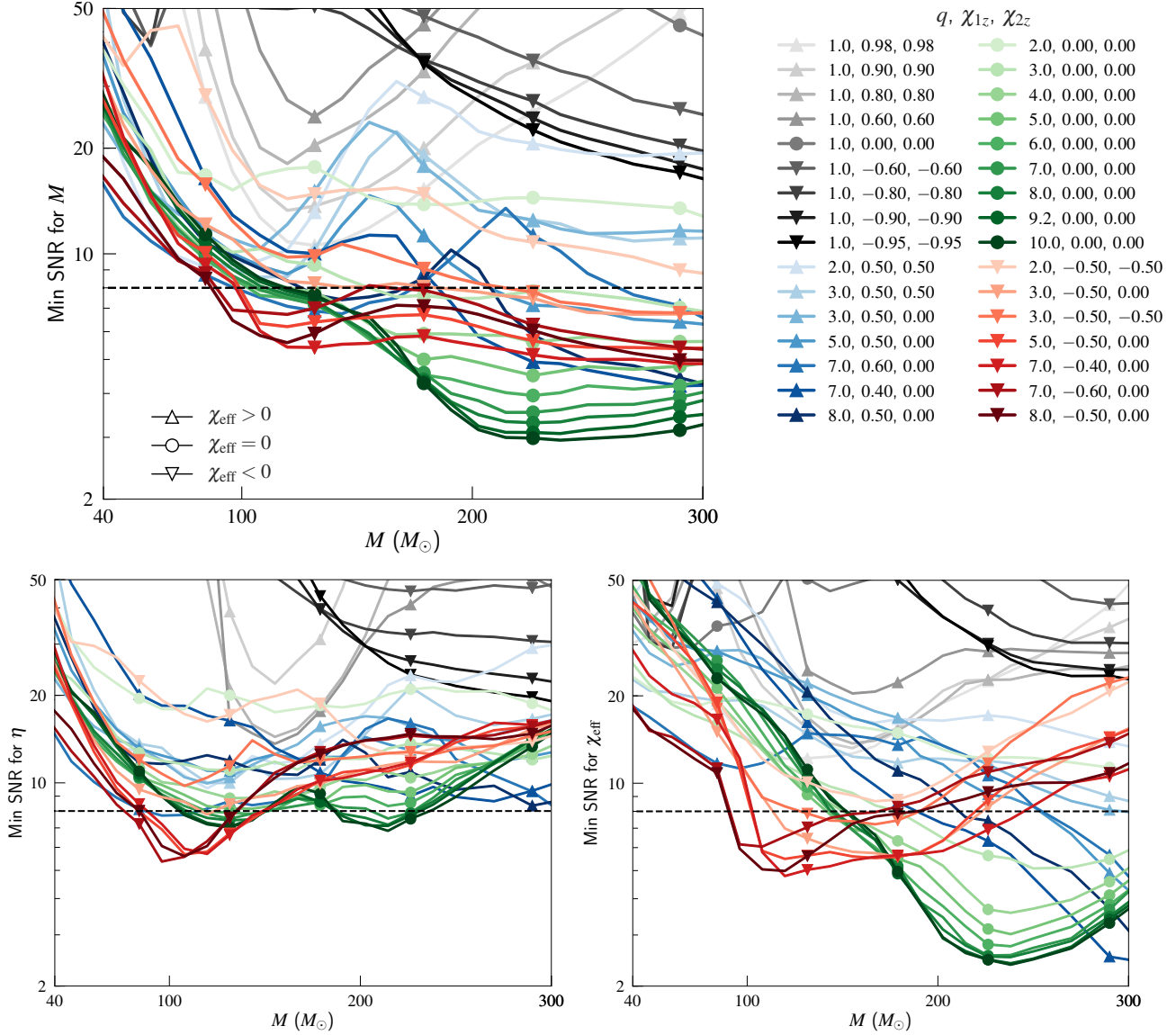


Figure 4.8: Lowest SNR (orientation-averaged) at which the statistical errors are low enough to equal the effective systematic bias in parameters, M , η , and χ_{eff} , when using quadrupole mode templates to estimate the parameters of hybrid waveforms including all modes. A dashed black line is used to denote minimum orientation-averaged SNR of 8 (optimal orientation SNR of 20).

the use of spinning templates essentially increases the region where the parameter estimation bias is dominated by systematic errors.

4.6 Conclusion

We studied the effects of sub-dominant modes in the detection and parameter estimation of GWs from black hole binaries with nonprecessing spins using Advanced LIGO detectors. The effect of sub-dominant modes on detection is quantified in terms of the effective detection volume (fraction of the optimal detection volume that the suboptimal search is sensitive to, for a given SNR threshold) and the effect on parameter estimation in terms of the effective bias (weighted average of the systematic errors for different orientations) in the estimated parameters. We compared quadrupole-mode templates with target signals (hybrid waveforms constructed by matching NR simulations describing the late inspiral, merger and ringdown with PN/EOB waveforms describing the early inspiral). These signals contained contributions from all the spherical harmonic modes up to $\ell = 4$ and $-\ell \leq m \leq \ell$ except the $m = 0$ modes.

Our study considered black hole binaries with total masses $40M_{\odot} \leq M \leq 300M_{\odot}$, mass ratios $1 \leq q \leq 10$, and various spins including $\chi_{\text{eff}} \sim -0.5, 0, 0.5$ ($|\chi_{\text{eff}}| \leq 0.98$ for $q = 1$). The results are appropriately averaged over all angles describing the orientation of the binary (the results are not explicitly averaged over the sky location because both the fitting factors and systematic biases are only weakly dependent on the sky location³). Figure 4.1 shows the regions in the parameter space where the contribution from nonquadrupole modes is important for GW detection and parameter estimation. In general, neglecting subdominant modes can cause unacceptable loss of SNR and unacceptably large systematic errors for binaries with high masses and large mass ratios. For a given mass ratio, subdominant modes are more important for positive (negative) spins for detection (parameter estimation). As compared to our previous study restricted to the case of nonspinning binaries, we see that the use of quadrupole mode templates with nonprecessing spins, enhances the effectualness for detection, but extends the region where systematic errors dominate.

Note that the scope of our study was rather restricted – while we conclude that subdominant mode templates are likely to improve the detection rates of binary black holes in certain regions in the parameter space (high mass and large mass ratios), a proper characterization of this will require characterizing the associated increase in the false alarm rate also (see, e.g., Ref. [21]). Also, we did not study the effect of

neglecting nonquadrupole modes on signal-based vetoes such as the “chi-square” veto [64]. Similarly, we have only investigated the region in the parameter space where the use of the quadrupole-only template would introduce systematic errors that are larger than the expected statistical errors. However, the use of full-mode templates in parameter estimation is likely to reduce the statistical errors, owing to the increased information content in the waveform. We have not explored this aspect of the problem here. The expected statistical errors were estimated using the Fisher matrix formalism. Since these error bounds are lower limits, our estimates on the region of the parameter space where the systematic errors are negligible should be treated as conservative estimates. We conclude that subdominant modes are important for parameter estimation when the systematic errors are greater than 1σ statistical errors at a sky and orientation averaged SNR of 8. If more stringent criteria are applied, our shaded regions in Fig. 4.1b would widen. Also, note that we restricted our study to the case of binaries with nonprecessing spins. Astrophysical black hole binaries may have generic spin orientations. It is not clear how our conclusions hold in the case of precessing spins (see Ref. [65] for some recent work in this direction). We leave some of these investigations as future work.

4.7 Acknowledgments

We are indebted to the SXS Collaboration for making a public catalog of numerical-relativity waveforms, and to Chandra Kant Mishra for sharing a notebook of post-Newtonian waveforms. We thank Abhirup Ghosh, Chandra Kant Mishra, Sascha Husa, Mark Hannam, Michael Pürrer, and Patricia Schmidt for useful discussions. We also thank Richard O’Shaughnessy, B. S. Sathyaprakash, Prayush Kumar, and the anonymous referee for several useful comments on the manuscript. P. A.’s research was supported by the AIRBUS Group Corporate Foundation through a chair in “Mathematics of Complex Systems” at the International Centre for Theoretical Sciences (ICTS); by a Ramanujan Fellowship from the Science and Engineering Research Board (SERB), India; by the SERB FastTrack fellowship SR/FTP/PS-191/2012; by Indo-US Centre for the Exploration of Extreme Gravity funded by the Indo-US Science and Technology Forum; and by the Max Planck Society and the Department of Science and Technology, India, through a Max Planck Partner Group at ICTS. V. V.’s research was supported by NSF Grant No. PHY-1404569 to Caltech and the Sherman Fairchild Foundation. Computations were performed at the ICTS clusters Mowgli, Dogmatix, and Alice.

APPENDIX

4.A Comparison with Bayesian parameter estimation

In this paper, we tried to quantify the loss of detection efficiency due to neglecting subdominant modes by computing the fitting factors of the dominant-mode templates with target signals including the effect of subdominant modes. Systematic errors in parameter estimation were computed by comparing the parameters of the “best-matched” subdominant-mode templates with the true parameters of the target signals, while statistical errors are computed from the Fisher information matrix. Since these calculations are computationally inexpensive, this allows us to study the impact of subdominant modes over the entire parameter space of interest, after averaging over extrinsic parameters such as the orientation angles. However, we know that the inverse of the Fisher matrix provides a *lower bound* of the statistical errors in the parameter estimation [66, 67]. In order to verify that our simplified estimates of the statistical and systematic errors give a good approximation to the true errors, we compare our estimates of the systematic and statistical errors with those derived from full Bayesian parameter estimation for one sample case.

Method	M_{bias}	η_{bias}	$\chi_{\text{bias}}^{\text{eff}}$	δM	$\delta \eta$	$\delta \chi_{\text{eff}}$
Bayesian	$7.6 \times 10^{-1} M_{\odot}$	2.2×10^{-3}	4.3×10^{-2}	$2.8 M_{\odot}$	2.4×10^{-3}	1.3×10^{-1}
FF/Fisher	$2.6 \times 10^{-1} M_{\odot}$	2.7×10^{-3}	5.4×10^{-2}	$1.9 M_{\odot}$	9.5×10^{-3}	7.0×10^{-2}

Table 4.A.1: Comparison of systematic and statistical biases as predicted by a full Bayesian parameter estimation (top row) study with a fitting factor/Fisher matrix study that is used in this paper (bottom row). The first three columns show the absolute systematic biases and the next three columns show the statistical errors in the estimation of total mass M , symmetric mass ratio η and effective spin χ_{eff} . For the Bayesian study (top row), systematic biases are inferred from the peaks of the posterior distributions and the statistical biases are given by the widths of 68% credible intervals. In the bottom row, the systematic biases are inferred from the best-match parameters and the statistical biases are given by 1σ errors from a Fisher matrix study.

We create a simulated data stream by injecting a numerical-relativity waveform from the SXS waveform catalog [31, 33, 68] into colored Gaussian noise with the power spectrum of Advanced LIGO. The injected waveform (SXS:BBH:0307) has the mass ratio $m_1/m_2 = 1.228$, aligned spins $\chi_1 = 0.32$, $\chi_2 = -0.5798$, and has a SNR of ~ 25 . We estimate the posterior distributions of the masses and spins

using the `LALINFERENCENEST` code [16, 69] that is part of the LSC Algorithms Library [70]. We compare the maximum a posteriori probability (MAP) estimates with the true parameters, which provides us an estimate of the systematic bias. Similarly, the width of the 68% credible regions provides us an estimate of the statistical errors. These estimates are compared with the same estimated using the methods that we use in the paper. Table 4.A.1 provides a comparison between these independent estimates. We see that, for the parameters that we consider, the two different estimates are in reasonable agreement. Although this provides some confidence in our results, extensive comparisons with Bayesian estimates over the full parameters space are required to confidently establish the accuracy of our approximate results. We leave this as future work.

References

- [1] B. P. Abbott et al. “Observation of Gravitational Waves from a Binary Black Hole Merger”. In: *Phys. Rev. Lett.* 116 (6 Feb. 2016), p. 061102. DOI: [10.1103/PhysRevLett.116.061102](https://doi.org/10.1103/PhysRevLett.116.061102). URL: <http://link.aps.org/doi/10.1103/PhysRevLett.116.061102>.
- [2] B. P. Abbott et al. “GW151226: Observation of Gravitational Waves from a 22-Solar-Mass Binary Black Hole Coalescence”. In: *Phys. Rev. Lett.* 116 (24 June 2016), p. 241103. DOI: [10.1103/PhysRevLett.116.241103](https://doi.org/10.1103/PhysRevLett.116.241103). URL: <http://link.aps.org/doi/10.1103/PhysRevLett.116.241103>.
- [3] B. P. Abbott et al. (LIGO Scientific Collaboration). “The Rate of Binary Black Hole Mergers Inferred from Advanced LIGO Observations Surrounding GW150914”. In: *ArXiv e-prints* (Feb. 2016). arXiv: [1602.03842](https://arxiv.org/abs/1602.03842) [[astro-ph.HE](https://arxiv.org/abs/1602.03842)].
- [4] B. P. Abbott et al. “Binary Black Hole Mergers in the First Advanced LIGO Observing Run”. In: *Phys. Rev. X* 6 (4 Oct. 2016), p. 041015. DOI: [10.1103/PhysRevX.6.041015](https://doi.org/10.1103/PhysRevX.6.041015). URL: <http://link.aps.org/doi/10.1103/PhysRevX.6.041015>.
- [5] B. P. Abbott et al. “Properties of the Binary Black Hole Merger GW150914”. In: *Phys. Rev. Lett.* 116 (24 June 2016), p. 241102. DOI: [10.1103/PhysRevLett.116.241102](https://doi.org/10.1103/PhysRevLett.116.241102). URL: <http://link.aps.org/doi/10.1103/PhysRevLett.116.241102>.
- [6] B. P. Abbott et al. (LIGO Scientific Collaboration). “Astrophysical Implications of the Binary Black-hole Merger GW150914”. In: *The Astrophysical Journal Letters* 818, L22 (Feb. 2016), p. L22. DOI: [10.3847/2041-8205/818/2/L22](https://doi.org/10.3847/2041-8205/818/2/L22). arXiv: [1602.03846](https://arxiv.org/abs/1602.03846) [[astro-ph.HE](https://arxiv.org/abs/1602.03846)].

- [7] B. P. Abbott et al. “Tests of General Relativity with GW150914”. In: *Phys. Rev. Lett.* 116 (22 May 2016), p. 221101. DOI: [10.1103/PhysRevLett.116.221101](https://doi.org/10.1103/PhysRevLett.116.221101). URL: <http://link.aps.org/doi/10.1103/PhysRevLett.116.221101>.
- [8] S. Klimenko et al. “Method for detection and reconstruction of gravitational wave transients with networks of advanced detectors”. In: *Phys. Rev. D* 93.4 (2016), p. 042004. DOI: [10.1103/PhysRevD.93.042004](https://doi.org/10.1103/PhysRevD.93.042004). arXiv: [1511.05999](https://arxiv.org/abs/1511.05999) [gr-qc].
- [9] Ryan Lynch et al. “An information-theoretic approach to the gravitational-wave burst detection problem”. In: (2015). arXiv: [1511.05955](https://arxiv.org/abs/1511.05955) [gr-qc].
- [10] S Klimenko et al. “A coherent method for detection of gravitational wave bursts”. In: *Classical and Quantum Gravity* 25.11 (2008), p. 114029. URL: <http://stacks.iop.org/0264-9381/25/i=11/a=114029>.
- [11] B. P. Abbott et al. “Observing gravitational-wave transient GW150914 with minimal assumptions”. In: *Phys. Rev. D* 93 (12 June 2016), p. 122004. DOI: [10.1103/PhysRevD.93.122004](https://doi.org/10.1103/PhysRevD.93.122004). URL: <http://link.aps.org/doi/10.1103/PhysRevD.93.122004>.
- [12] B. P. Abbott et al. “GW150914: First results from the search for binary black hole coalescence with Advanced LIGO”. In: *Phys. Rev. D* 93 (12 June 2016), p. 122003. DOI: [10.1103/PhysRevD.93.122003](https://doi.org/10.1103/PhysRevD.93.122003). URL: <http://link.aps.org/doi/10.1103/PhysRevD.93.122003>.
- [13] Tito Dal Canton et al. “Implementing a search for aligned-spin neutron star-black hole systems with advanced ground based gravitational wave detectors”. In: *Phys. Rev. D* 90.8 (2014), p. 082004. DOI: [10.1103/PhysRevD.90.082004](https://doi.org/10.1103/PhysRevD.90.082004). arXiv: [1405.6731](https://arxiv.org/abs/1405.6731) [gr-qc].
- [14] Samantha A. Usman et al. “The PyCBC search for gravitational waves from compact binary coalescence”. In: *Class. Quant. Grav.* 33.21 (2016), p. 215004. DOI: [10.1088/0264-9381/33/21/215004](https://doi.org/10.1088/0264-9381/33/21/215004). arXiv: [1508.02357](https://arxiv.org/abs/1508.02357) [gr-qc].
- [15] Kipp Cannon et al. “Toward Early-Warning Detection of Gravitational Waves from Compact Binary Coalescence”. In: *Astrophys. J.* 748 (2012), p. 136. DOI: [10.1088/0004-637X/748/2/136](https://doi.org/10.1088/0004-637X/748/2/136). arXiv: [1107.2665](https://arxiv.org/abs/1107.2665) [astro-ph.IM].
- [16] J. Veitch et al. “Parameter estimation for compact binaries with ground-based gravitational-wave observations using the LALInference software library”. In: *Phys. Rev. D* 91.4 (2015), p. 042003. DOI: [10.1103/PhysRevD.91.042003](https://doi.org/10.1103/PhysRevD.91.042003). arXiv: [1409.7215](https://arxiv.org/abs/1409.7215) [gr-qc].
- [17] T. Damour, B R Iyer, and B S Sathyaprakash. “Improved filters for gravitational waves from inspiraling compact binaries”. In: *Phys. Rev. D* 57 (1998), pp. 885–907.

- [18] B. P. Abbott et al. “Directly comparing GW150914 with numerical solutions of Einstein’s equations for binary black hole coalescence”. In: *Phys. Rev. D* 94 (2016), p. 064035. DOI: [10.1103/PhysRevD.94.064035](https://doi.org/10.1103/PhysRevD.94.064035). arXiv: [1606.01262](https://arxiv.org/abs/1606.01262) [gr-qc].
- [19] Larne Pekowsky et al. “Impact of higher-order modes on the detection of binary black hole coalescences”. In: *Phys. Rev. D* 87 (8 Apr. 2013), p. 084008.
- [20] Duncan A. Brown, Prayush Kumar, and Alexander H. Nitz. “Template banks to search for low-mass binary black holes in advanced gravitational-wave detectors”. In: *Phys. Rev. D* 87 (8 Apr. 2013), p. 082004.
- [21] Collin Capano, Yi Pan, and Alessandra Buonanno. “Impact of Higher Harmonics in Searching for Gravitational Waves from Non-Spinning Binary Black Holes”. In: (2013). arXiv: [1311.1286](https://arxiv.org/abs/1311.1286) [gr-qc].
- [22] Vijay Varma et al. “Gravitational-wave observations of binary black holes: Effect of nonquadrupole modes”. In: *Phys. Rev. D* 90 (12 Dec. 2014), p. 124004. DOI: [10.1103/PhysRevD.90.124004](https://doi.org/10.1103/PhysRevD.90.124004). URL: <http://link.aps.org/doi/10.1103/PhysRevD.90.124004>.
- [23] B. P. Abbott et al. “Effects of waveform model systematics on the interpretation of GW150914”. In: (2016). arXiv: [1611.07531](https://arxiv.org/abs/1611.07531) [gr-qc].
- [24] B. P. Abbott et al. “Directly comparing GW150914 with numerical solutions of Einstein’s equations for binary black hole coalescence”. In: *Phys. Rev. D* 94 (6 Sept. 2016), p. 064035. DOI: [10.1103/PhysRevD.94.064035](https://doi.org/10.1103/PhysRevD.94.064035). URL: <http://link.aps.org/doi/10.1103/PhysRevD.94.064035>.
- [25] Juan Calderón Bustillo et al. “Impact of gravitational radiation higher order modes on single aligned-spin gravitational wave searches for binary black holes”. In: *Phys. Rev. D* 93 (8 Apr. 2016), p. 084019. DOI: [10.1103/PhysRevD.93.084019](https://doi.org/10.1103/PhysRevD.93.084019). URL: <http://link.aps.org/doi/10.1103/PhysRevD.93.084019>.
- [26] B.S. Sathyaprakash and Bernard F. Schutz. “Physics, Astrophysics and Cosmology with Gravitational Waves”. In: *Living Reviews in Relativity* 12.2 (2009). DOI: [10.1007/lrr-2009-2](https://doi.org/10.1007/lrr-2009-2). URL: <http://www.livingreviews.org/lrr-2009-2>.
- [27] Luc Blanchet et al. “The Third post-Newtonian gravitational wave polarisations and associated spherical harmonic modes for inspiralling compact binaries in quasi-circular orbits”. In: *Class.Quant.Grav.* 25 (2008), p. 165003. DOI: [10.1088/0264-9381/25/16/165003](https://doi.org/10.1088/0264-9381/25/16/165003), [10.1088/0264-9381/29/23/239501](https://doi.org/10.1088/0264-9381/29/23/239501). arXiv: [0802.1249](https://arxiv.org/abs/0802.1249) [gr-qc].
- [28] K. G. Arun et al. “Higher-order spin effects in the amplitude and phase of gravitational waveforms emitted by inspiraling compact binaries: Ready-to-use gravitational waveforms”. In: 79.10 (May 2009), p. 104023. DOI:

- [10.1103/PhysRevD.79.104023](https://doi.org/10.1103/PhysRevD.79.104023). URL: <http://link.aps.org/doi/10.1103/PhysRevD.79.104023>.
- [29] Alessandra Buonanno, Guillaume Faye, and Tanja Hinderer. “Spin effects on gravitational waves from inspiraling compact binaries at second post-Newtonian order”. In: *Phys. Rev. D* 87.4 (2013), p. 044009. DOI: [10.1103/PhysRevD.87.044009](https://doi.org/10.1103/PhysRevD.87.044009). arXiv: [1209.6349](https://arxiv.org/abs/1209.6349) [gr-qc].
- [30] Andrea Taracchini et al. “Effective-one-body model for black-hole binaries with generic mass ratios and spins”. In: *Phys. Rev. D* 89 (6 Mar. 2014), p. 061502. DOI: [10.1103/PhysRevD.89.061502](https://doi.org/10.1103/PhysRevD.89.061502). URL: <http://link.aps.org/doi/10.1103/PhysRevD.89.061502>.
- [31] SXS Gravitational Waveform Database. URL: <http://www.black-holes.org/waveforms/>.
- [32] The Spectral Einstein Code. URL: <http://www.black-holes.org/SpEC.html>.
- [33] Abdul H. Mroue et al. “A catalog of 171 high-quality binary black-hole simulations for gravitational-wave astronomy”. In: (2013). arXiv: [1304.6077](https://arxiv.org/abs/1304.6077) [gr-qc].
- [34] Abdul H. Mroue and Harald P. Pfeiffer. “Precessing Binary Black Holes Simulations: Quasicircular Initial Data”. In: (2012). arXiv: [1210.2958](https://arxiv.org/abs/1210.2958) [gr-qc].
- [35] Geoffrey Lovelace, Mark.A. Scheel, and Bela Szilagyi. “Simulating merging binary black holes with nearly extremal spins”. In: *Phys.Rev. D* 83 (2011), p. 024010. DOI: [10.1103/PhysRevD.83.024010](https://doi.org/10.1103/PhysRevD.83.024010). arXiv: [1010.2777](https://arxiv.org/abs/1010.2777) [gr-qc].
- [36] Jonathan Blackman et al. “Fast and Accurate Prediction of Numerical Relativity Waveforms from Binary Black Hole Coalescences Using Surrogate Models”. In: *Phys. Rev. Lett.* 115.12 (2015), p. 121102. DOI: [10.1103/PhysRevLett.115.121102](https://doi.org/10.1103/PhysRevLett.115.121102). arXiv: [1502.07758](https://arxiv.org/abs/1502.07758) [gr-qc].
- [37] Luisa T. Buchman et al. “Simulations of non-equal mass black hole binaries with spectral methods”. In: *Phys.Rev. D* 86 (2012), p. 084033. DOI: [10.1103/PhysRevD.86.084033](https://doi.org/10.1103/PhysRevD.86.084033). arXiv: [1206.3015](https://arxiv.org/abs/1206.3015) [gr-qc].
- [38] Serguei Ossokine, Lawrence E. Kidder, and Harald P. Pfeiffer. “Precession-tracking coordinates for simulations of compact-object-binaries”. In: *Phys.Rev. D* 88 (2013), p. 084031. DOI: [10.1103/PhysRevD.88.084031](https://doi.org/10.1103/PhysRevD.88.084031). arXiv: [1304.3067](https://arxiv.org/abs/1304.3067) [gr-qc].
- [39] Daniel A. Hemberger et al. “Dynamical Excision Boundaries in Spectral Evolutions of Binary Black Hole Spacetimes”. In: *Class.Quant.Grav.* 30 (2013), p. 115001. DOI: [10.1088/0264-9381/30/11/115001](https://doi.org/10.1088/0264-9381/30/11/115001). arXiv: [1211.6079](https://arxiv.org/abs/1211.6079) [gr-qc].

- [40] Bela Szilagyi, Lee Lindblom, and Mark A. Scheel. “Simulations of Binary Black Hole Mergers Using Spectral Methods”. In: *Phys.Rev.* D80 (2009), p. 124010. DOI: [10.1103/PhysRevD.80.124010](https://doi.org/10.1103/PhysRevD.80.124010). arXiv: [0909.3557](https://arxiv.org/abs/0909.3557) [gr-qc].
- [41] Michael Boyle and Abdul H. Mroue. “Extrapolating gravitational-wave data from numerical simulations”. In: *Phys.Rev.* D80 (2009), p. 124045. DOI: [10.1103/PhysRevD.80.124045](https://doi.org/10.1103/PhysRevD.80.124045). arXiv: [0905.3177](https://arxiv.org/abs/0905.3177) [gr-qc].
- [42] Mark A. Scheel et al. “High-accuracy waveforms for binary black hole inspiral, merger, and ringdown”. In: *Phys.Rev.* D79 (2009), p. 024003. DOI: [10.1103/PhysRevD.79.024003](https://doi.org/10.1103/PhysRevD.79.024003). arXiv: [0810.1767](https://arxiv.org/abs/0810.1767) [gr-qc].
- [43] Michael Boyle et al. “High-accuracy comparison of numerical relativity simulations with post-Newtonian expansions”. In: *Phys. Rev.* D76 (2007), p. 124038. DOI: [10.1103/PhysRevD.76.124038](https://doi.org/10.1103/PhysRevD.76.124038). arXiv: [0710.0158](https://arxiv.org/abs/0710.0158) [gr-qc].
- [44] Mark A. Scheel et al. “Solving Einstein’s equations with dual coordinate frames”. In: *Phys.Rev.* D74 (2006), p. 104006. DOI: [10.1103/PhysRevD.74.104006](https://doi.org/10.1103/PhysRevD.74.104006). arXiv: [gr-qc/0607056](https://arxiv.org/abs/gr-qc/0607056) [gr-qc].
- [45] Lee Lindblom et al. “A New generalized harmonic evolution system”. In: *Class.Quant.Grav.* 23 (2006), S447–S462. DOI: [10.1088/0264-9381/23/16/S09](https://doi.org/10.1088/0264-9381/23/16/S09). arXiv: [gr-qc/0512093](https://arxiv.org/abs/gr-qc/0512093) [gr-qc].
- [46] Harald P. Pfeiffer et al. “A Multidomain spectral method for solving elliptic equations”. In: *Comput.Phys.Commun.* 152 (2003), pp. 253–273. DOI: [10.1016/S0010-4655\(02\)00847-0](https://doi.org/10.1016/S0010-4655(02)00847-0). arXiv: [gr-qc/0202096](https://arxiv.org/abs/gr-qc/0202096) [gr-qc].
- [47] Daniel A. Hemberger et al. “Final spin and radiated energy in numerical simulations of binary black holes with equal masses and equal, aligned or anti-aligned spins”. In: *Phys.Rev.* D88 (2013), p. 064014. DOI: [10.1103/PhysRevD.88.064014](https://doi.org/10.1103/PhysRevD.88.064014). arXiv: [1305.5991](https://arxiv.org/abs/1305.5991) [gr-qc].
- [48] Ilana MacDonald et al. “Suitability of hybrid gravitational waveforms for unequal-mass binaries”. In: *Phys. Rev.* D87.2 (2013), p. 024009. DOI: [10.1103/PhysRevD.87.024009](https://doi.org/10.1103/PhysRevD.87.024009). arXiv: [1210.3007](https://arxiv.org/abs/1210.3007) [gr-qc].
- [49] Ilana MacDonald et al. “Suitability of post-Newtonian/numerical-relativity hybrid waveforms for gravitational wave detectors”. In: *Class. Quant. Grav.* 28 (2011), p. 134002. DOI: [10.1088/0264-9381/28/13/134002](https://doi.org/10.1088/0264-9381/28/13/134002). arXiv: [1102.5128](https://arxiv.org/abs/1102.5128) [gr-qc].
- [50] Mark Hannam et al. “Where post-Newtonian and numerical-relativity waveforms meet”. In: *Phys. Rev.* D77 (2008), p. 044020. DOI: [10.1103/PhysRevD.77.044020](https://doi.org/10.1103/PhysRevD.77.044020). arXiv: [0706.1305](https://arxiv.org/abs/0706.1305) [gr-qc].
- [51] P. Ajith. “Gravitational-wave data analysis using binary black-hole waveforms”. In: *Class. Quant. Grav.* 25 (2008), p. 114033. DOI: [10.1088/0264-9381/25/11/114033](https://doi.org/10.1088/0264-9381/25/11/114033).

- [52] Mark Hannam et al. “Length requirements for numerical-relativity waveforms”. In: *Phys. Rev. D* 82 (2010), p. 124052. DOI: [10.1103/PhysRevD.82.124052](https://doi.org/10.1103/PhysRevD.82.124052). arXiv: [1008.2961](https://arxiv.org/abs/1008.2961) [gr-qc].
- [53] Sebastian Khan et al. “Frequency-domain gravitational waves from nonprecessing black-hole binaries. II. A phenomenological model for the advanced detector era”. In: *Phys. Rev. D* 93 (4 Feb. 2016), p. 044007. DOI: [10.1103/PhysRevD.93.044007](https://doi.org/10.1103/PhysRevD.93.044007). URL: <http://link.aps.org/doi/10.1103/PhysRevD.93.044007>.
- [54] Sascha Husa et al. “Frequency-domain gravitational waves from nonprecessing black-hole binaries. I. New numerical waveforms and anatomy of the signal”. In: *Phys. Rev. D* 93 (4 Feb. 2016), p. 044006. DOI: [10.1103/PhysRevD.93.044006](https://doi.org/10.1103/PhysRevD.93.044006). URL: <http://link.aps.org/doi/10.1103/PhysRevD.93.044006>.
- [55] LALSimulation is part of the LALSuite software package. URL: <https://www.lsc-group.phys.uwm.edu/daswg/projects/lalsuite.html>.
- [56] T. A. Apostolatos. “Search templates for gravitational waves from precessing, inspiraling binaries”. In: *Phys. Rev. D* 52 (1995), pp. 605–620.
- [57] Bruce Allen et al. “FINDCHIRP: An Algorithm for detection of gravitational waves from inspiraling compact binaries”. In: *Phys. Rev. D* 85 (2012), p. 122006. DOI: [10.1103/PhysRevD.85.122006](https://doi.org/10.1103/PhysRevD.85.122006). arXiv: [gr-qc/0509116](https://arxiv.org/abs/gr-qc/0509116) [gr-qc].
- [58] The SciPy software library. URL: <http://scipy.org/>.
- [59] *Advanced LIGO anticipated sensitivity curves*. LIGO Document T0900288-v3. URL: <https://dcc.ligo.org/LIGO-T0900288/public>.
- [60] Salvatore Vitale. “Three observational differences for binary black holes detections with second and third generation gravitational-wave detectors”. In: *Phys. Rev. D* 94.12 (2016), p. 121501. DOI: [10.1103/PhysRevD.94.121501](https://doi.org/10.1103/PhysRevD.94.121501). arXiv: [1610.06914](https://arxiv.org/abs/1610.06914) [gr-qc].
- [61] M. Campanelli, C. O. Lousto, and Y. Zlochower. “Spinning-black-hole binaries: The orbital hang-up”. In: *Phys. Rev. D* 74 (4 Aug. 2006), p. 041501. DOI: [10.1103/PhysRevD.74.041501](https://doi.org/10.1103/PhysRevD.74.041501). URL: <http://link.aps.org/doi/10.1103/PhysRevD.74.041501>.
- [62] Mark Hannam et al. “Comparison between numerical-relativity and post-Newtonian waveforms from spinning binaries: The orbital hang-up case”. In: *Phys. Rev. D* 78 (10 Nov. 2008), p. 104007. DOI: [10.1103/PhysRevD.78.104007](https://doi.org/10.1103/PhysRevD.78.104007). URL: <http://link.aps.org/doi/10.1103/PhysRevD.78.104007>.

- [63] Chris Van Den Broeck and Anand S. Sengupta. “Phenomenology of amplitude-corrected post-Newtonian gravitational waveforms for compact binary inspiral. I. Signal-to-noise ratios”. In: *Class.Quant.Grav.* 24 (2007), pp. 155–176. DOI: [10.1088/0264-9381/24/1/009](https://doi.org/10.1088/0264-9381/24/1/009). arXiv: [gr-qc/0607092](https://arxiv.org/abs/gr-qc/0607092) [[gr-qc](#)].
- [64] Bruce Allen. “A χ^2 time-frequency discriminator for gravitational wave detection”. In: *Phys. Rev. D* 71 (2005), p. 062001. DOI: [10.1103/PhysRevD.71.062001](https://doi.org/10.1103/PhysRevD.71.062001). arXiv: [gr-qc/0405045](https://arxiv.org/abs/gr-qc/0405045).
- [65] Juan Calderon Bustillo, Pablo Laguna, and Deirdre Shoemaker. “Detectability of gravitational waves from binary black holes: Impact of precession and higher modes”. In: (Dec. 2016), p. 6. arXiv: [1612.02340](https://arxiv.org/abs/1612.02340). URL: <http://arxiv.org/abs/1612.02340>.
- [66] H. Cramér. *Mathematical Methods of Statistics*. Princeton Mathematical Series. Princeton University Press, 1999. ISBN: 9780691005478. URL: <https://books.google.co.in/books?id=CRTKkaJ00DYC>.
- [67] C. Radhakrishna Rao. “Information and the accuracy attainable in the estimation of statistical parameters”. In: *Bull. Calcutta Math. Soc.* 37 (1945), pp. 81–91. ISSN: 0008-0659.
- [68] Patricia Schmidt, Ian W. Harry, and Harald P. Pfeiffer. “Numerical Relativity Injection Infrastructure”. In: (2017). arXiv: [1703.01076](https://arxiv.org/abs/1703.01076) [[gr-qc](#)].
- [69] J. Veitch and A. Vecchio. “Bayesian coherent analysis of in-spiral gravitational wave signals with a detector network”. In: *Phys. Rev. D* 81 (2010). DOI: [10.1103/PhysRevD.81.062003](https://doi.org/10.1103/PhysRevD.81.062003). arXiv: [0911.3820](https://arxiv.org/abs/0911.3820) [[astro-ph.CO](#)].
- [70] *LSC Algorithms Library*. URL: <https://www.lsc-group.phys.uwm.edu/daswg/projects/lalsuite.html>.

SURROGATE MODEL OF HYBRIDIZED NUMERICAL RELATIVITY BINARY BLACK HOLE WAVEFORMS

Vijay Varma, Scott E. Field, Mark A. Scheel, Jonathan Blackman, Lawrence E. Kidder, and Harald P. Pfeiffer. *Physical Review D.*, 99, 064045 (2019), [arxiv:1812.07865](https://arxiv.org/abs/1812.07865).

5.1 Executive summary

Surrogate models are capable of accurately, yet cheaply reproducing numerical relativity simulations. They are however restricted to the length of these simulations, which typically only include about 20 orbits before merger due to the computational expense. Fortunately, post-Newtonian theory is valid for earlier times, and can be combined with the numerical relativity waveform to produce a “hybrid” waveform. This Chapter presents the first surrogate model based on hybrid waveforms, and therefore covers the full range of frequencies relevant for stellar mass aligned-spin binary black holes with ground based detectors. This model is more accurate than existing aligned-spin models by about two orders of magnitudes.

5.2 Abstract

Numerical relativity (NR) simulations provide the most accurate binary black hole gravitational waveforms, but are prohibitively expensive for applications such as parameter estimation. Surrogate models of NR waveforms have been shown to be both fast and accurate. However, NR-based surrogate models are limited by the training waveforms’ length, which is typically about 20 orbits before merger. We remedy this by hybridizing the NR waveforms using both post-Newtonian and effective one body waveforms for the early inspiral. We present NRHybSur3dq8, a surrogate model for hybridized nonprecessing numerical relativity waveforms, that is valid for the entire LIGO band (starting at 20 Hz) for stellar mass binaries with total masses as low as $2.25 M_{\odot}$. We include the $\ell \leq 4$ and (5,5) spin-weighted spherical harmonic modes but not the (4,1) or (4,0) modes. This model has been trained against hybridized waveforms based on 104 NR waveforms with mass ratios $q \leq 8$, and $|\chi_{1z}|, |\chi_{2z}| \leq 0.8$, where χ_{1z} (χ_{2z}) is the spin of the heavier (lighter) BH in the direction of orbital angular momentum. The surrogate

reproduces the hybrid waveforms accurately, with mismatches $\lesssim 3 \times 10^{-4}$ over the mass range $2.25M_{\odot} \leq M \leq 300M_{\odot}$. At high masses ($M \gtrsim 40M_{\odot}$), where the merger and ringdown are more prominent, we show roughly two orders of magnitude improvement over existing waveform models. We also show that the surrogate works well even when extrapolated outside its training parameter space range, including at spins as large as 0.998. Finally, we show that this model accurately reproduces the spheroidal-spherical mode mixing present in the NR ringdown signal.

5.3 Introduction

The era of gravitational wave (GW) astronomy has been emphatically unveiled with the recent detections [1–7] by LIGO [8] and Virgo [9]. The detection of gravitational wave signals from compact binary sources is expected to become a routine occurrence as the advanced detectors reach their design sensitivity [10, 11]. The possible science output from these events crucially depends on the availability of an accurate waveform model to compare against observed signals.

Numerical relativity (NR) is the only *ab initio* approach that accurately produces waveforms from the merger of a binary black hole (BBH) system. However, because NR simulations are computationally expensive, it is impractical to use them directly for applications such as parameter estimation, which can require upwards of 10^7 waveform evaluations. Therefore, the GW community has developed several approximate waveform models [12–21], some of which are fast to evaluate. These models make certain physically-motivated assumptions about the underlying phenomenology of the waveforms, and they fit for any remaining free parameters using NR simulations.

Surrogate modeling [22, 23] is an alternative approach that doesn’t assume an underlying phenomenology and has been applied to a diverse range of problems [22–32]. NR Surrogate models follow a data-driven approach, directly using the NR waveforms to implicitly reconstruct the underlying phenomenology. Three NR surrogate models have been built so far [26–28], including a 7-dimensional (mass ratio q and two spin vectors) model for generically precessing systems in quasi-circular orbit [28]. Through cross-validation studies, these models were shown to be nearly as accurate as the NR waveforms they were trained against.

Despite the success of the surrogate modeling approach, existing surrogate models have two important limitations: (1) Because they are based solely on NR simulations, which typically are only able to cover the last ~ 20 orbits of a BBH inspiral, they

are not long enough to span the full LIGO band for stellar mass binaries. (2) Apart from the first non-spinning model [26], these models have been restricted to mass ratios $q \leq 2$ ¹. There are two reasons for this: (i) The 7d parameter space is vast, requiring at least a few thousand simulations to sufficiently cover it. (ii) Because of the smaller length scale introduced by the lighter black hole, NR simulations become increasingly more expensive with mass ratio.

In this work we address these limitations in the context of nonprecessing BBH systems. First, to include the early inspiral we “hybridize” the NR waveforms: each full waveform consists of a post-Newtonian (PN) and effective one body (EOB) waveform at early times that is smoothly attached to an NR waveform at late times. Second, since we restrict ourselves to the 3-dimensional space of nonprecessing BBHs, fewer simulations are necessary compared to the 7-dimensional case, and therefore we can direct computational resources to simulations with higher mass ratios. The resulting model, NRHybSur3dq8, is the first NR-based surrogate model to span the entire LIGO frequency band for stellar mass binaries; assuming a detector low-frequency cut-off of 20 Hz, this model is valid for total masses as low as $2.25M_{\odot}$. This model is based on 104 NR waveforms in the parameter range $q \leq 8$, and $|\chi_{1z}|, |\chi_{2z}| \leq 0.8$, where χ_{1z} (χ_{2z}) is the dimensionless spin of the heavier (lighter) black hole (BH).

The plus (h_+) and cross (h_{\times}) polarizations of GWs can be conveniently represented by a single complex time-series, $\hat{h} = h_+ - ih_{\times}$. The complex waveform on a sphere can be decomposed into a sum of spin-weighted spherical harmonic modes $\hat{h}_{\ell m}$ [33, 34], so that the waveform along any direction (ι, φ_0) in the binary’s source frame is given by

$$\hat{h}(t, \iota, \varphi_0) = \sum_{\ell=2}^{\infty} \sum_{m=-\ell}^{\ell} \hat{h}_{\ell m}(t) {}_{-2}Y_{\ell m}(\iota, \varphi_0), \quad (5.1)$$

where ${}_{-2}Y_{\ell m}$ are the spin = -2 weighted spherical harmonics, ι is the inclination angle between the orbital angular momentum of the binary and line-of-sight to the detector, and φ_0 is the initial binary phase. φ_0 can also be thought of as the azimuthal angle between the x -axis of the source frame and the line-of-sight to the detector. We define the source frame as follows: The z -axis is along the orbital angular momentum direction, which is constant for nonprecessing BBH. The x -axis is

¹We use the convention $q = m_1/m_2$, where m_1 and m_2 are the masses of the component black holes, with $m_1 \geq m_2$.

along the line of separation from the lighter BH to the heavier BH at some reference time/frequency. The y -axis completes the triad.

The $\ell=|m|=2$ terms typically dominate the sum in Eq. (5.1), and are referred to as the *quadrupole* modes. Studies [35–42] have shown that the nonquadrupole modes, while being subdominant, can play a nonnegligible role in detection and parameter estimation of GW sources, particularly for large signal to noise ratio (SNR), large total mass, large mass ratio, or large inclination angle ι . For the first event, GW150914 [1], the systematic errors due to the quadrupole-mode-only approximation are generally smaller than the statistical errors [43, 44], although higher modes may lead to modest changes in some of the extrinsic parameter values [45]. However, as the detectors approach their design sensitivity [10], one should prepare for high-SNR sources (particularly at larger mass ratios than those seen so far), where the quadrupole-mode-only approximation breaks down. In addition, nonquadrupole modes can help break the degeneracy between the binary inclination and distance, which is present for quadrupole-mode-only models (see e.g. [14, 46, 47]).

In this work, we model the following spin-weighted spherical harmonic modes: $\ell \leq 4$ and (5,5), but not the (4,1) or (4,0) modes ². Several inspiral-merger-ringdown waveform models [14, 15, 20, 21] that include nonquadrupole modes have been developed in recent years; however, compared to those models we show an improved accuracy and we include more modes.

The rest of the paper is organized as follows. In Sec. 5.4 we choose the parameters at which to perform NR simulations, which will be used for training the surrogate model. Sec. 5.5 describes the NR simulations. Sec. 5.6 describes our procedure to compute the waveform for the early inspiral using PN and EOB waveforms. Sec. 5.7 describes our hybridization procedure to attach the early inspiral waveform to the NR waveforms. Sec. 5.8 describes the construction of the surrogate model. In Sec. 5.9, we test the surrogate model by comparing against NR and hybrid waveforms. We end with some concluding remarks in Sec. 5.10. We make our model available publicly through the easy-to-use Python package *gwsurrogate* [48]. In addition, our model is implemented in C with Python wrapping in the LIGO Algorithm Library [49]. We provide an example Python evaluation code at [50].

²Because of the symmetries of nonprecessing BBHs (see Eq. (5.23)), the $m < 0$ modes contain the same information as the $m > 0$ modes, and do not need to be modeled separately.

5.4 Training set generation

Greedy parameters from PN surrogate model

We do not know a priori the distribution or number of NR simulations required to build an accurate surrogate model. Furthermore, we hope to select a representative distribution that will allow for an accurate surrogate to be built with as few NR simulations as possible. Therefore, we estimate this distribution by first building a surrogate model for PN waveforms; we find that parameters suitable for building an accurate PN surrogate are also suitable for building an NR or a hybrid NR-PN surrogate.

We use the same methods to build the PN surrogate as we use for the hybrid surrogate (cf. Sec. 5.8). We use the PN waveforms described in Sec. 5.6; however, for simplicity we only model the (2,2) mode. In addition, we restrict the length of the PN waveforms to be $5000M$, terminating at the innermost-stable-circular-orbit's orbital frequency, $\omega_{\text{orb}} = 6^{-3/2}$ rad/ M , where M is the total mass of the binary.

We determine the desired training data set of parameters as follows. We begin with just the corner cases of the parameter space; for the 3d case considered here, that consists of 8 points at $(q, \chi_{1z}, \chi_{2z}) = (1 \text{ or } 8, \pm 0.8, \pm 0.8)$. We build up the desired set of parameters iteratively, in a greedy manner: At each iteration we build a PN surrogate using the current training data set and test the model against a much larger (~ 10 times) validation data set. The validation data set is generated by randomly resampling the parameter space at each iteration. Since the boundary cases are expected to be more important, for 30% of the points in the validation set we sample only from the boundary of the parameter space, which corresponds to the faces of a cube in the 3d case. We select the parameter in the validation set that has the largest error (cf. Eq. (5.2)), and add this to our training set (hence the name greedy parameters). We repeat until the validation error reaches a certain threshold.

In order to estimate the difference between two complexified waveforms, h_1 and h_2 , we use the time-domain mismatch,

$$\mathcal{MM} = 1 - \frac{\langle h_1, h_2 \rangle}{\sqrt{\langle h_1, h_1 \rangle \langle h_2, h_2 \rangle}}, \quad (5.2)$$

$$\langle h_1, h_2 \rangle = \left| \int_{t_{\min}}^{t_{\max}} h_1(t) h_2^*(t) dt \right|, \quad (5.3)$$

where $*$ indicates a complex conjugation, and $|\cdot|$ indicates the absolute value. Note

that in this section, we do not perform an optimization over time and phase shifts. In addition, we assume a flat noise curve.

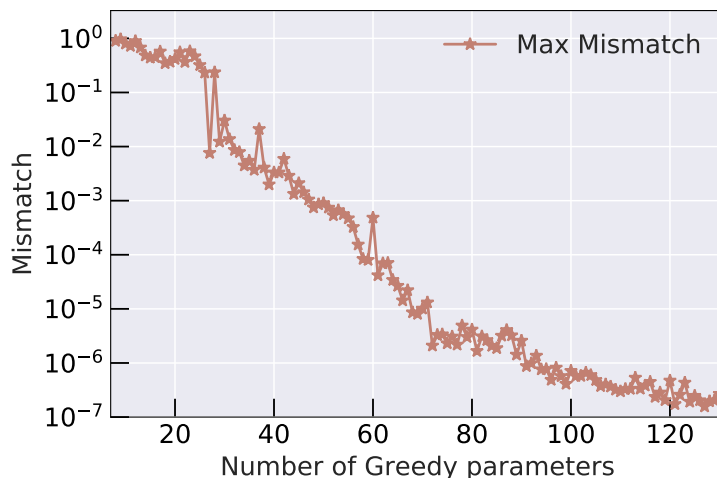


Figure 5.4.1: Largest mismatch of the surrogate (over the entire validation set) as a function of number of greedy parameters used to train the PN surrogate. The PN surrogate is seen to converge to the validation waveforms as the size of the training data set increases.

Figure 5.4.1 shows how the maximum validation error decreases as we add greedy parameters to our training data set. For our case, we stop at 100 greedy parameters (at which point the mismatch is $< 10^{-6}$) and use those parameters to perform the NR simulations. Note that we don't expect 100 NR simulations to produce an NR surrogate with comparable accuracy, $MM < 10^{-6}$, for two reasons. First, unlike the PN waveforms used here, the NR simulations also include the merger-ringdown part, which we expect to be more difficult to model. Second, the NR numerical truncation error is typically higher than 10^{-6} in mismatch, therefore the numerical noise will limit the accuracy.

5.5 NR simulations

The NR simulations for this model are performed using the Spectral Einstein Code (SpEC) [51–56] developed by the SXS [57] collaboration. Of the 100 cases determined in Sec. 5.4, only 91 simulations were successfully completed³. These simulations have been assigned the identifiers SXS:BBH:1419 - SXS:BBH:1509, and are made publicly available through the SXS public catalog [58]. For cases with

³The main reason for failure is large constraint violation as the binary approaches merger. We believe a better gauge condition may be needed for some of these simulations.

equal mass, but unequal spins, we can exchange the two BHs to get an extra data point. There are 13 such cases, leading to a total of 104 NR waveforms. These are shown as circular markers in Fig. 5.5.1.

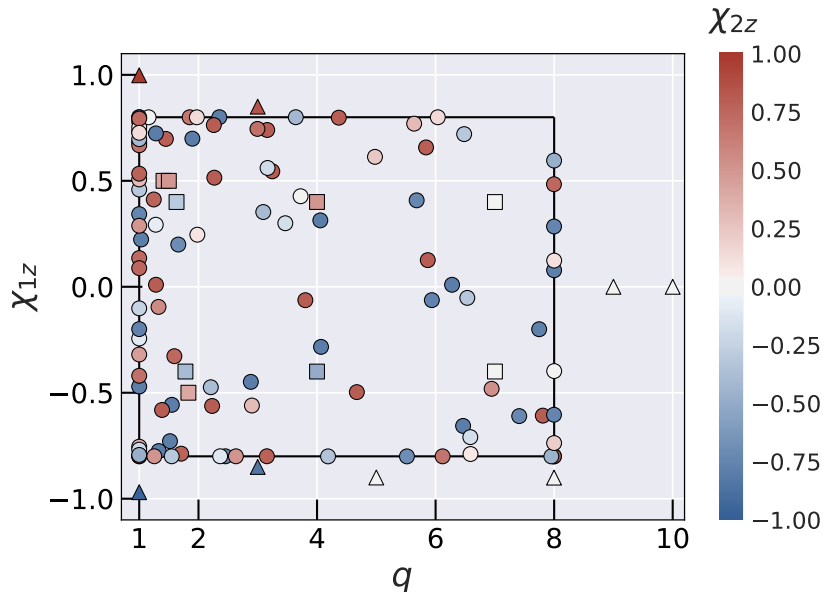


Figure 5.5.1: The parameter space covered by the 104 NR waveforms (circle markers) used in the construction of the surrogate model in Sec. 5.8. We also show the 9 long NR waveforms (square markers) used to test hybridization in Sec. 5.9, and the 8 NR waveforms (triangle markers) used to test extrapolation in Sec. 5.9. The axes show the mass ratio and the spin on the heavier BH, while the colors indicate the spin on the lighter BH. The black rectangle indicates the bounds of the training region: $1 \leq q \leq 8$, $-0.8 \leq \chi_{1z}, \chi_{2z} \leq 0.8$.

The start time of these simulations varies between $4270M$ and $5227M$ before the peak of the waveform amplitude (defined in Eq. (5.38)), where $M = m_1 + m_2$ is the total Christodoulou mass measured after the initial burst of junk radiation. The algorithm for choosing a fiducial time at which junk radiation ends is discussed in Ref. [59]. The initial orbital parameters are chosen through an iterative procedure [60] such that the orbits are quasicircular; the largest eccentricity for these simulations is 7.5×10^{-4} , while the median value is 4.2×10^{-4} . The waveforms are extracted at several extraction surfaces at varying finite radii from the origin and then extrapolated to future null infinity [61]. Finally, the extrapolated waveforms are corrected to account for the initial drift of the center of mass [62, 63]. The time steps during the simulations are chosen nonuniformly using an adaptive time-stepper [59]. We interpolate these data to a uniform time step of $0.1M$; this is dense enough to capture all frequencies of interest, including near merger.

5.6 Early inspiral waveforms

While NR provides accurate waveforms, computational constraints limit NR to only the late inspiral, merger, and ringdown phases. Fortunately, PN/EOB waveforms are expected to be accurate in the early inspiral. Hence we can “stitch” together an early inspiral waveform and an NR waveform, to get a *hybrid* waveform [40, 64–71] that spans the entire frequency range relevant for ground-based detectors. In this section, we describe the waveforms we use for the early inspiral, leaving the hybridization procedure for the next section.

PN waveforms

We first generate PN waveforms as implemented in the GWFrames package [72]. For the orbital phase we include nonspinning terms up to 4 PN order [73–77] and spin terms up to 2.5 PN order [78–80]. We use the TaylorT4 [81] approximant to generate the PN phase; however, as described below, we replace this phase with an EOB-derived phase. For the amplitudes, we include terms up to 3.5 PN order [82–84].

The spherical harmonic modes of the PN waveform can be written (after rescaling to unit total mass and unit distance) as [74, 82],

$$\hat{h}_{\ell m}^{\text{PN}} = 2 \eta (v^{\text{PN}})^2 \sqrt{\frac{16\pi}{5}} H_{\ell m}^{\text{PN}} e^{-im\phi_{\text{orb}}^{\text{PN}}}, \quad (5.4)$$

where $\eta = q/(1+q)^2$ is the symmetric mass ratio, v^{PN} is the characteristic speed that sets the perturbation scale in PN, $\phi_{\text{orb}}^{\text{PN}}$ is the (real) orbital phase, and $H_{\ell m}^{\text{PN}}$ are the complex amplitudes of different modes. Note that we ignore the tail distortions [85, 86] to the orbital phase as these are 4 PN corrections (see e.g. [87]).

The complex strain $\hat{h}_{\ell m}^{\text{PN}}$ is obtained as a time series from GWFrames. We can absorb the complex part of the amplitudes into the phases and rewrite the strain as

$$\hat{h}_{\ell m}^{\text{PN}} = A_{\ell m}^{\text{PN}} e^{-i\phi_{\ell m}^{\text{PN}}}, \quad (5.5)$$

$$\phi_{\ell m}^{\text{PN}} = m \phi_{\text{orb}}^{\text{PN}} + \xi_{\ell m}^{\text{PN}}, \quad (5.6)$$

$$\phi_{\text{orb}}^{\text{PN}} = \frac{\phi_{22}^{\text{PN}}}{2}, \quad (5.7)$$

where $A_{\ell m}^{\text{PN}}$ and $\phi_{\ell m}^{\text{PN}}$ are the real amplitude and phase of a given mode, and $\xi_{\ell m}^{\text{PN}}$ is an offset that captures the complex part of $H_{\ell m}^{\text{PN}}$. Note that Eqs. (5.6) and (5.7) together

imply $\xi_{22}^{\text{PN}} = 0$; H_{22}^{PN} contains complex terms starting at 2.5PN , but these appear as 5PN corrections in the phase (see e.g. [87]), which we can safely ignore.

At this stage, $A_{\ell m}^{\text{PN}}$, $\phi_{\ell m}^{\text{PN}}$, and $\xi_{\ell m}^{\text{PN}}$ are functions of time. But they can be recast as functions of the characteristic speed by first computing

$$v^{\text{PN}}(t) = \left(\frac{d\phi_{\text{orb}}^{\text{PN}}}{dt} \right)^{1/3}, \quad (5.8)$$

where the derivative is performed numerically, and then inverting Eq. (5.8) to obtain $t(v^{\text{PN}})$. Then we define

$$A_{\ell m}^{\text{PN}}(v^{\text{PN}}) = |\hat{h}_{\ell m}^{\text{PN}}(t(v^{\text{PN}}))|, \quad (5.9)$$

$$\xi_{\ell m}^{\text{PN}}(v^{\text{PN}}) = \phi_{\ell m}^{\text{PN}}(t(v^{\text{PN}})) - m \phi_{\text{orb}}^{\text{PN}}(t(v^{\text{PN}})). \quad (5.10)$$

Note that the PN waveform is generated in the source frame defined such that the reference time is the initial time. This also ensures that the heavier BH is on the positive x -axis at the initial time, and the initial orbital phase is zero.

To summarize: From the GWFrames package, we obtain the complex time series $\hat{h}_{\ell m}^{\text{PN}}$ (Eq. (5.5)). We compute the orbital phase (Eq. (5.7)), the real amplitudes (Eq. (5.9)), and the phase offsets (Eq. (5.10)). These three quantities are obtained as a time series but can be represented as functions of the characteristic speed using Eq. (5.8).

EOB correction

As was shown in previous works [35, 40], we find that the accuracy of the inspiral waveform can be improved by replacing the PN phase with the phase derived from an NR-calibrated EOB model. For this work we use SEOBNRv4 [17].

SEOBNRv4 is a time domain model that includes only the $(2, 2)$ mode, which we can decompose as follows:

$$\hat{h}_{22}^{\text{EOB}} = A_{22}^{\text{EOB}} e^{-i\phi_{22}^{\text{EOB}}}, \quad (5.11)$$

where A_{22}^{EOB} and ϕ_{22}^{EOB} are the real amplitude and phase of the $(2, 2)$ mode. These are functions of time, but following the same procedure as earlier, they can be recast

in terms of the characteristic speed:

$$\phi_{\text{orb}}^{\text{EOB}}(t) = \frac{\phi_{22}^{\text{EOB}}(t)}{2}, \quad (5.12)$$

$$v^{\text{EOB}}(t) = \left(\frac{d\phi_{\text{orb}}^{\text{EOB}}}{dt} \right)^{1/3}, \quad (5.13)$$

where the derivative is performed numerically, and we invert Eq. (5.13) to obtain $t(v^{\text{EOB}})$. We replace $v^{\text{PN}} \rightarrow v^{\text{EOB}}$ in Eqs. (5.9) and (5.10) to get, respectively, the EOB-corrected amplitudes and phase offsets:

$$A_{\ell m}^{\text{ins}}(t) = A_{\ell m}^{\text{PN}}(v^{\text{EOB}}(t)), \quad (5.14)$$

$$\xi_{\ell m}^{\text{ins}}(t) = \xi_{\ell m}^{\text{PN}}(v^{\text{EOB}}(t)). \quad (5.15)$$

Note that in practice, computing $A_{\ell m}^{\text{ins}}(t)$ and $\xi_{\ell m}^{\text{ins}}(t)$ is accomplished via an interpolation in v : $A_{\ell m}^{\text{PN}}(v)$ and $\xi_{\ell m}^{\text{PN}}(v)$ as computed in Eqs. (5.9) and (5.10) are known only at particular values of v , which are $v^{\text{PN}}(t_{i_{\text{PN}}})$ where $t_{i_{\text{PN}}}$ are the times in the PN time series; we interpolate $A_{\ell m}^{\text{PN}}(v)$ and $\xi_{\ell m}^{\text{PN}}(v)$ to the points $v^{\text{EOB}}(t_{i_{\text{EOB}}})$ where $t_{i_{\text{EOB}}}$ are the times in the EOB time series. We use a cubic-spline interpolation scheme as implemented in Scipy [88].

Following Eq. (5.6), the EOB-corrected phases are given by:

$$\phi_{\ell m}^{\text{ins}} = m \phi_{\text{orb}}^{\text{EOB}} + \xi_{\ell m}^{\text{ins}}, \quad (5.16)$$

where we use the EOB orbital phase from Eq. (5.12). Finally, our EOB-corrected inspiral waveform modes are given by:

$$\mathcal{h}_{\ell m}^{\text{ins}} = A_{\ell m}^{\text{ins}} e^{-i\phi_{\ell m}^{\text{ins}}}. \quad (5.17)$$

Fig. 5.6.1 shows an example of PN and EOB-corrected waveforms along with the corresponding NR waveform. All three waveforms have the same starting orbital frequency and their initial orbital phase is set to zero. We see that the PN waveform becomes inaccurate at late times, as expected. The EOB-corrected waveform, on the other hand, remains faithful to the NR waveform until much later times.

5.7 Hybridization

In this section we describe our procedure to “stitch” together an inspiral waveform (described in Sec. 5.6) to an NR waveform (described in Sec. 5.5).

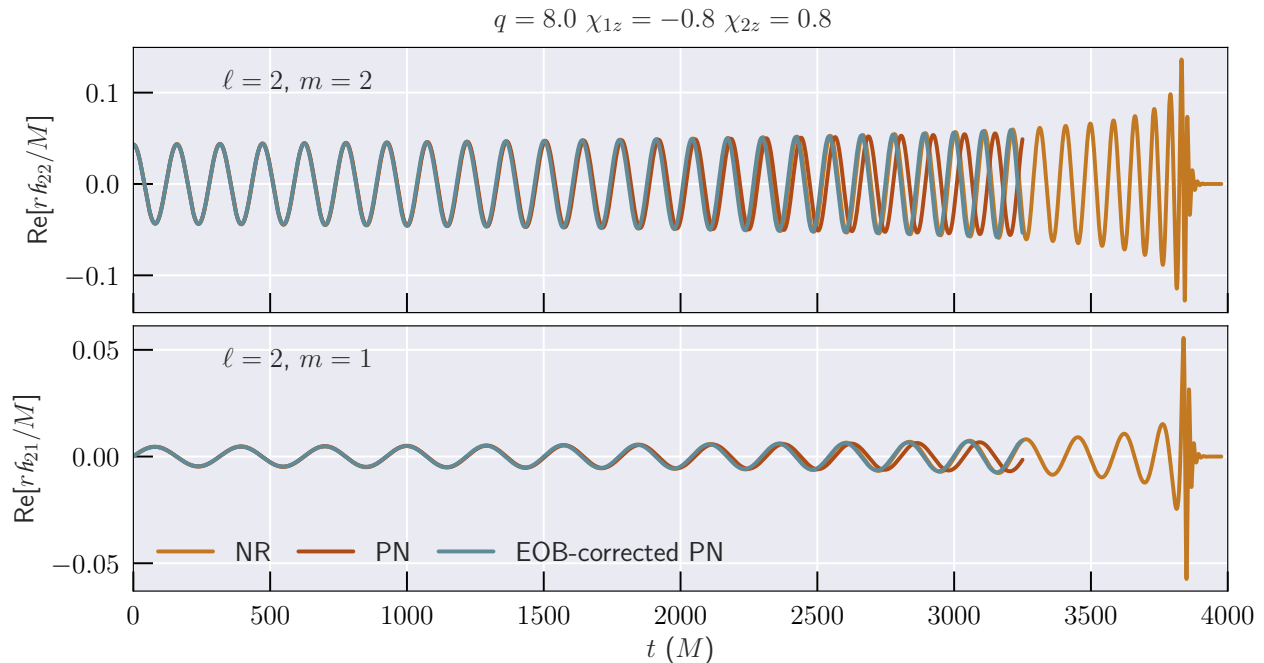


Figure 5.6.1: NR, PN (Sec. 5.6), and EOB-corrected PN (Sec. 5.6) waveforms for an example case. We show the (2,2) and (2,1) modes. The binary parameters are shown at the top of the plot. The EOB-corrected PN waveform [35, 40] stays faithful to the NR waveform until much later times, compared to the pure PN waveform.

We start by generating inspiral and NR waveforms with the same component masses and spins. We note that the spins measured in SpEC simulations agree well with PN theory [89]. However, the PN and NR waveforms are typically represented in different coordinate systems that need to be aligned with each other as follows. The two coordinate systems are related to each other by a possible time translation and a possible rotation by three Euler angles: inclination angle ι , initial binary phase φ_0 , and polarization angle ψ . For nonprecessing BBH the first angle ι , is trivially specified by requiring that the z-axis is along the direction of orbital angular momentum. This leaves us with the freedom to vary φ_0 and ψ . We choose the hybridization frame and time shifts by minimizing a cost function in a suitable matching region; this is described in more detail below.

Choice of cost function

We use the following cost function when comparing two waveforms, h and \tilde{h} , in the matching region:

$$\mathcal{E}[h, \tilde{h}] = \frac{1}{2} \frac{\sum_{\ell,m} \int_{t_1}^{t_2} |h_{\ell m}(t) - \tilde{h}_{\ell m}(t)|^2 dt}{\sum_{\ell,m} \int_{t_1}^{t_2} |h_{\ell m}(t)|^2 dt}, \quad (5.18)$$

where t_1 and t_2 denote the start and end of the matching region, to be defined in Sec. 5.7, and the sum does not include $m = 0$ modes for reasons described in Sec. 5.7. This cost function was introduced in Ref. [27] and is shown to be related to the weighted average of the mismatch over the sky.

We minimize the cost function by varying the time and frame shifts between the NR and inspiral waveforms

$$\min_{t_0, \varphi_0, \psi} \mathcal{E}[h^{\text{NR}}(t; \varphi_0, \psi), h^{\text{ins}}(t; t_0)], \quad (5.19)$$

$$h_{\ell m}^{\text{NR}}(t; \varphi_0, \psi) = h_{\ell m}^{\text{NR}}(t) e^{im\varphi_0} e^{2i\psi}, \quad (5.20)$$

$$h_{\ell m}^{\text{ins}}(t; t_0) = h_{\ell m}^{\text{ins}}(t - t_0). \quad (5.21)$$

We perform the time shifts on the inspiral waveform so that the matching region always corresponds to the same segment of the NR waveform. The frame shifts are performed on the NR waveform so as to preserve the initial frame alignment of the inspiral waveform (cf. Sec. 5.6). This alignment gets inherited by the hybrid waveform, and is important in the surrogate construction.

$m = 0$ modes

We find that the $m = 0$ modes of the inspiral waveforms do not agree very well with the NR waveforms. There are several possible reasons for this [90]: (1) The NR waveform does not have the correct “memory” contribution since this depends on the entire history of the system starting at $t = -\infty$, while the NR simulation covers only the last few orbits. (2) The extrapolation to future null infinity does not work as well for these modes [59]. This could be improved in the future with Cauchy Characteristic Extraction (CCE) [91–94]. (3) The amplitude of these modes is very small except very close to merger; therefore the early part of the NR waveform where we compare with the inspiral waveforms is contaminated by numerical noise.

Therefore, when constructing the hybrid waveforms, we set the entire inspiral waveform to zero for these modes,

$$h_{\ell, m=0}^{\text{ins}} = 0. \quad (5.22)$$

When computing the cost function (Eq. (5.18)), we ignore the $m = 0$ modes.

This means that our hybrid waveforms for these modes are equivalent to the NR waveforms. In addition, the main contribution for these modes comes from the region close to merger, which does not correspond to a memory signal, but instead is due to axisymmetric excitations near merger (cf. bottom panel of Fig. 5.7.2).

Choice of matching region

There are several considerations to take into account when choosing a matching region $[t_1, t_2]$ for the cost function (Eq. (5.18)): (1) The NR and inspiral waveforms should agree with each other reasonably in this region; at early times the NR waveform is contaminated by junk radiation while at late times the inspiral waveform deviates from NR (cf. Figs. 5.6.1 and 5.7.2). (2) The matching region should be wide enough that the cost function is meaningful.

Our matching region starts at $1000M$ after the start of the NR waveform; we find that this is necessary to avoid noise due to junk radiation in some of the higher order modes. The length of the NR waveforms from the start of the matching region to the peak of the waveform amplitude varies between $3270M$ and $4227M$. The width of the matching region is then chosen to be equal to the time taken for 3 orbits of the binary. We use the phase of the (2,2) mode of the NR waveform to determine this. This choice ensures the width of the matching region scales appropriately with the NR starting frequency, so that we get wider matching regions when the NR waveform starts early in the inspiral.

Allowed ranges for frame and time shifts

The allowed range for φ_0 is $[0, 2\pi]$. For nonprecessing binaries the allowed values for ψ can be restricted by taking into account the symmetries of the system. We will show that this restriction is a consequence of the well-known relationship

$$h_{\ell, -m} = (-1)^{\ell} h_{\ell, m}^*, \quad (5.23)$$

between the $m < 0$ modes and the $m > 0$ modes for nonprecessing binaries orbiting in the x - y plane [95]. We compute the shifted waveform

$$\begin{aligned}
h_{\ell,-m}(t) e^{-im\varphi_0} e^{2i\psi} &= h_{\ell,-m}(t; \varphi_0, \psi) \\
&= (-1)^\ell (h_{\ell,m}(t; \varphi_0, \psi))^* \\
&= (-1)^\ell e^{-2i\psi} e^{-im\varphi_0} h_{\ell,m}^*(t) \\
&= e^{-2i\psi} e^{-im\varphi_0} h_{\ell,-m}(t) \\
\implies e^{2i\psi} &= e^{-2i\psi}.
\end{aligned} \tag{5.24}$$

Eq. (5.24) implies that the only allowed values for ψ are 0 and $\pi/2$ ⁴. If the inspiral waveform and the NR waveform have the same sign convention, then $\psi = 0$. Unfortunately, not all NR catalogs and PN-waveform codes use the same sign convention, so we allow the possibility of $\psi = \pi/2$ to account for this.

To set the allowed range for t_0 , we begin by computing the orbital frequency of the inspiral waveform, ω^{ins} , as half the frequency of the (2,2) mode. Similarly, we compute the orbital frequency of the NR waveform, ω^{NR} . We first time-align the NR and inspiral waveforms such that their frequencies match at the start of the matching region. This gives us a good starting point to vary the time shift.

We also define,

$$\omega_{\text{mid}}^{\text{ins}} = \omega^{\text{NR}}(t = t_1), \tag{5.25}$$

$$\omega_{\text{low}}^{\text{ins}} = 0.995 \times \omega_{\text{mid}}^{\text{ins}}, \tag{5.26}$$

$$\omega_{\text{hi}}^{\text{ins}} = 1.005 \times \omega_{\text{mid}}^{\text{ins}}, \tag{5.27}$$

where $\omega^{\text{NR}}(t = t_1)$ is the NR frequency at the start of the matching region. The allowed range for time shifts t_0 is restricted to lie in the interval $[t_{\text{low}}^{\text{ins}} - t_{\text{mid}}^{\text{ins}}, t_{\text{hi}}^{\text{ins}} - t_{\text{mid}}^{\text{ins}}]$, where $t_{\text{low}}^{\text{ins}}$, $t_{\text{mid}}^{\text{ins}}$ and $t_{\text{hi}}^{\text{ins}}$ are the times at which $\omega^{\text{ins}}(t)$ is equal to $\omega_{\text{low}}^{\text{ins}}$, $\omega_{\text{mid}}^{\text{ins}}$ and $\omega_{\text{hi}}^{\text{ins}}$, respectively. In other words, the allowed range for t_0 is a region near $t_0 = 0$. $t_0 = 0$ is the case when the frequencies of the inspiral and the NR waveforms match at t_1 , the start of the matching region. The lower (upper) limit for t_0 is chosen such that the inspiral waveform has a frequency equal to 0.995 (1.005) times the NR frequency at t_1 .

The factors in Eqs. (5.26) and (5.27) are chosen such that the time shift that minimizes the cost function is always well within the range of allowed time shifts. Hence,

⁴ $\psi = \pi$ is also allowed, but it is degenerate with $\psi = 0$.

choosing a wider range (i.e. values of these factors farther from unity) does not improve the hybridization procedure. Note also that, like the width of the matching region in Sec. 5.7, setting the range of time shifts based on the orbital frequency ensures that it scales appropriately with the start frequency of the NR waveform.

The minimization in Eq. (5.19) is performed as follows. We vary the time shift t_0 over 500 uniformly spaced values in the above mentioned time range ⁵. For each of these time shifts t_0 , we try both allowed values of $\psi \in \{0, \pi/2\}$. For each t_0 and ψ , we minimize the cost function over φ_0 using the Nelder-Mead down-hill simplex minimization algorithm as implemented in Scipy [88]. To avoid local minima in the φ_0 minimization, we perform 10 searches with different initial guesses, which are sampled from a uniform random distribution in the range $[0, 2\pi]$.

Stitching NR and inspiral waveforms.

Having obtained the right frame and time shifts between the NR and inspiral waveforms, the final step is to smoothly stitch the inspiral waveform to the shifted NR waveform. The stitching is done using a smooth blending function:

$$\tau(t) = \begin{cases} 0, & \text{if } t < t_1 \\ \sin^2\left(\frac{\pi}{2} \frac{t-t_1}{t_2-t_1}\right), & \text{if } t_1 \leq t \leq t_2 \\ 1, & \text{if } t > t_2, \end{cases} \quad (5.28)$$

where t_1 and t_2 take on the same values as those appearing in Eq. (5.18). Different blending functions have been proposed in the literature [64, 67, 69, 96]. Our choice is equivalent to the blending function defined in Ref. [67]. We find that our results are not sensitive to the choice of blending function.

In what follows, for brevity, we drop the hybridization parameters φ_0 , ψ , t_0 with the understanding that the models are stitched together after transforming into hybridization frame,

$$h_{\ell m}^{\text{ins}}(t) \equiv h_{\ell m}^{\text{ins}}(t; t_0), \quad (5.29)$$

$$h_{\ell m}^{\text{NR}}(t) \equiv h_{\ell m}^{\text{NR}}(t; \varphi_0, \psi). \quad (5.30)$$

Given the shifted waveforms and the blending function, there are still several ways in which one can stitch the waveforms together.

⁵We find that increasing the number of time samples results in no noticeable improvement; the typical values of the cost function after minimization with 500 samples are $\mathcal{E} \sim 10^{-5}$, and using 1000 samples results in changes only of order $\Delta\mathcal{E} \lesssim 10^{-8}$.

Inertial frame stitching

One could work with the complex waveform strain and define:

$$h_{\ell m}^{\text{Hyb}} = (1 - \tau(t)) h_{\ell m}^{\text{ins}}(t) + \tau(t) h_{\ell m}^{\text{NR}}(t). \quad (5.31)$$

With this choice, by construction, the complex strain transitions smoothly from the inspiral part to the NR part over the matching region. However, the transition is more complicated for the frequency, since it involves time derivatives of the complex argument of the strain; the time derivatives of the blending function do not behave like a smooth blending function. This is demonstrated in the top panel of Fig. 5.7.1: the inspiral and NR frequencies agree well in the matching region but the frequency of the hybrid waveform deviates from this.

Amplitude-Frequency stitching

To avoid the undesirable artifacts described above, we choose to perform the inspiral-NR stitching using the amplitude and frequency rather than the inertial frame strain.

We begin by decomposing the NR and inspiral waveforms into their respective amplitude and phase:

$$h_{\ell m}^{\text{NR}}(t) = A_{\ell m}^{\text{NR}} e^{-i\phi_{\ell m}^{\text{NR}}}, \quad h_{\ell m}^{\text{ins}}(t) = A_{\ell m}^{\text{ins}} e^{-i\phi_{\ell m}^{\text{ins}}}. \quad (5.32)$$

The frequency of each mode

$$\omega_{\ell m}^{\text{NR}} = \frac{d\phi_{\ell m}^{\text{NR}}}{dt}, \quad \omega_{\ell m}^{\text{ins}} = \frac{d\phi_{\ell m}^{\text{ins}}}{dt}, \quad (5.33)$$

is then numerically computed from 4th-order finite difference approximations to the time derivative. Finally, we stitch the amplitude and frequency of each mode to get their hybrid versions:

$$A_{\ell m}^{\text{Hyb}} = (1 - \tau(t)) A_{\ell m}^{\text{ins}}(t) + \tau(t) A_{\ell m}^{\text{NR}}, \quad (5.34)$$

$$\omega_{\ell m}^{\text{Hyb}} = (1 - \tau(t)) \omega_{\ell m}^{\text{ins}}(t) + \tau(t) \omega_{\ell m}^{\text{NR}}. \quad (5.35)$$

To get the inertial frame strain we first need to integrate the frequency to get the phase. However, we already know the phase in the region before (only inspiral) and after (only NR) the matching region. So, we integrate the hybrid frequency

$$\phi_{\ell m}^{\text{Hyb-match-region}} = \int_{t_1}^{t_2} \omega_{\ell m}^{\text{Hyb}} dt, \quad (5.36)$$

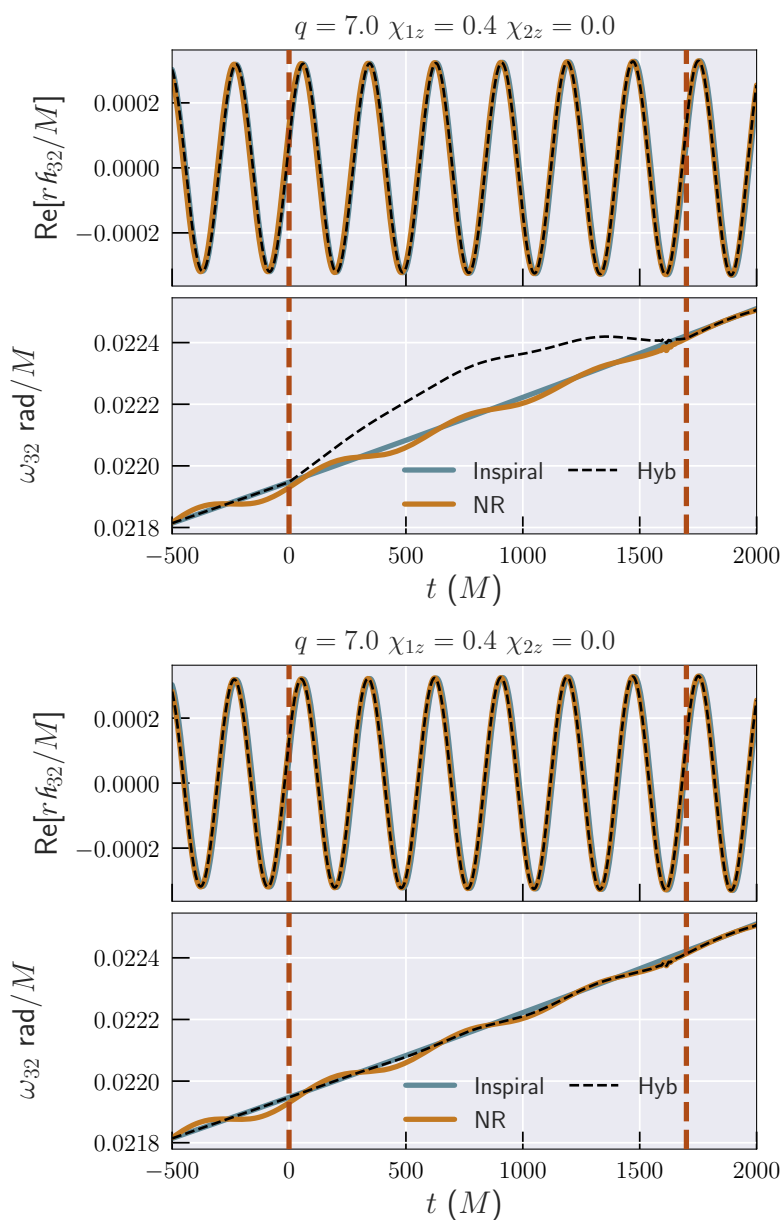


Figure 5.7.1: **Top:** The real part (top) and frequency (bottom) of the (3,2) mode using the inertial frame stitching described in Sec. 5.7. The binary parameters are shown on the top of the plot. The vertical red dashed lines indicate the matching region. Note that this plot shows the inspiral and NR waveforms after the time and frame shifts are performed. **Bottom:** Same, but using the amplitude-frequency stitching described in Sec. 5.7. Now we see that the frequency of the hybrid waveform agrees much better with the NR and inspiral data.

in the matching region using a 4th-order accurate Runge-Kutta scheme.

Finally, we set the phase of the hybrid waveform to,

$$\phi_{\ell m}^{\text{Hyb}} = \begin{cases} \phi_{\ell m}^{\text{ins}} + \delta_{\ell m}^1, & \text{if } t < t_1 \\ \phi_{\ell m}^{\text{Hyb-match-region}} + \delta_{\ell m}^2, & \text{if } t_1 \leq t \leq t_2 \\ \phi_{\ell m}^{\text{NR}}, & \text{if } t > t_2, \end{cases} \quad (5.37)$$

where $\delta_{\ell m}^1$ and $\delta_{\ell m}^2$ are chosen such that $\phi_{\ell m}^{\text{Hyb}}$ is continuous at t_1 and t_2 .

Since, by construction, the frequency transitions smoothly from the inspiral-waveform to NR data, we eliminate the artifact seen in the bottom left panel of Fig 5.7.1 (dashed line), as demonstrated in the bottom panel of Fig. 5.7.1.

We note that since the $m = 0$ modes are purely real/imaginary and nonoscillatory for nonprecessing systems, they do not have a frequency associated with them, therefore we use the inertial frame stitching of Sec. 5.7 for these modes. For these modes the waveform goes from zero to the NR value over the matching region.

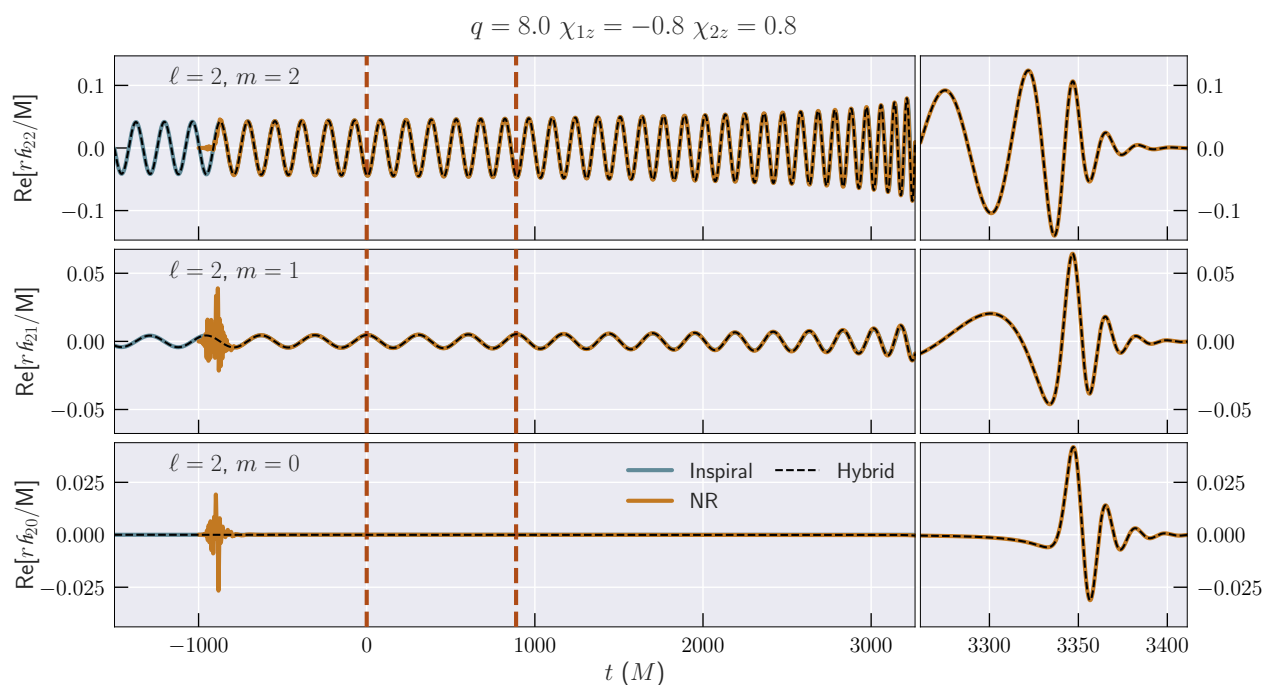


Figure 5.7.2: An example hybrid waveform used in this work. We show the $\ell = 2$ modes of the inspiral, NR and hybrid waveforms. The binary parameters are shown on the top of the plot. The vertical red dashed lines indicate the matching region. Note that this plot shows the inspiral and NR waveforms after the time and frame shifts are done.

In the hybridized waveform we include the $\ell \leq 4$ and (5, 5) modes, but not the (4, 1) or (4, 0) modes. For the (4, 1) and (4, 0) modes we find that the inspiral and NR waveforms do not agree very well. This is possibly due to issues in the extrapolation to future-null infinity [61] for these modes, and could be resolved in the future with CCE [91–94]. An example of the final NR, inspiral and hybrid waveforms is shown in Fig. 5.7.2.

5.8 Building the surrogate model

Starting from the 104 NR waveforms described in Sec. 5.4 and Sec. 5.5, we construct hybrid waveforms as described in Sec. 5.7. In this section we describe our method to construct a surrogate model for these hybrid waveforms.

Processing the training data

Before building a surrogate model, we process the hybrid waveforms as follows.

Time shift

We shift the time arrays of the hybrid waveforms such that the peak of the total amplitude

$$A_{tot} = \sqrt{\sum_{l,m} |f_{\ell m}|^2}, \quad (5.38)$$

occurs at $t = 0$ for each waveform.

Frequency and mass ranges of validity

The length of a hybrid waveform is set by choosing a starting orbital frequency ω_0 , for the inspiral waveform; we use $\omega_0 = 2 \times 10^{-4}$ rad/ M for all waveforms. However, for the same starting frequency, the length in time of the waveform is different for different mass ratios and spins. Since we want to construct a time-domain surrogate model, we require a common time array for all hybrid waveforms. The initial time for the surrogate is determined by the shortest hybrid waveform in the training data set; this waveform begins at a time $\sim 5.4 \times 10^8 M$ before the peak. We truncate all hybrid waveforms to this initial time value.

The largest starting orbital frequency among the truncated hybrid waveforms is $\omega_0 = 2.9 \times 10^{-4}$ rad/ M , which sets the low frequency limit of validity of the

surrogate. For LIGO, assuming a starting GW frequency of 20 Hz, the (2,2) mode of the surrogate is valid for total masses $M \geq 0.9M_\odot$. The highest spin-weighted spherical harmonic mode we include in the surrogate model is (5,5), for which the frequency is 5/2 times that of the (2,2) mode. Therefore, all modes of the surrogate are valid for $M \geq 2.25M_\odot$. This coverage of total mass is sufficient to model all stellar mass binaries of interest for ground based detectors; for an equal mass binary neutron star system, the total mass is $M \sim 2.7M_\odot$.

Downsampling and common time samples

Because the hybrid waveforms are so long, it is not practical to sample the entire waveform with the same step size we use for the NR waveforms ($0.1M$). Fortunately, the early low-frequency portion of each waveform requires sparser sampling than the later high-frequency portion. We therefore down-sample the time arrays of the truncated hybrid waveforms to a common set of time samples. We choose these samples so that there are 5 points per orbit for the above-mentioned shortest hybrid waveform in the training data set, except for $t \geq -1000M$ we choose uniform time samples separated by $0.1M$. This ensures that we have a denser sampling rate at late times when the frequency is higher. We retain times up to $135M$, which is sufficient to capture the entire ringdown.

Before downsampling, we first transform the waveform into the co-orbital frame, defined as:

$$h_{\ell m}^C = h_{\ell m} e^{im\phi_{\text{orb}}}, \quad (5.39)$$

$$f_{22} = A_{22} e^{-i\phi_{22}}, \quad (5.40)$$

$$\phi_{\text{orb}} = \frac{\phi_{22}}{2}, \quad (5.41)$$

where $h_{\ell m}$ is the inertial frame hybrid waveform, ϕ_{orb} is the orbital phase, and ϕ_{22} is the phase of the (2,2) mode. The co-orbital frame can be thought of as roughly co-rotating with the binary, since we perform a time-dependent rotation given by the instantaneous orbital phase. Therefore the waveform is a slowly varying function of time in this frame, increasing the accuracy of interpolation to the chosen common time samples. For the (2,2) mode we save the downsampled amplitude A_{22} and phase ϕ_{22} , while for all other modes we save $h_{\ell m}^C$. We find that this down-sampling results in interpolation errors $\mathcal{E} \lesssim 10^{-10}$ (defined in Eq. (5.18)) for all hybrid waveforms.

Phase alignment

After down-sampling to the common temporal grid of the surrogate, we rotate the waveforms about the z-axis such that the orbital phase ϕ_{orb} is zero at $t = -1000M$. Note that this by itself would fix the physical rotation up to a shift of π . When generating the inspiral waveforms for hybridization, we align the system such that the heavier BH is on the positive x -axis at the initial frequency; this fixes the π ambiguity. Therefore, after this phase rotation, the heavier BH is on the positive x -axis at $t = -1000M$ for all waveforms⁶.

Decomposing the data

It is much easier to build a model for slowly varying functions of time. Therefore, rather than work with the inertial frame strain $\hat{h}_{\ell m}$, which is oscillatory, we work with simpler “waveform data pieces”, as explained below. We build a separate surrogate for each waveform data piece. When evaluating the full surrogate model, we first evaluate the surrogate of each data piece and then recombine the data pieces to get the inertial frame strain.

A common choice in literature when working with nonprecessing waveforms has been to decompose the complex strain into an amplitude and phase, each of which is a slowly varying function of time:

$$\hat{h}_{\ell m} = A_{\ell m} e^{-i\phi_{\ell m}}. \quad (5.42)$$

However, when $q = 1$ and $\chi_{1z} = \chi_{2z}$, the amplitude of odd- m modes becomes zero due to symmetry. This means that the phase becomes meaningless, so one has to treat such cases separately. For example, Ref [26] used specialized basis functions for the odd- m modes that captured the divergent behavior of the phase in the equal-mass limit.

To avoid this issue, instead of using the amplitude and phase we use the real and imaginary parts of the co-orbital frame strain $\hat{h}_{\ell m}^C$, defined in Eq. (5.39), for all nonquadrupole modes. The co-orbital frame strain is always meaningful: in the special, symmetric case mentioned above, the co-orbital frame strain for the odd-

⁶Here the BH positions at $t = -1000M$ are defined from the waveform at future null infinity, using a phase rotation relative to the early inspiral where the BH positions are well-defined in PN theory; these positions do not necessarily correspond to the (gauge-dependent) coordinate BH positions in the NR simulation.

m modes just goes to zero, rather than diverge. For the (2,2) mode we use the amplitude⁷ A_{22} and phase ϕ_{22} .

As mentioned above, our hybrid waveforms are very long, typically containing $\sim 3 \times 10^4$ orbits. This presents new challenges that are not present for pure-NR surrogates. For instance, ϕ_{22} sweeps over $\sim 4 \times 10^5$ radians for a typical hybrid waveform. We find that the accuracy of the surrogate model at early times improves if we first subtract a PN-derived approximation to the phase, model the phase difference rather than ϕ_{22} , and then add back the PN contribution when evaluating the surrogate model. In particular, we use the leading order TaylorT3 approximant [97]. For this approximant, the phase is given as an analytic, closed-form, function of time. Therefore, even though TaylorT3 is known to be less accurate than some other approximants [98], its speed makes it ideal for our purpose as we only need it to capture the general trend. At leading order, the TaylorT3 phase is given by:

$$\phi_{22}^{T3} = \phi_{\text{ref}}^{T3} - \frac{2}{\eta \theta^5}, \quad (5.43)$$

where ϕ_{ref}^{T3} is an arbitrary integration constant, $\theta = [\eta (t_{\text{ref}} - t)/(5M)]^{-1/8}$, t_{ref} is an arbitrary time offset, and η is the symmetric mass ratio. Note that ϕ_{22}^{T3} diverges at $t = t_{\text{ref}}$. We choose $t_{\text{ref}} = 1000M$, long after the end of the waveform (recall that the peak is at $t = 0$), to ensure that we are always far away from this divergence. We choose ϕ_{ref}^{T3} such that $\phi_{22}^{T3} = 0$ at $t = -1000M$; this is the same time at which we align the hybrid phase in Sec. 5.8.

Instead of modeling ϕ_{22} , we model the residual

$$\phi_{22}^{\text{res}} = \phi_{22} - \phi_{22}^{T3}, \quad (5.44)$$

after removing the leading-order contribution ϕ_{22}^{T3} . By construction, ϕ_{22}^{res} goes to zero at $t = -1000M$. We find that after removing the leading order TaylorT3 phase, the scale of ϕ_{22}^{res} for a typical hybrid is $\sim 10^3$ radians, compared to $\sim 4 \times 10^5$ radians for ϕ_{22} . In essence, this captures almost all of the phase evolution in the early inspiral, simplifying the problem of modeling the phase to the same as modeling the phase of late-inspiral NR waveforms. We stress that the exact form of ϕ_{22}^{T3} (or its physical meaning) is not important, as long as it captures the general trend, since we add the exact same ϕ_{22}^{T3} to our model of ϕ_{22}^{res} when evaluating the surrogate. In

⁷Note that for the (2,2) mode $A_{22} = f_{22}^C$.

fact, we find that adding higher order PN terms in Eq. (5.43) does not improve the accuracy of the surrogate.

To summarize, we decompose the hybrid waveforms into the following waveform data pieces, each of which is a smooth, slowly varying function of time: $(A_{22}, \phi_{22}^{\text{res}})$ for the (2,2) mode, and the real and imaginary parts of $h_{\ell m}^C$ for all other modes⁸.

Building the surrogate

Once we have the waveform data pieces, we build a surrogate model for each data piece using the procedure outlined in Refs. [22, 27], which we only briefly describe here. Note that the steps below are applied independently for each waveform data piece.

Greedy basis

We first construct a greedy reduced-basis [99] such that the projection errors (cf. Eq. (5) of Ref. [27]) for the entire data set onto this basis are below a given tolerance. For the basis tolerances we use 10^{-2} radians for the ϕ_{22}^{res} data piece, 2×10^{-5} for A_{22} , and 8×10^{-6} for all other data pieces. These are chosen through visual inspection of the basis functions to ensure they are not noisy, and based on the expected truncation error of the NR waveforms. For instance, we expect the error in phase to be about 10^{-2} radians.

The greedy procedure is initialized with a single basis function as described in Ref. [27]. Then at each step in the greedy procedure, the waveform with the highest projection error onto the current basis is added to the basis. Previous work has shown that the resulting greedy reduced-basis is robust to different choices of initialization [100]. When computing the basis projection errors, we only include data up to $50M$ after the peak. We find that this helps avoid noisy basis functions. This is particularly important for the phase data piece as this becomes meaningless at late times, when the waveform amplitude becomes very small.

⁸For $m = 0$ modes of nonprecessing systems, $h_{\ell m}^C$ is purely real (imaginary) for even (odd) ℓ , so we ignore the imaginary (real) part for these modes.

Empirical interpolation

Next, using a different greedy procedure, we construct an empirical interpolant [101–103] in time. This picks out the most representative time nodes, where the number of time nodes is the same as the number of greedy basis functions. We require that the start of the waveform always be included as a time node for all data pieces. This is a useful modeling choice because the magnitude of the waveform data pieces in the very early inspiral can be smaller than the basis tolerances mentioned above. By requiring the first index to be an empirical time node, we enforce an anchor point that ensures the waveform data piece has the right magnitude at the start of the waveform. Furthermore, we do not allow any empirical time nodes at times $> 50M$, since we expect this part to be dominated by noise (especially for the phase data piece).

Parametric fits

Finally, for each time node, we construct a fit across the parameter space. The fits are done using the Gaussian process regression (GPR) fitting method described in the supplemental material of Ref. [104]. Following Ref. [104], we parameterize our fits using $\log(q)$, $\hat{\chi}$, and χ_a . Here $\hat{\chi}$ is the spin parameter entering the GW phase at leading order [16, 105–107] in the PN expansion,

$$\chi_{\text{eff}} = \frac{q \chi_{1z} + \chi_{2z}}{1 + q}, \quad (5.45)$$

$$\hat{\chi} = \frac{\chi_{\text{eff}} - 38\eta(\chi_{1z} + \chi_{2z})/113}{1 - 76\eta/113}, \quad (5.46)$$

and χ_a is the “anti-symmetric spin”,

$$\chi_a = \frac{1}{2}(\chi_{1z} - \chi_{2z}). \quad (5.47)$$

The fit accuracy, and as a result the accuracy of the surrogate model, improves noticeably when using $\log(q)$, compared to q or η .

Evaluating the surrogate

When evaluating the surrogate waveform, we first evaluate each surrogate waveform data piece. Next, we compute the phase of the (2, 2) mode,

$$\phi_{22}^S \equiv \phi_{22}^{\text{res},S} + \phi_{22}^{T3}, \quad (5.48)$$

where $\phi_{22}^{\text{res,S}} \approx \phi_{22}^{\text{res}}$ is the surrogate model for ϕ_{22}^{res} and ϕ_{22}^{T3} is given in Eq. (5.43). If the waveform is required at a uniform sampling rate, we interpolate each waveform data piece from the sparse time samples used to construct the model to the required time samples, using a cubic-spline interpolation scheme. Finally, we use Eqs. (5.39), (5.40), and (5.41) to reconstruct the surrogate prediction for the inertial frame strain.

5.9 Results

In order to estimate the difference between two waveforms, h_1 and h_2 , we use the mismatch, defined in Eq. (5.2), but in this section instead of Eq. (5.3) we use the frequency-domain inner product

$$\langle h_1, h_2 \rangle = 4\text{Re} \int_{f_{\min}}^{f_{\max}} \frac{\tilde{h}_1(f) \tilde{h}_2^*(f)}{S_n(f)} df, \quad (5.49)$$

where $\tilde{h}(f)$ indicates the Fourier transform of the complex strain $h(t)$, $*$ indicates a complex conjugation, Re indicates the real part, and $S_n(f)$ is the one-sided power spectral density of a GW detector. We taper the time domain waveform using a Planck window [108], and then zero-pad to the nearest power of two. We further zero-pad the waveform to increase the length by a factor of eight before performing the Fourier transform. The tapering at the start of the waveform is done over 1.5 cycles of the (2,2) mode. The tapering at the end is done over the last $20M$. Note that our model contains times up to $135M$ after the peak of the waveform amplitude, and the signal has essentially died down by the last $20M$.

We compute mismatches following the procedure described in Appendix D of Ref. [27]: the mismatches are optimized over shifts in time, polarization angle, and initial orbital phase. Both plus and cross polarizations are treated on an equal footing by using a two-detector setup where one detector sees only the plus and the other only the cross polarization. We compute the mismatches at 37 points uniformly distributed on the sky in the source frame, and we use all available modes of a given waveform model.

When computing flat noise mismatches ($S_n = 1$), we take f_{\min} to be the frequency of the (2,2) mode at the end of the initial tapering window, and $f_{\max} = 5f_{22}^{\text{peak}}$, where f_{22}^{peak} is the frequency of the (2,2) mode at its peak. This choice of f_{\max} ensures that we capture the peak frequencies of all modes considered in this work, including the (5,5) mode, whose frequency has the highest multiple of the (2,2) mode frequency of all the modes we model. We also compute mismatches with the Advanced-LIGO

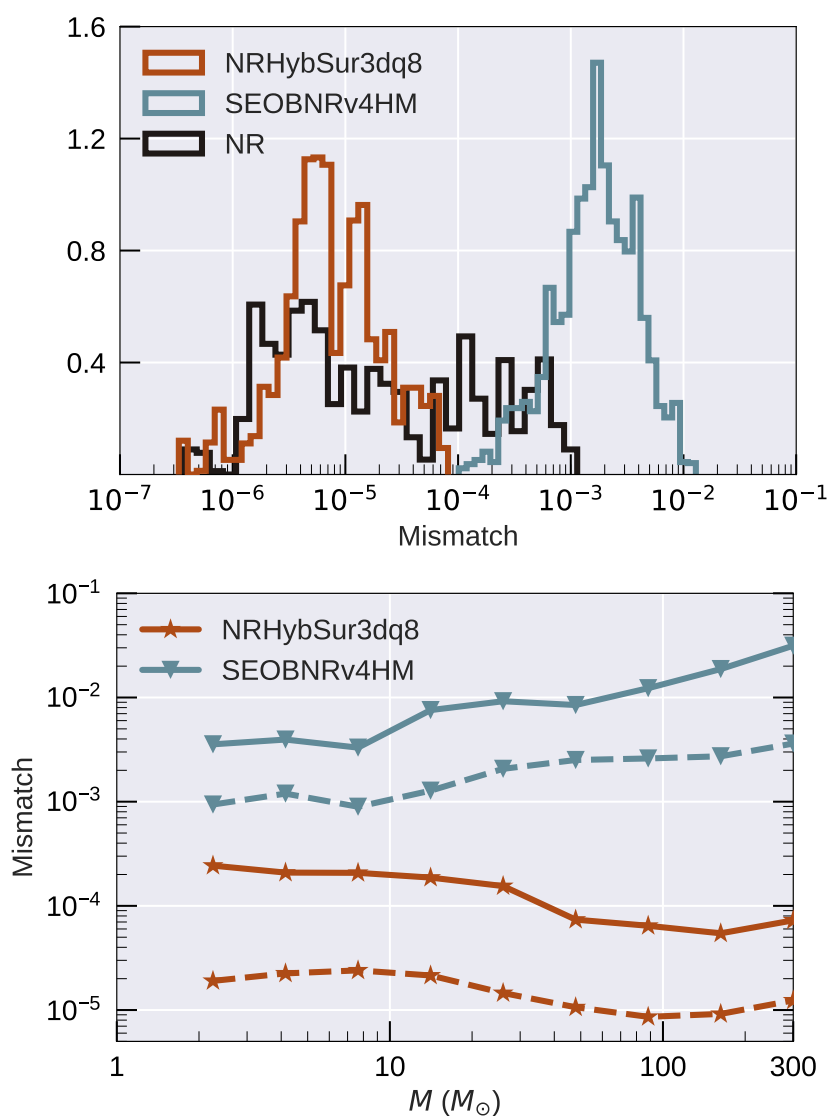


Figure 5.9.1: Errors in NRHybSur3dq8 and SEOBNRv4HM when compared against hybrid waveforms. For NRHybSur3dq8, we show out-of-sample errors. Mismatches are computed at several points in the sky of the source frame using all available modes in each waveform. **Top:** Mismatches computed using a flat noise curve, but including only the late inspiral part of the waveforms, starting at $-3500M$ before the peak. Therefore, we are essentially comparing only to the NR part of the hybrid waveforms. For comparison, we also show the NR resolution error, obtained by comparing the two highest available resolutions. The histograms are normalized such that the area under each curve is 1 when integrated over $\log_{10}(\text{Mismatch})$. **Bottom:** Mismatches as a function of total mass, computed using the Advanced LIGO design sensitivity noise curve. Here we compare against the full hybrid waveforms. The solid (dashed) lines show the 95th percentile (median) mismatch values over points on the sky as well as different hybrid waveforms.

design sensitivity Zero-Detuned-HighP noise curve [109] with $f_{\min} = 20\text{Hz}$ and $f_{\max} = 2000\text{Hz}$.

Surrogate errors

We evaluate the accuracy of our new surrogate model, NRHybSur3dq8, by computing mismatches against hybrid waveforms. For this, we compute “out-of-sample” errors as follows. We first randomly divide the 104 training waveforms into groups of ~ 5 waveforms each. For each group, we build a trial surrogate using the remaining ~ 99 training waveforms and test against these five validation ones. We also compute the mismatch between an existing higher-mode waveform model, SEOBNRv4HM [15], and the hybrid waveforms.

Figure 5.9.1 summarizes mismatches of both NRHybSur3dq8 and SEOBNRv4HM versus the hybrid waveforms. We use all available modes for each waveform model. In the top panel we show mismatches computed using a flat noise curve over the NR part of the hybrid waveforms (to do this, we truncate the waveforms and begin tapering at $t = -3500M$). We see that the mismatches for NRHybSur3dq8 are about two orders of magnitude lower than that of SEOBNRv4HM. We compare this with the truncation error in the NR waveforms themselves, by computing the mismatch between the two highest available resolutions of each NR waveform. The errors in the surrogate model are well within the truncation error of the NR simulations. Note that NR error estimated in this manner is a conservative estimate; if we treat the high resolution simulation as the fiducial case, the NR curve in Fig. 5.9.1 can be thought of as the error in the lower-resolution simulation. This explains why the errors in the surrogate are smaller than the NR errors. We suspect that the error of the high resolution simulations is close to the surrogate model’s error.

The bottom panel of Fig. 5.9.1 shows mismatches computed using the Advanced LIGO design sensitivity noise curve. The mismatches are now dependent on the total mass of the system, so we show mismatches for masses starting at the lower limit of the range of validity of the surrogate: $M \geq 2.25M_{\odot}$. 95th percentile mismatches for NRHybSur3dq8, are always below $\sim 3 \times 10^{-4}$ in the mass range $2.25M_{\odot} \leq M \leq 300M_{\odot}$. At high masses ($M \gtrsim 40M_{\odot}$), where the merger and ringdown are more prominent, our model is more accurate than SEOBNRv4HM by roughly two orders of magnitude, in agreement with the top panel of Fig. 5.9.1.

For high masses only the last few orbits of the hybrid waveforms are in the LIGO band, and the hybrid waveforms are effectively the same as the NR waveforms. For

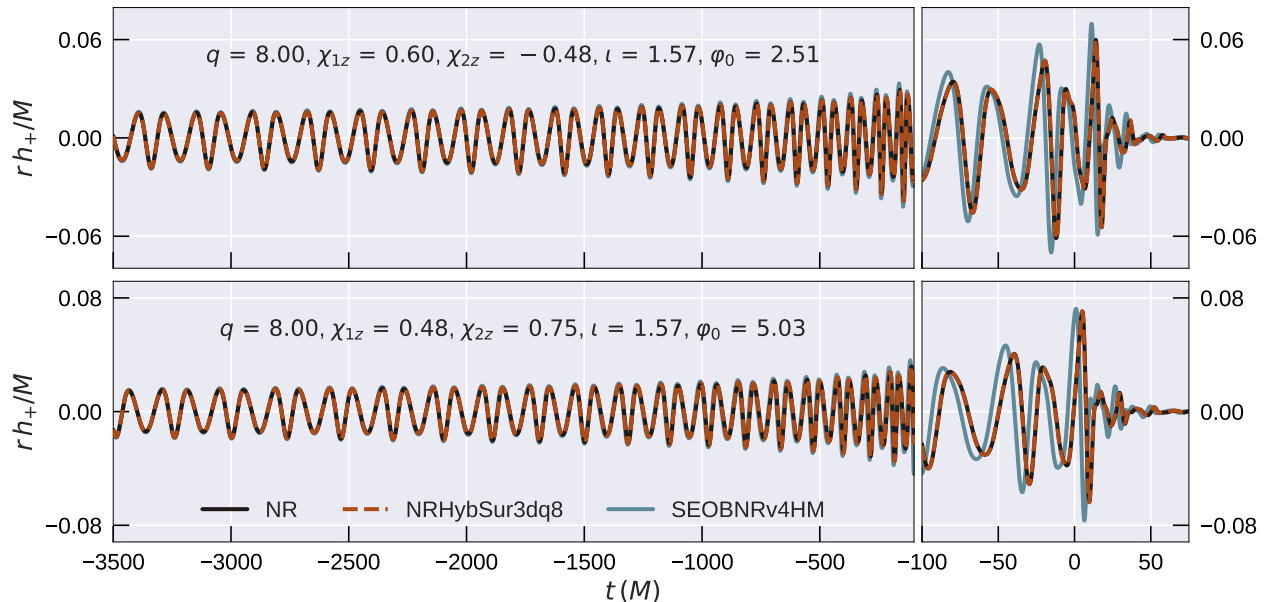


Figure 5.9.2: The plus polarization of the waveforms for the cases that result in the largest mismatch for NRHybSur3dq8 (top) and SEOBNRv4HM (bottom) in the left panel of Fig. 5.9.1. We also show the corresponding hybrid waveforms (labeled as NR because only the late part is shown). Each waveform is projected using all available modes for that model, along the direction which results in the largest mismatch for NRHybSur3dq8 (SEOBNRv4HM) in the top (bottom) panel. Note that NRHybSur3dq8 is evaluated using trial surrogates that are not trained using these cases. The binary parameters and the direction in the source frame are indicated in the inset text. All waveforms are time shifted such that the peak of the total waveform amplitude occurs at $t = 0$ (using all available modes, according to Eq. (5.38)). Then the waveform modes are rotated about the z -axis such that the orbital phase is zero at $t = -3500M$.

low masses, the errors in the bottom panel of Fig. 5.9.1 quantify how well different models reproduce the hybrid waveforms. However, this comparison cannot account for the errors in the hybridization procedure itself. We provide some evidence for the fidelity of the hybrid waveforms in Sec. 5.9, by comparing against some long NR waveforms.

Fig. 5.9.2 shows NRHybSur3dq8 and SEOBNRv4HM waveforms for the cases leading to the largest errors in the left panel of Fig. 5.9.1. The surrogate shows very good agreement with the NR waveform, even for its worst case. SEOBNRv4HM shows a noticeably larger deviation that cannot all be accounted for with a time and/or phase shift. Note that we align the time and orbital phase of the waveforms in Fig. 5.9.2.

We note that the main improvement over SEOBNRv4HM is not due to the inclusion of more modes. We find that the agreement between SEOBNRv4HM and the NR/hybrid waveforms in Figs. 5.9.1 and 5.9.2 improves only marginally when restricting the NR/hybrid waveforms to the same set of modes as SEOBNRv4HM.

Hybridization errors

The errors described in Sec. 5.9 are computed by comparing the surrogate against hybrid waveforms, hence they do not include the errors in the hybridization procedure or the errors from EOB-corrected-PN waveforms (cf. Sec. 5.6) we use for the early inspiral. To estimate these errors, we compare the surrogate against a few very long NR simulations⁹. We perform five new simulations that are $\sim 10^5 M$ long and two that are $\sim 3 \times 10^4 M$ long. These have been assigned the identifiers SXS:BBH:1412 - SXS:BBH:1418, and will be made publicly available in the upcoming update of the SXS public catalog [58]. In addition, we use two simulations of length $\sim 3 \times 10^4 M$ from Ref. [111]. These nine simulations are represented as square markers in Fig. 5.5.1, and have not been used in training the surrogate. The surrogate was trained against hybrid waveforms whose NR duration varied between $3270M$ and $4227M$. Therefore, comparing against long NR waveforms, which include the early inspiral, is a good way to estimate the hybridization error.

We begin by repeating the mismatch computation from the right panel of Fig. 5.9.1, using the $10^5 M$ long NR waveforms. This is shown in Fig. 5.9.3. We also show the errors in the NR simulations, estimated by comparing the two highest available NR resolutions. We find that the mismatches between the surrogate and the long NR waveforms for $M > 30M_\odot$ are below 10^{-4} , in agreement with Fig. 5.9.1. For lower masses, the mismatches quickly increase and can be as high as $\sim 10^{-2}$. However, this increase in mismatch is accompanied by an increase in the error of the NR waveforms. This is expected, since for very long NR waveforms the accumulated phase error is a dominant source of numerical error, which becomes increasingly relevant for low mass systems as more of the waveform moves in-band. Therefore, in Fig. 5.9.3, at low masses, the comparison between the surrogate and NR waveforms is largely dominated by the numerical resolution error of the long NR waveforms themselves.

⁹Note that for these long NR simulations, the outer boundary location is chosen based on the length of the simulations [59] so as to avoid unphysical center-of-mass accelerations seen in earlier long-duration runs [110].

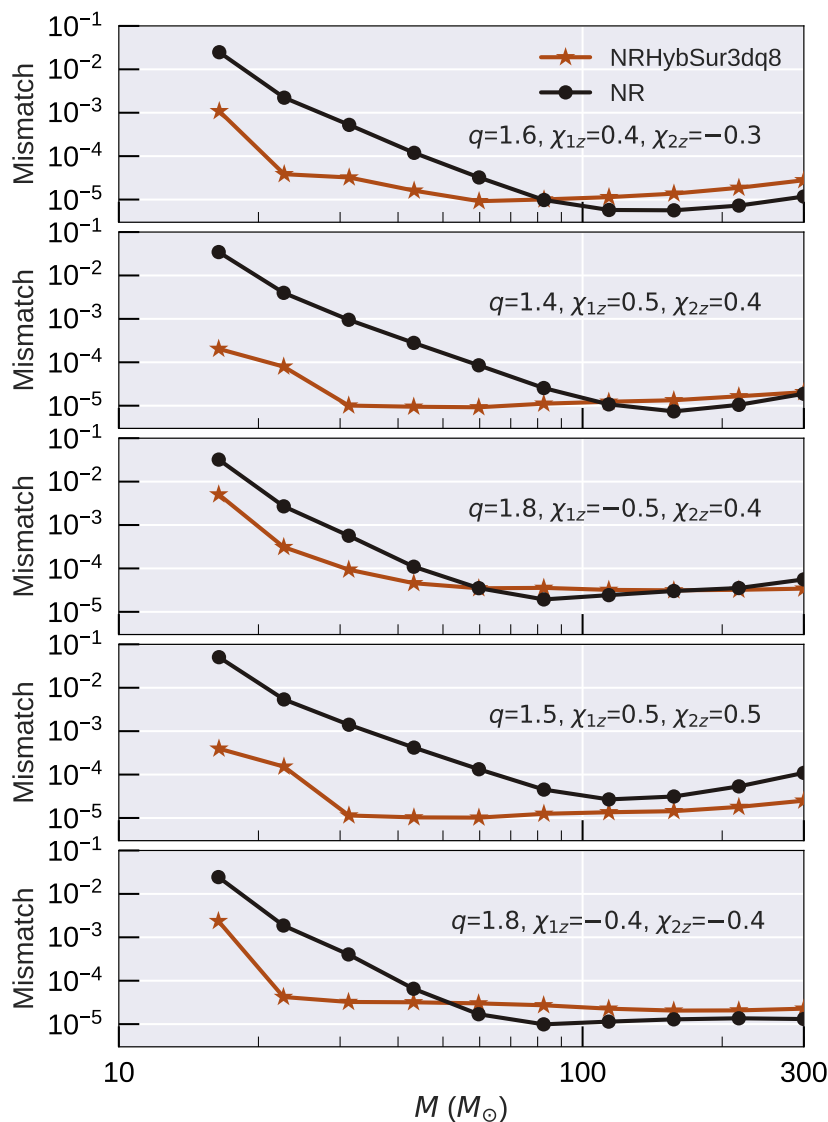


Figure 5.9.3: Comparisons between the NRHybSur3dq8 surrogate model and a few NR waveforms of $\sim 10^5 M$ in duration. We also show the NR resolution error. 95th percentile mismatches (over points in the sky) are shown as a function of total mass. The inset text indicates the mass ratio and component spins. Mismatches are computed using the Advanced LIGO design sensitivity noise curve. To best assess the error introduced by the hybridization procedure we use the same set of modes for the NR waveforms as the surrogate. At low masses, the hybridization errors (red circles) become less reliable measures of accuracy due to the large NR resolution error (black circles) itself. Fig. 5.9.4 describes a refined comparison to improve the assessment at low masses.

We find that a better test of the hybridization procedure, one that is less sensitive to NR phase accumulation errors, is to compare against different segments of the NR waveform. Since the phase errors accumulate over a large number of cycles, by looking at smaller segments we ensure that this contribution is not the dominant error. To be precise, we compare the surrogate and the NR data, using segments of length $\Delta t = 5 \times 10^3 M$ ending at a particular number of orbits before the peak of the waveform. For each segment we compute mismatches at several points in the sky using a flat noise curve. By varying the number of orbits to the peak, we can cover the entire NR waveform including the early inspiral region where the surrogate depends on the hybridization procedure. These errors are shown in Fig. 5.9.4. We find that in each segment, the mismatch between the surrogate and the NR data is, in general, lower or comparable to the NR resolution error. Therefore, the surrogate reproduces the NR data accurately in the early inspiral and the hybridization errors are smaller than or comparable to the NR resolution error for these cases. We note that the surrogate errors in Fig. 5.9.4 depend on the length of the segment considered and are only meaningful when compared to the NR errors in the same segment.

Unfortunately, long NR simulations such as these are not available at regions of the parameter space where both mass ratio and spin magnitudes are large. These are the cases where PN is expected to perform poorly, so we expect larger hybridization errors for these cases.

Extrapolation outside the training range

We now investigate the efficacy of NRHybSur3dq8 to extrapolate beyond its training parameter range by comparing against SpEC NR simulations [58, 111–114] at larger mass ratios ($8 < q \leq 10$) and/or larger spin magnitudes ($|\chi_{1z}| > 0.8$ or $|\chi_{12}| > 0.8$). These NR simulations are represented as triangle markers in Fig. 5.5.1.

Fig. 5.9.5 shows mismatches for NRHybSur3dq8 when compared against these simulations. We find that surrogate extrapolates remarkably well, with the mismatch always $\lesssim 4 \times 10^{-4}$ for all cases, which include mass ratios up to $q = 10$ and spin magnitudes up to $|\chi| = 0.998$. However, the extrapolation errors can be about half an order of magnitude larger than errors within the training range. Note that NR simulations with both high mass ratios and high spin magnitudes are not currently available, and the ones used here represent the most extreme cases found in the SXS Catalog. We do not hybridize these simulations before comparing to NRHybSur3dq8 because several of them are too short. In Fig. 5.9.5, the minimum

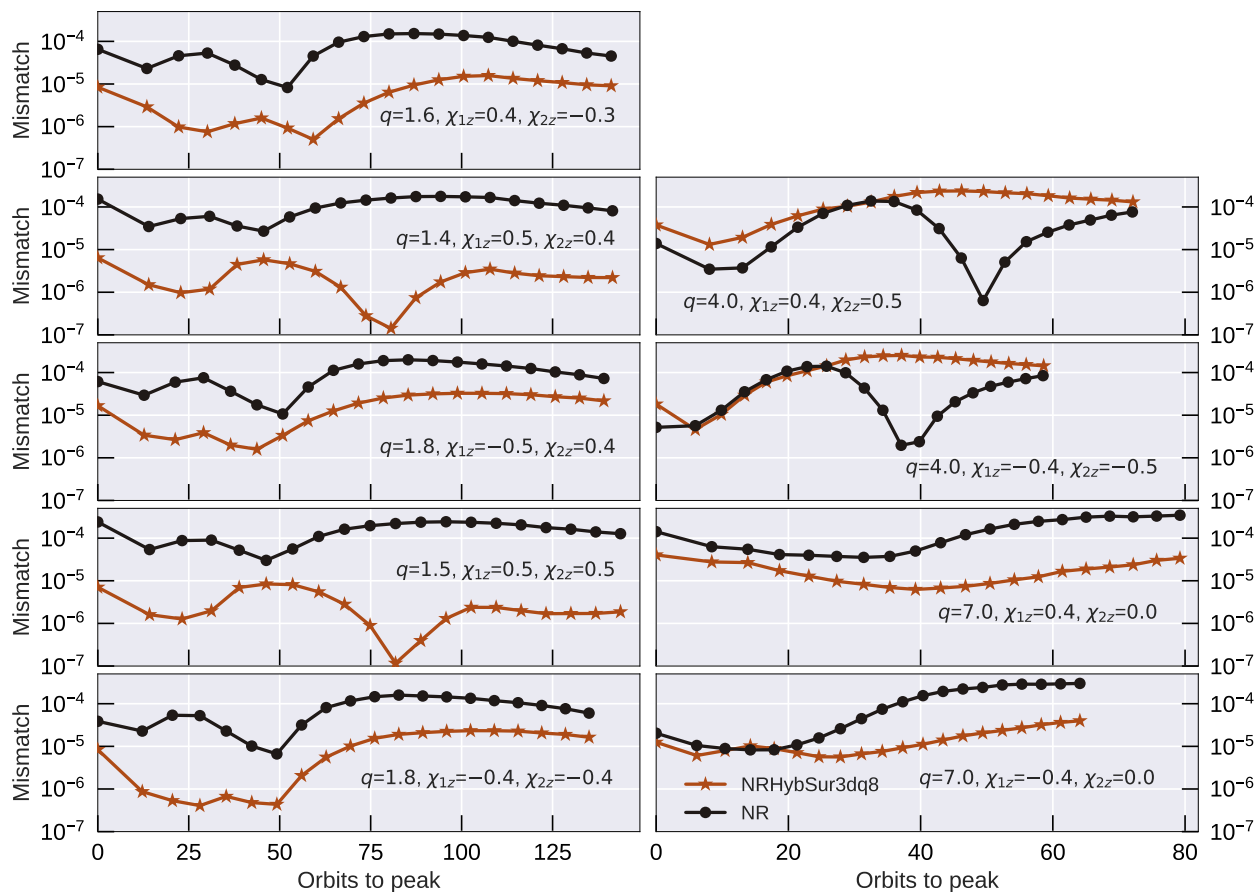


Figure 5.9.4: Errors in the NRHybSur3dq8 surrogate model against long NR waveforms, but only looking at segments of length $\Delta t = 5 \times 10^3 M$ individually. Each point represents one segment that ends at a specified number of orbits before the waveform peak, as plotted on the horizontal axis; Therefore, going from left to right in the figure, we plot segments that start earlier in the inspiral. We also show the NR resolution error in the same segments. The inset text indicates the mass ratio and component spins. We show 95th percentile mismatches (over points in the sky), computed using a flat noise curve. We use the same set of modes for the NR waveforms as the surrogate. We find that, in general, the surrogate error is lower than or comparable to the NR resolution error throughout the inspiral.

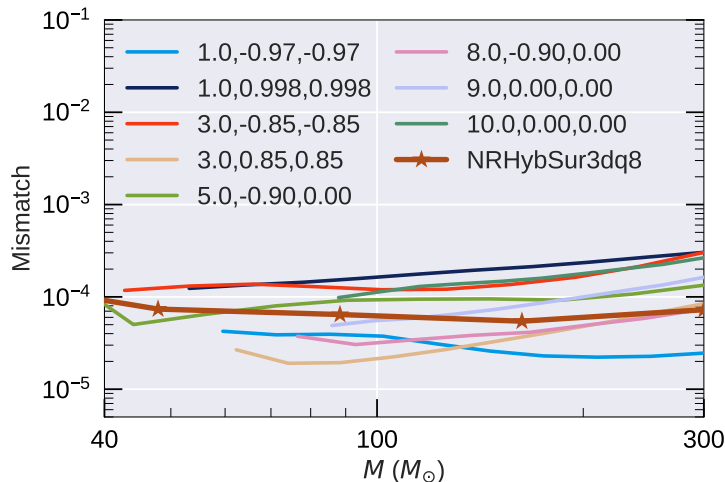


Figure 5.9.5: Errors in NRHybSur3dq8 when evaluated outside its training range. 95th percentile mismatches (over points in the sky) are shown as a function of total mass for different extrapolated cases. These are computed using the Advanced LIGO design sensitivity noise curve. To best assess the error introduced by the extrapolation, we use the same set of modes for the NR waveforms as the surrogate. The labels indicate the mass ratio and component spins $(q, \chi_{1z}, \chi_{2z})$. For comparison we reproduce the 95th percentile mismatches for NRHybSur3dq8 within its training range from the right panel of Fig. 5.9.1.

mass for each case is chosen to be the lowest mass at which all used modes of the NR simulation lie fully in the LIGO band with a low frequency cut-off of 20 Hz.

At much higher mass ratios than those tested here, such as $q = 15$, we find that the waveforms generated by the surrogate can have “glitches” in the time series. Therefore, we recommend the surrogate be used for $q \leq 10$ and $|\chi_{1z}|, |\chi_{2z}| \leq 1$. However, we advise caution with any extrapolation in general.

Mode mixing

Numerical relativity waveforms are extracted as spin-weighted spherical harmonic modes [33, 34]. However, in the ringdown regime, the natural basis to use is the spin-weighted *spheroidal* harmonic basis [115, 116]. A spherical harmonic mode $f_{\ell m}$ can be written as a linear combination of all spheroidal harmonic modes $f_{\ell m}^S$ with the same m index [117]. Therefore, during the ringdown, we expect leakage of power between different spherical harmonic modes with the same m . This is referred to as mode mixing.

Since the surrogate accurately reproduces the spherical harmonic modes from the NR

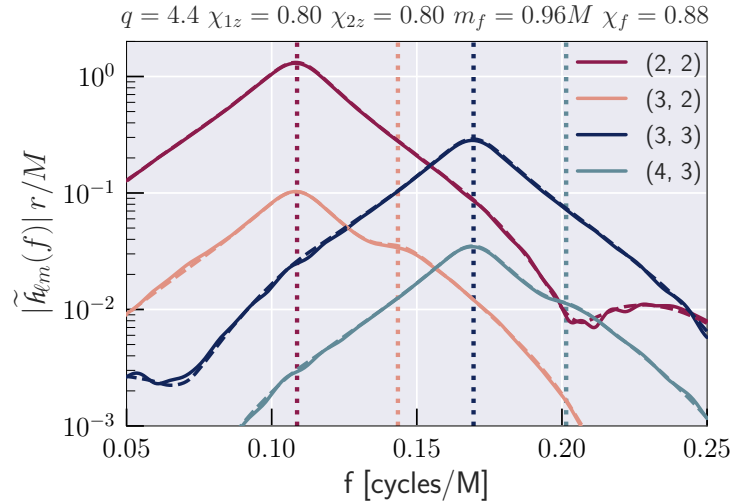


Figure 5.9.6: Mode mixing between spherical harmonic modes is clearly seen in the ringdown signal of the NR waveform and is accurately reproduced by the surrogate. The absolute values of the Fourier transform of different spherical harmonic modes are shown as solid (dashed) curves for the surrogate (NR). The dotted vertical lines indicate the frequencies of the fundamental QNM overtone of these modes. The component parameters as well as the remnant mass and spin are shown in the text above the figure.

simulations, it also captures this mode mixing. We demonstrate this for an example case in Fig. 5.9.6. Here we compute the Fourier transform of different spherical harmonic modes in the ringdown stage of the waveform. Before computing the Fourier transform, we first drop all data before $t = 20M$, where $t = 0$ corresponds to the peak of the waveform amplitude (cf. Eq. (5.38)). Then, we taper the data between $t = 20M$ and $t = 40M$, as well as the last $10M$ of the time series, using a Planck window [108]. The tapering width at the start is chosen such that the remaining signal is dominated by the fundamental quasi-normal mode (QNM) overtone. Fig. 5.9.6 shows the absolute value of these Fourier transforms for different modes, for both the surrogate and the NR waveform. In addition, we show the frequency of the fundamental QNM overtone for each mode [118].

Note that the (2,2) mode and the (3,2) mode have the same m index, the condition required for mode mixing. We see that the peak of the (2,2) mode agrees with the QNM frequency as expected. For the (3,2) mode however, while there are features of a peak at the expected QNM frequency, there is a much larger peak at the frequency of the (2,2) mode. This is because some of the power of the stronger (2,2) mode has leaked into the (3,2) mode due to mode mixing. Mode mixing can also be seen

for the (3,3) and (4,3) modes, which also have the same m index. Fig. 5.9.6 shows that not only does the surrogate agree with NR in the ringdown, it also reproduces the mode mixing present in the NR data.

Evaluation cost

Figure 5.9.7 shows the evaluation cost for NRHybSur3dq8, at different total masses, starting at 20Hz, and using a sampling rate of 4096Hz. This suggests that NRHybSur3dq8 is fast enough for direct use in parameter estimation. We also show the evaluation cost per mode. Note that the total cost as well the cost per mode in Fig. 5.9.7 include the cost of a Fast Fourier Transform (FFT). We perform the FFT only once, after summing over all modes in the time domain. This cost is also shown separately in Fig. 5.9.7. Finally, we show the evaluation cost of SEOBNRv4_ROM [17], a Fourier domain Reduced Order Model (ROM) version of SEOBNRv4. Note that SEOBNRv4_ROM models only the (2,2) mode. Comparing the cost for SEOBNRv4_ROM to the cost per mode of NRHybSur3dq8 suggests that the evaluation cost of NRHybSur3dq8 can be reduced by a factor of ~ 2.5 by building a Fourier domain ROM along the lines of Ref. [23].

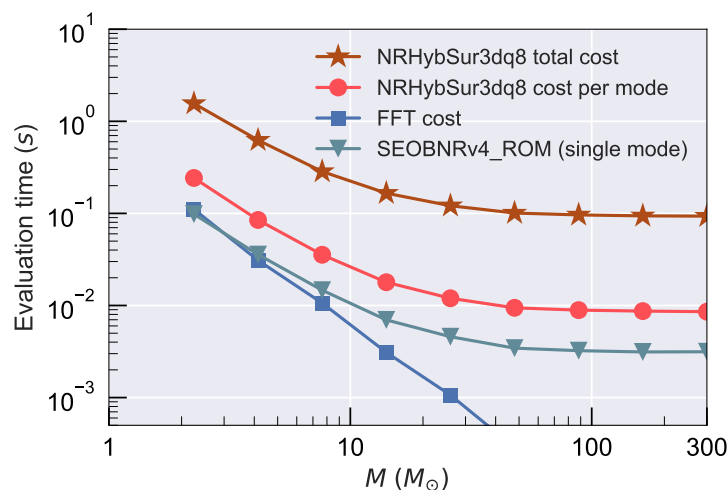


Figure 5.9.7: Evaluation cost for NRHybSur3dq8 including the cost of an FFT. We show the cost for evaluating all 11 modes modeled by NRHybSur3dq8, as well as the cost per mode. The FFT cost is included in both of the above but also shown separately. We also show the evaluation cost of SEOBNRv4_ROM which includes only the (2,2) mode. The evaluation cost is computed by averaging over 64 points uniformly distributed in the parameter space, $q \leq 8$ and $|\chi_{1z}|, |\chi_{2z}| \leq 0.8$.

At low masses, where the waveform is very long, the dominant costs for NRHyb-

Sur3dq8 are due to the temporal interpolation from the sparse domain of the surrogate to the required time samples, and the FFT. At high masses, where the waveform is short, the interpolation and FFT are cheap and the dominant cost for NRHyb-Sur3dq8 is due to the GPR evaluations for the parametric fits. SEOBNRv4_ROM instead uses tensor spline interpolation for the parametric fits [17], which accounts for the main difference in the evaluation cost per mode at high masses.

These tests were performed on a single core on a 3.1 GHz Intel Core i5 processor. Both NRHybSur3dq8 and SEOBNRv4_ROM were evaluated using a C implementation in the LIGO Algorithm Library [49]. The Python implementation of NRHybSur3dq8 in *gwsurrogate* [48] is slower than the C implementation by at most a factor of 2.

5.10 Conclusion

We present NRHybSur3dq8, the first NR-based surrogate waveform model that spans the entire LIGO bandwidth, valid for stellar mass binaries with total masses $M \geq 2.25M_{\odot}$. This model is trained on 104 NR-PN/EOB hybrid waveforms of nonprecessing quasicircular BBH systems with mass ratios $q \leq 8$, and spin magnitudes $|\chi_{1z}|, |\chi_{2z}| \leq 0.8$. The parametric fits for this model are performed using Gaussian process regression. This model includes the following spin-weighted spherical harmonic modes: $\ell \leq 4$ and (5,5), but not (4,1) or (4,0). We make our model available publicly through the easy-to-use Python package *gwsurrogate* [48]. In addition, our model is implemented in C with Python wrapping in the LIGO Algorithm Library [49]. We provide an example Python evaluation code at [50].

Through a cross-validation study, we show that the surrogate accurately reproduces the hybrid waveforms. The mismatch between them is always less than $\sim 3 \times 10^{-4}$ for total masses $2.25M_{\odot} \leq M \leq 300M_{\odot}$. For high masses ($M \gtrsim 40M_{\odot}$), where the merger and ringdown are more prominent, we show roughly a 2 orders of magnitude improvement over the current state-of-the-art model with nonquadrupole modes, SEOBNRv4HM [15].

By comparing against several long NR simulations, we show that the errors in our hybridization procedure are comparable or lower than the resolution error in current NR simulations. In addition, by comparing against available NR simulations at higher mass ratios and spins, we show that our model extrapolates reasonably well outside its training range. Based on these tests, we are cautiously optimistic that the

surrogate can be used for $q \leq 10$ and $|\chi_{1z}|, |\chi_{2z}| \leq 1$, and we leave a more detailed investigation for future work.

Future work

While our tests of the hybridization procedure are encouraging, long NR simulations are available only for low mass ratios and low spin magnitudes. Therefore, we have no means to test hybridization at high mass ratios and/or high spins, where PN is expected to perform poorly. An improved surrogate model and refined study of the hybridization errors will require longer inspiral waveforms with greater coverage of the parameter space.

Another extension of interest is towards larger mass ratios and spin magnitudes. While the surrogate extrapolates very well when compared to available simulations at larger mass ratios and spins, no NR simulations are available with both large mass ratios ($q > 8$) and large spins ($\chi > 0.8$). Therefore, our model is untested in that region of parameter space and it might be necessary to add training points there. The model could also be extended to include precession and/or eccentricity, however this is more challenging because of the enlarged parameter space as well as more complicated hybridization.

Finally, as mentioned in Sec. 5.9, the evaluation time of NRHybSur3dq8 can likely be reduced by constructing a Fourier domain ROM [23] of the time-domain model.

We leave these explorations to future work.

5.11 Acknowledgments

We thank Matt Giesler for helping carry out the new SpEC simulations used in this work. We thank Michael Boyle, Kevin Barkett, Matt Giesler, Yanbei Chen, and Saul Teukolsky for useful discussions. We thank Patricia Schmidt for careful and detailed feedback on an earlier draft of this manuscript. V.V. and M.S. are supported by the Sherman Fairchild Foundation, and NSF grants PHY-170212 and PHY-1708213 at Caltech. L.E.K. acknowledges support from the Sherman Fairchild Foundation and NSF grant PHY-1606654 at Cornell. S.E.F is partially supported by NSF grant PHY-1806665. This work used the Extreme Science and Engineering Discovery Environment (XSEDE), which is supported by National Science Foundation grant number ACI-1548562. This research is part of the Blue Waters sustained-petascale computing project, which is supported by the National Science Foundation (awards

OCI-0725070 and ACI-1238993) and the state of Illinois. Blue Waters is a joint effort of the University of Illinois at Urbana-Champaign and its National Center for Supercomputing Applications. Simulations were performed on NSF/NCSA Blue Waters under allocation NSF PRAC-1713694; on the Wheeler cluster at Caltech, which is supported by the Sherman Fairchild Foundation and by Caltech; and on XSEDE resources Bridges at the Pittsburgh Supercomputing Center, Comet at the San Diego Supercomputer Center, and Stampede and Stampede2 at the Texas Advanced Computing Center, through allocation TG-PHY990007N. Computations for building the model were performed on Wheeler and Stampede2.

References

- [1] B. P. Abbott et al. “Observation of Gravitational Waves from a Binary Black Hole Merger”. In: *Phys. Rev. Lett.* 116 (6 Feb. 2016), p. 061102. doi: [10.1103/PhysRevLett.116.061102](https://doi.org/10.1103/PhysRevLett.116.061102). arXiv: [1602.03837 \[gr-qc\]](https://arxiv.org/abs/1602.03837). URL: <http://link.aps.org/doi/10.1103/PhysRevLett.116.061102>.
- [2] Benjamin P. Abbott et al. “GW170817: Observation of Gravitational Waves from a Binary Neutron Star Inspiral”. In: *Phys. Rev. Lett.* 119.16 (2017), p. 161101. doi: [10.1103/PhysRevLett.119.161101](https://doi.org/10.1103/PhysRevLett.119.161101). arXiv: [1710.05832 \[gr-qc\]](https://arxiv.org/abs/1710.05832).
- [3] B. P. Abbott et al. “GW151226: Observation of Gravitational Waves from a 22-Solar-Mass Binary Black Hole Coalescence”. In: *Phys. Rev. Lett.* 116.24 (2016), p. 241103. doi: [10.1103/PhysRevLett.116.241103](https://doi.org/10.1103/PhysRevLett.116.241103). arXiv: [1606.04855 \[gr-qc\]](https://arxiv.org/abs/1606.04855).
- [4] Benjamin P. Abbott et al. “GW170104: Observation of a 50-Solar-Mass Binary Black Hole Coalescence at Redshift 0.2”. In: *Phys. Rev. Lett.* 118.22 (2017), p. 221101. doi: [10.1103/PhysRevLett.118.221101](https://doi.org/10.1103/PhysRevLett.118.221101). arXiv: [1706.01812 \[gr-qc\]](https://arxiv.org/abs/1706.01812).
- [5] B. P. Abbott et al. “GW170608: Observation of a 19-solar-mass Binary Black Hole Coalescence”. In: *Astrophys. J.* 851.2 (2017), p. L35. doi: [10.3847/2041-8213/aa9f0c](https://doi.org/10.3847/2041-8213/aa9f0c). arXiv: [1711.05578 \[astro-ph.HE\]](https://arxiv.org/abs/1711.05578).
- [6] B. P. Abbott et al. “GW170814: A Three-Detector Observation of Gravitational Waves from a Binary Black Hole Coalescence”. In: *Phys. Rev. Lett.* 119.14 (2017), p. 141101. doi: [10.1103/PhysRevLett.119.141101](https://doi.org/10.1103/PhysRevLett.119.141101). arXiv: [1709.09660 \[gr-qc\]](https://arxiv.org/abs/1709.09660).
- [7] B. P. Abbott et al. “GWTC-1: A Gravitational-Wave Transient Catalog of Compact Binary Mergers Observed by LIGO and Virgo during the First and Second Observing Runs”. In: (2018). arXiv: [1811.12907 \[astro-ph.HE\]](https://arxiv.org/abs/1811.12907).

- [8] J. Aasi et al. “Advanced LIGO”. In: 32 (2015), p. 074001. doi: [10.1088/0264-9381/32/7/074001](https://doi.org/10.1088/0264-9381/32/7/074001). arXiv: [1411.4547](https://arxiv.org/abs/1411.4547) [gr-qc].
- [9] F. Acernese et al. “Advanced Virgo: a second-generation interferometric gravitational wave detector”. In: 32.2 (2015), p. 024001. doi: [10.1088/0264-9381/32/2/024001](https://doi.org/10.1088/0264-9381/32/2/024001). arXiv: [1408.3978](https://arxiv.org/abs/1408.3978) [gr-qc].
- [10] B. P. Abbott et al. “Prospects for Observing and Localizing Gravitational-Wave Transients with Advanced LIGO and Advanced Virgo”. In: 19 (2016), p. 1. doi: [10.1007/lrr-2016-1](https://doi.org/10.1007/lrr-2016-1). arXiv: [1304.0670v3](https://arxiv.org/abs/1304.0670v3) [gr-qc]. URL: <http://www.livingreviews.org/lrr-2016-1>.
- [11] B. P. Abbott et al. “Binary Black Hole Population Properties Inferred from the First and Second Observing Runs of Advanced LIGO and Advanced Virgo”. In: (2018). arXiv: [1811.12940](https://arxiv.org/abs/1811.12940) [astro-ph.HE].
- [12] Sebastian Khan et al. “Phenomenological model for the gravitational-wave signal from precessing binary black holes with two-spin effects”. In: (2018). arXiv: [1809.10113](https://arxiv.org/abs/1809.10113) [gr-qc].
- [13] Yi Pan et al. “Inspiral-merger-ringdown waveforms of spinning, precessing black-hole binaries in the effective-one-body formalism”. In: *Phys. Rev. D* 89.8 (2014), p. 084006. doi: [10.1103/PhysRevD.89.084006](https://doi.org/10.1103/PhysRevD.89.084006). arXiv: [1307.6232](https://arxiv.org/abs/1307.6232) [gr-qc].
- [14] Lionel London et al. “First higher-multipole model of gravitational waves from spinning and coalescing black-hole binaries”. In: *Phys. Rev. Lett.* 120.16 (2018), p. 161102. doi: [10.1103/PhysRevLett.120.161102](https://doi.org/10.1103/PhysRevLett.120.161102). arXiv: [1708.00404](https://arxiv.org/abs/1708.00404) [gr-qc].
- [15] Roberto Cotesta et al. “Enriching the Symphony of Gravitational Waves from Binary Black Holes by Tuning Higher Harmonics”. In: *Phys. Rev. D* 98.8 (2018), p. 084028. doi: [10.1103/PhysRevD.98.084028](https://doi.org/10.1103/PhysRevD.98.084028). arXiv: [1803.10701](https://arxiv.org/abs/1803.10701) [gr-qc].
- [16] Sebastian Khan et al. “Frequency-domain gravitational waves from non-precessing black-hole binaries. II. A phenomenological model for the advanced detector era”. In: *Phys. Rev. D* 93.4 (2016), p. 044007. doi: [10.1103/PhysRevD.93.044007](https://doi.org/10.1103/PhysRevD.93.044007). arXiv: [1508.07253](https://arxiv.org/abs/1508.07253) [gr-qc].
- [17] Alejandro Bohé et al. “Improved effective-one-body model of spinning, non-precessing binary black holes for the era of gravitational-wave astrophysics with advanced detectors”. In: *Phys. Rev. D* 95 (4 Feb. 2017), p. 044028. doi: [10.1103/PhysRevD.95.044028](https://doi.org/10.1103/PhysRevD.95.044028). arXiv: [1611.03703](https://arxiv.org/abs/1611.03703) [gr-qc]. URL: <https://link.aps.org/doi/10.1103/PhysRevD.95.044028>.
- [18] Mark Hannam et al. “A simple model of complete precessing black-hole-binary gravitational waveforms”. In: *Phys. Rev. Lett.* 113 (2014), p. 151101. doi: [10.1103/PhysRevLett.113.151101](https://doi.org/10.1103/PhysRevLett.113.151101). arXiv: [1308.3271](https://arxiv.org/abs/1308.3271) [gr-qc].

- [19] Andrea Taracchini et al. “Effective-one-body model for black-hole binaries with generic mass ratios and spins”. In: *Phys. Rev. D* 89.6 (2014), p. 061502. doi: [10.1103/PhysRevD.89.061502](https://doi.org/10.1103/PhysRevD.89.061502). arXiv: [1311.2544](https://arxiv.org/abs/1311.2544) [gr-qc].
- [20] Yi Pan et al. “Inspirational-merger-ringdown multipolar waveforms of nonspinning black-hole binaries using the effective-one-body formalism”. In: *Phys. Rev. D* 84 (2011), p. 124052. doi: [10.1103/PhysRevD.84.124052](https://doi.org/10.1103/PhysRevD.84.124052). arXiv: [1106.1021](https://arxiv.org/abs/1106.1021) [gr-qc].
- [21] Ajit Kumar Mehta et al. “Accurate inspiral-merger-ringdown gravitational waveforms for nonspinning black-hole binaries including the effect of subdominant modes”. In: *Phys. Rev. D* 96.12 (2017), p. 124010. doi: [10.1103/PhysRevD.96.124010](https://doi.org/10.1103/PhysRevD.96.124010). arXiv: [1708.03501](https://arxiv.org/abs/1708.03501) [gr-qc].
- [22] S. E. Field et al. “Fast Prediction and Evaluation of Gravitational Waveforms Using Surrogate Models”. In: 4.3, 031006 (July 2014), p. 031006. doi: [10.1103/PhysRevX.4.031006](https://doi.org/10.1103/PhysRevX.4.031006). arXiv: [1308.3565](https://arxiv.org/abs/1308.3565) [gr-qc].
- [23] M. Pürrer. “Frequency domain reduced order models for gravitational waves from aligned-spin compact binaries”. In: 31.19 (2014), p. 195010. doi: [10.1088/0264-9381/31/19/195010](https://doi.org/10.1088/0264-9381/31/19/195010). arXiv: [1402.4146](https://arxiv.org/abs/1402.4146) [gr-qc].
- [24] Benjamin D. Lackey et al. “Effective-one-body waveforms for binary neutron stars using surrogate models”. In: *Phys. Rev. D* 95.10 (2017), p. 104036. doi: [10.1103/PhysRevD.95.104036](https://doi.org/10.1103/PhysRevD.95.104036). arXiv: [1610.04742](https://arxiv.org/abs/1610.04742) [gr-qc].
- [25] Zoheyr Doctor et al. “Statistical Gravitational Waveform Models: What to Simulate Next?” In: *Phys. Rev. D* 96.12 (2017), p. 123011. doi: [10.1103/PhysRevD.96.123011](https://doi.org/10.1103/PhysRevD.96.123011). arXiv: [1706.05408](https://arxiv.org/abs/1706.05408) [astro-ph.HE].
- [26] Jonathan Blackman et al. “Fast and Accurate Prediction of Numerical Relativity Waveforms from Binary Black Hole Coalescences Using Surrogate Models”. In: *Phys. Rev. Lett.* 115.12 (2015), p. 121102. doi: [10.1103/PhysRevLett.115.121102](https://doi.org/10.1103/PhysRevLett.115.121102). arXiv: [1502.07758](https://arxiv.org/abs/1502.07758) [gr-qc].
- [27] Jonathan Blackman et al. “A Surrogate Model of Gravitational Waveforms from Numerical Relativity Simulations of Precessing Binary Black Hole Mergers”. In: *Phys. Rev. D* 95.10 (2017), p. 104023. doi: [10.1103/PhysRevD.95.104023](https://doi.org/10.1103/PhysRevD.95.104023). arXiv: [1701.00550](https://arxiv.org/abs/1701.00550) [gr-qc].
- [28] Jonathan Blackman et al. “Numerical relativity waveform surrogate model for generically precessing binary black hole mergers”. In: *Phys. Rev. D* 96.2 (2017), p. 024058. doi: [10.1103/PhysRevD.96.024058](https://doi.org/10.1103/PhysRevD.96.024058). arXiv: [1705.07089](https://arxiv.org/abs/1705.07089) [gr-qc].
- [29] E. A. Huerta et al. “Eccentric, nonspinning, inspiral, Gaussian-process merger approximant for the detection and characterization of eccentric binary black hole mergers”. In: 97.2 (2018), p. 024031. doi: [10.1103/PhysRevD.97.024031](https://doi.org/10.1103/PhysRevD.97.024031). arXiv: [1711.06276](https://arxiv.org/abs/1711.06276) [gr-qc].

- [30] Alvin J. K. Chua, Chad R. Galley, and Michele Vallisneri. “ROMAN: Reduced-Order Modeling with Artificial Neurons”. In: (2018). arXiv: [1811.05491 \[astro-ph.IM\]](#).
- [31] Priscilla Canizares et al. “Accelerated gravitational-wave parameter estimation with reduced order modeling”. In: *Phys. Rev. Lett.* 114.7 (2015), p. 071104. DOI: [10.1103/PhysRevLett.114.071104](#). arXiv: [1404.6284 \[gr-qc\]](#).
- [32] Chad R. Galley and Patricia Schmidt. “Fast and efficient evaluation of gravitational waveforms via reduced-order spline interpolation”. In: (2016). arXiv: [1611.07529 \[gr-qc\]](#).
- [33] E. T. Newman and R. Penrose. “Note on the Bondi–Metzner–Sachs Group”. In: 7 (1966), pp. 863–870. DOI: [10.1063/1.1931221](#). URL: <http://link.aip.org/link/?JMP/7/863/1>.
- [34] J. N. Goldberg et al. “Spin- s Spherical Harmonics and δ ”. In: *Journal of Mathematical Physics* 8.11 (1967), pp. 2155–2161. DOI: [10.1063/1.1705135](#). URL: <http://link.aip.org/link/?JMP/8/2155/1>.
- [35] Vijay Varma and Parameswaran Ajith. “Effects of nonquadrupole modes in the detection and parameter estimation of black hole binaries with non-precessing spins”. In: *Phys. Rev. D* 96.12 (2017), p. 124024. DOI: [10.1103/PhysRevD.96.124024](#). arXiv: [1612.05608 \[gr-qc\]](#).
- [36] Collin Capano, Yi Pan, and Alessandra Buonanno. “Impact of higher harmonics in searching for gravitational waves from nonspinning binary black holes”. In: *Phys. Rev. D* 89.10 (2014), p. 102003. DOI: [10.1103/PhysRevD.89.102003](#). arXiv: [1311.1286 \[gr-qc\]](#).
- [37] Tyson B. Littenberg et al. “Systematic biases in parameter estimation of binary black-hole mergers”. In: 87 (2013), p. 104003. DOI: [10.1103/PhysRevD.87.104003](#). arXiv: [1210.0893 \[gr-qc\]](#).
- [38] Juan Calderón Bustillo, Pablo Laguna, and Deirdre Shoemaker. “Detectability of gravitational waves from binary black holes: Impact of precession and higher modes”. In: *Phys. Rev. D* 95.10 (2017), p. 104038. DOI: [10.1103/PhysRevD.95.104038](#). arXiv: [1612.02340 \[gr-qc\]](#).
- [39] Duncan A. Brown, Prayush Kumar, and Alexander H. Nitz. “Template banks to search for low-mass binary black holes in advanced gravitational-wave detectors”. In: 87 (2013), p. 082004. DOI: [10.1103/PhysRevD.87.082004](#). arXiv: [1211.6184 \[gr-qc\]](#).
- [40] V. Varma et al. “Gravitational-wave observations of binary black holes: Effect of nonquadrupole modes”. In: 90.12 (2014), p. 124004. DOI: [10.1103/PhysRevD.90.124004](#). arXiv: [1409.2349 \[gr-qc\]](#).

- [41] Philip B. Graff, Alessandra Buonanno, and B. S. Sathyaprakash. “Missing Link: Bayesian detection and measurement of intermediate-mass black-hole binaries”. In: 92.2 (2015), p. 022002. DOI: [10.1103/PhysRevD.92.022002](https://doi.org/10.1103/PhysRevD.92.022002). arXiv: [1504.04766](https://arxiv.org/abs/1504.04766) [gr-qc].
- [42] Ian Harry, Juan Calderón Bustillo, and Alex Nitz. “Searching for the full symphony of black hole binary mergers”. In: *Phys. Rev. D* 97.2 (2018), p. 023004. DOI: [10.1103/PhysRevD.97.023004](https://doi.org/10.1103/PhysRevD.97.023004). arXiv: [1709.09181](https://arxiv.org/abs/1709.09181) [gr-qc].
- [43] B. P. Abbott et al. “Effects of waveform model systematics on the interpretation of GW150914”. In: (2016). arXiv: [1611.07531](https://arxiv.org/abs/1611.07531) [gr-qc].
- [44] B. P. Abbott et al. “Directly comparing GW150914 with numerical solutions of Einstein’s equations for binary black hole coalescence”. In: *Phys. Rev. D* 94 (2016), p. 064035. DOI: [10.1103/PhysRevD.94.064035](https://doi.org/10.1103/PhysRevD.94.064035). arXiv: [1606.01262](https://arxiv.org/abs/1606.01262) [gr-qc].
- [45] Prayush Kumar et al. “Constraining the parameters of GW150914 & GW170104 with numerical relativity surrogates”. In: (2018). arXiv: [1808.08004](https://arxiv.org/abs/1808.08004) [gr-qc].
- [46] R. O’Shaughnessy et al. “Parameter estimation of gravitational waves from precessing black hole-neutron star inspirals with higher harmonics”. In: *Phys. Rev. D* 89.10 (2014), p. 102005. DOI: [10.1103/PhysRevD.89.102005](https://doi.org/10.1103/PhysRevD.89.102005). arXiv: [1403.0544](https://arxiv.org/abs/1403.0544) [gr-qc].
- [47] Samantha A. Usman, Joseph C. Mills, and Stephen Fairhurst. “Constraining the Inclination of Binary Mergers from Gravitational-wave Observations”. In: (2018). arXiv: [1809.10727](https://arxiv.org/abs/1809.10727) [gr-qc].
- [48] Jonathan Blackman et al. *gwsurrogate*. <https://pypi.python.org/pypi/gwsurrogate/>.
- [49] LIGO Scientific Collaboration. *LIGO Algorithm Library - LALSuite*. free software (GPL). 2018. DOI: [10.7935/GT1W-FZ16](https://doi.org/10.7935/GT1W-FZ16).
- [50] *Binary black-hole surrogate waveform catalog*. <http://www.black-holes.org/surrogates/>. Sept. 2018.
- [51] *The Spectral Einstein Code*. <http://www.black-holes.org/SpEC.html>.
- [52] H. P. Pfeiffer et al. “A multidomain spectral method for solving elliptic equations”. In: 152 (May 2003), pp. 253–273. DOI: [10.1016/S0010-4655\(02\)00847-0](https://doi.org/10.1016/S0010-4655(02)00847-0). eprint: [gr-qc/0202096](https://arxiv.org/abs/gr-qc/0202096).
- [53] Geoffrey Lovelace et al. “Binary-black-hole initial data with nearly-extremal spins”. In: *Phys. Rev. D* 78 (2008), p. 084017. DOI: [10.1103/PhysRevD.78.084017](https://doi.org/10.1103/PhysRevD.78.084017). arXiv: [0805.4192](https://arxiv.org/abs/0805.4192) [gr-qc].

- [54] L. Lindblom et al. “A new generalized harmonic evolution system”. In: 23 (Aug. 2006), S447. DOI: [10.1088/0264-9381/23/16/S09](https://doi.org/10.1088/0264-9381/23/16/S09). eprint: [gr-qc/0512093](https://arxiv.org/abs/gr-qc/0512093).
- [55] Bela Szilagyi, Lee Lindblom, and Mark A. Scheel. “Simulations of Binary Black Hole Mergers Using Spectral Methods”. In: *Phys.Rev. D*80 (2009), p. 124010. DOI: [10.1103/PhysRevD.80.124010](https://doi.org/10.1103/PhysRevD.80.124010). arXiv: [0909.3557](https://arxiv.org/abs/0909.3557) [gr-qc].
- [56] Mark A. Scheel et al. “High-accuracy waveforms for binary black hole inspiral, merger, and ringdown”. In: *Phys. Rev. D*79 (2009), p. 024003. DOI: [10.1103/PhysRevD.79.024003](https://doi.org/10.1103/PhysRevD.79.024003). arXiv: [0810.1767](https://arxiv.org/abs/0810.1767) [gr-qc].
- [57] *Simulating eXtreme Spacetimes*. <http://www.black-holes.org/>.
- [58] SXS Collaboration. *The SXS Collaboration catalog of gravitational waveforms*. <http://www.black-holes.org/waveforms>.
- [59] M. Boyle et al. “The SXS Collaboration catalog of gravitational waveforms for merging black holes”. In: (2019). In preparation.
- [60] Alessandra Buonanno et al. “Reducing orbital eccentricity of precessing black-hole binaries”. In: 83 (2011), p. 104034. DOI: [10.1103/PhysRevD.83.104034](https://doi.org/10.1103/PhysRevD.83.104034). arXiv: [1012.1549](https://arxiv.org/abs/1012.1549) [gr-qc].
- [61] Michael Boyle and Abdul H. Mroué. “Extrapolating gravitational-wave data from numerical simulations”. In: 80.12 (Dec. 2009), pp. 124045–14. DOI: [10.1103/PhysRevD.80.124045](https://doi.org/10.1103/PhysRevD.80.124045). arXiv: [0905.3177](https://arxiv.org/abs/0905.3177) [gr-qc]. URL: <http://link.aps.org/abstract/PRD/v80/e124045>.
- [62] Michael Boyle. “Transformations of asymptotic gravitational-wave data”. In: *Phys. Rev. D*93.8 (2016), p. 084031. DOI: [10.1103/PhysRevD.93.084031](https://doi.org/10.1103/PhysRevD.93.084031). arXiv: [1509.00862](https://arxiv.org/abs/1509.00862) [gr-qc].
- [63] Michael Boyle. *Scri*. <https://github.com/moble/scri>.
- [64] L. Santamaría et al. “Matching post-Newtonian and numerical relativity waveforms: Systematic errors and a new phenomenological model for non-precessing black hole binaries”. In: 82 (2010), p. 064016. DOI: [10.1103/PhysRevD.82.064016](https://doi.org/10.1103/PhysRevD.82.064016). arXiv: [1005.3306](https://arxiv.org/abs/1005.3306) [gr-qc].
- [65] Frank Ohme. “Analytical meets numerical relativity - status of complete gravitational waveform models for binary black holes”. In: *Class. Quant. Grav.* 29 (2012), p. 124002. DOI: [10.1088/0264-9381/29/12/124002](https://doi.org/10.1088/0264-9381/29/12/124002). arXiv: [1111.3737](https://arxiv.org/abs/1111.3737) [gr-qc].
- [66] Frank Ohme, Mark Hannam, and Sascha Husa. “Reliability of complete gravitational waveform models for compact binary coalescences”. In: *Phys. Rev. D*84 (2011), p. 064029. DOI: [10.1103/PhysRevD.84.064029](https://doi.org/10.1103/PhysRevD.84.064029). arXiv: [1107.0996](https://arxiv.org/abs/1107.0996) [gr-qc].

- [67] Ilana MacDonald et al. “Suitability of post-Newtonian/numerical-relativity hybrid waveforms for gravitational wave detectors”. In: *Class. Quant. Grav.* 28 (2011), p. 134002. DOI: [10.1088/0264-9381/28/13/134002](https://doi.org/10.1088/0264-9381/28/13/134002). arXiv: [1102.5128](https://arxiv.org/abs/1102.5128) [gr-qc].
- [68] Ilana MacDonald et al. “Suitability of hybrid gravitational waveforms for unequal-mass binaries”. In: *Phys. Rev. D* 87.2 (2013), p. 024009. DOI: [10.1103/PhysRevD.87.024009](https://doi.org/10.1103/PhysRevD.87.024009). arXiv: [1210.3007](https://arxiv.org/abs/1210.3007) [gr-qc].
- [69] P. Ajith et al. “The NINJA-2 catalog of hybrid post-Newtonian/numerical-relativity waveforms for non-precessing black-hole binaries”. In: *Class. Quant. Grav.* 29 (2012). [Erratum: *Class. Quant. Grav.* 30, 199401 (2013)], p. 124001. DOI: [10.1088/0264-9381/30/19/199401](https://doi.org/10.1088/0264-9381/30/19/199401), [10.1088/0264-9381/29/12/124001](https://doi.org/10.1088/0264-9381/29/12/124001). arXiv: [1201.5319](https://arxiv.org/abs/1201.5319) [gr-qc].
- [70] Michael Boyle. “Uncertainty in hybrid gravitational waveforms: Optimizing initial orbital frequencies for binary black-hole simulations”. In: *Phys. Rev. D* 84 (2011), p. 064013. DOI: [10.1103/PhysRevD.84.064013](https://doi.org/10.1103/PhysRevD.84.064013). arXiv: [1103.5088](https://arxiv.org/abs/1103.5088) [gr-qc].
- [71] Juan Calderón Bustillo et al. “Comparison of subdominant gravitational wave harmonics between post-Newtonian and numerical relativity calculations and construction of multi-mode hybrids”. In: (2015). arXiv: [1501.00918](https://arxiv.org/abs/1501.00918) [gr-qc].
- [72] Michael Boyle. *GWFrames*. <https://github.com/moble/GWFrames>.
- [73] Luc Blanchet et al. “Gravitational radiation from inspiralling compact binaries completed at the third post-Newtonian order”. In: *Phys. Rev. Lett.* 93 (2004), p. 091101. DOI: [10.1103/PhysRevLett.93.091101](https://doi.org/10.1103/PhysRevLett.93.091101). arXiv: [gr-qc/0406012](https://arxiv.org/abs/gr-qc/0406012) [gr-qc].
- [74] Luc Blanchet. “Gravitational Radiation from Post-Newtonian Sources and Inspiralling Compact Binaries”. In: *Living Rev. Rel.* 17 (2014), p. 2. DOI: [10.12942/lrr-2014-2](https://doi.org/10.12942/lrr-2014-2). arXiv: [1310.1528](https://arxiv.org/abs/1310.1528) [gr-qc].
- [75] Piotr Jaranowski and Gerhard Schäfer. “Dimensional regularization of local singularities in the 4th post-Newtonian two-point-mass Hamiltonian”. In: *Phys. Rev. D* 87 (2013), p. 081503. DOI: [10.1103/PhysRevD.87.081503](https://doi.org/10.1103/PhysRevD.87.081503). arXiv: [1303.3225](https://arxiv.org/abs/1303.3225) [gr-qc].
- [76] Donato Bini and Thibault Damour. “Analytical determination of the two-body gravitational interaction potential at the 4th post-Newtonian approximation”. In: 87 (12 June 2013), p. 121501. DOI: [10.1103/PhysRevD.87.121501](https://doi.org/10.1103/PhysRevD.87.121501). arXiv: [1305.4884](https://arxiv.org/abs/1305.4884) [gr-qc]. URL: <http://link.aps.org/doi/10.1103/PhysRevD.87.121501>.
- [77] Donato Bini and Thibault Damour. “High-order post-Newtonian contributions to the two-body gravitational interaction potential from analytical gravitational self-force calculations”. In: *Phys. Rev. D* 89.6 (2014), p. 064063. DOI: [10.1103/PhysRevD.89.064063](https://doi.org/10.1103/PhysRevD.89.064063). arXiv: [1312.2503](https://arxiv.org/abs/1312.2503) [gr-qc].

- [78] Lawrence E. Kidder. “Coalescing binary systems of compact objects to post-Newtonian 5/2 order. 5. Spin effects”. In: *Phys. Rev. D* 52 (1995), pp. 821–847. DOI: [10.1103/PhysRevD.52.821](https://doi.org/10.1103/PhysRevD.52.821). arXiv: [gr-qc/9506022](https://arxiv.org/abs/gr-qc/9506022).
- [79] Clifford M. Will and Alan G. Wiseman. “Gravitational radiation from compact binary systems: Gravitational wave forms and energy loss to second postNewtonian order”. In: *Phys. Rev. D* 54 (1996), pp. 4813–4848. DOI: [10.1103/PhysRevD.54.4813](https://doi.org/10.1103/PhysRevD.54.4813). arXiv: [gr-qc/9608012](https://arxiv.org/abs/gr-qc/9608012) [gr-qc].
- [80] Alejandro Bohe et al. “Next-to-next-to-leading order spin-orbit effects in the near-zone metric and precession equations of compact binaries”. In: 30 (2013), p. 075017. DOI: [10.1088/0264-9381/30/7/075017](https://doi.org/10.1088/0264-9381/30/7/075017). arXiv: [1212.5520](https://arxiv.org/abs/1212.5520).
- [81] Michael Boyle et al. “High-accuracy comparison of numerical relativity simulations with post-Newtonian expansions”. In: *Phys. Rev. D* 76 (2007), p. 124038. DOI: [10.1103/PhysRevD.76.124038](https://doi.org/10.1103/PhysRevD.76.124038). arXiv: [0710.0158](https://arxiv.org/abs/0710.0158) [gr-qc].
- [82] Luc Blanchet et al. “The Third post-Newtonian gravitational wave polarisations and associated spherical harmonic modes for inspiralling compact binaries in quasi-circular orbits”. In: 25 (2008), p. 165003. DOI: [10.1088/0264-9381/25/16/165003](https://doi.org/10.1088/0264-9381/25/16/165003). arXiv: [0802.1249](https://arxiv.org/abs/0802.1249) [gr-qc].
- [83] Guillaume Faye et al. “The third and a half post-Newtonian gravitational wave quadrupole mode for quasi-circular inspiralling compact binaries”. In: *Class. Quant. Grav.* 29 (2012), p. 175004. DOI: [10.1088/0264-9381/29/17/175004](https://doi.org/10.1088/0264-9381/29/17/175004). arXiv: [1204.1043](https://arxiv.org/abs/1204.1043) [gr-qc].
- [84] Guillaume Faye, Luc Blanchet, and Bala R. Iyer. “Non-linear multipole interactions and gravitational-wave octupole modes for inspiralling compact binaries to third-and-a-half post-Newtonian order”. In: 32.4 (2015), p. 045016. arXiv: [1409.3546](https://arxiv.org/abs/1409.3546) [gr-qc]. URL: <http://stacks.iop.org/0264-9381/32/i=4/a=045016>.
- [85] Luc Blanchet and Gerhard Schäfer. “Gravitational wave tails and binary star systems”. In: 10.12 (1993), pp. 2699–2721. URL: <http://stacks.iop.org/0264-9381/10/2699>.
- [86] K. G. Arun et al. “The 2.5PN gravitational wave polarizations from inspiralling compact binaries in circular orbits”. In: 21 (Aug. 2004), pp. 3771–3801. DOI: [10.1088/0264-9381/21/15/010](https://doi.org/10.1088/0264-9381/21/15/010). eprint: [arXiv:gr-qc/0404085](https://arxiv.org/abs/gr-qc/0404085).
- [87] Kevin Barkett et al. “Detailed Expansion of PN Tidal Splicing Method”. In: (2018). in preparation.
- [88] The SciPy software library. URL: <http://scipy.org/>.

- [89] S. Ossokine et al. “Comparing post-Newtonian and numerical relativity precession dynamics”. In: 92.10, 104028 (Nov. 2015), p. 104028. DOI: [10.1103/PhysRevD.92.104028](https://doi.org/10.1103/PhysRevD.92.104028). arXiv: [1502.01747](https://arxiv.org/abs/1502.01747) [gr-qc].
- [90] Marc Favata. “The gravitational-wave memory effect”. In: 27 (2010), p. 084036. DOI: [10.1088/0264-9381/27/8/084036](https://doi.org/10.1088/0264-9381/27/8/084036). arXiv: [1003.3486](https://arxiv.org/abs/1003.3486) [gr-qc].
- [91] C. J. Handmer, B. Szilágyi, and J. Winicour. “Gauge invariant spectral Cauchy characteristic extraction”. In: 32.23, 235018 (Dec. 2015), p. 235018. DOI: [10.1088/0264-9381/32/23/235018](https://doi.org/10.1088/0264-9381/32/23/235018). arXiv: [1502.06987](https://arxiv.org/abs/1502.06987) [gr-qc].
- [92] Casey J. Handmer, Béla Szilágyi, and Jeffrey Winicour. “Spectral Cauchy Characteristic Extraction of strain, news and gravitational radiation flux”. In: *Class. Quant. Grav.* 33.22 (2016), p. 225007. DOI: [10.1088/0264-9381/33/22/225007](https://doi.org/10.1088/0264-9381/33/22/225007). arXiv: [1605.04332](https://arxiv.org/abs/1605.04332) [gr-qc].
- [93] Jeffrey Winicour. “Characteristic Evolution and Matching”. In: *Living Rev. Rel.* 12 (2009), p. 3. DOI: [10.12942/lrr-2009-3](https://doi.org/10.12942/lrr-2009-3). arXiv: [0810.1903](https://arxiv.org/abs/0810.1903) [gr-qc].
- [94] Nigel T. Bishop et al. “Cauchy-characteristic extraction in numerical relativity”. In: 54.10 (Nov. 1996), pp. 6153–6165. DOI: [10.1103/PhysRevD.54.6153](https://doi.org/10.1103/PhysRevD.54.6153). arXiv: [9705033](https://arxiv.org/abs/9705033) [gr-qc]. URL: <http://link.aps.org/abstract/PRD/v54/p6153>.
- [95] M. Boyle et al. “Gravitational-wave modes from precessing black-hole binaries”. In: (2014). arXiv:1409.4431. arXiv: [1409.4431](https://arxiv.org/abs/1409.4431).
- [96] P. Ajith et al. “A Template bank for gravitational waveforms from coalescing binary black holes. I. Non-spinning binaries”. In: 77 (2008), p. 104017. DOI: [10.1103/PhysRevD.77.104017](https://doi.org/10.1103/PhysRevD.77.104017), [10.1103/PhysRevD.79.129901](https://doi.org/10.1103/PhysRevD.79.129901), [10.1103/PhysRevD.77.104017](https://doi.org/10.1103/PhysRevD.77.104017), [10.1103/PhysRevD.79.129901](https://doi.org/10.1103/PhysRevD.79.129901). arXiv: [0710.2335](https://arxiv.org/abs/0710.2335) [gr-qc].
- [97] Thibault Damour, Bala R. Iyer, and B. S. Sathyaprakash. “A Comparison of search templates for gravitational waves from binary inspiral”. In: *Phys. Rev. D* 63 (2001). [Erratum: *Phys. Rev. D* 72, 029902 (2005)], p. 044023. DOI: [10.1103/PhysRevD.63.044023](https://doi.org/10.1103/PhysRevD.63.044023), [10.1103/PhysRevD.72.029902](https://doi.org/10.1103/PhysRevD.72.029902). arXiv: [gr-qc/0010009](https://arxiv.org/abs/gr-qc/0010009) [gr-qc].
- [98] Alessandra Buonanno et al. “Comparison of post-Newtonian templates for compact binary inspiral signals in gravitational-wave detectors”. In: *Phys. Rev. D* 80 (2009), p. 084043. DOI: [10.1103/PhysRevD.80.084043](https://doi.org/10.1103/PhysRevD.80.084043). arXiv: [0907.0700](https://arxiv.org/abs/0907.0700) [gr-qc].
- [99] S. E. Field et al. “Reduced basis catalogs for gravitational wave templates”. In: 106 (2011), p. 221102. DOI: [10.1103/PhysRevLett.106.221102](https://doi.org/10.1103/PhysRevLett.106.221102). arXiv: [1101.3765](https://arxiv.org/abs/1101.3765) [gr-qc].

- [100] F. Herrmann et al. “Towards beating the curse of dimensionality for gravitational waves using Reduced Basis”. In: 86 (2012), p. 084046. DOI: [10.1103/PhysRevD.86.084046](https://doi.org/10.1103/PhysRevD.86.084046). arXiv: [1205.6009](https://arxiv.org/abs/1205.6009) [gr-qc].
- [101] Maxime Barrault et al. “An ‘empirical interpolation’ method: application to efficient reduced-basis discretization of partial differential equations”. In: *Comptes Rendus Mathematique* 339.9 (2004), pp. 667–672. ISSN: 1631-073X. DOI: <http://dx.doi.org/10.1016/j.crma.2004.08.006>. URL: <http://www.sciencedirect.com/science/article/pii/S1631073X04004248>.
- [102] Y. Maday et al. “A general multipurpose interpolation procedure: the magic points”. In: *Communications on Pure and Applied Analysis* 8 (2009), pp. 383–404. DOI: [10.3934/cpaa.2009.8.383](https://doi.org/10.3934/cpaa.2009.8.383).
- [103] Hesthaven, Jan S., Stamm, Benjamin, and Zhang, Shun. “Efficient greedy algorithms for high-dimensional parameter spaces with applications to empirical interpolation and reduced basis methods”. In: *ESAIM: M2AN* 48.1 (2014), pp. 259–283. DOI: [10.1051/m2an/2013100](https://doi.org/10.1051/m2an/2013100). URL: <https://doi.org/10.1051/m2an/2013100>.
- [104] Vijay Varma et al. “High-accuracy mass, spin, and recoil predictions of generic black-hole merger remnants”. In: *Phys. Rev. Lett.* 122 (2019), p. 011101. DOI: [10.1103/PhysRevLett.122.011101](https://doi.org/10.1103/PhysRevLett.122.011101). arXiv: [1809.09125](https://arxiv.org/abs/1809.09125) [gr-qc].
- [105] P. Ajith. “Addressing the spin question in gravitational-wave searches: Waveform templates for inspiralling compact binaries with nonprecessing spins”. In: 84 (2011), p. 084037. DOI: [10.1103/PhysRevD.84.084037](https://doi.org/10.1103/PhysRevD.84.084037). arXiv: [1107.1267](https://arxiv.org/abs/1107.1267) [gr-qc].
- [106] Curt Cutler and Eanna E. Flanagan. “Gravitational waves from merging compact binaries: How accurately can one extract the binary’s parameters from the inspiral wave form?” In: *Phys. Rev. D* 49 (1994), pp. 2658–2697. DOI: [10.1103/PhysRevD.49.2658](https://doi.org/10.1103/PhysRevD.49.2658). arXiv: [gr-qc/9402014](https://arxiv.org/abs/gr-qc/9402014) [gr-qc].
- [107] Eric Poisson and Clifford M. Will. “Gravitational waves from inspiraling compact binaries: Parameter estimation using second postNewtonian wave forms”. In: *Phys. Rev. D* 52 (1995), pp. 848–855. DOI: [10.1103/PhysRevD.52.848](https://doi.org/10.1103/PhysRevD.52.848). arXiv: [gr-qc/9502040](https://arxiv.org/abs/gr-qc/9502040) [gr-qc].
- [108] D.J.A. McKechn, C. Robinson, and B.S. Sathyaprakash. “A tapering window for time-domain templates and simulated signals in the detection of gravitational waves from coalescing compact binaries”. In: 27 (2010), p. 084020. DOI: [10.1088/0264-9381/27/8/084020](https://doi.org/10.1088/0264-9381/27/8/084020). arXiv: [1003.2939](https://arxiv.org/abs/1003.2939) [gr-qc].
- [109] LIGO Scientific Collaboration. *Advanced LIGO anticipated sensitivity curves*. Tech. rep. <https://dcc.ligo.org/LIGO-T0900288/public>. 2011.

- [110] B. Szilágyi et al. “Approaching the Post-Newtonian Regime with Numerical Relativity: A Compact-Object Binary Simulation Spanning 350 Gravitational-Wave Cycles”. In: 115 (2015), p. 031102. doi: [10.1103/PhysRevLett.115.031102](https://doi.org/10.1103/PhysRevLett.115.031102). arXiv: [1502.04953](https://arxiv.org/abs/1502.04953) [gr-qc].
- [111] P. Kumar et al. “Accuracy and precision of gravitational-wave models of inspiraling neutron star-black hole binaries with spin: Comparison with matter-free numerical relativity in the low-frequency regime”. In: 92.10 (2015), p. 102001. doi: [10.1103/PhysRevD.92.102001](https://doi.org/10.1103/PhysRevD.92.102001). arXiv: [1507.00103](https://arxiv.org/abs/1507.00103) [gr-qc].
- [112] T. Chu et al. “On the accuracy and precision of numerical waveforms: effect of waveform extraction methodology”. In: 33.16, 165001 (Aug. 2016), p. 165001. doi: [10.1088/0264-9381/33/16/165001](https://doi.org/10.1088/0264-9381/33/16/165001). arXiv: [1512.06800](https://arxiv.org/abs/1512.06800) [gr-qc].
- [113] M. A. Scheel et al. “Improved methods for simulating nearly extremal binary black holes”. In: 32.10, 105009 (May 2015), p. 105009. doi: [10.1088/0264-9381/32/10/105009](https://doi.org/10.1088/0264-9381/32/10/105009). arXiv: [1412.1803](https://arxiv.org/abs/1412.1803) [gr-qc].
- [114] Katerina Chatziioannou et al. “Measuring the properties of nearly extremal black holes with gravitational waves”. In: *Phys. Rev. D* 98.4 (2018), p. 044028. doi: [10.1103/PhysRevD.98.044028](https://doi.org/10.1103/PhysRevD.98.044028). arXiv: [1804.03704](https://arxiv.org/abs/1804.03704) [gr-qc].
- [115] Saul A. Teukolsky. “Perturbations of a rotating black hole. 1. Fundamental equations for gravitational electromagnetic and neutrino field perturbations”. In: *Astrophys. J.* 185 (1973), pp. 635–647. doi: [10.1086/152444](https://doi.org/10.1086/152444).
- [116] S.A. Teukolsky. “Rotating black holes - separable wave equations for gravitational and electromagnetic perturbations”. In: *Phys. Rev. Lett.* 29 (1972), pp. 1114–1118. doi: [10.1103/PhysRevLett.29.1114](https://doi.org/10.1103/PhysRevLett.29.1114).
- [117] Emanuele Berti and Antoine Klein. “Mixing of spherical and spheroidal modes in perturbed Kerr black holes”. In: *Phys. Rev. D* 90.6 (2014), p. 064012. doi: [10.1103/PhysRevD.90.064012](https://doi.org/10.1103/PhysRevD.90.064012). arXiv: [1408.1860](https://arxiv.org/abs/1408.1860) [gr-qc].
- [118] Emanuele Berti and Antoine Klein. <http://www.phy.olemiss.edu/~berti/qnms.html>.

HIGH-ACCURACY MASS, SPIN, AND RECOIL PREDICTIONS OF GENERIC BLACK-HOLE MERGER REMNANTS

Vijay Varma, Davide Gerosa, Leo C. Stein, Francois Hebert, and Hao Zhang.
Physical Review Letters, 122, 011101 (2019), [arxiv:1809.09125](https://arxiv.org/abs/1809.09125).

6.1 Executive summary

This Chapter presents models for the final black hole left behind after the merger of two black holes. The final black hole is fully characterized by its mass, linear momentum, and angular momentum. The prediction of these properties is of utmost importance in gravitational wave astronomy, from the construction of waveform models to developing tests of general relativity. For the first time, we make these predictions in a purely data-driven approach by training directly against hundreds of numerical relativity simulations. Our fits are extremely accurate- surpassing present models used in LIGO/Virgo analyses by an order of magnitude.

6.2 Abstract

We present accurate fits for the remnant properties of generically precessing binary black holes, trained on large banks of numerical-relativity simulations. We use Gaussian process regression to interpolate the remnant mass, spin, and recoil velocity in the 7-dimensional parameter space of precessing black-hole binaries with mass ratios $q \leq 2$, and spin magnitudes $\chi_1, \chi_2 \leq 0.8$. For precessing systems, our errors in estimating the remnant mass, spin magnitude, and kick magnitude are lower than those of existing fitting formulae by at least an order of magnitude (improvement is also reported in the extrapolated region at high mass ratios and spins). In addition, we also model the remnant spin and kick directions. Being trained directly on precessing simulations, our fits are free from ambiguities regarding the initial frequency at which precessing quantities are defined. We also construct a model for remnant properties of aligned-spin systems with mass ratios $q \leq 8$, and spin magnitudes $\chi_1, \chi_2 \leq 0.8$. As a byproduct, we also provide error estimates for all fitted quantities, which can be consistently incorporated into current and future gravitational-wave parameter-estimation analyses. Our model(s) are made publicly

available through a fast and easy-to-use Python module called *surfinBH*.

6.3 Introduction

As two black holes (BHs) come together and merge, they emit copious gravitational waves (GWs) and leave behind a BH remnant. The strong-field dynamics of this process are analytically intractable and must be simulated using numerical relativity (NR). However, from very far away, the merger can be viewed as a scattering problem, depicted in Fig. 6.3.1. The complicated dynamics of the near zone can be overlooked in favor of the gauge-invariant observables of the in- and out-states: the initial BH masses and spins, the outgoing GWs, and the final BH remnant. This final BH is fully characterized by its mass, spin, and recoil velocity; all additional complexities (“hair”) of the merging binary are dissipated away in GWs [1–3].

All GW models designed to capture the entire inspiral-merger-ringdown (IMR) signal from BH binary coalescences need to be calibrated to NR simulations (e.g., [4–12]). In particular, the BH ringdown emission is crucially dependent on the properties of the BH remnant — properties obtained from NR simulations. Accurate modeling of the merger remnant is therefore vital for construction of accurate IMR templates.

Besides waveform building, accurate knowledge of the remnant properties is also instrumental to fulfill one of the greatest promises of GW astronomy: testing Einstein’s general relativity (GR) in its strong-field, highly dynamical regime. Current approaches to test the Kerr hypothesis attempt to measure the properties of the inspiralling BHs from the low frequency part of the GW signal, then use NR fits to predict the corresponding remnant mass and spin; this final-state prediction is compared to the properties inferred from the high frequency part of the GW signal [13, 14]. Inaccuracies in remnant models therefore directly propagate to the final fundamental-physics test.

The importance of building fits for the remnant properties was realized soon after the NR breakthrough [15–17] and has been periodically revisited by several groups since then [18–39]. There are two important shortcomings in all existing fitting formulae. First, they enforce analytic ansätze (with NR-calibrated coefficients) that are physically motivated, but lack a rigorous mathematical justification. Therefore, current fits can be prone to systematic errors, especially in regions of parameter space where the intuition used to design the formulae become less accurate. Second, current expressions for remnant mass and spins are calibrated on aligned-spin

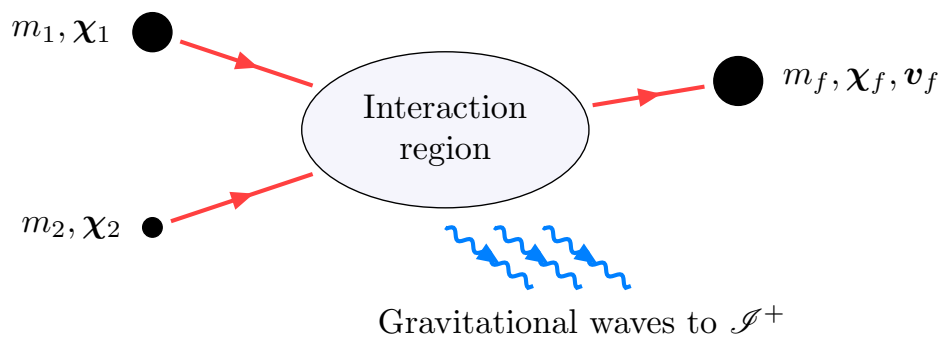


Figure 6.3.1: Quasi-circular binary BH merger problem viewed as a scattering process via a “Feynman” diagram. Time flows to the right. All quantities are well defined in the asymptotically flat region far from the interaction (merger).

simulations and therefore fail to fully capture the rich physics of precessing systems (but see e.g. [34] where a non-generic subspace of precessing configurations is considered). For example, current LIGO/Virgo parameter-estimation pipelines [40, 41] rely on ad-hoc corrections to partially account for precession effects [42]. Aligned fits applied to precessing systems are inevitably ambiguous, as the outcome will depend on *where* (in time, separation, or frequency) the spins are defined and inserted into the fits (e.g., [43]).

In this *Letter* we tackle both these issues for the first time. We construct surrogate models that fit the remnant properties from a large sample of generic, precessing, quasi-circular binary BH simulations performed with the Spectral Einstein Code (SpEC) [44]. Surrogates are trained directly against the NR simulations, using Gaussian process regression (GPR) without any phenomenological ansatz, and achieve accuracies comparable to those of the NR simulations themselves. In their regime of validity, the models presented here are at least an order of magnitude more accurate than previous fits.

In particular, we present two models:

1. *surfinBH7dq2*: a fit trained against precessing systems with mass ratios $q \leq 2$ and dimensionless spin magnitudes $\chi_1, \chi_2 \leq 0.8$.
2. *surfinBH3dq8*: an aligned-spin model trained against systems with mass ratios up to $q \leq 8$ and (anti-)aligned spin magnitudes $\chi_1, \chi_2 \leq 0.8$.

Both these models can be easily accessed using the publicly available Python module *surfinBH* [45], and are ready to be incorporated in both waveform constructions and

GW parameter-estimation studies.

6.4 Fitting procedure

We construct fits for the BH remnant mass m_f , spin vector χ_f , and recoil kick vector \mathbf{v}_f as functions of the binary mass ratio q and spin vectors χ_1, χ_2 . Our fits for *surfinBH7dq2* (*surfinBH3dq8*) map a 7- (3-)dimensional input parameter space to a 7- (4-)dimensional output parameter space. The fits are performed in the coorbital frame at $t = -100M$, with $t = 0$ at the peak of the total waveform amplitude (cf. Ref. [12] for details). The coorbital frame is defined such that the z -axis lies along the direction of the orbital angular momentum, the x -axis runs from the smaller BH to the larger BH, and the y -axis completes the triad.

All fits are performed using GPR [46]; details are provided in the supplemental material [47]. Notably, GPR naturally returns estimates of the errors of the fitted quantities across the parameter space.

The values of spins, masses, and kicks used in the training process are extracted directly from the NR simulations. We use the simulations presented in Ref. [12] for *surfinBH7dq2* and those of Ref. [48] for *surfinBH3dq8*. Both spins and masses are evaluated on apparent horizons [49]; the dimensionful spin \mathbf{S} solves an eigenvalue problem for an approximate Killing vector, and the mass is determined from the spin and area A following the Christodoulou relation $m^2 = m_{\text{irr}}^2 + S^2/(4m_{\text{irr}}^2)$, where $m_{\text{irr}}^2 = A/16\pi$ is the irreducible mass. The masses $m_{1,2}$ are determined close to the beginning of the simulation at the “relaxation time” [50], whereas the spins $\chi_{1,2} \equiv \mathbf{S}_{1,2}/m_{1,2}^2$ are measured at $t = -100M$. The remnant mass m_f and spin χ_f are determined long after ringdown, as detailed in [50]. All masses are in units of the total mass $M = m_1 + m_2$ at relaxation. The remnant kick velocity is derived from conservation of momentum, $\mathbf{v}_f = -\mathbf{P}^{\text{rad}}/m_f$ [51]. The radiated momentum flux \mathbf{P}^{rad} is integrated [52] from the GWs extrapolated to future null infinity [50, 53]. Before constructing the fits, χ_f and \mathbf{v}_f are transformed into the coorbital frame at $t = -100M$.

Besides the GPR error estimate, we further address the accuracy of our procedure using “k-fold” cross validations with $k = 20$. First, we randomly divide our training dataset into k mutually exclusive sets. For each set, we construct the fits using the data in the other $k - 1$ sets and then test the fits by evaluating them at the data points in the considered set. We thus obtain “out-of-sample” errors which conservatively indicate the (in)accuracies of our fits. We compare these errors

against the intrinsic error present in the NR waveforms, estimated by comparing the two highest resolutions available. We also compare the performance of our fits against several existing fitting formulae for remnant mass, spin, and kick which we denote as follows: HBMR ([30, 35] with $n_M = n_J = 3$), UIB [37], HL [38], HLZ [33], and CLZM ([21, 22, 27, 31, 32] as summarized in [36]). To partially account for spin precession, fits are corrected as described in Ref. [42] and used in current LIGO/Virgo analyses [40, 41]: spins are evolved from relaxation to the Schwarzschild innermost stable circular orbit, and final UIB and HL spins are post-processed adding the sum of the in-plane spins in quadrature. We note these fitting formulae were calibrated against different sets of simulations. Fitting methods, number of simulations, their quality, and their distribution in parameter space all contribute to the accuracy of the fits.

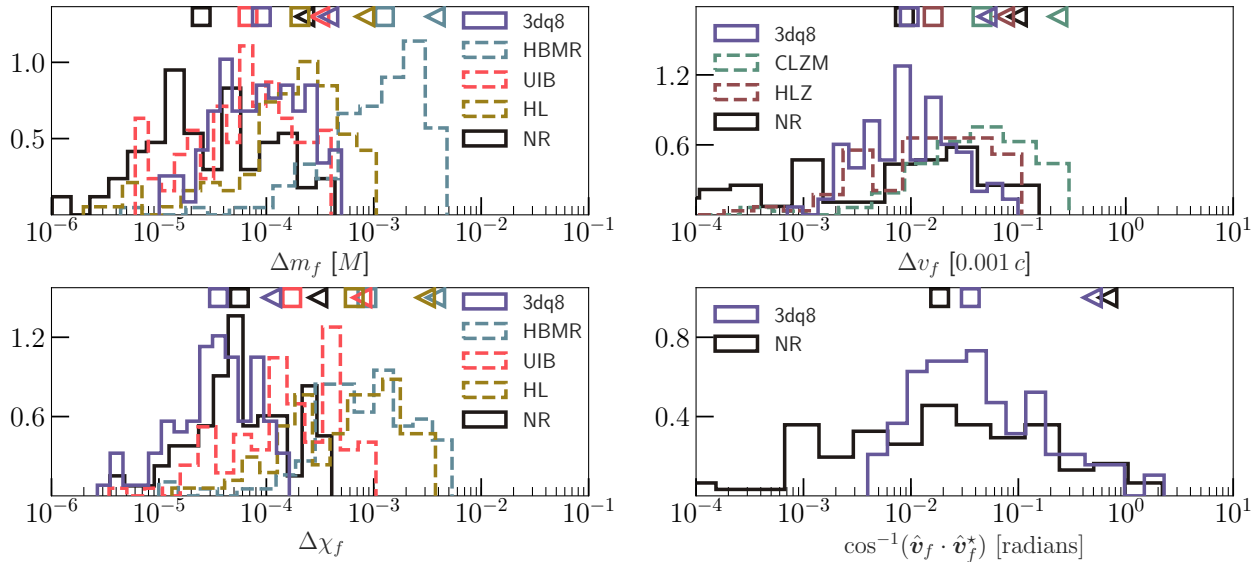


Figure 6.4.1: Errors in predicting remnant mass, spin, kick magnitude, and kick direction for non-precessing binary BHs with mass ratios $q \leq 8$, and spin magnitudes $\chi_1, \chi_2 \leq 0.8$. The direction error is the angle between the predicted vector and a fiducial vector, taken to be the high-resolution NR case and indicated by a \star . The square (triangle) markers indicate median (95^{th} percentile) values. Our model *surfinBH3dq8* is referred to as 3dq8. The black histogram shows the NR resolution error while the dashed histograms show errors for different existing fitting formulae.

6.5 Aligned-spin model

We first present our fit *surfinBH3dq8*, which is trained against 104 aligned-spin simulations [48] with $q \leq 8$ and $-0.8 \leq \chi_{1z}, \chi_{2z} \leq 0.8$. Symmetry implies that

the kick lies in the orbital plane while the final spin is orthogonal to it [54]. We therefore only fit for four quantities: m_f , χ_{fz} , v_{fx} , and v_{fy} .

Figure 6.4.1 shows the out-of-sample errors of *surfinBH3dq8*. Our fits are as accurate as the NR simulations used in the training process. 95th percentile errors lie at $\Delta m_f \sim 4 \times 10^{-4} M$, $\Delta \chi_f \sim 10^{-4}$, and $\Delta v_f \sim 5 \times 10^{-5} c$. The kick direction is predicted with an accuracy of ~ 0.5 radians, which is the inherent accuracy of the NR simulations. Our errors for the remnant mass and kick magnitude are comparable to the most accurate existing fits. On the other hand, for the final spin, our procedure outperforms all other formulae by at least a factor of 5.

6.6 Precessing model

We now present *surfinBH7dq2*, a remnant model trained on 890 simulations [12] of generic, fully precessing BH binaries with mass ratios $q \leq 2$ and spin magnitudes $\chi_1, \chi_2 \leq 0.8$. Out-of-sample errors are shown in Fig. 6.6.1. 95th percentiles are $\sim 5 \times 10^{-4} M$ for mass, $\sim 2 \times 10^{-3}$ for spin magnitude, $\sim 4 \times 10^{-3}$ radians for spin direction, $\sim 4 \times 10^{-4} c$ for kick magnitude, and ~ 0.2 radians for kick direction. As in the aligned-spin case above, our errors are at the same level as the NR resolution error, thus showing that we are not limited by our fitting procedure but rather by the quality of the training dataset. Our fits appear to outperform the NR simulations when estimating the spin direction, which suggests this quantity has not fully converged in the NR runs, and that the difference between the two highest resolution simulations is an overestimate of the NR error in this quantity.

Figure 6.6.1 shows that our procedure to predict remnant mass, spin magnitude, and kick magnitude for precessing systems is more precise than all existing fits by at least an order of magnitude. These existing fits presented significantly lower errors when applied to aligned binaries (cf. Fig. 6.4.1), which suggests that they fail to fully capture precession effects despite the augmentation of Ref. [42]. Some impact of precession effects on the final spin and recoil is expected, since both of these quantities have been found to depend strongly on the in-plane orientations of the spins of the merging BHs [43, 51, 55]. More surprisingly, we find that spin precession significantly affects the energy radiated as well, which was expected to depend mostly on the aligned-spin components via the orbital hang-up effect [56–58].

The largest errors in the kick direction can be of order ~ 1 radian. The bottom-right panel of Fig. 6.6.1 shows the joint distribution of kick magnitude and kick direction

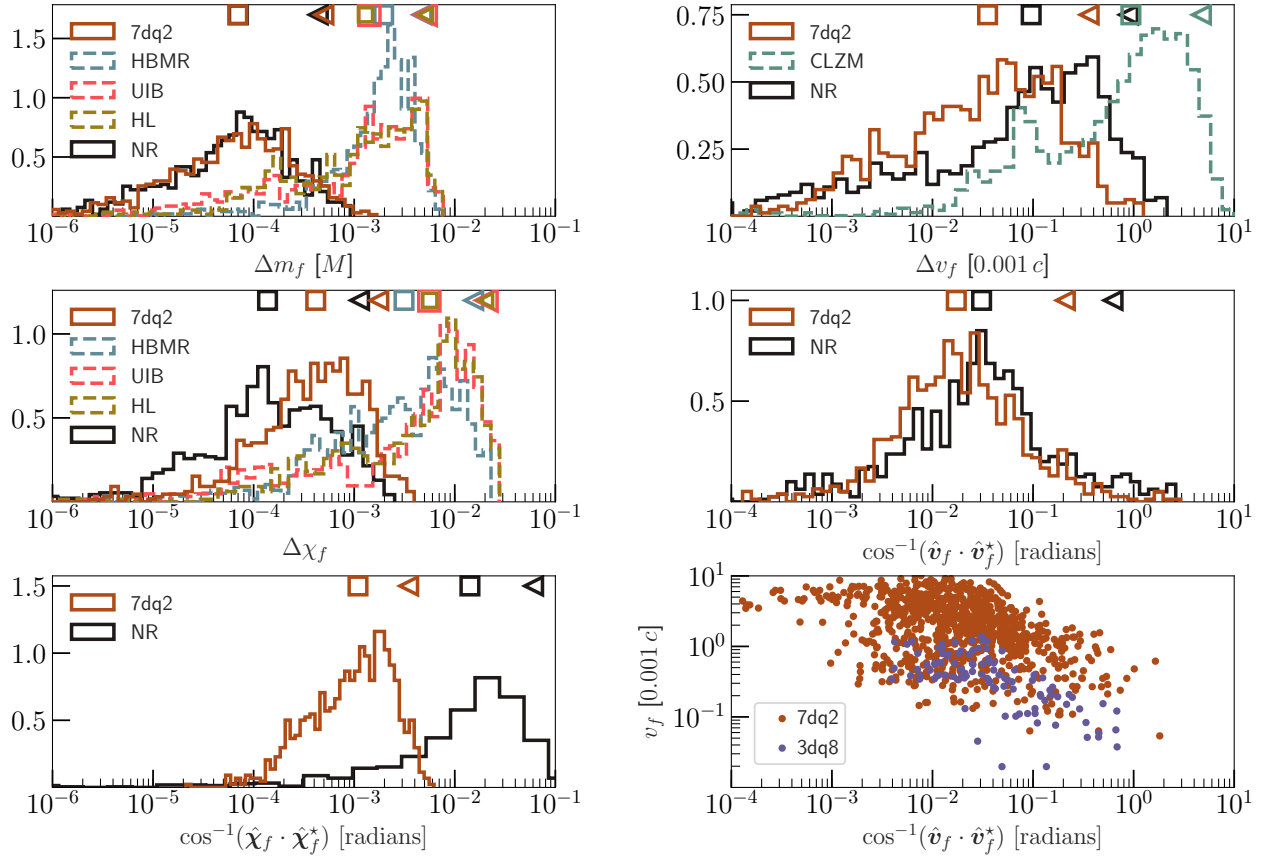


Figure 6.6.1: Errors in predicting the remnant mass, spin magnitude, spin direction, kick magnitude, and kick direction for precessing binary BHs with mass ratios $q \leq 2$, and spin magnitudes $\chi_1, \chi_2 \leq 0.8$. Our model, *surfinBH7dq2* is referred to as 7dq2. The black histogram shows the NR resolution error while the dashed histograms show errors for different existing fitting formulae. In the bottom-right panel we show the distribution of kick magnitude vs. error in kick direction.

error for both *surfinBH7dq2* and *surfinBH3dq8*, showing that errors are larger at low kick magnitudes. Our error in kick direction is below ~ 0.1 radians whenever $v_f \gtrsim 10^{-3}c$.

6.7 Regime of validity

The errors in Fig. 6.6.1 are obtained by evaluating fits using input spins specified at $t = -100M$, i.e., where the GPR interpolation is performed. The input spins can also be specified at earlier times; this case is handled by two additional layers of time evolution. Given the spins at an initial orbital frequency f_0 , we first evolve the spins using a post-Newtonian (PN) approximant — 3.5PN SpinTaylorT4 [59–61]— until the orbital frequency reaches a value of $0.018 \text{ rad}/M$. At this point, we are in the

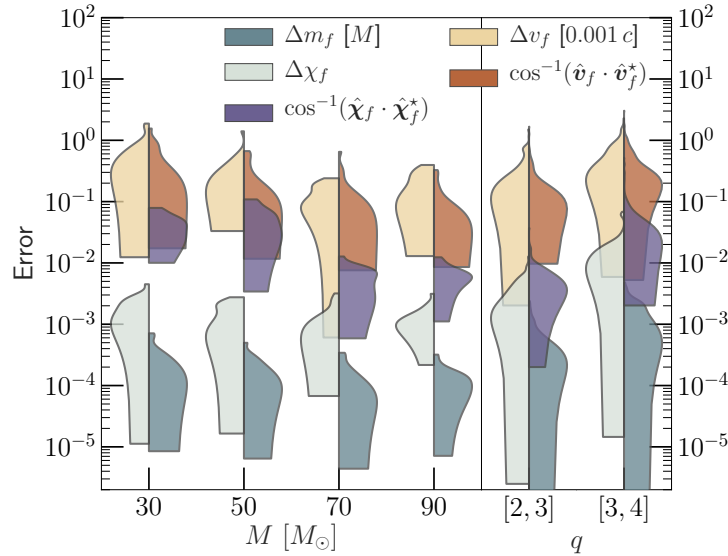


Figure 6.6.2: Left panel: Errors for *surfinBH7dq2* in predicting remnant properties when the spins are specified at an orbital frequency of $f_0 = 10$ Hz, for different total masses. Right panel: Errors for *surfinBH7dq2* when extrapolating to higher mass ratios, with the spins specified at $t = -100M$. The labels on the horizontal axis indicate the range of mass ratios being tested. Note that the distributions in these plots are normalized to have a fixed height, not fixed area.

range of validity of the (more accurate) NRSur7dq2 approximant [12], which we use to evolve the spins until $t = -100M$. Thus, spins can be specified at any given orbital frequency and are evolved consistently before estimating the final BH properties. This is a crucial improvement over previous results, which, being calibrated solely to non-precessing systems, suffer from ambiguities regarding the separation/frequency at which spins are defined.

The left panel of Fig. 6.6.2 shows the errors when the spins are specified at an orbital frequency $f_0 = 10$ Hz. These errors are computed by comparing against 20 long NR simulations [50] with mass ratios $q \leq 2$ and generically oriented spins with magnitudes $\chi_1, \chi_2 \leq 0.5$. None of these simulations were used to train the fits. Longer PN evolutions are needed at lower total masses, and the errors are therefore larger. These errors will decrease with an improved spin evolution procedure. Note, however, that our predictions are still more accurate (and, crucially, unambiguous) than those of existing fitting formulae (cf. Fig. 6.6.1).

Finally, the right panel of Fig. 6.6.2 shows the performance of *surfinBH7dq2* when extrapolating to more extreme mass ratios. We compare against 175 (225) NR simulations [62] with $2 \leq q \leq 3$ ($3 \leq q \leq 4$), and generically oriented spins with magnitudes $\chi_1, \chi_2 \leq 0.8$ specified at $t = -100M$. The error distribution broadens,

but our fits still provide a reasonable estimate of the final remnant properties even far out of the training parameter space. Detailed results on extrapolation accuracy are provided in the supplemental materials [47].

6.8 Conclusion

We have presented two highly accurate surrogate models for the remnant properties of BH binaries. *surfinBH7dq2* (*surfinBH3dq8*) is trained against 890 (104) NR simulations with mass ratios $q \leq 2$ ($q \leq 8$) and precessing (aligned) spins with magnitude $\chi_1, \chi_2 \leq 0.8$. Both models use GPR to provide fits for the remnant mass, spin, and kick velocity (both magnitudes and directions). Our findings are implemented in a public Python module named *surfinBH* (details are provided in the supplemental materials [47]).

For aligned spins, errors in *surfinBH3dq8* are comparable to existing fitting formulae for the final mass and kick magnitude, while the spin is predicted about 5 times more accurately. For precessing systems, errors in *surfinBH7dq2* for final mass, spin magnitude, and kick magnitude are lower than all existing models by at least an order of magnitude. Crucially, our fits are free from ambiguities regarding the time/frequency at which precessing quantities are specified. This is a point of major improvement over previous models, which all fail to fully capture precession effects.

Is this increased accuracy necessary? For current events like GW150914, the estimated error in the remnant properties are $\Delta m_f \sim 0.1M$ and $\Delta \chi_f \sim 0.1$ [40]. These measurements are currently dominated by statistical errors, as the systematics introduced by existing fits used in the analysis are $\Delta m_f \sim 5 \times 10^{-3}M$ and $\Delta \chi_f \sim 2 \times 10^{-2}$ (see 95th percentile values in Fig. 6.6.1). Because statistical errors scale approximately linearly with the detector sensitivity [63], we estimate that systematic errors in current models for χ_f will start dominating over statistical uncertainties at signal-to-noise ratios which are ~ 5 times larger than that of GW150914. This will happen sooner rather than later, with current interferometers expected to reach their design sensitivity in a few years [64], and future instruments already being scheduled [65] or planned [66, 67]. Our fits, being an order of magnitude more accurate (see Fig. 6.6.1), introduce systematic errors which are expected to be relevant only at SNRs ~ 50 times larger than that of GW150914. As shown above, errors are largely dominated by the underlying NR resolution, not by our fitting procedure. The inclusion of self-force evolutions alongside NR in the training dataset might also be exploited to improve extrapolation performance at $q \gg 1$; we leave this to future

work.

Moreover, the GPR methods employed here naturally provide error estimates along with the fitted values (some results are provided in the supplemental material [47]). This constitutes a further key application of our results: when performing, e.g., consistency tests of GR [13, 14], systematic uncertainties introduced by remnant fits can be naturally incorporated into the statistical analysis and marginalized over (cf. Ref. [68] for a similar application of GPR and Refs. [69–73] for other applications to GW science).

As GW astrophysics turns into a mature field, increasingly accurate tools such as those presented here will become crucial to uncover more hidden secrets in this new field of science.

6.9 Acknowledgments

We thank Jonathan Blackman, Stephen Taylor, David Keitel, Anuradha Gupta, and Serguei Ossokine for useful discussions. We made use of the public LIGO Algorithm Library [74] in the evaluation of existing fitting formulae and to perform PN evolutions. We thank Nathan Johnson-McDaniel for useful discussions, comments on the manuscript, and for sharing his code to evaluate the HLZ kick fits. V.V. and F.H. are supported by the Sherman Fairchild Foundation and NSF grants PHY–1404569, PHY–170212, and PHY–1708213 at Caltech. D.G. is supported by NASA through Einstein Postdoctoral Fellowship Grant No. PF6–170152 awarded by the Chandra X-ray Center, which is operated by the Smithsonian Astrophysical Observatory for NASA under Contract NAS8-03060. L.C.S. acknowledges support from NSF grant PHY–1404569 and the Brinson Foundation. H.Z. acknowledges support from the Caltech SURF Program and NSF Grant No. PHY–1404569. Computations were performed on NSF/NCSA Blue Waters under allocation NSF PRAC–1713694 and on the Wheeler cluster at Caltech, which is supported by the Sherman Fairchild Foundation and by Caltech.

APPENDIX

6.A Gaussian process regression

We construct fits in this work using Gaussian process regression (GPR) [46, 75] as implemented in *scikit-learn* [76].

The starting point is a training set of n observations, $\mathcal{TS} = \{(x^i, f(x^i)) | i = 1, \dots, n\}$, where x^i denotes an input vector of dimension D and $f(x^i)$ is the corresponding output. In our case, x is mass ratio and spins of the merging binary, and $f(x)$ is the remnant property we are fitting. Our goal is to use \mathcal{TS} to make predictions for the underlying $f(x)$ at any point x_* that is not in \mathcal{TS} .

A Gaussian process (GP) can be thought of as a probability distribution of functions. More formally, a GP is a collection of random variables, any finite number of which have a joint Gaussian distribution [46]. A GP is completely specified by its mean function $m(x)$ and covariance function $k(x, x')$, i.e. $f(x) \sim \mathcal{GP}(m(x), k(x, x'))$. Consider a prediction set of n_* test inputs and their corresponding outputs (which are unknown): $\mathcal{PS} = \{(x_*^i, f(x_*^i)) | i = 1, \dots, n_*\}$. By the definition of a GP, outputs of \mathcal{TS} and \mathcal{PS} (respectively $\mathbf{f} = \{f(x^i)\}$, $\mathbf{f}_* = \{f(x_*^i)\}$) are related by a joint Gaussian distribution

$$\begin{bmatrix} \mathbf{f} \\ \mathbf{f}_* \end{bmatrix} = \mathcal{N} \left(\mathbf{0}, \begin{bmatrix} K_{xx} & K_{xx_*} \\ K_{x_*x} & K_{x_*x_*} \end{bmatrix} \right), \quad (6.1)$$

where K_{xx_*} denotes the $n \times n_*$ matrix of the covariance $k(x, x_*)$ evaluated at all pairs of training and prediction points, and similarly for the other K matrices.

Eq. (6.1) provides the Bayesian prior distribution for \mathbf{f}_* . The posterior distribution is obtained by restricting this joint prior to contain only those functions which agree with the observed data points, i.e. [46]

$$p(\mathbf{f}_* | \mathcal{TS}) = \mathcal{N} \left(K_{x_*x} K_{xx}^{-1} \mathbf{f}, K_{x_*x_*} - K_{x_*x} K_{xx}^{-1} K_{xx_*} \right). \quad (6.2)$$

The mean of this posterior provides an estimator for $f(x)$ at x_* , while its width is the prediction error.

Finally, one needs to specify the covariance (or kernel) function $k(x, x')$. In this

Letter we implement the following kernel

$$k(x, x') = \sigma_k^2 \exp \left[-\frac{1}{2} \sum_{j=1}^D \left(\frac{x^j - x'^j}{\sigma_j} \right)^2 \right] + \sigma_n^2 \delta_{x, x'}, \quad (6.3)$$

where $\delta_{x, x'}$ is the Kronecker delta. In words, we use a product between a squared exponential kernel and a constant kernel, to which we add a white kernel term to account for additional noise in the training data [46, 76].

GPR fit construction involves determining the $D+2$ hyperparameters (σ_k , σ_n and σ_j) which maximize the marginal likelihood of the training data under the GP prior [46]. Local maxima are avoided by repeating the optimization with 10 different initial guesses, obtained by sampling uniformly in log in the hyperparameter space described below.

Before constructing the GPR fit, we pre-process the training data as follows. We first subtract a linear fit and the mean of the resulting values. Datapoints are then normalized by dividing by the standard deviation of the resulting values. The inverse of these transformations is applied at the time of the fit evaluation.

For each dimension of x , we define Δx^j to be the range of the values of x^j in \mathcal{TS} and consider $\sigma_j \in [0.01 \times \Delta x^j, 10 \times \Delta x^j]$. Larger length scales are unlikely to be relevant and smaller length scales are unlikely to be resolvable. The remaining hyperparameters are sampled in $\sigma_k^2 \in [10^{-2}, 10^2]$ and $\sigma_n^2 \in [10^{-7}, 10^{-2}]$. These choices are meant to be conservative and are based on prior exploration of the typical magnitude and noise level in our pre-processed training data.

6.B Input parameter space

Fits for *surfinBH3dq8* are parameterized using $x = [\log(q), \hat{\chi}, \chi_a]$, where $\hat{\chi}$ is the spin parameter entering the GW phase at leading order [5, 77–79] in the PN expansion,

$$\chi_{\text{eff}} = \frac{q \chi_{1z} + \chi_{2z}}{1 + q}, \quad \eta = \frac{q}{(1 + q)^2}, \quad (6.4)$$

$$\hat{\chi} = \frac{\chi_{\text{eff}} - 38\eta(\chi_{1z} + \chi_{2z})/113}{1 - 76\eta/113}, \quad (6.5)$$

and χ_a is the “anti-symmetric spin”,

$$\chi_a = \frac{1}{2}(\chi_{1z} - \chi_{2z}). \quad (6.6)$$

For *surfinBH7dq2* we use $x = [\log(q), \chi_{1x}, \chi_{1y}, \hat{\chi}, \chi_{2x}, \chi_{2y}, \chi_a]$. Subscripts x, y and z refer to components specified in the coorbital frame at $t = -100M$. We empirically found these parameterizations to perform more accurately than the more intuitive choice $x = [q, \chi_{1x}, \chi_{1y}, \chi_{1z}, \chi_{2x}, \chi_{2y}, \chi_{2z}]$.

In the main text we describe how we evolve spins given at earlier times to $t = -100M$, using PN and NRSur7qd2. Is it worth noting that the NR spins used to train NRSur7qd2 had some additional smoothening filters applied to them (see Eq. 6 in [12]). This introduces additional systematics when evolving spins from times $t < -100M$. We verified that the resulting errors on our fits are subdominant.

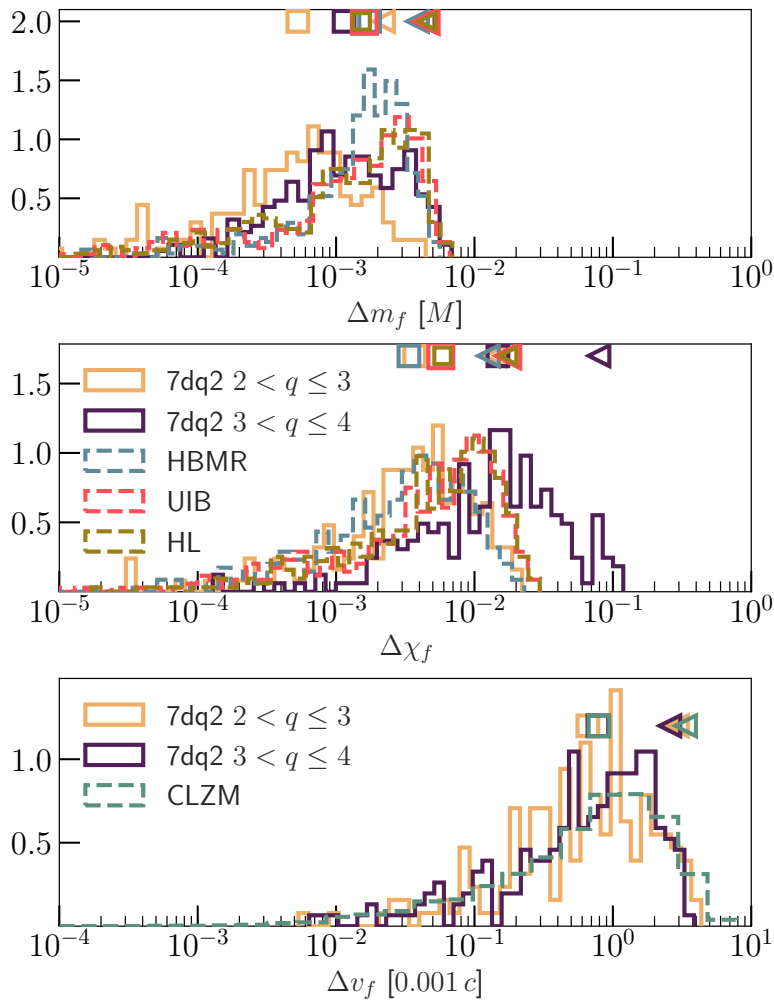


Figure 6.B.1: Errors in *surfinBH7dq2* when extrapolating to higher mass ratios, and the spins are specified at an orbital frequency $f_0 = 10$ Hz, for a total mass $M = 70M_\odot$.

6.C Extrapolation errors

The right panel of Fig. 4 shows the errors in remnant quantities when extrapolating *surfinBH7dq2* to mass ratios beyond its training range ($q \leq 2$). These errors are computed using the spins at $t = -100M$. If the spins are given at earlier times, we expect larger extrapolation errors as this also involves extrapolation of the NRSur7dq2 waveform model (which was also trained in the $q \leq 2$ space). Figure 6.B.1 shows the extrapolation errors when the spins are specified at orbital frequency $f_0 = 10$ Hz for a total mass $M = 70M_\odot$, computed by comparing against the same NR simulations as in Fig. 4. Errors are comparable to or lower than those of existing fits for $q \leq 3$. For $3 < q \leq 4$, our errors for the remnant spin magnitude can become larger, but the remnant mass and kick magnitude remains as accurate as in other fits.

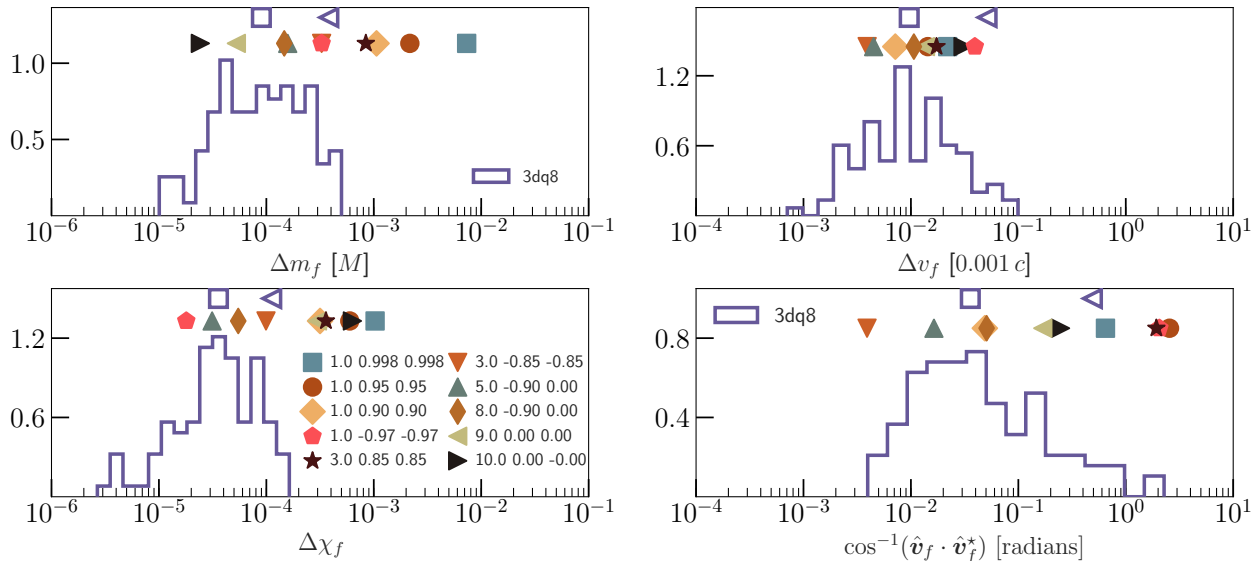


Figure 6.C.1: Errors in predicting the remnant mass, spin, kick magnitude and kick direction for nonprecessing BBH when *surfinBH3dq8* is extrapolated outside of the training region (i.e. $q > 8$ and $\chi_1, \chi_2 > 0.8$). Each solid symbol marks the error of the extrapolated model against a single nonprecessing NR simulation. The legend in the bottom-left panel displays the mass ratio and spin components of the two BHs along the orbital angular momentum direction. Histograms of errors within the training region (from Fig. 2) are reproduced here for comparison. The hollow square (triangle) markers indicate the median (95th percentile) values for those errors.

Figure 6.C.1 shows errors in *surfinBH3dq8* when extrapolated beyond its training space to higher mass ratios and/or spin magnitudes (this figure complements the results shown in Fig. 4 of the main text for *surfinBH7dq2*). Here we used some of the

simulations of [50, 80–83] with $q > 8$ and/or $\chi_1, \chi_2 > 0.8$. Accuracy in the remnant mass degrades noticeably only at high (~ 0.9) co-aligned spins. Errors in final spin become larger at both high spins and extreme mass ratios. For counter-aligned spins, our errors are always comparable to those found within the training region. Errors in kick magnitude and direction appear to be insensitive to extrapolation.

6.D GPR error prediction

As stressed above and in the main body of our *Letter*, GPR naturally associates errors to the estimated quantities. In this Section we test the efficacy of this prediction by comparing the GPR errors against the out-of-sample errors. The GPR errors shown here are evaluated using the same cross-validation data sets used to generate the out-of-sample errors. Therefore, both error estimates are evaluated at points in parameter space where models were not trained.

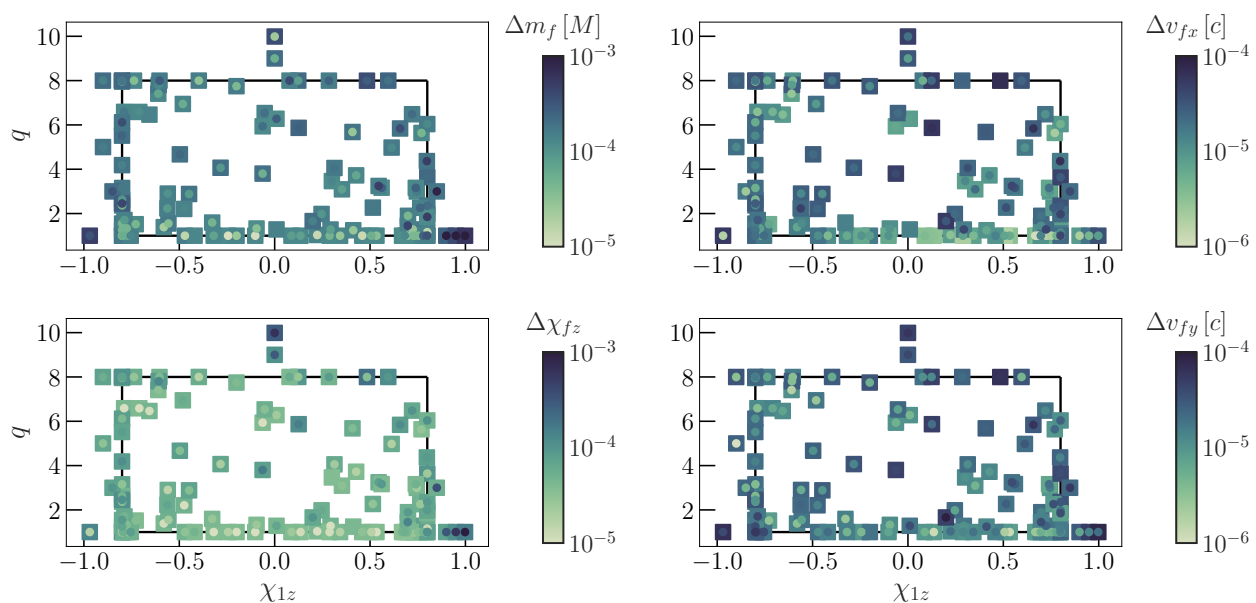


Figure 6.D.1: Prediction errors for remnant mass, spin and kick for the model *surfinBH3dq8* against NR simulations. Two error estimates, as reported on the color scale, are compared: out-of-sample errors marked with circles, and 1σ GPR errors marked with squares. We include cases where *surfinBH3dq8* needs to be extrapolated to higher mass ratios and/or spin magnitudes. The bounds of the training parameter space are indicated as a black rectangle.

Error comparisons for *surfinBH3dq8* and *surfinBH7dq2* are reported in Figs. 6.D.1 and 6.D.2, respectively. While GPR predictions miss some of the features captured

by the “k-fold” cross validations, overall it provides faithful estimates of the fit errors.

6.E Public Python implementation

Our fits are made publicly available through the easy-to-use Python package, *surfinBH* [45]. Our code is compatible with both Python 2 and Python 3. The latest release can be installed from the Python Package Index using

```
pip install surfinBH
```

Python packages *numpy* [84], *scipy* [85], *h5py* [86], *scikit-learn* [76], *lalsuite* [74], and *NRSur7dq2* [12] are specified as dependencies and are automatically installed if missing. *surfinBH* is hosted on GitHub at github.com/vijayvarma392/surfinBH, from which development versions can be installed. Continuous integration is provided by *Travis* [87]

The *surfinBH* module can be imported in Python using

```
import surfinBH
```

Documentation is provided for each submodule of *surfinBH* and can be accessed via Python’s `help()` function. The fit class has to be initialized using, e.g.

```
fit = surfinBH.LoadFits("surfinBH7dq2")
```

Given mass ratio and component spins, the fits and 1σ GPR error estimates of the remnant mass, spin vector and kick vector can be evaluated as follows:

```
q = 1.2
chiA = [0.5, 0.05, 0.3]
chiB = [-0.5, -0.05, 0.1]
mf, mf_err = fit.mf(q, chiA, chiB)
chif, chif_err = fit.chif(q, chiA, chiB)
vf, vf_err = fit.vf(q, chiA, chiB)
```

Both the input spins as well as the remnant spin and kick vectors are assumed to be specified in the coorbital frame at $t = -100M$. Performance of *surfinBH* was tested

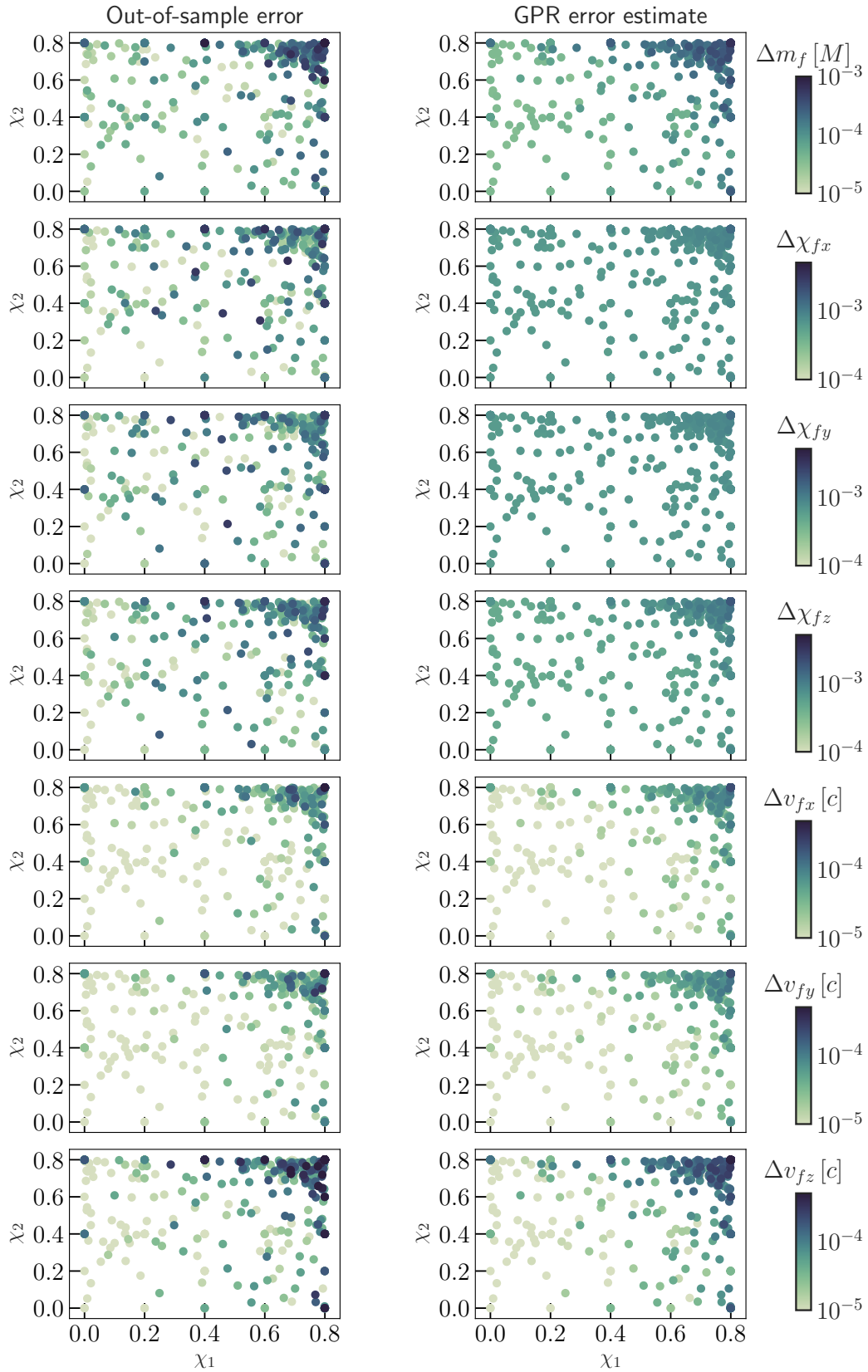


Figure 6.D.2: Comparison between out-of-sample (left), and 1σ GPR (right) errors for *surfnBH7dq2*. The axes show the magnitudes of the component spins, and the color scale indicates the parameter error being plotted.

on a 3.1 GHz Intel Core i5 processor by averaging over 10^3 evaluations at randomly chosen points in parameter space. For *surfinBH7dq2*, evaluation cost of final mass (spin) [kick] is 2.5 ms (7 ms) [7 ms]. For *surfinBH3dq8*, evaluation cost of final mass (spin) [kick] is 0.4 ms (0.4 ms) [0.6 ms].

We also allow specifying an orbital frequency (in units of rad/M), e.g.:

```
omega0 = 5e-3
mf, mf_err = fit.mf(q, chiA, chiB,
                    omega0 = omega0)
chif, chif_err = fit.chif(q, chiA, chiB,
                           omega0 = omega0)
vf, vf_err = fit.vf(q, chiA, chiB,
                    omega0 = omega0)
```

In this case, the component spins, as well as the final remnant spin/kick vectors are specified in the coorbital frame at this orbital frequency. The evaluation costs are larger when specifying an initial orbital frequency since this involves two additional stages of spin evolution. Execution times depend on the initial frequency, the specific PN approximant used and the time step size in the integration routine. For instance, with $\omega_0 = 5e-3$, SpinTaylorT4, and a step size of $0.1M$ the evaluation cost is $\sim 0.5s$ for each of the remnant quantities.

Additional resources are provided in the package installation page [45]. This includes example jupyter notebooks for both models presented in this *Letter*.

References

- [1] W. Israel. “Event horizons in static electrovac space-times”. In: *Communications in Mathematical Physics* 8 (Sept. 1968), pp. 245–260. doi: [10.1007/BF01645859](https://doi.org/10.1007/BF01645859).
- [2] B. Carter. “Axisymmetric Black Hole Has Only Two Degrees of Freedom”. In: *PRL* 26 (Feb. 1971), pp. 331–333. doi: [10.1103/PhysRevLett.26.331](https://doi.org/10.1103/PhysRevLett.26.331).
- [3] M. Heusler. 1996.
- [4] M. Hannam et al. “Simple Model of Complete Precessing Black-Hole-Binary Gravitational Waveforms”. In: *PRL* 113.15, 151101 (Oct. 2014), p. 151101. doi: [10.1103/PhysRevLett.113.151101](https://doi.org/10.1103/PhysRevLett.113.151101). arXiv: [1308.3271](https://arxiv.org/abs/1308.3271) [gr-qc].

- [5] S. Khan et al. “Frequency-domain gravitational waves from nonprecessing black-hole binaries. II. A phenomenological model for the advanced detector era”. In: *PRD* 93.4, 044007 (Feb. 2016), p. 044007. DOI: [10.1103/PhysRevD.93.044007](https://doi.org/10.1103/PhysRevD.93.044007). arXiv: [1508.07253](https://arxiv.org/abs/1508.07253) [gr-qc].
- [6] S. Husa et al. “Frequency-domain gravitational waves from nonprecessing black-hole binaries. I. New numerical waveforms and anatomy of the signal”. In: *PRD* 93.4, 044006 (Feb. 2016), p. 044006. DOI: [10.1103/PhysRevD.93.044006](https://doi.org/10.1103/PhysRevD.93.044006). arXiv: [1508.07250](https://arxiv.org/abs/1508.07250) [gr-qc].
- [7] A. Buonanno et al. “Effective-one-body waveforms calibrated to numerical relativity simulations: Coalescence of nonspinning, equal-mass black holes”. In: *PRD* 79.12, 124028 (June 2009), p. 124028. DOI: [10.1103/PhysRevD.79.124028](https://doi.org/10.1103/PhysRevD.79.124028). arXiv: [0902.0790](https://arxiv.org/abs/0902.0790) [gr-qc].
- [8] A. Bohé et al. “Improved effective-one-body model of spinning, nonprecessing binary black holes for the era of gravitational-wave astrophysics with advanced detectors”. In: *PRD* 95.4, 044028 (Feb. 2017), p. 044028. DOI: [10.1103/PhysRevD.95.044028](https://doi.org/10.1103/PhysRevD.95.044028). arXiv: [1611.03703](https://arxiv.org/abs/1611.03703) [gr-qc].
- [9] S. Babak, A. Taracchini, and A. Buonanno. “Validating the effective-one-body model of spinning, precessing binary black holes against numerical relativity”. In: *PRD* 95.2, 024010 (Jan. 2017), p. 024010. DOI: [10.1103/PhysRevD.95.024010](https://doi.org/10.1103/PhysRevD.95.024010). arXiv: [1607.05661](https://arxiv.org/abs/1607.05661) [gr-qc].
- [10] S. E. Field et al. “Fast Prediction and Evaluation of Gravitational Waveforms Using Surrogate Models”. In: *PRX* 4.3, 031006 (July 2014), p. 031006. DOI: [10.1103/PhysRevX.4.031006](https://doi.org/10.1103/PhysRevX.4.031006). arXiv: [1308.3565](https://arxiv.org/abs/1308.3565) [gr-qc].
- [11] J. Blackman et al. “A Surrogate model of gravitational waveforms from numerical relativity simulations of precessing binary black hole mergers”. In: *PRD* 95.10, 104023 (May 2017), p. 104023. DOI: [10.1103/PhysRevD.95.104023](https://doi.org/10.1103/PhysRevD.95.104023). arXiv: [1701.00550](https://arxiv.org/abs/1701.00550) [gr-qc].
- [12] J. Blackman et al. “Numerical relativity waveform surrogate model for generically precessing binary black hole mergers”. In: *PRD* 96.2, 024058 (July 2017), p. 024058. DOI: [10.1103/PhysRevD.96.024058](https://doi.org/10.1103/PhysRevD.96.024058). arXiv: [1705.07089](https://arxiv.org/abs/1705.07089) [gr-qc].
- [13] A. Ghosh et al. “Testing general relativity using gravitational wave signals from the inspiral, merger and ringdown of binary black holes”. In: *CQG* 35.1, 014002 (Jan. 2018), p. 014002. DOI: [10.1088/1361-6382/aa972e](https://doi.org/10.1088/1361-6382/aa972e). arXiv: [1704.06784](https://arxiv.org/abs/1704.06784) [gr-qc].
- [14] B. P. Abbott et al. “Tests of General Relativity with GW150914”. In: *PRL* 116.22, 221101 (June 2016), p. 221101. DOI: [10.1103/PhysRevLett.116.221101](https://doi.org/10.1103/PhysRevLett.116.221101). arXiv: [1602.03841](https://arxiv.org/abs/1602.03841) [gr-qc].
- [15] F. Pretorius. “Evolution of Binary Black-Hole Spacetimes”. In: *PRL* 95.12, 121101 (Sept. 2005), p. 121101. DOI: [10.1103/PhysRevLett.95.121101](https://doi.org/10.1103/PhysRevLett.95.121101). eprint: [gr-qc/0507014](https://arxiv.org/abs/gr-qc/0507014).

- [16] M. Campanelli et al. “Accurate Evolutions of Orbiting Black-Hole Binaries without Excision”. In: *PRL* 96.11, 111101 (Mar. 2006), p. 111101. DOI: [10.1103/PhysRevLett.96.111101](https://doi.org/10.1103/PhysRevLett.96.111101). eprint: [gr-qc/0511048](https://arxiv.org/abs/gr-qc/0511048).
- [17] M. A. Scheel et al. “High-accuracy waveforms for binary black hole inspiral, merger, and ringdown”. In: *PRD* 79.2, 024003 (Jan. 2009), p. 024003. DOI: [10.1103/PhysRevD.79.024003](https://doi.org/10.1103/PhysRevD.79.024003). arXiv: [0810.1767](https://arxiv.org/abs/0810.1767) [gr-qc].
- [18] F. Herrmann et al. “Binary black holes: Spin dynamics and gravitational recoil”. In: *PRD* 76.8, 084032 (Oct. 2007), p. 084032. DOI: [10.1103/PhysRevD.76.084032](https://doi.org/10.1103/PhysRevD.76.084032). arXiv: [0706.2541](https://arxiv.org/abs/0706.2541) [gr-qc].
- [19] M. Campanelli et al. “Maximum Gravitational Recoil”. In: *PRL* 98.23, 231102 (June 2007), p. 231102. DOI: [10.1103/PhysRevLett.98.231102](https://doi.org/10.1103/PhysRevLett.98.231102). eprint: [gr-qc/0702133](https://arxiv.org/abs/gr-qc/0702133).
- [20] J. A. González et al. “Supermassive Recoil Velocities for Binary Black-Hole Mergers with Antialigned Spins”. In: *PRL* 98.23, 231101 (June 2007), p. 231101. DOI: [10.1103/PhysRevLett.98.231101](https://doi.org/10.1103/PhysRevLett.98.231101). eprint: [gr-qc/0702052](https://arxiv.org/abs/gr-qc/0702052).
- [21] J. A. González et al. “Maximum Kick from Nonspinning Black-Hole Binary Inspiral”. In: *PRL* 98.9, 091101 (Mar. 2007), p. 091101. DOI: [10.1103/PhysRevLett.98.091101](https://doi.org/10.1103/PhysRevLett.98.091101). eprint: [gr-qc/0610154](https://arxiv.org/abs/gr-qc/0610154).
- [22] M. Campanelli et al. “Large Merger Recoils and Spin Flips from Generic Black Hole Binaries”. In: *ApJ* 659 (Apr. 2007), pp. L5–L8. DOI: [10.1086/516712](https://doi.org/10.1086/516712). eprint: [gr-qc/0701164](https://arxiv.org/abs/gr-qc/0701164).
- [23] L. Rezzolla et al. “Final spin from the coalescence of two black holes”. In: *PRD* 78.4, 044002 (Aug. 2008), p. 044002. DOI: [10.1103/PhysRevD.78.044002](https://doi.org/10.1103/PhysRevD.78.044002). arXiv: [0712.3541](https://arxiv.org/abs/0712.3541) [gr-qc].
- [24] L. Rezzolla et al. “The Final Spin from the Coalescence of Aligned-Spin Black Hole Binaries”. In: *ApJ* 674 (Feb. 2008), p. L29. DOI: [10.1086/528935](https://doi.org/10.1086/528935). arXiv: [0710.3345](https://arxiv.org/abs/0710.3345) [gr-qc].
- [25] M. Kesden. “Can binary mergers produce maximally spinning black holes?” In: *PRD* 78.8, 084030 (Oct. 2008), p. 084030. DOI: [10.1103/PhysRevD.78.084030](https://doi.org/10.1103/PhysRevD.78.084030). arXiv: [0807.3043](https://arxiv.org/abs/0807.3043).
- [26] W. Tichy and P. Marronetti. “Final mass and spin of black-hole mergers”. In: *PRD* 78.8, 081501 (Oct. 2008), p. 081501. DOI: [10.1103/PhysRevD.78.081501](https://doi.org/10.1103/PhysRevD.78.081501). arXiv: [0807.2985](https://arxiv.org/abs/0807.2985) [gr-qc].
- [27] C. O. Lousto and Y. Zlochower. “Further insight into gravitational recoil”. In: *PRD* 77.4, 044028 (Feb. 2008), p. 044028. DOI: [10.1103/PhysRevD.77.044028](https://doi.org/10.1103/PhysRevD.77.044028). arXiv: [0708.4048](https://arxiv.org/abs/0708.4048) [gr-qc].
- [28] E. Barausse and L. Rezzolla. “Predicting the Direction of the Final Spin from the Coalescence of Two Black Holes”. In: *ApJ* 704 (Oct. 2009), pp. L40–L44. DOI: [10.1088/0004-637X/704/1/L40](https://doi.org/10.1088/0004-637X/704/1/L40). arXiv: [0904.2577](https://arxiv.org/abs/0904.2577) [gr-qc].

- [29] Y. Pan et al. “Inspirals-mergers-ringdown multipolar waveforms of nonspinning black-hole binaries using the effective-one-body formalism”. In: *PRD* 84.12, 124052 (Dec. 2011), p. 124052. DOI: [10.1103/PhysRevD.84.124052](https://doi.org/10.1103/PhysRevD.84.124052). arXiv: [1106.1021](https://arxiv.org/abs/1106.1021) [gr-qc].
- [30] E. Barausse, V. Morozova, and L. Rezzolla. “On the Mass Radiated by Coalescing Black Hole Binaries”. In: *ApJ* 758, 63 (Oct. 2012). [Erratum: *ApJ*, 2014, 786, 76], p. 63. DOI: [10.1088/0004-637X/758/1/63](https://doi.org/10.1088/0004-637X/758/1/63). arXiv: [1206.3803](https://arxiv.org/abs/1206.3803) [gr-qc].
- [31] C. O. Lousto et al. “Gravitational recoil from accretion-aligned black-hole binaries”. In: *PRD* 85.8, 084015 (Apr. 2012), p. 084015. DOI: [10.1103/PhysRevD.85.084015](https://doi.org/10.1103/PhysRevD.85.084015). arXiv: [1201.1923](https://arxiv.org/abs/1201.1923) [gr-qc].
- [32] C. O. Lousto and Y. Zlochower. “Nonlinear gravitational recoil from the mergers of precessing black-hole binaries”. In: *PRD* 87.8, 084027 (Apr. 2013), p. 084027. DOI: [10.1103/PhysRevD.87.084027](https://doi.org/10.1103/PhysRevD.87.084027). arXiv: [1211.7099](https://arxiv.org/abs/1211.7099) [gr-qc].
- [33] J. Healy, C. O. Lousto, and Y. Zlochower. “Remnant mass, spin, and recoil from spin aligned black-hole binaries”. In: *PRD* 90.10, 104004 (Nov. 2014), p. 104004. DOI: [10.1103/PhysRevD.90.104004](https://doi.org/10.1103/PhysRevD.90.104004). arXiv: [1406.7295](https://arxiv.org/abs/1406.7295) [gr-qc].
- [34] Y. Zlochower and C. O. Lousto. “Modeling the remnant mass, spin, and recoil from unequal-mass, precessing black-hole binaries: The intermediate mass ratio regime”. In: *PRD* 92.2, 024022 (July 2015), p. 024022. DOI: [10.1103/PhysRevD.92.024022](https://doi.org/10.1103/PhysRevD.92.024022). arXiv: [1503.07536](https://arxiv.org/abs/1503.07536) [gr-qc].
- [35] F. Hofmann, E. Barausse, and L. Rezzolla. “The Final Spin from Binary Black Holes in Quasi-circular Orbits”. In: *ApJ* 825, L19 (July 2016), p. L19. DOI: [10.3847/2041-8205/825/2/L19](https://doi.org/10.3847/2041-8205/825/2/L19). arXiv: [1605.01938](https://arxiv.org/abs/1605.01938) [gr-qc].
- [36] D. Gerosa and M. Kesden. “precession: Dynamics of spinning black-hole binaries with python”. In: *PRD* 93.12, 124066 (June 2016), p. 124066. DOI: [10.1103/PhysRevD.93.124066](https://doi.org/10.1103/PhysRevD.93.124066). arXiv: [1605.01067](https://arxiv.org/abs/1605.01067) [astro-ph.HE].
- [37] X. Jiménez-Forteza et al. “Hierarchical data-driven approach to fitting numerical relativity data for nonprecessing binary black holes with an application to final spin and radiated energy”. In: *PRD* 95.6, 064024 (Mar. 2017), p. 064024. DOI: [10.1103/PhysRevD.95.064024](https://doi.org/10.1103/PhysRevD.95.064024). arXiv: [1611.00332](https://arxiv.org/abs/1611.00332) [gr-qc].
- [38] J. Healy and C. O. Lousto. “Remnant of binary black-hole mergers: New simulations and peak luminosity studies”. In: *PRD* 95.2, 024037 (Jan. 2017), p. 024037. DOI: [10.1103/PhysRevD.95.024037](https://doi.org/10.1103/PhysRevD.95.024037). arXiv: [1610.09713](https://arxiv.org/abs/1610.09713) [gr-qc].

- [39] J. Healy and C. O. Lousto. “Hangup effect in unequal mass binary black hole mergers and further studies of their gravitational radiation and remnant properties”. In: *PRD* 97.8, 084002 (Apr. 2018), p. 084002. DOI: [10.1103/PhysRevD.97.084002](https://doi.org/10.1103/PhysRevD.97.084002). arXiv: [1801.08162](https://arxiv.org/abs/1801.08162) [gr-qc].
- [40] B. P. Abbott et al. “Binary Black Hole Mergers in the First Advanced LIGO Observing Run”. In: *PRX* 6.4, 041015 (Oct. 2016), p. 041015. DOI: [10.1103/PhysRevX.6.041015](https://doi.org/10.1103/PhysRevX.6.041015). arXiv: [1606.04856](https://arxiv.org/abs/1606.04856) [gr-qc].
- [41] B. P. Abbott et al. “GW170104: Observation of a 50-Solar-Mass Binary Black Hole Coalescence at Redshift 0.2”. In: *PRL* 118.22, 221101 (June 2017). [Erratum PRL, 2018, 21, 129901], p. 221101. DOI: [10.1103/PhysRevLett.118.221101](https://doi.org/10.1103/PhysRevLett.118.221101). arXiv: [1706.01812](https://arxiv.org/abs/1706.01812) [gr-qc].
- [42] N. K. Johnson-McDaniel et al. In: (). dcc.ligo.org/T1600168/public.
- [43] M. Kesden, U. Sperhake, and E. Berti. “Final spins from the merger of precessing binary black holes”. In: *PRD* 81.8, 084054 (Apr. 2010), p. 084054. DOI: [10.1103/PhysRevD.81.084054](https://doi.org/10.1103/PhysRevD.81.084054). arXiv: [1002.2643](https://arxiv.org/abs/1002.2643) [astro-ph.GA].
- [44] L. E. Kidder et al. “Black hole evolution by spectral methods”. In: *PRD* 62.8, 084032 (Oct. 2000), p. 084032. DOI: [10.1103/PhysRevD.62.084032](https://doi.org/10.1103/PhysRevD.62.084032). eprint: [gr-qc/0005056](https://arxiv.org/abs/gr-qc/0005056).
- [45] V. Varma et al. “surfinBH”. In: (). pypi.org/project/surfinBH, doi.org/10.5281/zenodo.1418525.
- [46] C. E. Rasmussen and C. K. I. Williams. *Gaussian Processes for Machine Learning*. 2006.
- [47] See Supplemental Material [here](#), for details of the GPR fitting method, more detailed exploration of extrapolation errors, tests on the efficacy of GPR’s error prediction, and details of the public Python implementation. This further includes Refs. [75– 87].
- [48] Vijay Varma et al. “Surrogate model of hybridized numerical relativity binary black hole waveforms”. In: (2018). DOI: [10.1103/PhysRevD.99.064045](https://doi.org/10.1103/PhysRevD.99.064045). arXiv: [1812.07865](https://arxiv.org/abs/1812.07865) [gr-qc].
- [49] G. Lovelace et al. “Binary-black-hole initial data with nearly extremal spins”. In: *PRD* 78.8, 084017 (Oct. 2008), p. 084017. DOI: [10.1103/PhysRevD.78.084017](https://doi.org/10.1103/PhysRevD.78.084017). arXiv: [0805.4192](https://arxiv.org/abs/0805.4192) [gr-qc].
- [50] M. Boyle et al. In: (2018). in preparation.
- [51] D. Gerosa, F. Hébert, and L. C. Stein. “Black-hole kicks from numerical-relativity surrogate models”. In: *PRD* 97.10, 104049 (May 2018), p. 104049. DOI: [10.1103/PhysRevD.97.104049](https://doi.org/10.1103/PhysRevD.97.104049). arXiv: [1802.04276](https://arxiv.org/abs/1802.04276) [gr-qc].
- [52] M. Ruiz et al. “Multiple expansions for energy and momenta carried by gravitational waves”. In: *General Relativity and Gravitation* 40 (Aug. 2008), pp. 1705–1729. DOI: [10.1007/s10714-007-0570-8](https://doi.org/10.1007/s10714-007-0570-8). arXiv: [0707.4654](https://arxiv.org/abs/0707.4654) [gr-qc].

- [53] M. Boyle and A. H. Mroué. “Extrapolating gravitational-wave data from numerical simulations”. In: *PRD* 80.12, 124045 (Dec. 2009), p. 124045. DOI: [10.1103/PhysRevD.80.124045](https://doi.org/10.1103/PhysRevD.80.124045). arXiv: [0905.3177](https://arxiv.org/abs/0905.3177) [gr-qc].
- [54] L. Boyle, M. Kesden, and S. Nissanke. “Binary Black-Hole Merger: Symmetry and the Spin Expansion”. In: *PRL* 100.15, 151101 (Apr. 2008), p. 151101. DOI: [10.1103/PhysRevLett.100.151101](https://doi.org/10.1103/PhysRevLett.100.151101). arXiv: [0709.0299](https://arxiv.org/abs/0709.0299) [gr-qc].
- [55] E. Berti, M. Kesden, and U. Sperhake. “Effects of post-Newtonian spin alignment on the distribution of black-hole recoils”. In: *PRD* 85.12, 124049 (June 2012), p. 124049. DOI: [10.1103/PhysRevD.85.124049](https://doi.org/10.1103/PhysRevD.85.124049). arXiv: [1203.2920](https://arxiv.org/abs/1203.2920) [astro-ph.HE].
- [56] M. Campanelli, C. O. Lousto, and Y. Zlochower. “Spinning-black-hole binaries: The orbital hang-up”. In: *PRD* 74.4, 041501 (Aug. 2006), p. 041501. DOI: [10.1103/PhysRevD.74.041501](https://doi.org/10.1103/PhysRevD.74.041501). eprint: [gr-qc/0604012](https://arxiv.org/abs/gr-qc/0604012).
- [57] C. O. Lousto and Y. Zlochower. “Where angular momentum goes in a precessing black-hole binary”. In: *PRD* 89.2, 021501 (Jan. 2014), p. 021501. DOI: [10.1103/PhysRevD.89.021501](https://doi.org/10.1103/PhysRevD.89.021501). arXiv: [1307.6237](https://arxiv.org/abs/1307.6237) [gr-qc].
- [58] M. A. Scheel et al. “Improved methods for simulating nearly extremal binary black holes”. In: *CQG* 32.10, 105009 (May 2015), p. 105009. DOI: [10.1088/0264-9381/32/10/105009](https://doi.org/10.1088/0264-9381/32/10/105009). arXiv: [1412.1803](https://arxiv.org/abs/1412.1803) [gr-qc].
- [59] A. Buonanno, Y. Chen, and M. Vallisneri. “Detecting gravitational waves from precessing binaries of spinning compact objects: Adiabatic limit”. In: *PRD* 67.10, 104025 (May 2003), p. 104025. DOI: [10.1103/PhysRevD.67.104025](https://doi.org/10.1103/PhysRevD.67.104025). eprint: [gr-qc/0211087](https://arxiv.org/abs/gr-qc/0211087).
- [60] M. Boyle et al. “High-accuracy comparison of numerical relativity simulations with post-Newtonian expansions”. In: *PRD* 76.12, 124038 (Dec. 2007), p. 124038. DOI: [10.1103/PhysRevD.76.124038](https://doi.org/10.1103/PhysRevD.76.124038). arXiv: [0710.0158](https://arxiv.org/abs/0710.0158) [gr-qc].
- [61] S. Ossokine et al. “Comparing post-Newtonian and numerical relativity precession dynamics”. In: *PRD* 92.10, 104028 (Nov. 2015), p. 104028. DOI: [10.1103/PhysRevD.92.104028](https://doi.org/10.1103/PhysRevD.92.104028). arXiv: [1502.01747](https://arxiv.org/abs/1502.01747) [gr-qc].
- [62] V. Varma, S. Field, M. A. Scheel, et al. “A Numerical Relativity Surrogate Waveform Model for Generically Precessing High Mass-ratio Binary Black Hole Mergers”. In: (2019). in preparation.
- [63] M. Vallisneri. “Use and abuse of the Fisher information matrix in the assessment of gravitational-wave parameter-estimation prospects”. In: *PRD* 77.4, 042001 (Feb. 2008), p. 042001. DOI: [10.1103/PhysRevD.77.042001](https://doi.org/10.1103/PhysRevD.77.042001). eprint: [gr-qc/0703086](https://arxiv.org/abs/gr-qc/0703086).

- [64] B. P. Abbott et al. “Prospects for observing and localizing gravitational-wave transients with Advanced LIGO, Advanced Virgo and KAGRA”. In: *LRR* 21, 3 (Apr. 2018), p. 3. doi: [10.1007/s41114-018-0012-9](https://doi.org/10.1007/s41114-018-0012-9). arXiv: [1304.0670](https://arxiv.org/abs/1304.0670) [gr-qc].
- [65] P. Amaro-Seoane et al. “Laser Interferometer Space Antenna”. In: (Feb. 2017). arXiv: [1702.00786](https://arxiv.org/abs/1702.00786) [astro-ph.IM].
- [66] M. Punturo et al. “The Einstein Telescope: a third-generation gravitational wave observatory”. In: *CQG* 27.19, 194002 (Oct. 2010), p. 194002. doi: [10.1088/0264-9381/27/19/194002](https://doi.org/10.1088/0264-9381/27/19/194002).
- [67] B. P. Abbott et al. “Exploring the sensitivity of next generation gravitational wave detectors”. In: *CQG* 34.4, 044001 (Feb. 2017), p. 044001. doi: [10.1088/1361-6382/aa51f4](https://doi.org/10.1088/1361-6382/aa51f4). arXiv: [1607.08697](https://arxiv.org/abs/1607.08697) [astro-ph.IM].
- [68] C. Cahillane et al. “Calibration uncertainty for Advanced LIGO’s first and second observing runs”. In: *PRD* 96.10, 102001 (Nov. 2017), p. 102001. doi: [10.1103/PhysRevD.96.102001](https://doi.org/10.1103/PhysRevD.96.102001). arXiv: [1708.03023](https://arxiv.org/abs/1708.03023) [astro-ph.IM].
- [69] C. J. Moore and J. R. Gair. “Novel Method for Incorporating Model Uncertainties into Gravitational Wave Parameter Estimates”. In: *Physical Review Letters* 113.25, 251101 (Dec. 2014), p. 251101. doi: [10.1103/PhysRevLett.113.251101](https://doi.org/10.1103/PhysRevLett.113.251101). arXiv: [1412.3657](https://arxiv.org/abs/1412.3657) [gr-qc].
- [70] C. J. Moore et al. “Improving gravitational-wave parameter estimation using Gaussian process regression”. In: *PRD* 93.6, 064001 (Mar. 2016), p. 064001. doi: [10.1103/PhysRevD.93.064001](https://doi.org/10.1103/PhysRevD.93.064001). arXiv: [1509.04066](https://arxiv.org/abs/1509.04066) [gr-qc].
- [71] Z. Doctor et al. “Statistical gravitational waveform models: What to simulate next?” In: *PRD* 96.12, 123011 (Dec. 2017), p. 123011. doi: [10.1103/PhysRevD.96.123011](https://doi.org/10.1103/PhysRevD.96.123011). arXiv: [1706.05408](https://arxiv.org/abs/1706.05408) [astro-ph.HE].
- [72] E. A. Huerta et al. “Eccentric, nonspinning, inspiral, Gaussian-process merger approximant for the detection and characterization of eccentric binary black hole mergers”. In: *PRD* 97.2, 024031 (Jan. 2018), p. 024031. doi: [10.1103/PhysRevD.97.024031](https://doi.org/10.1103/PhysRevD.97.024031). arXiv: [1711.06276](https://arxiv.org/abs/1711.06276) [gr-qc].
- [73] S. R. Taylor and D. Gerosa. “Mining Gravitational-wave Catalogs To Understand Binary Stellar Evolution: A New Hierarchical Bayesian Framework”. In: *PRD* 98 (June 2018), p. 083017. doi: [10.1103/PhysRevD.98.083017](https://doi.org/10.1103/PhysRevD.98.083017). arXiv: [1806.08365](https://arxiv.org/abs/1806.08365) [astro-ph.HE].
- [74] *LSC Algorithms Library*. URL: <https://www.lsc-group.phys.uwm.edu/daswg/projects/lalsuite.html>.
- [75] D. J. C. Mackay. *Information Theory, Inference and Learning Algorithms*. Oct. 2003, p. 640.
- [76] F. Pedregosa et al. “Scikit-learn: Machine Learning in Python”. In: *Journal of Machine Learning Research* 12 (Jan. 2012), pp. 2825–2830. eprint: [1201.0490](https://arxiv.org/abs/1201.0490).

- [77] P. Ajith. “Addressing the spin question in gravitational-wave searches: Waveform templates for inspiralling compact binaries with nonprecessing spins”. In: *PRD* 84.8, 084037 (Oct. 2011), p. 084037. DOI: [10.1103/PhysRevD.84.084037](https://doi.org/10.1103/PhysRevD.84.084037). arXiv: [1107.1267](https://arxiv.org/abs/1107.1267) [gr-qc].
- [78] C. Cutler and É. E. Flanagan. “Gravitational waves from merging compact binaries: How accurately can one extract the binary’s parameters from the inspiral waveform\?” In: *PRD* 49 (Mar. 1994), pp. 2658–2697. DOI: [10.1103/PhysRevD.49.2658](https://doi.org/10.1103/PhysRevD.49.2658). eprint: [gr-qc/9402014](https://arxiv.org/abs/gr-qc/9402014).
- [79] E. Poisson and C. M. Will. “Gravitational waves from inspiraling compact binaries: Parameter estimation using second-post-Newtonian waveforms”. In: *PRD* 52 (July 1995), pp. 848–855. DOI: [10.1103/PhysRevD.52.848](https://doi.org/10.1103/PhysRevD.52.848). eprint: [gr-qc/9502040](https://arxiv.org/abs/gr-qc/9502040).
- [80] A. H. Mroué et al. “Catalog of 174 Binary Black Hole Simulations for Gravitational Wave Astronomy”. In: *PRL* 111.24, 241104 (Dec. 2013), p. 241104. DOI: [10.1103/PhysRevLett.111.241104](https://doi.org/10.1103/PhysRevLett.111.241104). arXiv: [1304.6077](https://arxiv.org/abs/1304.6077) [gr-qc].
- [81] P. Kumar et al. “Accuracy and precision of gravitational-wave models of inspiraling neutron star-black hole binaries with spin: Comparison with matter-free numerical relativity in the low-frequency regime”. In: *PRD* 92.10, 102001 (Nov. 2015), p. 102001. DOI: [10.1103/PhysRevD.92.102001](https://doi.org/10.1103/PhysRevD.92.102001). arXiv: [1507.00103](https://arxiv.org/abs/1507.00103) [gr-qc].
- [82] J. Blackman et al. “Fast and Accurate Prediction of Numerical Relativity Waveforms from Binary Black Hole Coalescences Using Surrogate Models”. In: *PRL* 115.12, 121102 (Sept. 2015), p. 121102. DOI: [10.1103/PhysRevLett.115.121102](https://doi.org/10.1103/PhysRevLett.115.121102). arXiv: [1502.07758](https://arxiv.org/abs/1502.07758) [gr-qc].
- [83] T. Chu et al. “On the accuracy and precision of numerical waveforms: effect of waveform extraction methodology”. In: *CQG* 33.16, 165001 (Aug. 2016), p. 165001. DOI: [10.1088/0264-9381/33/16/165001](https://doi.org/10.1088/0264-9381/33/16/165001). arXiv: [1512.06800](https://arxiv.org/abs/1512.06800) [gr-qc].
- [84] S. van der Walt, S.C. Colbert, and G. Varoquaux. “The NumPy Array: A Structure for Efficient Numerical Computation”. In: *Computing in Science Engineering* 13.2 (Mar. 2011), pp. 22–30. ISSN: 1521-9615. DOI: [10.1109/MCSE.2011.37](https://doi.org/10.1109/MCSE.2011.37).
- [85] Eric Jones, Travis Oliphant, Pearu Peterson, et al. *SciPy: Open source scientific tools for Python*. <http://www.scipy.org/>. 2001–.
- [86] A. Collette. *Python and HDF5*. O’Reilly, 2013.
- [87] Travis Continuous Integration. In: (). travis-ci.org.

SURROGATE MODELS FOR PRECESSING BINARY BLACK HOLE SIMULATIONS WITH UNEQUAL MASSES

Vijay Varma, Scott E. Field, Mark A. Scheel, Jonathan Blackman, Davide Gerosa, Leo Stein, Lawrence E. Kidder, and Harald P. Pfeiffer. [arxiv:1905.09300](https://arxiv.org/abs/1905.09300).

7.1 Executives summary

Surrogate models are capable of accurately, yet cheaply reproducing numerical relativity simulations. However, previous surrogate models of precessing binary black holes have been restricted to nearly equal masses due to unavailability of numerical simulations. This Chapter presents extensions of these models to more generic mass ratios. These models are more accurate than existing models by about an order of magnitude.

7.2 Abstract

Only numerical relativity simulations can capture the full complexities of binary black hole mergers. These simulations, however, are prohibitively expensive for direct data analysis applications such as parameter estimation. We present two new fast and accurate surrogate models for the outputs of these simulations: the first model, NRSur7dq4, predicts the gravitational waveform and the second model, surfinBH7dq4, predicts the properties of the remnant black hole. These models extend previous 7-dimensional, non-eccentric precessing models to higher mass ratios, and have been trained against 1528 simulations with mass ratios $q \leq 4$ and spin magnitudes $\chi_1, \chi_2 \leq 0.8$, with generic spin directions. The waveform model, NRSur7dq4, which begins about 20 orbits before merger, includes all $\ell \leq 4$ spin-weighted spherical harmonic modes, as well as the precession frame dynamics and spin evolution of the black holes. The final black hole model, surfinBH7dq4, models the mass, spin, and recoil kick velocity of the remnant black hole. In their regime of validity, both models are shown to be more accurate than existing models by at least an order of magnitude, with errors comparable to the estimated errors in the numerical relativity simulations.

7.3 Introduction

As the LIGO [1] and Virgo [2] detectors reach their design sensitivity, gravitational wave (GW) detections [3–9] are becoming routine [10, 11]. To maximize the science output of the data collected by the network of detectors, it is crucial to accurately model the source of the GWs. Among the most important sources for these detectors are binary black hole (BBH) systems, in which two black holes (BHs) lose energy through GWs, causing them to inspiral and eventually merge.

Numerical relativity (NR) simulations are necessary to accurately model the late inspiral and merger stages of the BBH evolution. These simulations accurately solve Einstein’s equations to predict the evolution of the BBH spacetime. The most important outputs of NR simulations are the gravitational waveform and the mass, spin, and recoil kick velocity of the remnant BH left after the merger.

For interpreting detected signals, model waveforms are used to compare with detector data and infer the properties of the source [12–14]. The mass and spin of the remnant determine the black hole ringdown frequencies, which are used in testing general relativity [15–17]. In addition, the recoil kick is astrophysically important because it can cause the remnant BH to be ejected from its host galaxy [18–20].

Unfortunately, NR simulations are too expensive to be directly used in data analysis applications and incorporated into astrophysical models. As a result, several approximate models that are much faster to evaluate have been developed for both waveforms [21–31] and remnant properties [18, 19, 32–50]. These models typically assume an underlying phenomenology based on physical motivations, and calibrate any remaining free parameters to NR simulations.

Among BBHs, systems with BH spins that are misaligned with respect to the orbital angular momentum are complicated to model analytically or semi-analytically. For these systems, the spins interact with both the orbital angular momentum and each other, causing the system to precess about the direction of the total angular momentum [51]. This precession is imprinted on the waveform as characteristic modulations in the amplitude and frequency of the GWs, and can be used to extract information about the spins of the source. One important application of the extracted spins is to distinguish between formation channels of BBHs [52–55].

The precessing BBH problem for quasicircular orbits is parametrized by seven parameters: the mass ratio $q = m_1/m_2 \geq 1$ and two spin vectors $\chi_{1,2}$, where the index 1 (2) refers to the heavier (lighter) BH. The total mass scales out of the

problem and does not constitute an additional parameter for modeling. The surrogate models NRSur7dq2 [56] for the gravitational waveform, and surfinBH7dq2 [57] for the remnant properties, were the first to model the 7-dimensional space of generically precessing BBH systems, albeit restricted to mass ratios $q \leq 2$, and dimensionless spin magnitudes $\chi_{1,2} \leq 0.8$. Trained directly against numerical simulations, these models do not need to introduce additional assumptions about the underlying phenomenology of the waveform or remnant properties that necessarily introduces some systematic error. Through cross-validation studies, it was shown that both these models achieve accuracies comparable to the numerical simulations themselves [56, 57], and as a result, are the most accurate models currently available for precessing systems, within their parameter space of validity.

In this paper, we present extensions of the above surrogate models to larger mass ratios. Our new surrogate models are called NRSur7dq4 and surfinBH7dq4, for the gravitational waveform and remnant properties, respectively. They are trained against 1528 precessing NR simulations with mass ratios $q \leq 4$, spin magnitudes $\chi_1, \chi_2 \leq 0.8$, and generic spin directions.

The rest of the paper is organized as follows. Section 7.4 covers some preliminaries to set up the modeling problem for precessing BBH systems. Section 7.5 describes the training simulations. Sec. 7.6 describes the NRSur7dq4 waveform surrogate model. Section 7.7 describes the surfinBH7dq4 remnant properties surrogate model. Section 7.8 compares these models against NR simulations to assess their accuracy. Finally, Sec. 7.9 presents some concluding remarks. In App. 7.A we examine how accurate these models are when extrapolated beyond mass ratio $q = 4$, and in App. 7.B we investigate some features in the error distribution of the NR simulations.

7.4 Preliminaries and notation

It is convenient to combine the two polarizations of the waveform into a single complex, dimensionless strain $\hat{h} = h_+ - ih_\times$, and to represent the waveform on a sphere as a sum of spin-weighted spherical harmonic modes:

$$\hat{h}(t, \iota, \varphi_0) = \sum_{\ell=2}^{\infty} \sum_{m=-\ell}^{\ell} \hat{h}_{\ell m}(t) {}_{-2}Y_{\ell m}(\iota, \varphi_0). \quad (7.1)$$

Here ${}_{-2}Y_{\ell m}$ are the spin $= -2$ weighted spherical harmonics, and ι and φ_0 are the polar and azimuthal angles on the sky in the source frame.

For nonprecessing systems, the direction of orbital angular momentum (\mathbf{L}) is fixed and the \hat{z} direction of the source frame is chosen to be along $\hat{\mathbf{L}}$ by convention. The gravitational radiation is strongest along the directions parallel and antiparallel to $\hat{\mathbf{L}}$. Therefore, for nonprecessing systems the quadrupole modes ($\ell = 2, m = \pm 2$) dominate the sum in Eq. (7.1), but the nonquadrupole modes can become important at large mass ratios or ι close to $\pi/2$ [58–67].

By contrast, for precessing systems the direction of \mathbf{L} varies due to precession [51] and so there is not a fixed axis along which the radiation is dominant. The standard practice is to choose \hat{z} of the source frame along the direction of \mathbf{L} (or the total angular momentum) at a reference time or frequency.

Heuristically, one can think of a precessing system as a nonprecessing system with time-dependent frame rotations applied to it. In this non-inertial frame the rotation causes mixing of power between modes of fixed ℓ . For example, the power of the $(2, \pm 2)$ modes leaks into the $(2, \pm 1)$ and $(2, 0)$ modes. This means that all $\ell = 2$ modes can be dominant in Eq. (7.1). While this rotating-frame picture ignores some dynamical features such as nutation, it accounts for most of the effects of precession in the waveform.

By the same logic, one could apply a time-dependent rotation to a precessing system such that \hat{z} always lies along $\hat{\mathbf{L}}(t)$. In this non-inertial frame, referred to as the coprecessing frame [68–70], the radiation is always strongest along \hat{z} , and the $(\ell = 2, m = \pm 2)$ modes are dominant. In fact, since most precessional effects are accounted for by the frame rotation, the waveform in the coprecessing frame is qualitatively similar to that of a nonprecessing system (cf. Fig. 7.4.1). This observation has been exploited in the literature [21, 24, 27, 56, 71] to simplify the modeling of precessing systems. Here we proceed similarly, using the coprecessing frame described in Ref. [70] and denoting the strain in this frame as $h_{\ell m}^{\text{copr}}$.

The waveform can be made even simpler, and therefore easier to model, by applying an additional rotation about the z -axis of the coprecessing frame by an amount equal to the instantaneous orbital phase:

$$h_{\ell m}^{\text{coorb}}(t) = h_{\ell m}^{\text{copr}}(t) e^{im\phi(t)}. \quad (7.2)$$

Here we define the orbital phase,

$$\phi(t) = \frac{\arg[h_{2,-2}^{\text{copr}}(t)] - \arg[h_{2,2}^{\text{copr}}(t)]}{4}, \quad (7.3)$$

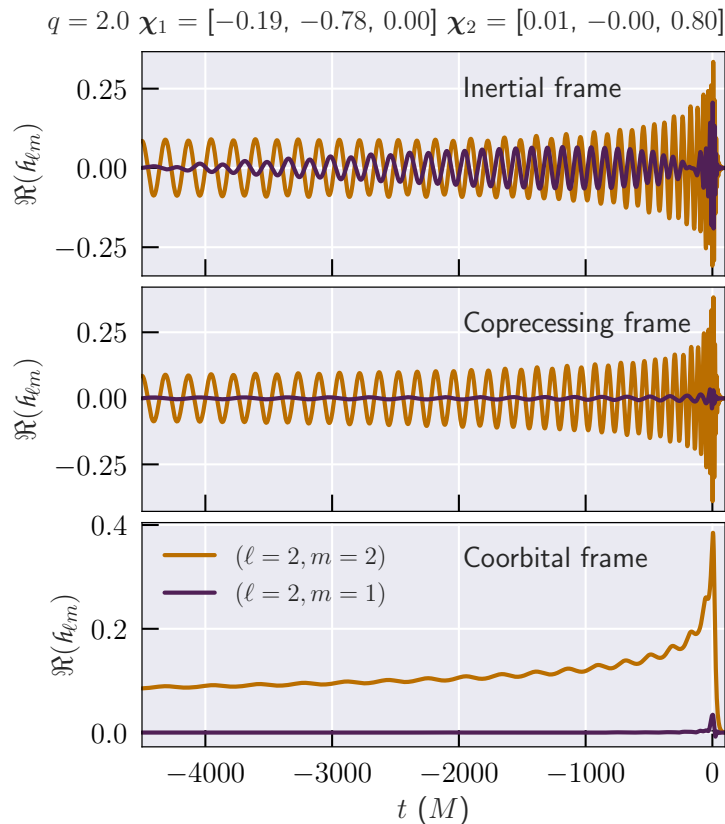


Figure 7.4.1: The real part of the (2, 2) and (2, 1) modes of the gravitational waveform in the inertial (top), coprocessing (middle), and coorbital (bottom) frames. In the inertial frame, the amplitude of the (2, 1) mode can be comparable to that of the (2, 2) mode. In the coprocessing frame, on the other hand, the (2, 2) mode always dominates. In addition, most effects of precession are removed by the rotation and the waveform in the coprocessing frame resembles that of a nonprecessing system. In the coorbital frame, finally, the waveform is further simplified and does not oscillate about zero. Mass ratio and initial spins used to produce this figure are indicated at the top of the plot.

using the coprocessing frame strain. The waveform $h_{\ell m}^{\text{coorb}}(t)$ corresponds to a new frame, called the coorbital frame, in which the BHs are always on the x -axis, with the heavier BH on the positive x -axis¹. More importantly, the waveform in the coorbital frame is nearly nonoscillatory, simplifying the modeling problem greatly. Figure 7.4.1 shows an example of a waveform in the inertial, coprocessing, and coorbital frames.

¹Here the BH positions are defined from the waveform at future null infinity and do not necessarily correspond to the (gauge-dependent) coordinate BH positions in the NR simulation.

7.5 NR simulations

Our NR simulations are performed using the Spectral Einstein Code (SpEC) [72–77] developed by the SXS [78] collaboration.

Parameter space coverage

We use 890 precessing NR simulations used in the construction of the surrogate models NRSur7dq2 [56] and surfinBH7dq2 [57], which provide coverage in the $q \leq 2$ and $\chi_1, \chi_2 \leq 0.8$ regions of the parameter space. We also make use of 64 aligned-spin simulations with $q \leq 4$ and $\chi_1, \chi_2 \leq 0.8$ used in the construction of the surrogate model presented in Ref. [79]. Finally, we performed 574 new simulations with $2 < q \leq 4$, $\chi_1, \chi_2 \leq 0.8$ and generic spin directions—these simulations are presented here for the first time. The parameters for the first 204 of these are chosen based on sparse grids as detailed in Appendix A of Ref. [56]. The remaining parameters are chosen as follows. We randomly sample 1000 points uniformly in mass ratio, spin magnitude, and spin direction on the sphere. We compute the distance between points a and b using the metric

$$ds^2 = \left(\frac{q^a - q^b}{\Delta q} \right)^2 + \sum_{i \in \{1,2\}} \left(\frac{|\chi_i^a - \chi_i^b|}{\Delta \chi} \right)^2, \quad (7.4)$$

where $\Delta q = 4 - 1 = 3$ and $\Delta \chi = 0.8$ are the ranges of these parameters. These normalization factors are somewhat arbitrary, although any choice of order unity should provide a reasonable criteria for point selection. For each sampled parameter, we compute the minimum distance to all previously chosen parameters. We then add the sampled parameter maximizing this minimum distance to the set of chosen parameters. This is done iteratively for 370 additional parameters. The new simulations have identifiers SXS:BBH:1346-1350 and SXS:BBH:1514-2082, and are made publicly available through the SXS public catalog [80]. The parameter space covered by the $890+64+574=1528$ NR simulations used in this work is shown in Fig. 7.5.1. Note that not all of these are independent simulations: for 154 of these cases we have $q = 1$, with $\chi_1 \neq \chi_2$; for each of these cases we effectively obtain an additional simulation by exchanging the labels of the two BHs.

The start time of these simulations varies between $4693M$ and $5234M$ before the peak of the waveform amplitude, where $M = m_1 + m_2$ is the total Christodoulou mass measured close to the beginning of the simulation at the “relaxation time” [81]. The initial orbital parameters are chosen through an iterative procedure [82]

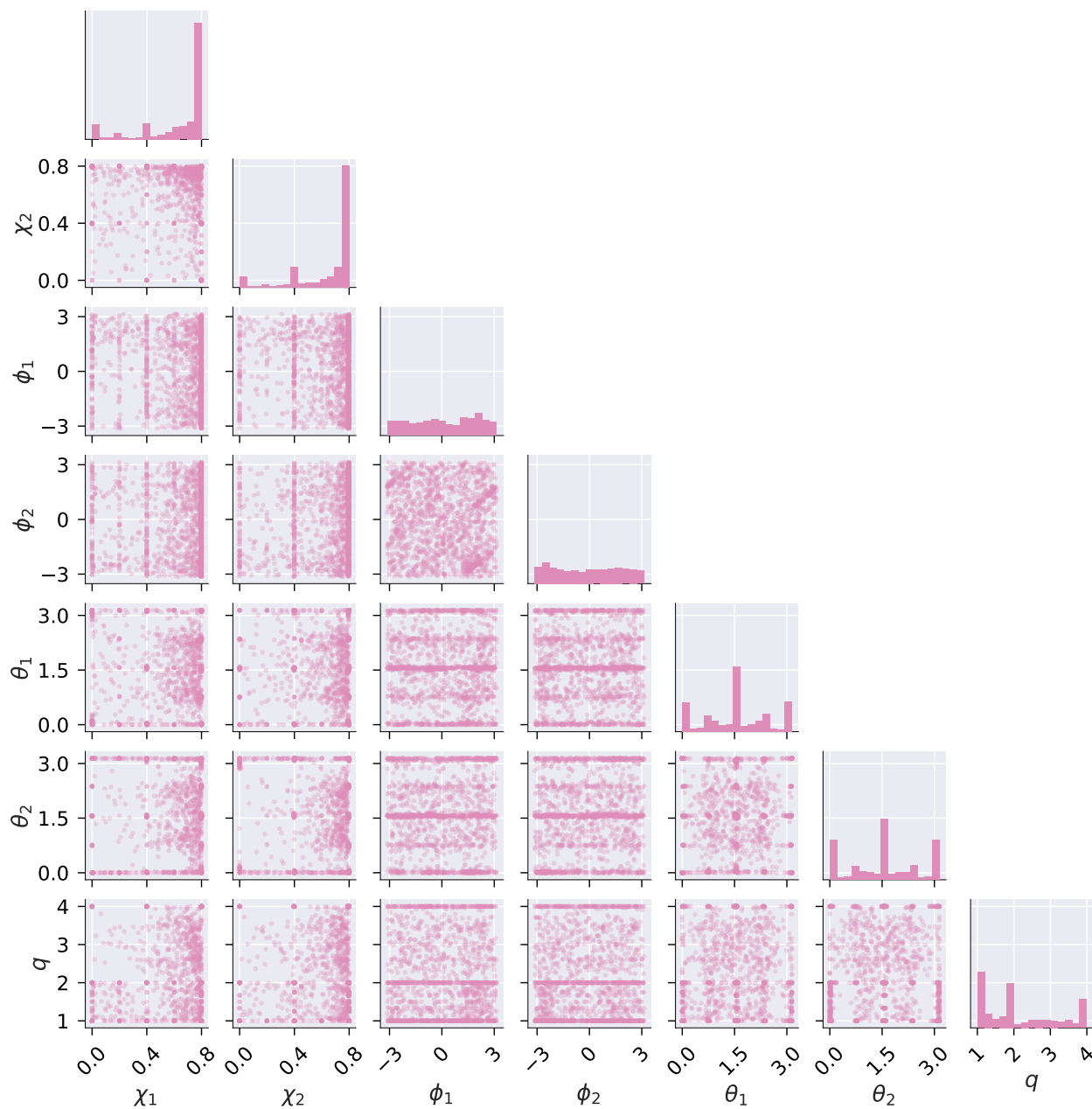


Figure 7.5.1: Parameters of the 1528 NR simulations used in the construction of the surrogate models in this paper. We show the distribution of mass ratio q and the spin components in standard spherical polar coordinates (χ, θ, ϕ) at $-4300M$ from the waveform amplitude peak. The index 1 (2) refers to the heavier (lighter) BH.

such that the orbits are quasicircular; the largest eccentricity for these simulations is 9.8×10^{-4} , while the median value is 3.8×10^{-4} .

Data extracted from simulations

We make use of the following quantities extracted from the NR simulations: the waveform modes $h_{\ell m}(t)$, the component spins $\chi(t)$, the mass ratio q , and the remnant mass m_f , spin χ_f , and kick velocity \mathbf{v}_f .

The waveform is extracted at several extraction spheres at varying finite radii from the origin and then extrapolated to future null infinity [81, 83]. Then the extrapolated waveforms are corrected to account for the initial drift of the center of mass [84, 85]. The time steps during the simulations are chosen nonuniformly using an adaptive time-stepper [81]. Using cubic splines, we interpolate the real and imaginary parts of the waveform modes to a uniform time step of $0.1M$; this is dense enough to capture all frequencies of interest, including near merger. The interpolated waveform at future null infinity, scaled to unit mass and unit distance, is denoted as $\hat{h}_{\ell m}(t)$ in this paper.

The component spins $\chi_{1,2}(t)$ and masses $m_{1,2}$ are evaluated on the apparent horizons [74] of the BHs. The masses at the relaxation time [81] are used to define the mass ratio $q = m_1/m_2$. Unless otherwise specified, all masses in this paper are given in units of the total mass $M = m_1 + m_2$ at relaxation. The spins are interpolated onto the same time array² as used for the waveform, using cubic splines.

The remnant mass m_f and spin χ_f are determined from the common apparent horizon long after ringdown, as detailed in Ref. [81]. The remnant kick velocity is derived from conservation of momentum, $\mathbf{v}_f = -\mathbf{P}^{\text{rad}}/m_f$ [87]. The radiated momentum flux \mathbf{P}^{rad} is integrated [88] from the strain $\hat{h}_{\ell m}$.

Post-processing the output of NR simulations

After extracting the strain and spins from the simulations, we apply the following post processing steps before building the surrogate models.

First, we shift the time arrays of all waveforms such that $t = 0$ occurs at the peak (see Ref. [56] for how the peak is determined) of the total waveform amplitude, defined

²The waveforms at future null infinity use a time coordinate t that is different from the simulation time \tilde{t} at which the spins are measured in the near zone [81]. In this paper, we identify t with \tilde{t} . While this identification is gauge-dependent, the spin directions are already gauge-dependent. We, however, note that the spin and orbital angular momentum vectors in the damped harmonic gauge used by SpEC agree quite well with the corresponding vectors in post-Newtonian (PN) theory [86].

as:

$$A(t) = \sqrt{\sum_{\ell m} |h_{\ell m}(t)|^2}. \quad (7.5)$$

Then we rotate the waveform modes such that at a reference time $t_0 = -4300M$, the inertial frame coincides with the coorbital frame. This means that the \hat{z} direction of the inertial frame is along the principal eigenvector of the angular momentum operator [70] at the reference time. In addition, the \hat{x} direction of the inertial frame is along the line of separation from the lighter BH to the heavier BH (in other words, the orbital phase is zero). The spin vectors $\chi_{1,2}(t)$ are also transformed into the same inertial frame.

We then truncate the waveform and spin time series by dropping all times $t < -4300M$ to exclude the initial transients known as “junk radiation”. After the truncation, the reference time $t = -4300M$ is also the start time of the data.

For $t > -100M$, the spin measurements from the apparent horizons start to become unreliable as the horizons become highly distorted. Following Ref. [56], starting at $t = -100M$, we extend the spins to later times using PN spin evolution equations. This evolution is done even past the merger stage, into the ringdown. We stress that the extended spins are unphysical but are a useful parametrization to construct fits at late times.

Finally we apply a smoothing filter (see Eq. (6) of Ref. [56]) on the spin time series to remove fast oscillations taking place on the orbital timescale. This smoothing helps improve the numerical stability of the ordinary differential equation (ODE) integrations described in Sec. 7.6. Note that we use the filtered spins for the waveform surrogate (Sec. 7.6) but not for the remnant surrogate (Sec. 7.7), for which we just use the unfiltered spins since there are no ODE integrations involved.

7.6 Waveform surrogate

To construct the waveform surrogate, we closely follow the NRSur7dq2 model of Ref. [56], with some modifications to adapt it to higher mass ratios. We refer to the new waveform model as NRSur7dq4.

Coorbital frame surrogate

Modelling slowly varying functions of time, rather than oscillatory functions, inevitably results in higher accuracy. Therefore, we first decompose the strain into

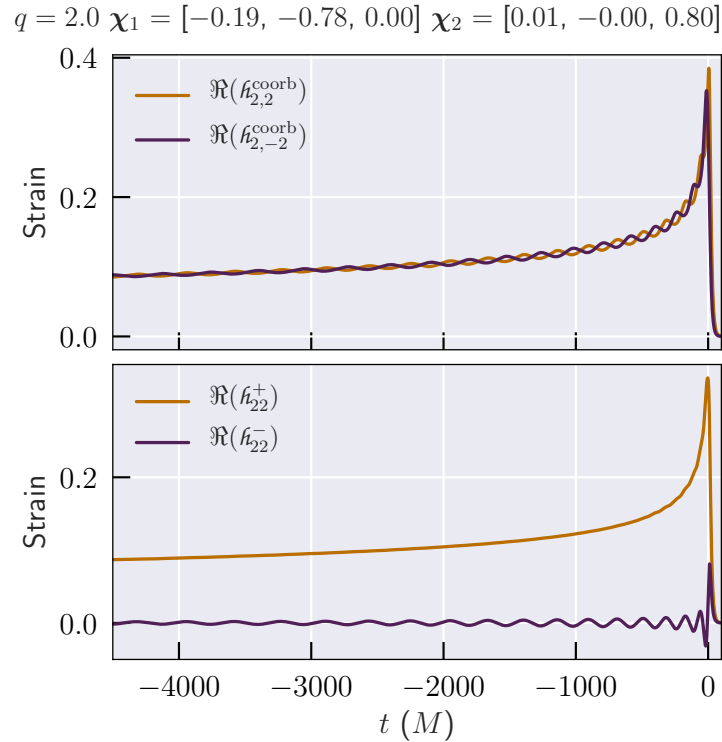


Figure 7.6.1: The top panel shows the real part of the $(2, 2)$ and $(2, -2)$ modes of the waveform in the coorbital frame. Notice that the orbital time scale oscillations of these two modes have opposite signs. The bottom panel shows the real parts of $h_{2,2}^+$ and $h_{2,2}^-$ (cf. Eq. 7.6), we take advantage of the above fact to move most of the oscillations from the larger to the smaller data piece.

several “data pieces”, each of which is a slowly varying function of time, and build a surrogate for each of them. At evaluation time, we combine the various data pieces to reconstruct the inertial frame strain. To reduce the cost of these transformations, we first downsample the inertial frame strain onto a set of 2000 time values t_i^{coorb} that are approximately uniformly spaced in the orbital phase (using the method described in App. B of Ref. [56]).

As described in Sec. 7.4, the waveform is simpler in the coorbital frame. A further simplification is possible by considering combinations of $m > 0$ and $m < 0$ counterparts of a fixed ℓ mode:

$$h_{\ell m}^{\pm} = \frac{h_{\ell, m}^{\text{coorb}} \pm h_{\ell, -m}^{\text{coorb} *}}{2}. \quad (7.6)$$

Figure 7.6.1 shows an example of the simplification obtained with this combination. For all $m \neq 0$ modes we model the real and imaginary parts of $h_{\ell m}^{\pm}$. For $m = 0$ modes, we directly model the real and imaginary parts of the coorbital frame strain

$f_{\ell,m}^{\text{coorb}}$. We construct an independent surrogate model for each of these data pieces and refer to the combination of these models as the coorbital frame surrogate.

As described in Ref. [56], for each waveform data piece, we construct a linear basis using singular value decomposition with an RMS tolerance of 3×10^{-4} . We then construct an empirical time interpolant with the same number of empirical time nodes as basis functions for that data piece [89–91]. The empirical time nodes are chosen as a subset of the 2000 coorbital time values (t_i^{coorb}) and are specific to each data piece. Finally, for each empirical time node, we construct a parametric fit for the waveform data piece. The fits are parametrized as functions of the mass ratio and the spins in the coorbital frame at that time. We describe our fitting procedure in Sec. 7.6. At evaluation time, the coorbital frame spins at any time are obtained using the dynamics surrogate described in Sec. 7.6.

Dynamics surrogate

The surrogate described in Sec. 7.6 only models the strain in the coorbital frame. We also need to model the following quantities:

1. The orbital phase in the coprecessing frame, which is required to transform the strain from the coorbital frame to the coprecessing frame [cf. Eq. (7.2)];
2. The quaternions describing the coprecessing frame, which are required to transform the strain from the coprecessing frame to the inertial frame;
3. The spins as a function of time, which are used in the evaluation of the parametric fits described in Sec. 7.6.

We refer to the model for these quantities as the dynamics surrogate. Using the fitting method of Sec. 7.6, we first construct parametric fits for $\omega(t)$, $\Omega_{x,y}^{\text{coorb}}(t)$, and $\dot{\chi}_{1,2}^{\text{coorb}}(t)$ at selected time nodes referred to as the dynamical time nodes t_i^{dyn} . Here $\dot{\chi}_{1,2}^{\text{coorb}}(t)$ are the time derivatives of the coprecessing frame spins transformed to the coorbital frame, $\omega(t)$ is $d\phi/dt$ (cf. Eq. (7.3)), and $\Omega_{x,y}^{\text{coorb}}(t)$ is the angular velocity of the coprecessing frame, transformed to the coorbital frame. These quantities are described in more detail in Sec. III of Ref. [56]. Note that $\Omega_z^{\text{coorb}}(t) \sim 0$. For the dynamical time nodes t_i^{dyn} we chose 238 time values such that there are approximately 10 nodes per orbit (see App. B of Ref. [56] for details).

We use a fourth-order Adams-Bashforth scheme to integrate $\omega(t_i^{\text{dyn}})$, $\Omega_{x,y}^{\text{coorb}}(t_i^{\text{dyn}})$, and $\chi_{1,2}^{\text{coorb}}(t_i^{\text{dyn}})$ over the set of dynamical time nodes t_i^{dyn} providing the time evolution of the orbital phase $\phi(t_i^{\text{dyn}})$, the coprecessing frame quaternions $\hat{Q}(t_i^{\text{dyn}})$, and the component spins in the coorbital frame $\chi_{1,2}^{\text{coorb}}(t_i^{\text{dyn}})$. This involves solving a coupled ODE as described in Sec. V of Ref. [56]. At each step of the ODE integration, the coorbital frame spins at the current node t_i^{dyn} are first obtained. These are then used to evaluate the parametric fits for the derivative quantities mentioned above. Note that the spins used in the dynamics surrogate are the filtered spins mentioned in Sec. 7.5; this improves the accuracy of the ODE integration by making the spin time derivatives easier to model.

Parametric fits

For the coorbital frame surrogate of Sec. 7.6, we need to construct parametric fits at various empirical time nodes for the different data pieces. Similarly, for the dynamics surrogate of Sec. 7.6, we need to construct fits for various time derivatives at the dynamical time nodes t_i^{dyn} . We use the same procedure for each of these fits. Let us refer to the data to be fitted as $y(\Lambda)$, where Λ is a seven-dimensional set of parameters.

For each of these fits, the seven parameters Λ must contain information on mass ratio q and coorbital frame spins $\chi_{1,2}^{\text{coorb}}(t_i)$ at the time corresponding to the fit. Following Ref. [57], we parametrize the fits using

$$\Lambda = [\log(q), \chi_{1x}^{\text{coorb}}, \chi_{1y}^{\text{coorb}}, \hat{\chi}^{\text{coorb}}, \chi_{2x}^{\text{coorb}}, \chi_{2y}^{\text{coorb}}, \chi_a^{\text{coorb}}], \quad (7.7)$$

where $\hat{\chi}^{\text{coorb}}$ is the spin parameter entering the GW phase at leading order [12, 26, 92, 93] in the PN expansion

$$\hat{\chi}^{\text{coorb}} = \frac{\chi_{\text{eff}}^{\text{coorb}} - 38\eta(\chi_{1z}^{\text{coorb}} + \chi_{2z}^{\text{coorb}})/113}{1 - 76\eta/113}, \quad (7.8)$$

$$\chi_{\text{eff}}^{\text{coorb}} = \frac{q \chi_{1z}^{\text{coorb}} + \chi_{2z}^{\text{coorb}}}{1 + q}, \quad (7.9)$$

$$\eta = \frac{q}{(1 + q)^2}, \quad (7.10)$$

and χ_a^{coorb} is the ‘‘anti-symmetric spin’’,

$$\chi_a^{\text{coorb}} = \frac{1}{2}(\chi_{1z}^{\text{coorb}} - \chi_{2z}^{\text{coorb}}). \quad (7.11)$$

We empirically found this parameterization to perform more accurately than the more intuitive choice $\Lambda_{\text{ref56}} = [q, \chi_{1x}^{\text{coorb}}, \chi_{1y}^{\text{coorb}}, \chi_{1z}^{\text{coorb}}, \chi_{2x}^{\text{coorb}}, \chi_{2y}^{\text{coorb}}, \chi_{2z}^{\text{coorb}}]$ used in Ref. [56].

Fits are constructed using the forward-stepwise greedy fitting method described in App. A of Ref. [71]. We choose the basis functions to be a tensor product of 1D monomials in the components of Λ . The components of Λ are first affine mapped to the interval $[-1, 1]$ before constructing the tensor product. We consider up to fourth powers in $\log(q)$ and up to quadratic powers in the spin parameters. Note that fits of Ref. [56], which were restricted to $q \leq 2$, used only up to cubic powers in q . Here we allow higher powers as we extend the dataset in the mass ratio direction to $q \leq 4$. It is always possible to improve the accuracy of a fit by adding more basis functions. However, this can lead to over-fitting when the data contain some noise. Our source of noise is mostly due to NR truncation error, but also systematic errors such as waveform extrapolation and residual eccentricity. In order to safeguard against over-fitting, we perform 10 trial fits, leaving a random 10% of the dataset out as validation points in each trial, to determine the set of basis functions used in constructing the final fit. We allow a maximum of 100 basis functions for each fit. See App. A of Ref. [71] for more details.

Surrogate evaluation

To evaluate the surrogate, we begin with a user-specified mass ratio q and spins $\chi_{1,2}^{\text{coorb}}$ at the initial time $t = -4300M$. Note that at this time, the inertial frame coincides with the coorbital frame. These values are used to initialize the dynamics surrogate described in Sec. 7.6, which predicts the coprecessing frame quaternions $\hat{Q}(t_i^{\text{dyn}})$, the orbital phase $\phi(t_i^{\text{dyn}})$ in the coprecessing frame, and the coorbital frame spins $\chi_{1,2}^{\text{coorb}}(t_i^{\text{dyn}})$ at the dynamic time nodes t_i^{dyn} . We then use cubic splines to interpolate these quantities on to the time array for the coorbital frame surrogate t_i^{coorb} , giving us $\hat{Q}(t_i^{\text{coorb}})$, $\phi(t_i^{\text{coorb}})$, and $\chi_{1,2}^{\text{coorb}}(t_i^{\text{coorb}})$.

The coorbital frame surrogate described in Sec. 7.6 is used to predict the strain in the coorbital frame. This involves evaluating the fits at the empirical time nodes for this surrogate using $\chi_{1,2}^{\text{coorb}}(t_i^{\text{coorb}})$ and q . Then, the orbital phase $\phi(t_i^{\text{coorb}})$ is used to transform the strain from the coorbital frame to the coprecessing frame (cf. Eq. 7.2). Finally, the coprecessing frame quaternions $\hat{Q}(t_i^{\text{coorb}})$ are used to transform the strain from the coprecessing frame to the inertial frame (this involves Wigner matrices, see App. A of Ref. [70]). This gives us $h_{\ell m}(t_i^{\text{coorb}})$, which is interpolated onto any

required time array t using cubic splines to get $h_{\ell m}(t)$.

7.7 Remnant surrogate

To construct the remnant properties surrogate, we closely follow the surfinBH7dq2 model of Ref. [57]. We refer to the new model presented here as surfinBH7dq4.

We model the remnant mass m_f , spin χ_f , and kick velocity \mathbf{v}_f . Before constructing the fits, χ_f and \mathbf{v}_f are transformed into the coorbital frame at $t = -100M$. We model each component of the vectors independently. The fits are parametrized by the same Λ of Eq. (7.7), but using the component spins at $t = -100M$. Unlike the waveform surrogate case, we do not filter out orbital-timescale oscillations. The filtered spins were found to be necessary for the accuracy of the time integration in Sec. 7.6, which is not necessary here because the remnant properties can be evaluated from the BBH parameters at a single time $t = -100M$.

All fits are performed using Gaussian Process Regression (GPR), as described in the supplementary materials of Ref. [57]. We find that GPR fitting is, in most cases, more accurate but also significantly more expensive than the polynomial fitting method described in Sec. 7.6. GPR becomes impractical to use for the waveform surrogate as there are hundreds of fits that need to be evaluated to generate the waveform. For the remnant fits, however, the additional cost of GPR is acceptable because one is only fitting 7 quantities (m, χ_f, \mathbf{v}_f). In addition, GPR naturally provides error estimates which can be useful in data analysis applications. The efficacy of the GPR error estimate in reproducing the underlying error of the surrogate models was investigated thoroughly in the supplementary materials of Ref. [57].

Although surfinBH7dq4 is parameterized internally by input spins specified in the coorbital frame at $t = -100M$, we allow the user to specify input spins at earlier times, and in the inertial frame; this case is handled by two additional layers of spin evolution. Given the inertial-frame input spins at an initial orbital frequency f_0 , we first evolve the spins using a post-Newtonian (PN) approximant — 3.5PN SpinTaylorT4 [86, 94, 95] — until we reach the domain of validity of the more accurate NRSur7dq4 ($t = -4300M$ from the peak). We then use the dynamics surrogate of NRSur7dq4 to evolve the spins until $t = -100M$. These spins are then transformed to the coorbital frame and used to evaluate the remnant fits. Thus, spins can be specified at any given orbital frequency and are evolved consistently before estimating the final BH properties. Note that NRSur7dq4 uses the filtered spins, while surfinBH7dq4 expects unfiltered spins at $t = -100M$, but we find that the

errors introduced by this discrepancy are negligible compared to the errors due to PN spin evolution.

7.8 Results

We evaluate the accuracy of our new surrogate models by comparing against the waveform and remnant properties from the NR simulations used in this work. For this, we perform a 20-fold cross-validation study to compute “out-of-sample” errors as follows. We first randomly divide the 1528 training simulations into 20 groups of ~ 76 simulations each. For each group, we build a trial surrogate using the ~ 1452 remaining training simulations and test against these ~ 76 validation ones, which may include points on the boundary of the training set.

Waveform surrogate errors

To estimate the difference between two waveforms, h_1 and h_2 , we use the mismatch

$$\mathcal{MM} = 1 - \frac{\langle h_1, h_2 \rangle}{\sqrt{\langle h_1, h_1 \rangle \langle h_2, h_2 \rangle}}, \quad (7.12)$$

$$\langle h_1, h_2 \rangle = 4\text{Re} \int_{f_{\min}}^{f_{\max}} \frac{\tilde{h}_1(f) \tilde{h}_2^*(f)}{S_n(f)} df, \quad (7.13)$$

where $\tilde{h}(f)$ indicates the Fourier transform of the complex strain $h(t)$, * indicates a complex conjugation, Re indicates the real part, and $S_n(f)$ is the one-sided power spectral density of a GW detector. We taper the time domain waveform using a Planck window [96], and then zero-pad to the nearest power of two. We further zero-pad the waveform to increase the length by a factor of eight before performing the Fourier transform. The tapering at the start of the waveform is done over 1.5 cycles of the (2,2) mode. The tapering at the end is done over the last $30M$. Note that our model contains times up to $100M$ after the peak of the waveform amplitude, and the signal has essentially died down by the last $30M$. We take f_{\min} to be twice the waveform angular velocity (as defined by Ref. [97]) at the end of the initial tapering window, and f_{\max} is chosen to be 4 times the waveform angular velocity at $t = 0$; the extra factor of 4 is chosen to resolve up to $m = 4$ spherical-harmonic modes, with an extra margin of a factor of 2. We compute mismatches with a flat noise curve ($S_n = 1$) as well as with the Advanced-LIGO design sensitivity noise curve [98]. Mismatches are computed following the procedure described in Appendix D of Ref. [71]. In particular, we optimize over shifts in time, polarization

angle, and initial orbital phase. Both plus and cross polarizations are treated on an equal footing by using a two-detector setup where one detector sees only the plus and the other only the cross polarization. We compute the mismatches at 37 points uniformly distributed on the sky in the source frame, and we use all available modes of a given waveform model.

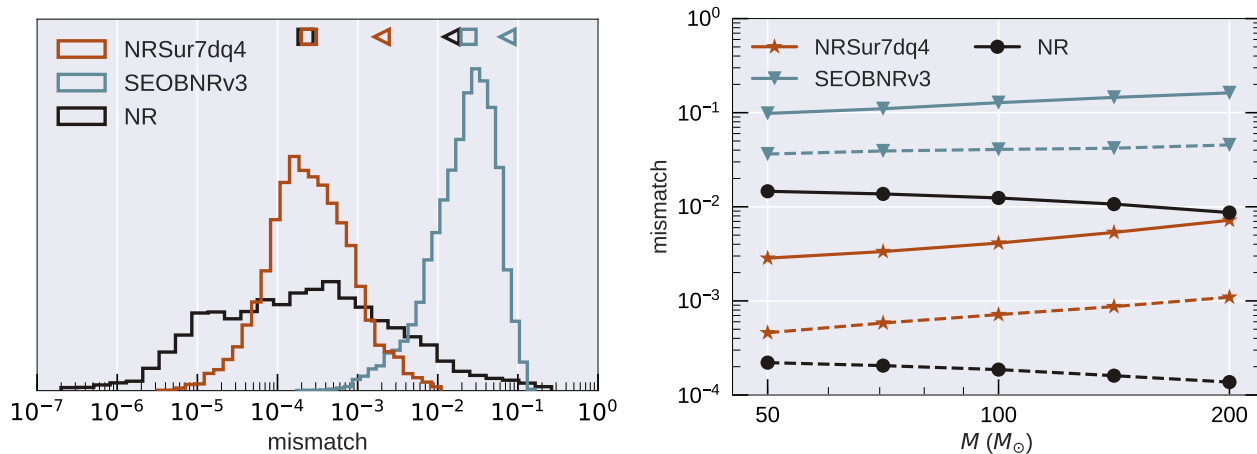


Figure 7.8.1: Mismatches for NRSur7dq4 and SEOBNRv3 models, when compared against precessing NR simulations using all $\ell \leq 5$ modes with mass ratios $q \leq 4$, and spin magnitudes $\chi_1, \chi_2 \leq 0.8$. The NRSur7dq4 errors shown are out-of-sample errors. Also shown are the NR resolution errors. Mismatches are computed at several sky locations using all available modes for each model: $\ell \leq 4$ for NRSur7dq4, and $\ell = 2$ for SEOBNRv3. The NR error is computed using all $\ell \leq 5$ modes from the two highest available resolutions. *Left panel*: Mismatches computed using a flat noise curve. The square (triangle) markers at the top indicate the median (95th percentile) values. *Right panel*: Mismatches computed using the Advanced LIGO design sensitivity noise curve, as a function of total mass. The dashed (solid) lines indicate the median (95th percentile) values over different NR simulations and points in the sky.

Figure 7.8.1 summarizes the out-of-sample mismatches for NRSur7dq4 against the NR waveforms. In the left panel we show mismatches computed using a flat noise curve. We compare this with the truncation error in the NR waveforms themselves, estimated by computing the mismatch between the two highest available resolutions of each NR simulation. The errors in the surrogate model are well within the estimated truncation errors of the NR simulations. In addition, we also show the errors for the waveform model SEOBNRv3 [24, 31], which also includes spin precession effects³. The surrogate errors are at least an order of magnitude lower than those of SEOBNRv3.

³Note that SEOBNRv3 spins are specified at a reference frequency, rather than a time before

Apart from SEOBNRv3, another model commonly used in data analysis applications is IMRPhenomPv2 [27]. IMRPhenomPv2 was shown to be comparable in accuracy to SEOBNRv3 in Ref. [56], at least in order of magnitude. Therefore, for simplicity, we do not show comparisons of IMRPhenomPv2 to NR here. Note that updated versions of both SEOBNRv3 (based on Ref. [22]) and IMRPhenomPv2 (see Ref. [21]) are under development, but are not currently available publicly. We note that these models are calibrated only against aligned-spin NR simulations, using a much smaller set of simulations than our model. Both these factors contribute to the accuracy of these models. On the other hand, these models are expected to be valid for larger mass ratios and spin magnitudes than our model, although their accuracy in that region is unknown due to lack of sufficient number of simulations.

We note that the NR truncation mismatch distribution in the left panel of Fig. 7.8.1 has a tail extending to $\mathcal{M}\mathcal{M} \sim 0.1$. We find that these cases occur when the spins of the two highest resolutions of the simulation are inconsistent with each other because of unresolved effects during junk-radiation emission, meaning that the two resolutions represent different physical systems. This means that comparing the resolutions for these cases gives us an error estimate that is too conservative and does not reflect the actual truncation error of the simulations. We expect the actual truncation error to be closer to the errors reproduced by the surrogate model (which is trained on the high resolution data set) in Fig. 7.8.1. Evidence for these claims is provided in App. 7.B.

The right panel of Fig. 7.8.1 shows mismatches computed using the Advanced LIGO design sensitivity noise curve [98]. In this case, results depend on the total mass M of the system. Consequently, we show the median and 95th percentile values at different M , rather than full histograms. Once again, the surrogate errors are comparable to those of the NR simulations, and are at least an order of magnitude lower than that of SEOBNRv3. Over the mass range $50 - 200M_{\odot}$, mismatches for NRSur7dq4 are always $\lesssim 8 \times 10^{-3}$ at the 95 percentile level.

Fig. 7.8.2 shows a comparison of waveforms computed via NRSur7dq4, SEOBNRv3, and NR for the cases that lead to the largest error for NRSur7dq2 and SEOBNRv3 in the left panel of Fig. 7.8.1. The surrogate shows reasonable agreement with NR, even for its worst case, while SEOBNRv3 shows a noticeably larger deviation in both cases.

merger. We choose the reference frequency such that the waveform begins at $t = -4300M$ before the waveform amplitude peak (as defined in Eq. 7.5).

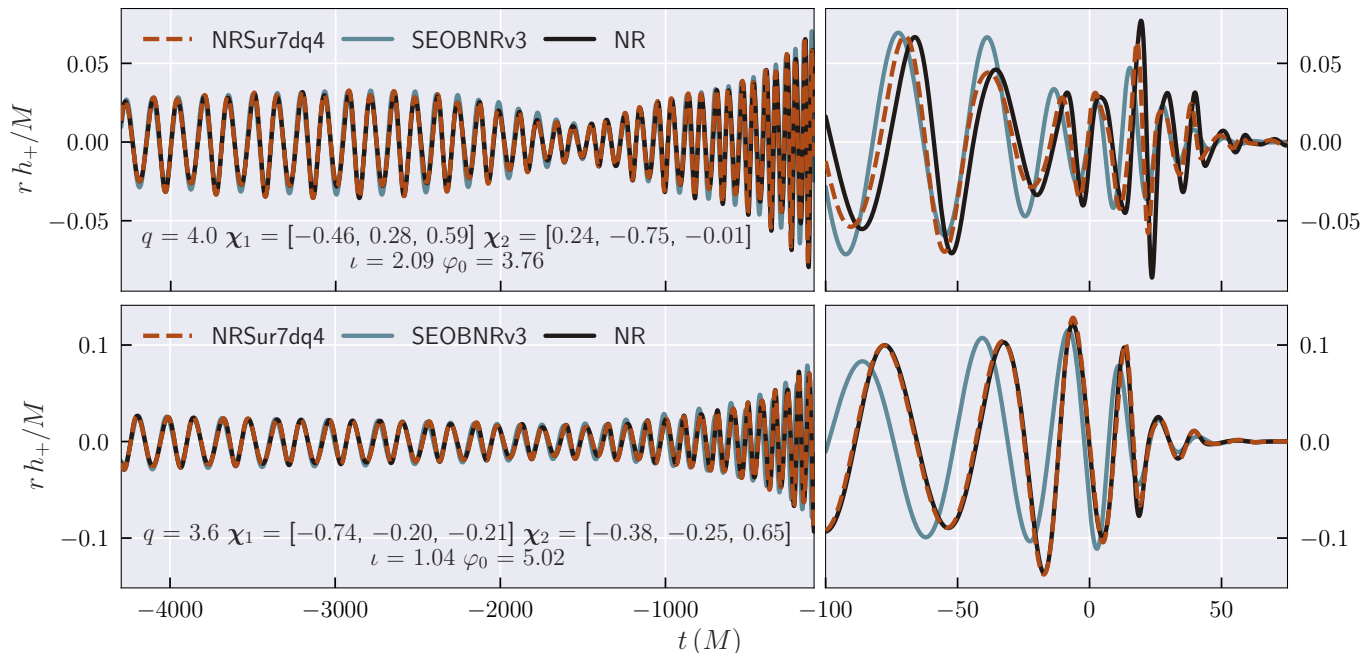


Figure 7.8.2: The plus polarization of the waveforms for the cases that result in the largest mismatch for NRSur7dq4 (top) and SEOBNRv3 (bottom) in the left panel of Fig. 7.8.1. We also show the corresponding NR waveforms. Each waveform is projected using all available modes for that model, along the direction that results in the largest mismatch for NRSur7dq4 (SEOBNRv3) in the top (bottom) panel. Note that NRSur7dq4 is evaluated using trial surrogates that are not trained using these cases. The binary parameters and the direction in the source frame are indicated in the figure text. All waveforms are time shifted such that the peak of the total amplitude occurs at $t = 0$ [using all available modes, according to Eq. (7.5)]. The waveform modes are then rotated to have their orbital angular momentum aligned with the z -axis, and such that the orbital phase is equal to zero at $t = -4300M$.

In Figs. 7.8.1 and 7.8.2 we use all available modes for NRSur7dq4 and SEOBNRv3. NRSur7dq4 models all modes $\ell \leq 4$, while SEOBNRv3 models only the $\ell = 2$ modes. For the NR waveforms in Figs. 7.8.1 and 7.8.2, we include all modes $\ell \leq 5$ to account for the error due to neglecting $\ell > 4$ modes in NRSur7dq4. To better understand what fraction of the SEOBNRv3 error comes from neglecting modes with $\ell > 2$, we repeat the calculations leading to the SEOBNRv3 histogram in the left panel of Fig. 7.8.1 in Fig. 7.8.3, while restricting all waveforms to $\ell = 2$. While there is a noticeable move towards lower mismatches when restricted to $\ell = 2$, the median and 95th percentile values change only marginally, suggesting that the main error source for SEOBNRv3 are the $\ell = 2$ modes themselves.

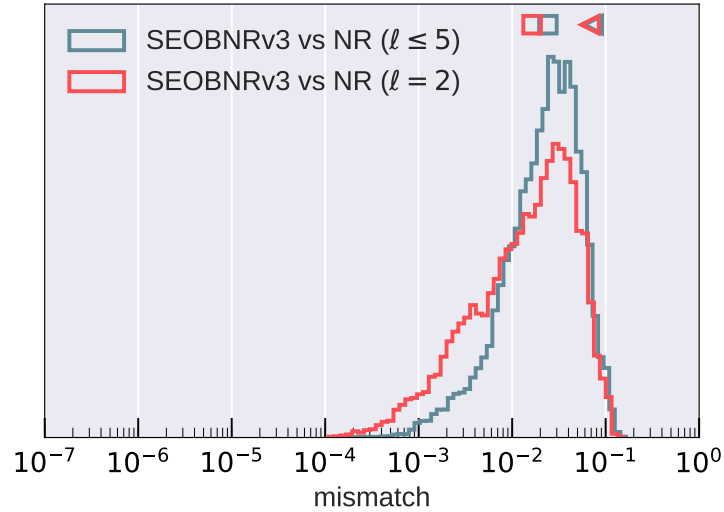


Figure 7.8.3: Same as the left panel of Fig. 7.8.1 but using only $\ell = 2$ modes for NR when compared to SEOBNRv3. The blue histogram from the left panel of Fig. 7.8.1, where SEOBNRv3 is compared to NR with all $\ell \leq 5$ modes, is reproduced here for comparison. The square (triangle) markers at the top indicate the median (95th percentile) values.

Remnant surrogate errors

We evaluate the accuracy of the remnant surrogate `surfinBH7dq4` by comparing against the NR simulations through a cross-validation study as in Sec. 7.8. Out-of-sample errors for the remnant properties predicted by `surfinBH7dq4` are shown in Fig. 7.8.4. 95th percentile errors are $\sim 5 \times 10^{-4} M$ for mass, $\sim 2 \times 10^{-3}$ for spin magnitude, $\sim 4 \times 10^{-3}$ radians for spin direction, $\sim 4 \times 10^{-4} c$ for kick magnitude, and ~ 0.2 radians for kick direction. Our errors are at the same level as the NR resolution error, estimated by comparing the two highest NR resolutions. The largest errors in the kick direction can be of order ~ 1 radian. The bottom-right panel of Fig. 7.8.4 shows the joint distribution of kick magnitude and kick direction error for `surfinBH7dq4`, showing that direction errors are larger at low kick magnitudes. Our error in kick direction is below ~ 0.2 radians whenever $v_f \gtrsim 2 \times 10^{-3} c$.

We also compare the performance of our fits against several existing fitting formulae for remnant mass, spin, and kick which we denote as follows: HBMR ([32, 33] with $n_M = n_J = 3$), UIB [34], HL [35], HLZ [36], and CLZM ([37–41] as summarized in [42]). To partially account for spin precession, these fits are corrected as described in Ref. [99] and used in current LIGO/Virgo analyses [6, 100]: spins are evolved using PN from relaxation to the Schwarzschild innermost stable circular orbit, and

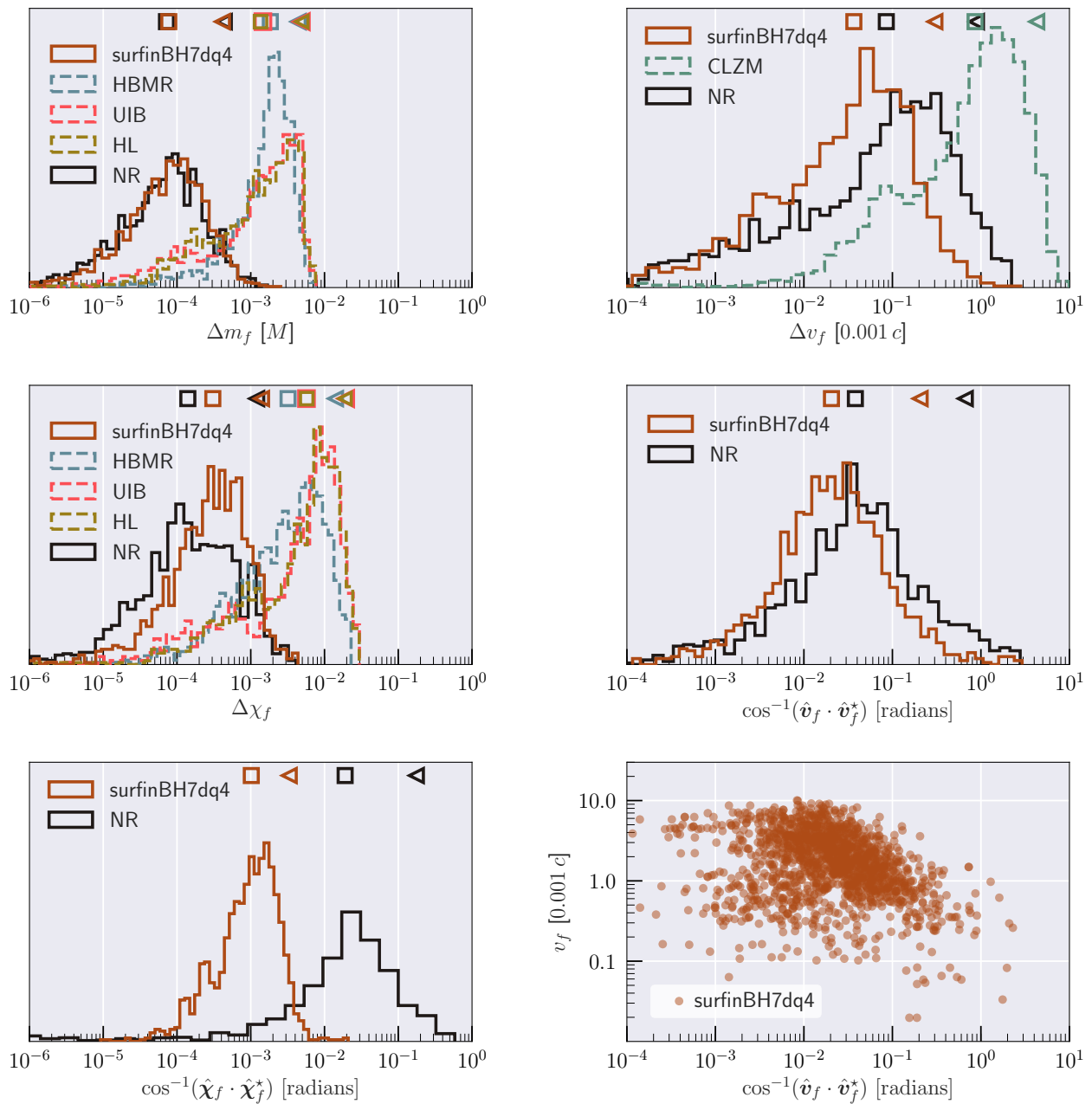


Figure 7.8.4: Error histograms for surfBH7dq4 for the remnant mass, spin magnitude, spin direction, kick magnitude, and kick direction for precessing BBH with mass ratios $q \leq 4$ and spin magnitudes $\chi_1, \chi_2 \leq 0.8$. The direction error is the angle between the predicted vector and a fiducial vector, taken to be the high-resolution NR case and indicated by $*$. Square (triangle) markers indicate median (95th percentile) values. Also shown are the NR resolution errors and errors for different existing fitting formulae. In the bottom-right panel we show the joint distribution of kick magnitude and kick-direction error.

final UIB and HL spins are post-processed by adding the sum of the in-plane spins in quadrature. Figure 7.8.4 shows that our procedure to predict remnant mass, spin magnitude, and kick magnitude for precessing systems is more accurate than these existing fits by at least an order of magnitude.

Our fits appear to outperform the NR simulations when estimating the spin direction. Once again, this is due to the post-junk-radiation initial spins of the two highest resolutions being inconsistent with each other for some of our simulations, so that different resolutions represent different physical systems (cf. App. 7.B). Therefore, the errors estimated by comparing the two highest resolutions is a poor estimate of the actual truncation error for these cases. The actual truncation error is likely to be close to the errors reproduced by the surrogate.

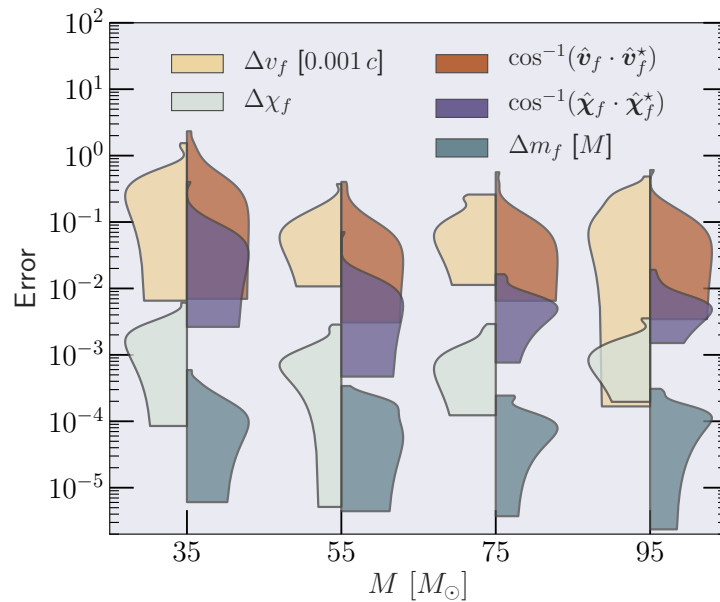


Figure 7.8.5: Errors for surfinBH7dq4 in predicting remnant properties when spins are specified at an orbital frequency of $f_0 = 10$ Hz. For four different total masses, we compute the differences between the surrogate prediction of various remnant properties with the value obtained in the NR simulation. For each mass, these differences are shown as a vertical histogram. Note that the distributions in these plots are normalized to have a fixed height, not fixed area.

The surfinBH7dq4 fits in Fig. 7.8.4 are evaluated using the NR spins at $t = -100M$ as inputs. In typical applications, one may have access to the spins only at the start of the waveform, rather than at $t = -100M$. For this case, as described in Sec. 7.7, we use a combination of PN and NRSur7dq4 to evolve the spins from any given starting frequency to $t = -100M$. These spins are then used to evaluate

the `surfinBH7dq4` fits. Thus, spins can be specified at any given orbital frequency and are evolved consistently before estimating the final BH properties. This is a crucial improvement (introduced by Ref. [57]) over previous results, which, being calibrated solely to non-precessing systems, suffer from ambiguities regarding the time/frequency at which spins are defined.

Figure 7.8.5 shows the errors in `surfinBH7dq4` when the spins are specified at an orbital frequency $f_0 = 10$ Hz. These errors are computed by comparing against 23 long NR ($3 \times 10^4 M$ to $10^5 M$ in length) simulations [81] with mass ratios $q \leq 4$ and generically oriented spins with magnitudes $\chi_1, \chi_2 \sim 0.5$. None of these simulations were used to train the fits. Longer PN evolutions are needed at lower total masses, and the errors are therefore larger. These errors will decrease with an improved spin evolution procedure. Note, however, that our predictions are still more accurate than those of existing fitting formulae (cf. Fig. 7.8.4).

7.9 Conclusion

We present new NR surrogate models for precessing BBH systems with generic spins and unequal masses. In particular, we model the two most-used outputs of NR simulations: the gravitational waveform and the properties (mass, spin, and recoil kick) of the final BH formed after the merger. Trained against 1528 NR simulations with mass ratios $q \leq 4$, spin magnitudes $\chi_{1,2} \leq 0.8$, and generic spin directions, both these models are shown to reproduce the NR simulations with accuracies comparable to those of the simulations themselves.

The waveform model, `NRSur7dq4`, includes all spin-weighted spherical harmonic modes up to $\ell = 4$. The precession frame dynamics and spin evolution of the BHs are also modeled as byproducts. Through a cross-validation study, we show that the mismatches for `NRSur7dq4` against NR computed with the Advanced LIGO design sensitivity noise curve are always $\lesssim 8 \times 10^{-3}$ at the 95 percentile level over the mass range $50 - 200 M_\odot$. This is at least an order of magnitude improvement over existing waveform models. Compared to `NRSur7dq2` [56], which was trained on $q \leq 2$, the new `NRSur7dq4` model extends the range of accessible mass ratios while being just as accurate as the `NRSur7dq2` model over their common domain of applicability.

For the final BH model, `surfinBH7dq4`, the 95th percentile errors are $\sim 5 \times 10^{-4} M$ for mass, $\sim 2 \times 10^{-3}$ for spin magnitude, $\sim 4 \times 10^{-4} c$ for kick magnitude. Once again, these are lower than that of existing models by at least an order of magnitude. In addition, we also model the spin and kick directions. Moreover, the GPR methods employed

here naturally provide error estimates along with the fitted values. These uncertainty estimates can be incorporated into data analysis applications to marginalize over systematic uncertainties.

Future work

In App. 7.A we test the performance of these surrogate models when extrapolated outside their training range to $q = 6$. We find that our models degrade significantly at these mass ratios, but suitable precessing simulations are currently not available for testing at intermediate mass ratios $4 < q < 6$. In general, we advice caution with extrapolation. A natural improvement of both NRSur7dq4 and surfinBH7dq4 is to extend their range of validity with new training simulations at higher mass ratios and spin magnitudes. We note, however, that both these regimes are increasingly expensive to model in NR.

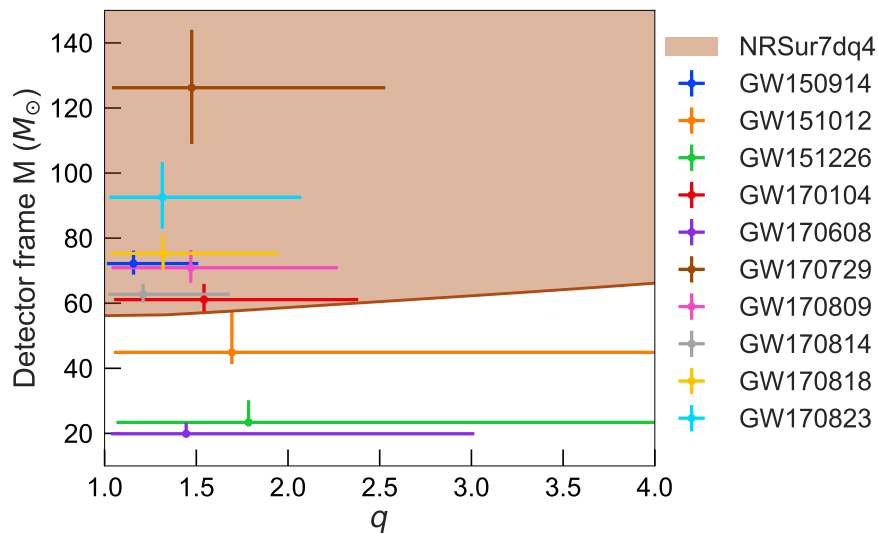


Figure 7.9.1: The shaded region shows the regime of validity of the (2,2) mode of NRSur7dq4 with a starting frequency of 20 Hz. Also shown are the parameter ranges for the 10 BBH signals seen by LIGO and Virgo during the first two observing runs [9]. The markers indicate the median values of the marginalized posteriors for the detector frame total mass M and mass ratio q . The error bars indicate the range between the 5th percentile and 95th percentile values of the posteriors.

Another important limitation of these models is that they are restricted to the same length as the NR simulations (starting time of $\sim 4300M$ before the peak or about 20 orbits). For LIGO, assuming a starting GW frequency of 20 Hz, the (2, 2) mode of the surrogate is valid for total masses $M \gtrsim 66M_{\odot}$. This number, however, depends

on the mass ratio. Fig. 7.9.1 shows the mass range of validity of NRSur7dq4 as a function of mass ratio. We compare this with the parameters of the 10 BBH detections seen by LIGO and Virgo in the first two observing runs [9]. NRSur7dq4 sufficiently covers the posterior spread of most but not all of these detections, the main limitation being the number of orbits covered by the model. However, see Ref. [101] for an example of NR surrogates used in data analysis with GW signals.

A promising avenue to extend the length of the waveforms is to “hybridize” the simulations using PN waveforms in the early inspiral. This approach already was found to be successful for the case of aligned-spin BBH [79], but still needs to be generalized to precessing spins. Furthermore, it is not clear if the current length of the NR simulations is sufficient to guarantee good attachment of the PN and NR waveforms for precessing BBH.

Despite these limitations, in their regime of validity, the models presented in the paper are the most accurate models currently available for precessing BBHs. As shown in this paper, our models rival the accuracy of the NR simulations, while being very cheap to evaluate. As more and more BBHs are detected at higher signal-to-noise ratios, fast yet accurate models such as these will contribute to turning GW astronomy into high precision science.

7.10 Acknowledgments

We thank Dan Hemberger, Kevin Barkett, Marissa Walker, Matt Giesler, Nils Deppe, Francois Hebert, Maria Okounkova, and Geoffrey Lovelace for helping carry out the new SpEC simulations used in this work. V.V. and M.S. are supported by the Sherman Fairchild Foundation, and NSF grants PHY-170212 and PHY-1708213 at Caltech. L.E.K. acknowledges support from the Sherman Fairchild Foundation and NSF grant PHY-1606654 at Cornell. S.E.F is partially supported by NSF grant PHY-1806665. This work used the Extreme Science and Engineering Discovery Environment (XSEDE), which is supported by National Science Foundation grant number ACI-1548562. This research is part of the Blue Waters sustained-petascale computing project, which is supported by the National Science Foundation (awards OCI-0725070 and ACI-1238993) and the state of Illinois. Blue Waters is a joint effort of the University of Illinois at Urbana-Champaign and its National Center for Supercomputing Applications. Simulations were performed on NSF/NCSA Blue Waters under allocation NSF PRAC-1713694; on the Wheeler cluster at Caltech, which is supported by the Sherman Fairchild Foundation and by Caltech; and

on XSEDE resources Bridges at the Pittsburgh Supercomputing Center, Comet at the San Diego Supercomputer Center, and Stampede and Stampede2 at the Texas Advanced Computing Center, through allocation TG-PHY990007N. Computations for building the model were performed on Wheeler.

APPENDIX

7.A Evaluating surrogates at larger mass ratios

In this Appendix we assess the performance of the NRSur7dq4 and surfinBH7dq4 models when evaluated at mass ratio $q = 6$. Doing so is effectively an extrapolation because $q = 6$ is outside the training range of the surrogates ($q \leq 4$). Figure 7.A.1 shows the errors for NRSur7dq4 when compared against 100 NR simulations with $q = 6$ and generically precessing spins with magnitudes $\chi_1, \chi_2 \leq 0.8$. These simulations have been assigned the identifiers SXS:BBH:2164 - SXS:BBH:2263, and are made publicly available through the SXS public catalog [80]. The mismatches are computed in the same manner as in the left panel of Fig. 7.8.1, which we reproduce here for comparison.

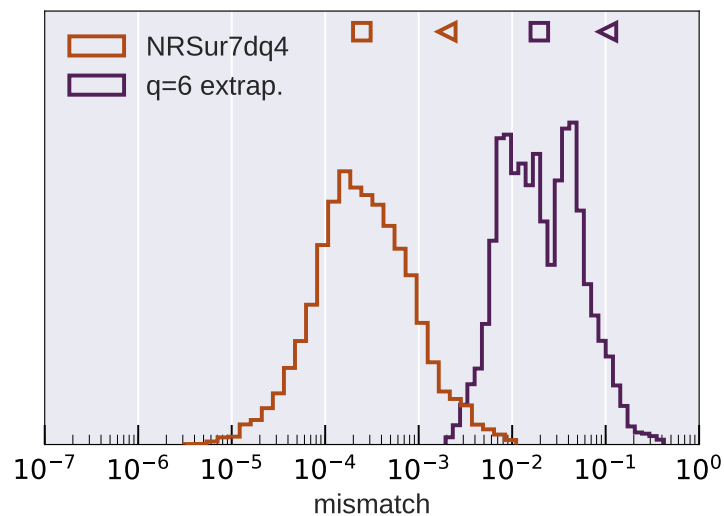


Figure 7.A.1: Mismatch histogram when extrapolating the NRSur7dq4 waveform model to mass ratio $q = 6$. The mismatches are computed using a flat noise curve. The training range errors from the left panel of Fig. 7.8.1 are reproduced here for comparison. The square (triangle) markers indicate median (95th percentile) values.

Similarly, Fig. 7.A.2 shows the performance of surfinBH7dq4 when extrapolating to $q = 6$. We show the errors when the fits are evaluated using the NR spins at $t = -100M$ as well as when the spins are specified at the start of the NR simulations. In the latter case, we use the extrapolated dynamics surrogate of NRSur7dq4 to evolve the spins to $t = -100M$ and then evaluate the fits. We reproduce the training range errors from Fig. 7.8.4 for comparison.

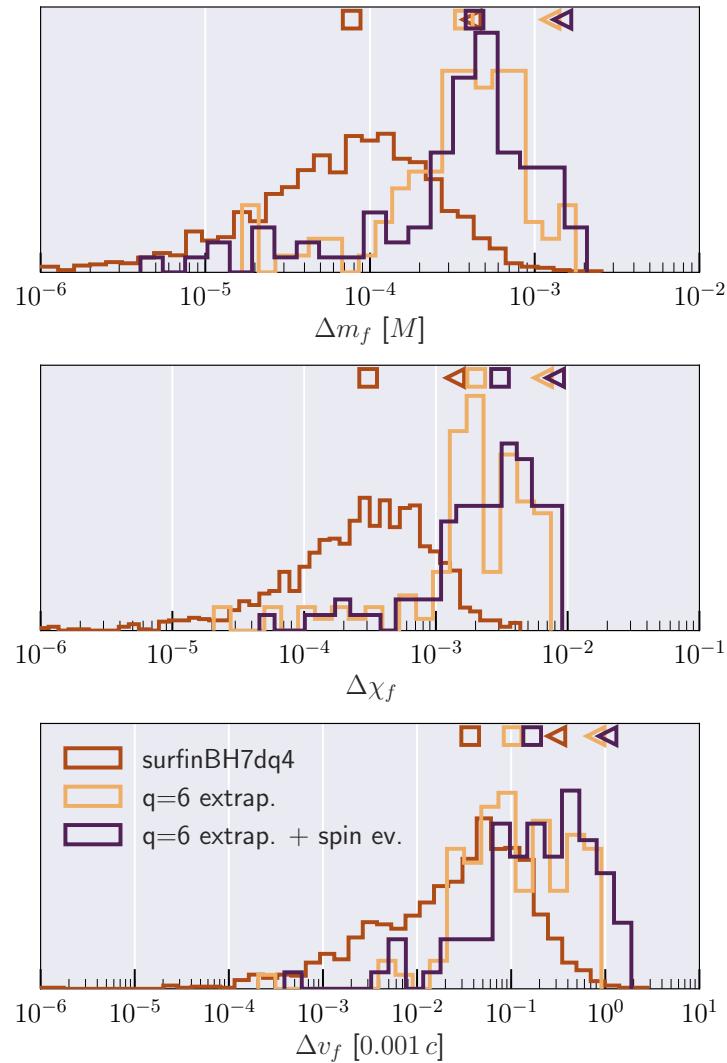


Figure 7.A.2: Error histograms of the remnant mass, spin magnitude and kick magnitude when extrapolating surfinBH7dq4 to mass ratio $q = 6$. The training range errors from Fig. 7.8.4 are reproduced here for comparison. We show errors using the NR spins at $t = -100M$ (yellow) as well as the initial NR spins (blue) as inputs for the model. The square (triangle) markers indicate median (95th percentile) values.

We find that both surrogate models degrade significantly when extrapolated to $q = 6$ and we do not recommend their usage for such mass ratios. Unfortunately, we do not have enough suitable precessing simulations with $4 < q < 6$ with which to test at what mass ratio the degradation becomes significant. We leave these tests, as well as extending the models to larger mass ratios by adding NR simulations, to future work.

7.B On the high mismatch tail in NR errors

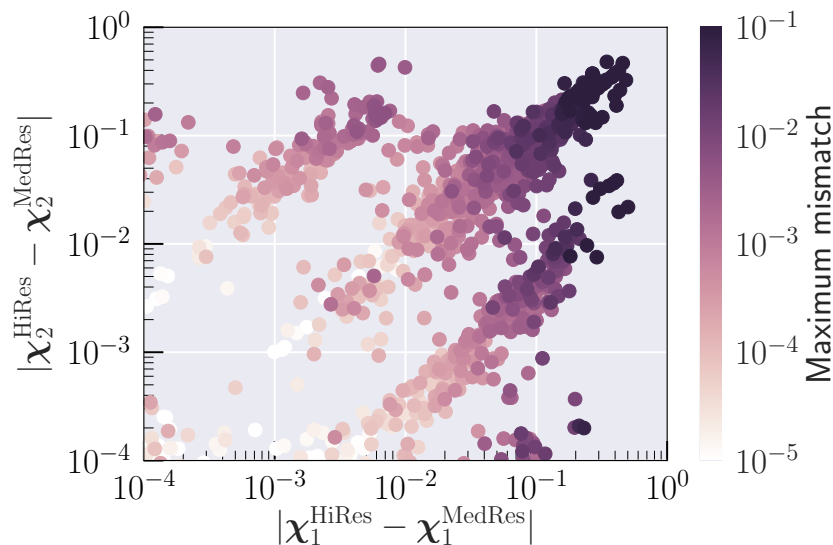


Figure 7.B.1: Dependence of the NR resolution error on the difference in the relaxation-time spins of the two highest resolutions (labeled HiRes and MedRes). The horizontal (vertical) axis shows the difference between the spin of the heavier (lighter) BH. The colors show the largest (flat noise) mismatch between the waveforms of the two resolutions over different points in the sky. Large mismatches occur when the difference between the relaxation-time spins of the two resolutions is large.

The histogram of NR errors in the left panel of Fig. 7.8.1 shows a significant tail to the right, i.e. at large mismatches. In Sec. 7.8, this tail was attributed to different resolutions of the same NR simulation having different physical parameters, namely the “initial” spins, which are measured at the relaxation time [81] after the poorly-resolved junk-radiation transients have settled. In this Appendix we provide some evidence for this claim. Figure 7.B.1 shows the maximum mismatch (with a flat noise curve) over points in the sky versus the difference in the relaxation-time dimensionless spins between the two highest resolutions. We refer to the two highest resolutions as HiRes and MedRes, and their corresponding relaxation-

time dimensionless spins are denoted by $(\chi_1^{\text{HiRes}}, \chi_2^{\text{HiRes}})$ and $(\chi_1^{\text{MedRes}}, \chi_2^{\text{MedRes}})$, respectively. We note that the largest mismatch occurs when the spin difference is largest between the two resolutions. For a significant fraction of the simulations the spins can be different by about 0.1; for these cases the two resolutions essentially represent two different physical systems, so the difference in waveforms between the two resolutions fails to be a good estimate of the truncation error in the simulations.

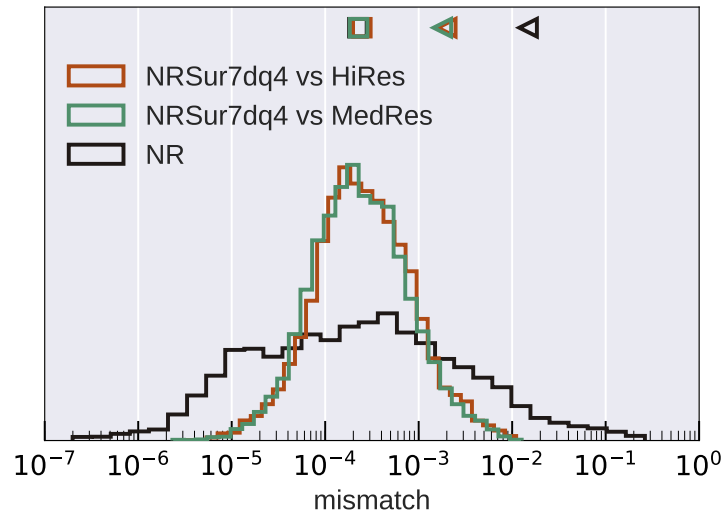


Figure 7.B.2: Mismatch histograms for NRSur7dq4 when compared against the two highest available NR simulations (referred to as HiRes and MedRes). Also shown are mismatches between the two resolutions (labeled NR). The “NRSur7dq4 vs HiRes” and NR errors are the same as the red and black histograms, respectively, in the left panel of Fig. 7.8.1. These are flat noise mismatches, computed at several points in the sky. The square (triangle) markers indicate median (95th percentile) values.

Figure 7.B.1 suggests that the high NR mismatch tail of Fig. 7.8.1 is artificially large, and if the two resolutions were to correspond to the same physical system, the tail would be shorter. We test this in Fig. 7.B.2, where we compare the surrogate against the MedRes simulations, but use the spins of the MedRes simulation $(\chi_1^{\text{MedRes}}, \chi_2^{\text{MedRes}})$ to evaluate the surrogate. The surrogate mismatches against the HiRes simulations as well as the NR resolution mismatches (HiRes vs MedRes) are reproduced from Fig. 7.8.1 for comparison. We note that the surrogate mismatches when compared against the MedRes simulations always lie below $\sim 10^{-2}$ and do not have the high mismatch tail seen for the NR resolution mismatches. In this test, we are treating the surrogate, which is trained on the HiRes simulations, as a proxy for the HiRes dataset. Evaluating the surrogate with the parameters of a

MedRes simulation is treated as a proxy for performing the HiRes simulation with the same parameters. Therefore, the green histogram in Fig. 7.B.2 can be treated as the “true” resolution error when the parameters of the resolutions are the same. As expected for this case, this estimate of the resolution error agrees with the errors for the surrogate model (red histogram).

Together, Figs. 7.B.1 and 7.B.2 show that the high NR mismatch tail in the left panel of Fig. 7.8.1 is due to the difference in the parameters of the different NR resolutions. We believe this difference arises from spurious initial transients known as “junk radiation”. These transients result from initial data that do not precisely represent a snapshot of a binary that has evolved from $t = -\infty$. The transients quickly leave the simulation domain after about one or two binary orbits. It is computationally expensive to resolve the high spatial and temporal frequencies of the transients, so we typically choose not to resolve these transients at all, and instead we simply discard the initial part of the waveform. Because some of the transients carry energy and angular momentum down the BHs, the masses and spins are modified, so we measure “initial” masses and spins at a relaxation time [81] deemed sufficiently late that the transients have decayed away. Because we do not fully resolve the transients, their effect on the masses and spins are not always convergent with resolution.

This issue should ideally be resolved with improved, junk-free initial data (see Ref. [102] for steps in this direction). In the meantime, we propose a change in how SpEC performs different resolutions for the same simulation. Currently, initial data are constructed by solving the Einstein constraint equations [74, 103]. The same constraint-satisfying initial data are then interpolated onto several grids of different resolution, and Einstein’s equations are evolved on each grid independently. Our proposal is to first evolve the initial data using the high resolution grid until the transients leave the simulation domain, and then interpolate the data at that time onto grids of lower resolution, and evolve Einstein’s equations on these lower-resolution grids independently. This way all resolutions start with the same initial data at a time after transients have decayed away instead of at the start of the simulation, and the masses and spins of the black holes should be convergent.

This proposal is tested in Fig. 7.B.3 for the case leading to the largest NR mismatch in the left panel of Fig. 7.8.1. We perform the resolution branching at $t \sim 1000M$ after the start of the high resolution simulation. The outer boundary is at $\sim 600M$ and this is sufficient time for junk radiation to leave the simulation domain. We find

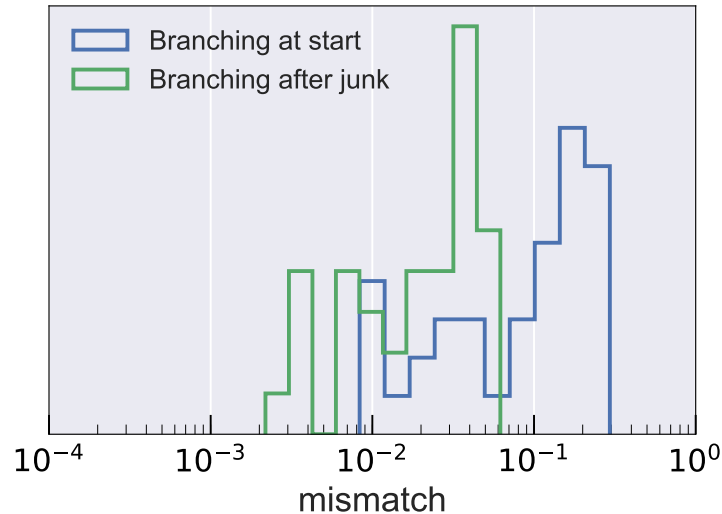


Figure 7.B.3: NR resolution mismatches for the simulation leading to the largest NR mismatch in the left panel of Fig. 7.8.1. The different samples in the histogram correspond to comparisons at different angles on the sky. The blue histogram shows the current resolution errors when the two resolutions start with the same initial data at the start of the simulation. All points in the blue histogram are the same as those included in the left panel of Fig. 7.8.1. The green histogram shows the resolution errors for the same case when the two resolutions start with the same initial data at $\sim 1000M$ after start, at which point the junk radiation has left the simulation domain.

that the mismatches decrease significantly when the resolution branching is done post-junk, as the resolutions now correspond to the same physical system.

References

- [1] J. Aasi et al. “Advanced LIGO”. In: *Class. Quant. Grav.* 32 (2015), p. 074001. DOI: [10.1088/0264-9381/32/7/074001](https://doi.org/10.1088/0264-9381/32/7/074001). arXiv: 1411.4547 [gr-qc].
- [2] F. Acernese et al. “Advanced Virgo: a second-generation interferometric gravitational wave detector”. In: 32.2 (2015), p. 024001. DOI: [10.1088/0264-9381/32/2/024001](https://doi.org/10.1088/0264-9381/32/2/024001). arXiv: 1408.3978 [gr-qc].
- [3] B. P. Abbott et al. “Observation of Gravitational Waves from a Binary Black Hole Merger”. In: *Phys. Rev. Lett.* 116.6 (2016), p. 061102. DOI: [10.1103/PhysRevLett.116.061102](https://doi.org/10.1103/PhysRevLett.116.061102). arXiv: 1602.03837 [gr-qc].
- [4] Benjamin P. Abbott et al. “GW170817: Observation of Gravitational Waves from a Binary Neutron Star Inspiral”. In: *Phys. Rev. Lett.* 119.16 (2017), p. 161101. DOI: [10.1103/PhysRevLett.119.161101](https://doi.org/10.1103/PhysRevLett.119.161101). arXiv: 1710.05832 [gr-qc].

- [5] B. P. Abbott et al. “GW151226: Observation of Gravitational Waves from a 22-Solar-Mass Binary Black Hole Coalescence”. In: *Phys. Rev. Lett.* 116.24 (2016), p. 241103. doi: [10.1103/PhysRevLett.116.241103](https://doi.org/10.1103/PhysRevLett.116.241103). arXiv: [1606.04855](https://arxiv.org/abs/1606.04855) [gr-qc].
- [6] Benjamin P. Abbott et al. “GW170104: Observation of a 50-Solar-Mass Binary Black Hole Coalescence at Redshift 0.2”. In: *Phys. Rev. Lett.* 118.22 (2017), p. 221101. doi: [10.1103/PhysRevLett.118.221101](https://doi.org/10.1103/PhysRevLett.118.221101). arXiv: [1706.01812](https://arxiv.org/abs/1706.01812) [gr-qc].
- [7] B. P. Abbott et al. “GW170608: Observation of a 19-solar-mass Binary Black Hole Coalescence”. In: *Astrophys. J.* 851.2 (2017), p. L35. doi: [10.3847/2041-8213/aa9f0c](https://doi.org/10.3847/2041-8213/aa9f0c). arXiv: [1711.05578](https://arxiv.org/abs/1711.05578) [astro-ph.HE].
- [8] B. P. Abbott et al. “GW170814: A Three-Detector Observation of Gravitational Waves from a Binary Black Hole Coalescence”. In: *Phys. Rev. Lett.* 119.14 (2017), p. 141101. doi: [10.1103/PhysRevLett.119.141101](https://doi.org/10.1103/PhysRevLett.119.141101). arXiv: [1709.09660](https://arxiv.org/abs/1709.09660) [gr-qc].
- [9] B. P. Abbott et al. “GWTC-1: A Gravitational-Wave Transient Catalog of Compact Binary Mergers Observed by LIGO and Virgo during the First and Second Observing Runs”. In: (2018). arXiv: [1811.12907](https://arxiv.org/abs/1811.12907) [astro-ph.HE].
- [10] B. P. Abbott et al. “Prospects for Observing and Localizing Gravitational-Wave Transients with Advanced LIGO, Advanced Virgo and KAGRA”. In: *Living Rev. Rel.* 21.1 (2018), p. 3. doi: [10.1007/s41114-018-0012-9](https://doi.org/10.1007/s41114-018-0012-9), [10.1007/lrr-2016-1](https://doi.org/10.1007/lrr-2016-1). arXiv: [1304.0670](https://arxiv.org/abs/1304.0670) [gr-qc].
- [11] B. P. Abbott et al. “Binary Black Hole Population Properties Inferred from the First and Second Observing Runs of Advanced LIGO and Advanced Virgo”. In: (2018). arXiv: [1811.12940](https://arxiv.org/abs/1811.12940) [astro-ph.HE].
- [12] Curt Cutler and Eanna E. Flanagan. “Gravitational waves from merging compact binaries: How accurately can one extract the binary’s parameters from the inspiral wave form?” In: *Phys. Rev. D* 49 (1994), pp. 2658–2697. doi: [10.1103/PhysRevD.49.2658](https://doi.org/10.1103/PhysRevD.49.2658). arXiv: [gr-qc/9402014](https://arxiv.org/abs/gr-qc/9402014) [gr-qc].
- [13] B. P. Abbott et al. “Properties of the binary black hole merger GW150914”. In: *Phys. Rev. Lett.* 116 (2016), p. 241102. doi: [10.1103/PhysRevLett.116.241102](https://doi.org/10.1103/PhysRevLett.116.241102). arXiv: [1602.03840](https://arxiv.org/abs/1602.03840) [gr-qc].
- [14] J. Veitch et al. “Parameter estimation for compact binaries with ground-based gravitational-wave observations using the LALInference software library”. In: *Phys. Rev. D* 91.4 (2015), p. 042003. doi: [10.1103/PhysRevD.91.042003](https://doi.org/10.1103/PhysRevD.91.042003). arXiv: [1409.7215](https://arxiv.org/abs/1409.7215) [gr-qc].
- [15] B. P. Abbott et al. “Tests of general relativity with GW150914”. In: *Phys. Rev. Lett.* 116 (2016), p. 221101. arXiv: [1602.03841](https://arxiv.org/abs/1602.03841) [gr-qc].
- [16] “Tests of General Relativity with the Binary Black Hole Signals from the LIGO-Virgo Catalog GWTC-1”. In: (2019). arXiv: [1903.04467](https://arxiv.org/abs/1903.04467) [gr-qc].

- [17] Abhirup Ghosh et al. “Testing general relativity using gravitational wave signals from the inspiral, merger and ringdown of binary black holes”. In: *Class. Quant. Grav.* 35.1 (2018), p. 014002. DOI: [10.1088/1361-6382/aa972e](https://doi.org/10.1088/1361-6382/aa972e). arXiv: [1704.06784](https://arxiv.org/abs/1704.06784) [gr-qc].
- [18] Manuela Campanelli et al. “Maximum gravitational recoil”. In: *Phys. Rev. Lett.* 98 (2007), p. 231102. DOI: [10.1103/PhysRevLett.98.231102](https://doi.org/10.1103/PhysRevLett.98.231102). arXiv: [gr-qc/0702133](https://arxiv.org/abs/gr-qc/0702133) [GR-QC].
- [19] J. A. Gonzalez et al. “Supermassive recoil velocities for binary black-hole mergers with antialigned spins”. In: *Phys. Rev. Lett.* 98 (2007), p. 231101. DOI: [10.1103/PhysRevLett.98.231101](https://doi.org/10.1103/PhysRevLett.98.231101). arXiv: [gr-qc/0702052](https://arxiv.org/abs/gr-qc/0702052) [GR-QC].
- [20] Davide Gerosa and Alberto Sesana. “Missing black holes in brightest cluster galaxies as evidence for the occurrence of superkicks in nature”. In: *Mon. Not. Roy. Astron. Soc.* 446 (2015), pp. 38–55. DOI: [10.1093/mnras/stu2049](https://doi.org/10.1093/mnras/stu2049). arXiv: [1405.2072](https://arxiv.org/abs/1405.2072) [astro-ph.GA].
- [21] Sebastian Khan et al. “Phenomenological model for the gravitational-wave signal from precessing binary black holes with two-spin effects”. In: (2018). arXiv: [1809.10113](https://arxiv.org/abs/1809.10113) [gr-qc].
- [22] Roberto Cotesta et al. “Enriching the Symphony of Gravitational Waves from Binary Black Holes by Tuning Higher Harmonics”. In: *Phys. Rev. D* 98.8 (2018), p. 084028. DOI: [10.1103/PhysRevD.98.084028](https://doi.org/10.1103/PhysRevD.98.084028). arXiv: [1803.10701](https://arxiv.org/abs/1803.10701) [gr-qc].
- [23] Lionel London et al. “First higher-multipole model of gravitational waves from spinning and coalescing black-hole binaries”. In: *Phys. Rev. Lett.* 120.16 (2018), p. 161102. DOI: [10.1103/PhysRevLett.120.161102](https://doi.org/10.1103/PhysRevLett.120.161102). arXiv: [1708.00404](https://arxiv.org/abs/1708.00404) [gr-qc].
- [24] Yi Pan et al. “Inspirational-merger-ringdown waveforms of spinning, precessing black-hole binaries in the effective-one-body formalism”. In: *Phys. Rev. D* 89.8 (2014), p. 084006. DOI: [10.1103/PhysRevD.89.084006](https://doi.org/10.1103/PhysRevD.89.084006). arXiv: [1307.6232](https://arxiv.org/abs/1307.6232) [gr-qc].
- [25] Alejandro Bohé et al. “Improved effective-one-body model of spinning, non-precessing binary black holes for the era of gravitational-wave astrophysics with advanced detectors”. In: *Phys. Rev. D* 95 (4 Feb. 2017), p. 044028. DOI: [10.1103/PhysRevD.95.044028](https://doi.org/10.1103/PhysRevD.95.044028). arXiv: [1611.03703](https://arxiv.org/abs/1611.03703) [gr-qc]. URL: <https://link.aps.org/doi/10.1103/PhysRevD.95.044028>.
- [26] Sebastian Khan et al. “Frequency-domain gravitational waves from non-precessing black-hole binaries. II. A phenomenological model for the advanced detector era”. In: *Phys. Rev. D* 93.4 (2016), p. 044007. DOI: [10.1103/PhysRevD.93.044007](https://doi.org/10.1103/PhysRevD.93.044007). arXiv: [1508.07253](https://arxiv.org/abs/1508.07253) [gr-qc].

- [27] Mark Hannam et al. “A simple model of complete precessing black-hole-binary gravitational waveforms”. In: *Phys. Rev. Lett.* 113 (2014), p. 151101. doi: [10.1103/PhysRevLett.113.151101](https://doi.org/10.1103/PhysRevLett.113.151101). arXiv: [1308.3271](https://arxiv.org/abs/1308.3271) [gr-qc].
- [28] Andrea Taracchini et al. “Effective-one-body model for black-hole binaries with generic mass ratios and spins”. In: *Phys. Rev. D* 89.6 (2014), p. 061502. doi: [10.1103/PhysRevD.89.061502](https://doi.org/10.1103/PhysRevD.89.061502). arXiv: [1311.2544](https://arxiv.org/abs/1311.2544) [gr-qc].
- [29] Yi Pan et al. “Inspirational-merger-ringdown multipolar waveforms of nonspinning black-hole binaries using the effective-one-body formalism”. In: *Phys. Rev. D* 84 (2011), p. 124052. doi: [10.1103/PhysRevD.84.124052](https://doi.org/10.1103/PhysRevD.84.124052). arXiv: [1106.1021](https://arxiv.org/abs/1106.1021) [gr-qc].
- [30] Ajit Kumar Mehta et al. “Accurate inspiral-merger-ringdown gravitational waveforms for nonspinning black-hole binaries including the effect of subdominant modes”. In: *Phys. Rev. D* 96.12 (2017), p. 124010. doi: [10.1103/PhysRevD.96.124010](https://doi.org/10.1103/PhysRevD.96.124010). arXiv: [1708.03501](https://arxiv.org/abs/1708.03501) [gr-qc].
- [31] Stanislav Babak, Andrea Taracchini, and Alessandra Buonanno. “Validating the effective-one-body model of spinning, precessing binary black holes against numerical relativity”. In: *Phys. Rev. D* 95.2 (2017), p. 024010. doi: [10.1103/PhysRevD.95.024010](https://doi.org/10.1103/PhysRevD.95.024010). arXiv: [1607.05661](https://arxiv.org/abs/1607.05661) [gr-qc].
- [32] Fabian Hofmann, Enrico Barausse, and Luciano Rezzolla. “The final spin from binary black holes in quasi-circular orbits”. In: *Astrophys. J.* 825.2 (2016), p. L19. doi: [10.3847/2041-8205/825/2/L19](https://doi.org/10.3847/2041-8205/825/2/L19). arXiv: [1605.01938](https://arxiv.org/abs/1605.01938) [gr-qc].
- [33] Enrico Barausse, Viktoriya Morozova, and Luciano Rezzolla. “On the mass radiated by coalescing black-hole binaries”. In: *Astrophys. J.* 758 (2012). [Erratum: *Astrophys. J.* 786,76(2014)], p. 63. doi: [10.1088/0004-637X/758/1/63](https://doi.org/10.1088/0004-637X/758/1/63). arXiv: [1206.3803](https://arxiv.org/abs/1206.3803) [gr-qc].
- [34] Xisco Jiménez-Forteza et al. “Hierarchical data-driven approach to fitting numerical relativity data for nonprecessing binary black holes with an application to final spin and radiated energy”. In: *Phys. Rev. D* 95.6 (2017), p. 064024. doi: [10.1103/PhysRevD.95.064024](https://doi.org/10.1103/PhysRevD.95.064024). arXiv: [1611.00332](https://arxiv.org/abs/1611.00332) [gr-qc].
- [35] James Healy and Carlos O. Lousto. “Remnant of binary black-hole mergers: New simulations and peak luminosity studies”. In: *Phys. Rev. D* 95.2 (2017), p. 024037. doi: [10.1103/PhysRevD.95.024037](https://doi.org/10.1103/PhysRevD.95.024037). arXiv: [1610.09713](https://arxiv.org/abs/1610.09713) [gr-qc].
- [36] James Healy, Carlos O. Lousto, and Yosef Zlochower. “Remnant mass, spin, and recoil from spin aligned black-hole binaries”. In: *Phys. Rev. D* 90.10 (2014), p. 104004. doi: [10.1103/PhysRevD.90.104004](https://doi.org/10.1103/PhysRevD.90.104004). arXiv: [1406.7295](https://arxiv.org/abs/1406.7295) [gr-qc].

- [37] Jose A. Gonzalez et al. “Total recoil: The Maximum kick from nonspinning black-hole binary inspiral”. In: *Phys. Rev. Lett.* 98 (2007), p. 091101. DOI: [10.1103/PhysRevLett.98.091101](https://doi.org/10.1103/PhysRevLett.98.091101). arXiv: [gr-qc/0610154](https://arxiv.org/abs/gr-qc/0610154) [gr-qc].
- [38] Manuela Campanelli et al. “Large merger recoils and spin flips from generic black-hole binaries”. In: *Astrophys. J.* 659 (2007), pp. L5–L8. DOI: [10.1086/516712](https://doi.org/10.1086/516712). arXiv: [gr-qc/0701164](https://arxiv.org/abs/gr-qc/0701164) [gr-qc].
- [39] Carlos O. Lousto and Yosef Zlochower. “Further insight into gravitational recoil”. In: *Phys. Rev.* D77 (2008), p. 044028. DOI: [10.1103/PhysRevD.77.044028](https://doi.org/10.1103/PhysRevD.77.044028). arXiv: [0708.4048](https://arxiv.org/abs/0708.4048) [gr-qc].
- [40] Carlos O. Lousto et al. “Gravitational Recoil From Accretion-Aligned Black-Hole Binaries”. In: *Phys. Rev.* D85 (2012), p. 084015. DOI: [10.1103/PhysRevD.85.084015](https://doi.org/10.1103/PhysRevD.85.084015). arXiv: [1201.1923](https://arxiv.org/abs/1201.1923) [gr-qc].
- [41] Carlos O. Lousto and Yosef Zlochower. “Nonlinear Gravitational Recoil from the Mergers of Precessing Black-Hole Binaries”. In: *Phys. Rev.* D87.8 (2013), p. 084027. DOI: [10.1103/PhysRevD.87.084027](https://doi.org/10.1103/PhysRevD.87.084027). arXiv: [1211.7099](https://arxiv.org/abs/1211.7099) [gr-qc].
- [42] Davide Gerosa and Michael Kesden. “PRECESSION: Dynamics of spinning black-hole binaries with python”. In: *Phys. Rev.* D93.12 (2016), p. 124066. DOI: [10.1103/PhysRevD.93.124066](https://doi.org/10.1103/PhysRevD.93.124066). arXiv: [1605.01067](https://arxiv.org/abs/1605.01067) [astro-ph.HE].
- [43] James Healy and Carlos O. Lousto. “Hangup effect in unequal mass binary black hole mergers and further studies of their gravitational radiation and remnant properties”. In: *Phys. Rev.* D97.8 (2018), p. 084002. DOI: [10.1103/PhysRevD.97.084002](https://doi.org/10.1103/PhysRevD.97.084002). arXiv: [1801.08162](https://arxiv.org/abs/1801.08162) [gr-qc].
- [44] Frank Herrmann et al. “Binary Black Holes: Spin Dynamics and Gravitational Recoil”. In: *Phys. Rev.* D76 (2007), p. 084032. DOI: [10.1103/PhysRevD.76.084032](https://doi.org/10.1103/PhysRevD.76.084032). arXiv: [0706.2541](https://arxiv.org/abs/0706.2541) [gr-qc].
- [45] Luciano Rezzolla et al. “On the final spin from the coalescence of two black holes”. In: *Phys. Rev.* D78 (2008), p. 044002. DOI: [10.1103/PhysRevD.78.044002](https://doi.org/10.1103/PhysRevD.78.044002). arXiv: [0712.3541](https://arxiv.org/abs/0712.3541) [gr-qc].
- [46] Luciano Rezzolla et al. “The Final spin from the coalescence of aligned-spin black-hole binaries”. In: *Astrophys. J.* 674 (2008), pp. L29–L32. DOI: [10.1086/528935](https://doi.org/10.1086/528935). arXiv: [0710.3345](https://arxiv.org/abs/0710.3345) [gr-qc].
- [47] Michael Kesden. “Can binary mergers produce maximally spinning black holes?” In: *Phys. Rev.* D78 (2008), p. 084030. DOI: [10.1103/PhysRevD.78.084030](https://doi.org/10.1103/PhysRevD.78.084030). arXiv: [0807.3043](https://arxiv.org/abs/0807.3043) [astro-ph].
- [48] Wolfgang Tichy and Pedro Marronetti. “The Final mass and spin of black hole mergers”. In: *Phys. Rev.* D78 (2008), p. 081501. DOI: [10.1103/PhysRevD.78.081501](https://doi.org/10.1103/PhysRevD.78.081501). arXiv: [0807.2985](https://arxiv.org/abs/0807.2985) [gr-qc].

- [49] Enrico Barausse and Luciano Rezzolla. “Predicting the direction of the final spin from the coalescence of two black holes”. In: *Astrophys. J.* 704 (2009), pp. L40–L44. DOI: [10.1088/0004-637X/704/1/L40](https://doi.org/10.1088/0004-637X/704/1/L40). arXiv: [0904.2577](https://arxiv.org/abs/0904.2577) [gr-qc].
- [50] Yosef Zlochower and Carlos O. Lousto. “Modeling the remnant mass, spin, and recoil from unequal-mass, precessing black-hole binaries: The Intermediate Mass Ratio Regime”. In: *Phys. Rev. D* 92.2 (2015). [Erratum: *Phys. Rev. D* 94, no. 2, 029901 (2016)], p. 024022. DOI: [10.1103/PhysRevD.92.024022](https://doi.org/10.1103/PhysRevD.92.024022). arXiv: [1503.07536](https://arxiv.org/abs/1503.07536) [gr-qc].
- [51] Theocharis A. Apostolatos et al. “Spin-induced orbital precession and its modulation of the gravitational waveforms from merging binaries”. In: *Phys. Rev. D* 49 (12 June 1994), pp. 6274–6297. DOI: [10.1103/PhysRevD.49.6274](https://doi.org/10.1103/PhysRevD.49.6274). URL: <https://link.aps.org/doi/10.1103/PhysRevD.49.6274>.
- [52] Davide Gerosa et al. “Resonant-plane locking and spin alignment in stellar-mass black-hole binaries: a diagnostic of compact-binary formation”. In: *Phys. Rev. D* 87 (2013), p. 104028. DOI: [10.1103/PhysRevD.87.104028](https://doi.org/10.1103/PhysRevD.87.104028). arXiv: [1302.4442](https://arxiv.org/abs/1302.4442) [gr-qc].
- [53] Salvatore Vitale et al. “Use of gravitational waves to probe the formation channels of compact binaries”. In: *Class. Quant. Grav.* 34.3 (2017), 03LT01. DOI: [10.1088/1361-6382/aa552e](https://doi.org/10.1088/1361-6382/aa552e). arXiv: [1503.04307](https://arxiv.org/abs/1503.04307) [gr-qc].
- [54] Ben Farr, Daniel E. Holz, and Will M. Farr. “Using Spin to Understand the Formation of LIGO and Virgo’s Black Holes”. In: *Astrophys. J.* 854.1 (2018), p. L9. DOI: [10.3847/2041-8213/aaa64](https://doi.org/10.3847/2041-8213/aaa64). arXiv: [1709.07896](https://arxiv.org/abs/1709.07896) [astro-ph.HE].
- [55] Davide Gerosa et al. “Spin orientations of merging black holes formed from the evolution of stellar binaries”. In: *Phys. Rev. D* 98.8 (2018), p. 084036. DOI: [10.1103/PhysRevD.98.084036](https://doi.org/10.1103/PhysRevD.98.084036). arXiv: [1808.02491](https://arxiv.org/abs/1808.02491) [astro-ph.HE].
- [56] Jonathan Blackman et al. “Numerical relativity waveform surrogate model for generically precessing binary black hole mergers”. In: *Phys. Rev. D* 96.2 (2017), p. 024058. DOI: [10.1103/PhysRevD.96.024058](https://doi.org/10.1103/PhysRevD.96.024058). arXiv: [1705.07089](https://arxiv.org/abs/1705.07089) [gr-qc].
- [57] Vijay Varma et al. “High-accuracy mass, spin, and recoil predictions of generic black-hole merger remnants”. In: *Phys. Rev. Lett.* 122 (2019), p. 011101. DOI: [10.1103/PhysRevLett.122.011101](https://doi.org/10.1103/PhysRevLett.122.011101). arXiv: [1809.09125](https://arxiv.org/abs/1809.09125) [gr-qc].
- [58] Vijay Varma and Parameswaran Ajith. “Effects of nonquadrupole modes in the detection and parameter estimation of black hole binaries with non-precessing spins”. In: *Phys. Rev. D* 96.12 (2017), p. 124024. DOI: [10.1103/PhysRevD.96.124024](https://doi.org/10.1103/PhysRevD.96.124024). arXiv: [1612.05608](https://arxiv.org/abs/1612.05608) [gr-qc].

- [59] Collin Capano, Yi Pan, and Alessandra Buonanno. “Impact of higher harmonics in searching for gravitational waves from nonspinning binary black holes”. In: *Phys. Rev. D* 89.10 (2014), p. 102003. doi: [10.1103/PhysRevD.89.102003](https://doi.org/10.1103/PhysRevD.89.102003). arXiv: [1311.1286 \[gr-qc\]](https://arxiv.org/abs/1311.1286).
- [60] Tyson B. Littenberg et al. “Systematic biases in parameter estimation of binary black-hole mergers”. In: 87 (2013), p. 104003. doi: [10.1103/PhysRevD.87.104003](https://doi.org/10.1103/PhysRevD.87.104003). arXiv: [1210.0893 \[gr-qc\]](https://arxiv.org/abs/1210.0893).
- [61] Juan Calderón Bustillo, Pablo Laguna, and Deirdre Shoemaker. “Detectability of gravitational waves from binary black holes: Impact of precession and higher modes”. In: *Phys. Rev. D* 95.10 (2017), p. 104038. doi: [10.1103/PhysRevD.95.104038](https://doi.org/10.1103/PhysRevD.95.104038). arXiv: [1612.02340 \[gr-qc\]](https://arxiv.org/abs/1612.02340).
- [62] Duncan A. Brown, Prayush Kumar, and Alexander H. Nitz. “Template banks to search for low-mass binary black holes in advanced gravitational-wave detectors”. In: 87 (2013), p. 082004. doi: [10.1103/PhysRevD.87.082004](https://doi.org/10.1103/PhysRevD.87.082004). arXiv: [1211.6184 \[gr-qc\]](https://arxiv.org/abs/1211.6184).
- [63] Vijay Varma et al. “Gravitational-wave observations of binary black holes: Effect of nonquadrupole modes”. In: *Phys. Rev. D* 90.12 (2014), p. 124004. doi: [10.1103/PhysRevD.90.124004](https://doi.org/10.1103/PhysRevD.90.124004). arXiv: [1409.2349 \[gr-qc\]](https://arxiv.org/abs/1409.2349).
- [64] Philip B. Graff, Alessandra Buonanno, and B. S. Sathyaprakash. “Missing Link: Bayesian detection and measurement of intermediate-mass black-hole binaries”. In: 92.2 (2015), p. 022002. doi: [10.1103/PhysRevD.92.022002](https://doi.org/10.1103/PhysRevD.92.022002). arXiv: [1504.04766 \[gr-qc\]](https://arxiv.org/abs/1504.04766).
- [65] Ian Harry, Juan Calderón Bustillo, and Alex Nitz. “Searching for the full symphony of black hole binary mergers”. In: *Phys. Rev. D* 97.2 (2018), p. 023004. doi: [10.1103/PhysRevD.97.023004](https://doi.org/10.1103/PhysRevD.97.023004). arXiv: [1709.09181 \[gr-qc\]](https://arxiv.org/abs/1709.09181).
- [66] Juan Calderón Bustillo et al. “Impact of gravitational radiation higher order modes on single aligned-spin gravitational wave searches for binary black holes”. In: *Phys. Rev. D* 93.8 (2016), p. 084019. doi: [10.1103/PhysRevD.93.084019](https://doi.org/10.1103/PhysRevD.93.084019). arXiv: [1511.02060 \[gr-qc\]](https://arxiv.org/abs/1511.02060).
- [67] Larne Pekowsky et al. “Impact of higher-order modes on the detection of binary black hole coalescences”. In: *Phys. Rev. D* 87.8 (2013), p. 084008. doi: [10.1103/PhysRevD.87.084008](https://doi.org/10.1103/PhysRevD.87.084008). arXiv: [1210.1891 \[gr-qc\]](https://arxiv.org/abs/1210.1891).
- [68] Patricia Schmidt et al. “Tracking the precession of compact binaries from their gravitational-wave signal”. In: *Phys. Rev. D* 84 (2011), p. 024046. doi: [10.1103/PhysRevD.84.024046](https://doi.org/10.1103/PhysRevD.84.024046). arXiv: [1012.2879 \[gr-qc\]](https://arxiv.org/abs/1012.2879).
- [69] R. O’Shaughnessy et al. “Efficient asymptotic frame selection for binary black hole spacetimes using asymptotic radiation”. In: *Phys. Rev. D* 84 (2011), p. 124002. doi: [10.1103/PhysRevD.84.124002](https://doi.org/10.1103/PhysRevD.84.124002). arXiv: [1109.5224 \[gr-qc\]](https://arxiv.org/abs/1109.5224).

- [70] Michael Boyle, Robert Owen, and Harald P. Pfeiffer. “A geometric approach to the precession of compact binaries”. In: 84 (2011), p. 124011. doi: [10.1103/PhysRevD.84.124011](https://doi.org/10.1103/PhysRevD.84.124011). eprint: [arXiv:1110.2965](https://arxiv.org/abs/1110.2965) [gr-qc].
- [71] Jonathan Blackman et al. “A Surrogate Model of Gravitational Waveforms from Numerical Relativity Simulations of Precessing Binary Black Hole Mergers”. In: *Phys. Rev. D* 95.10 (2017), p. 104023. doi: [10.1103/PhysRevD.95.104023](https://doi.org/10.1103/PhysRevD.95.104023). arXiv: [1701.00550](https://arxiv.org/abs/1701.00550) [gr-qc].
- [72] *The Spectral Einstein Code*. <http://www.black-holes.org/SpEC.html>.
- [73] Harald P. Pfeiffer et al. “A Multidomain spectral method for solving elliptic equations”. In: *Comput.Phys.Commun.* 152 (2003), pp. 253–273. doi: [10.1016/S0010-4655\(02\)00847-0](https://doi.org/10.1016/S0010-4655(02)00847-0). arXiv: [gr-qc/0202096](https://arxiv.org/abs/gr-qc/0202096) [gr-qc].
- [74] Geoffrey Lovelace et al. “Binary-black-hole initial data with nearly-extremal spins”. In: *Phys. Rev. D* 78 (2008), p. 084017. doi: [10.1103/PhysRevD.78.084017](https://doi.org/10.1103/PhysRevD.78.084017). arXiv: [0805.4192](https://arxiv.org/abs/0805.4192) [gr-qc].
- [75] Lee Lindblom et al. “A New generalized harmonic evolution system”. In: *Class.Quant.Grav.* 23 (2006), S447–S462. doi: [10.1088/0264-9381/23/16/S09](https://doi.org/10.1088/0264-9381/23/16/S09). arXiv: [gr-qc/0512093](https://arxiv.org/abs/gr-qc/0512093) [gr-qc].
- [76] Bela Szilagyi, Lee Lindblom, and Mark A. Scheel. “Simulations of Binary Black Hole Mergers Using Spectral Methods”. In: *Phys.Rev. D* 80 (2009), p. 124010. doi: [10.1103/PhysRevD.80.124010](https://doi.org/10.1103/PhysRevD.80.124010). arXiv: [0909.3557](https://arxiv.org/abs/0909.3557) [gr-qc].
- [77] Mark A. Scheel et al. “High-accuracy waveforms for binary black hole inspiral, merger, and ringdown”. In: *Phys.Rev. D* 79 (2009), p. 024003. doi: [10.1103/PhysRevD.79.024003](https://doi.org/10.1103/PhysRevD.79.024003). arXiv: [0810.1767](https://arxiv.org/abs/0810.1767) [gr-qc].
- [78] *Simulating eXtreme Spacetimes*. <http://www.black-holes.org/>.
- [79] Vijay Varma et al. “Surrogate model of hybridized numerical relativity binary black hole waveforms”. In: *Phys. Rev. D* 99.6 (2019), p. 064045. doi: [10.1103/PhysRevD.99.064045](https://doi.org/10.1103/PhysRevD.99.064045). arXiv: [1812.07865](https://arxiv.org/abs/1812.07865) [gr-qc].
- [80] SXS Collaboration. *The SXS Collaboration catalog of gravitational waveforms*. <http://www.black-holes.org/waveforms>.
- [81] M. Boyle et al. “The SXS Collaboration catalog of gravitational waveforms for merging black holes”. In: (2019). In preparation.
- [82] Alessandra Buonanno et al. “Reducing orbital eccentricity of precessing black-hole binaries”. In: 83 (2011), p. 104034. doi: [10.1103/PhysRevD.83.104034](https://doi.org/10.1103/PhysRevD.83.104034). arXiv: [1012.1549](https://arxiv.org/abs/1012.1549) [gr-qc].
- [83] Michael Boyle and Abdul H. Mroue. “Extrapolating gravitational-wave data from numerical simulations”. In: *Phys.Rev. D* 80 (2009), p. 124045. doi: [10.1103/PhysRevD.80.124045](https://doi.org/10.1103/PhysRevD.80.124045). arXiv: [0905.3177](https://arxiv.org/abs/0905.3177) [gr-qc].

- [84] Michael Boyle. “Transformations of asymptotic gravitational-wave data”. In: *Phys. Rev. D* 93.8 (2016), p. 084031. DOI: [10.1103/PhysRevD.93.084031](https://doi.org/10.1103/PhysRevD.93.084031). arXiv: [1509.00862](https://arxiv.org/abs/1509.00862) [gr-qc].
- [85] Michael Boyle. *Scri*. <https://github.com/moble/scri>.
- [86] S. Ossokine et al. “Comparing post-Newtonian and numerical relativity precession dynamics”. In: 92.10, 104028 (Nov. 2015), p. 104028. DOI: [10.1103/PhysRevD.92.104028](https://doi.org/10.1103/PhysRevD.92.104028). arXiv: [1502.01747](https://arxiv.org/abs/1502.01747) [gr-qc].
- [87] Davide Gerosa, François Hébert, and Leo C. Stein. “Black-hole kicks from numerical-relativity surrogate models”. In: *Phys. Rev. D* 97.10 (2018), p. 104049. DOI: [10.1103/PhysRevD.97.104049](https://doi.org/10.1103/PhysRevD.97.104049). arXiv: [1802.04276](https://arxiv.org/abs/1802.04276) [gr-qc].
- [88] Milton Ruiz et al. “Multipole expansions for energy and momenta carried by gravitational waves”. In: *Gen. Rel. Grav.* 40 (2008), p. 2467. DOI: [10.1007/s10714-007-0570-8](https://doi.org/10.1007/s10714-007-0570-8). arXiv: [0707.4654](https://arxiv.org/abs/0707.4654) [gr-qc].
- [89] S. E. Field et al. “Fast Prediction and Evaluation of Gravitational Waveforms Using Surrogate Models”. In: 4.3, 031006 (July 2014), p. 031006. DOI: [10.1103/PhysRevX.4.031006](https://doi.org/10.1103/PhysRevX.4.031006). arXiv: [1308.3565](https://arxiv.org/abs/1308.3565) [gr-qc].
- [90] Y. Maday et al. “A general multipurpose interpolation procedure: the magic points”. In: *Communications on Pure and Applied Analysis* 8 (2009), pp. 383–404. DOI: [10.3934/cpaa.2009.8.383](https://doi.org/10.3934/cpaa.2009.8.383).
- [91] Saifon Chaturantabut and Danny C Sorensen. “Nonlinear model reduction via discrete empirical interpolation”. In: *SIAM Journal on Scientific Computing* 32.5 (2010), pp. 2737–2764.
- [92] P. Ajith. “Addressing the spin question in gravitational-wave searches: Waveform templates for inspiralling compact binaries with nonprecessing spins”. In: 84 (2011), p. 084037. DOI: [10.1103/PhysRevD.84.084037](https://doi.org/10.1103/PhysRevD.84.084037). arXiv: [1107.1267](https://arxiv.org/abs/1107.1267) [gr-qc].
- [93] Eric Poisson and Clifford M. Will. “Gravitational waves from inspiraling compact binaries: Parameter estimation using second postNewtonian wave forms”. In: *Phys. Rev. D* 52 (1995), pp. 848–855. DOI: [10.1103/PhysRevD.52.848](https://doi.org/10.1103/PhysRevD.52.848). arXiv: [gr-qc/9502040](https://arxiv.org/abs/gr-qc/9502040) [gr-qc].
- [94] Alessandra Buonanno, Yan-bei Chen, and Michele Vallisneri. “Detecting gravitational waves from precessing binaries of spinning compact objects: Adiabatic limit”. In: *Phys. Rev. D* 67 (2003). [Erratum: *Phys. Rev. D* 74,029904(2006)], p. 104025. DOI: [10.1103/PhysRevD.67.104025](https://doi.org/10.1103/PhysRevD.67.104025), [10.1103/PhysRevD.74.029904](https://doi.org/10.1103/PhysRevD.74.029904). arXiv: [gr-qc/0211087](https://arxiv.org/abs/gr-qc/0211087) [gr-qc].
- [95] Michael Boyle et al. “High-accuracy comparison of numerical relativity simulations with post-Newtonian expansions”. In: *Phys. Rev. D* 76 (2007), p. 124038. DOI: [10.1103/PhysRevD.76.124038](https://doi.org/10.1103/PhysRevD.76.124038). arXiv: [0710.0158](https://arxiv.org/abs/0710.0158) [gr-qc].

- [96] D.J.A. McKechn, C. Robinson, and B.S. Sathyaprakash. “A tapering window for time-domain templates and simulated signals in the detection of gravitational waves from coalescing compact binaries”. In: 27 (2010), p. 084020. DOI: [10.1088/0264-9381/27/8/084020](https://doi.org/10.1088/0264-9381/27/8/084020). arXiv: [1003.2939](https://arxiv.org/abs/1003.2939) [gr-qc].
- [97] Michael Boyle. “Angular velocity of gravitational radiation from precessing binaries and the corotating frame”. In: *Phys. Rev. D* 87.10 (2013), p. 104006. DOI: [10.1103/PhysRevD.87.104006](https://doi.org/10.1103/PhysRevD.87.104006). arXiv: [1302.2919](https://arxiv.org/abs/1302.2919) [gr-qc].
- [98] LIGO Scientific Collaboration. *Updated Advanced LIGO sensitivity design curve*. Tech. rep. <https://dcc.ligo.org/LIGO-T1800044/public>. 2018.
- [99] Nathan K. Johnson-McDaniel et al. *Determining the final spin of a binary black hole system including in-plane spins: Method and checks of accuracy*. Tech. rep. LIGO-T1600168. <https://dcc.ligo.org/LIGO-T1600168/public>. Aug. 2016.
- [100] B. P. Abbott et al. “Binary Black Hole Mergers in the first Advanced LIGO Observing Run”. In: *Phys. Rev. X* 6.4 (2016). [erratum: *Phys. Rev. X* 8,no.3,039903(2018)], p. 041015. DOI: [10.1103/PhysRevX.6.041015](https://doi.org/10.1103/PhysRevX.6.041015), [10.1103/PhysRevX.8.039903](https://doi.org/10.1103/PhysRevX.8.039903). arXiv: [1606.04856](https://arxiv.org/abs/1606.04856) [gr-qc].
- [101] Prayush Kumar et al. “Constraining the parameters of GW150914 & GW170104 with numerical relativity surrogates”. In: (2018). arXiv: [1808.08004](https://arxiv.org/abs/1808.08004) [gr-qc].
- [102] Vijay Varma, Mark A. Scheel, and Harald P. Pfeiffer. “Comparison of binary black hole initial data sets”. In: *Phys. Rev. D* 98.10 (2018), p. 104011. DOI: [10.1103/PhysRevD.98.104011](https://doi.org/10.1103/PhysRevD.98.104011). arXiv: [1808.08228](https://arxiv.org/abs/1808.08228) [gr-qc].
- [103] S. Ossokine et al. “Improvements to the construction of binary black hole initial data”. In: 32.24, 245010 (Dec. 2015), p. 245010. DOI: [10.1088/0264-9381/32/24/245010](https://doi.org/10.1088/0264-9381/32/24/245010). arXiv: [1506.01689](https://arxiv.org/abs/1506.01689) [gr-qc].

THE BINARY BLACK HOLE EXPLORER: ON-THE-FLY VISUALIZATIONS OF PRECESSING BINARY BLACK HOLES

Vijay Varma, Leo C. Stein, and Davide Gerosa, *Classical and Quantum Gravity*, 36, 095007 (2019), [arxiv:1811.06552](https://arxiv.org/abs/1811.06552).

8.1 Executive summary

An important application of numerical relativity simulations is in visualizing the complex dynamics of a black hole merger. However, these simulations are very expensive, taking a month on a supercomputer. This Chapter presents a Python visualization package based on numerical relativity surrogate models. These models are very accurate yet cheap, meaning that the visualizations can be generated within a few seconds on a laptop. This demonstrates the power of surrogate models: from supercomputers to your laptop!

8.2 Abstract

Binary black hole mergers are of great interest to the astrophysics community, not least because of their promise to test general relativity in the highly dynamic, strong field regime. Detections of gravitational waves from these sources by LIGO and Virgo have garnered widespread media and public attention. Among these sources, precessing systems (with misaligned black-hole spin/orbital angular momentum) are of particular interest because of the rich dynamics they offer. However, these systems are, in turn, more complex compared to nonprecessing systems, making them harder to model or develop intuition about. Visualizations of numerical simulations of precessing systems provide a means to understand and gain insights about these systems. However, since these simulations are very expensive, they can only be performed at a small number of points in parameter space. We present *binaryBHexp*, a tool that makes use of surrogate models of numerical simulations to generate on-the-fly interactive visualizations of precessing binary black holes. These visualizations can be generated in a few seconds, and at any point in the 7-dimensional parameter space of the underlying surrogate models. With illustrative examples, we demonstrate how this tool can be used to learn about precessing binary

black hole systems.

8.3 Introduction

The merger of two black holes (BHs) is one of the most violent events in the Universe. In the span of a few seconds, the incredible amount of energy $\sim 10^{60}$ MeV [1] is liberated in gravitational waves (GWs). These “ripples in spacetime” travel across the Universe at the speed of light to our detectors, providing us unique insights into these spectacular astrophysical events.

The first direct detection [1] of GWs from a BH merger was achieved in 2015 by the LIGO [2] twin detectors. This is one of the greatest achievements in modern science, crowning decades of theoretical and experimental efforts in gravitational physics. The detection of GWs not only earned the 2017 Nobel Prize in physics [3], but also sparked an unprecedented interest in science among the general public. For a few days, BHs were on the front pages of most newspapers in the world!

Despite the immense technical difficulties in detecting them, astrophysical BHs are remarkably simple objects, characterized only by their mass and spin. From far away they can be thought of as the analogs of Newtonian point masses in Einstein’s general relativity (GR). Near a BH, departures from Newtonian gravity such as the event horizon, gravitational lensing, gravitational time dilation, frame dragging, etc, become apparent.

When in a binary system, the departure is even more drastic. First, there are no stable binary orbits in GR: emission of GWs takes away energy, angular momentum, and linear momentum from the system, causing the binary’s orbit to shrink. Second, in Newtonian gravity, a point-mass binary orbit that starts in the equatorial plane remains in the equatorial plane. In GR, on the other hand, if the BH spins are misaligned with respect to the orbital angular momentum, relativistic spin-spin and spin-orbit couplings cause the system to precess [4–7]. Much like a top whose spin axis is misaligned with the orbital angular momentum, the spins and the orbital angular momentum oscillate about the direction of the total angular momentum. This precession is imprinted on the observed gravitational waves as characteristic modulations of amplitude and frequency.

The evolution of a binary BH system can be divided into three stages: inspiral, merger, and ringdown. During the inspiral, the BHs gradually approach each other due to loss of energy and angular momentum to GWs. As they get closer, they

eventually coalesce and merge. After the merger, one is left with a single, but highly distorted, BH. In the final stage, called ringdown, all these perturbations (“hairs”) are radiated away and the remnant settles down to its final steady state. The remnant BH is characterized entirely by its mass, spin, and recoil velocity (or “kick”). These properties are associated with the asymptotic conservation laws of energy, angular momentum, and linear momentum, respectively.

Modeling GWs emitted during all three stages is crucial to interpreting observations from detectors like LIGO [2] and Virgo [8]. The merger phase, in particular, can only be captured accurately with expensive numerical-relativity (NR) simulations (see e.g. Ref. [9] for a review). Obtaining a single merger waveform prediction might take months of computational time on powerful supercomputers. Visualizations [10] of these simulations have been instrumental in disseminating GW discoveries for outreach and educational purposes. To some extent, experts in the field also rely on visual products to develop intuition and illuminate future directions for research. In particular, visualizations of precessing binary BHs can give valuable insights into their complex dynamics. Available visualizations directly rely on NR simulations, and are therefore restricted to the small number of configurations which have been simulated. Generating a new visualization at a generic point in parameter space would involve a new, expensive NR simulation.

In this paper, we present the “binary Black Hole explorer” (*surfinBH*): a new tool to generate on-the-fly, yet accurate, interactive visualizations of precessing binary black hole evolutions with arbitrary parameters. We rely on recent NR surrogate models. Trained against several hundreds of numerical simulations, these models have been shown to accurately model both the emitted gravitational waveform [11] and the BH remnant properties [12] of precessing binary BH systems. With our easy-to-install-and-use Python package, one can generate visualizations within a few seconds on a standard, off-the-shelf, laptop computer. Some examples are available at vijayvarma392.github.io/binaryBHexp.

Figure 8.3.1 shows snapshots from a visualization generated with *surfinBH*. During the inspiral, both radiation reaction and spin precession are at play. While the separation shrinks because of GW emission, the orientations of the spins, and the orbital angular momentum, all vary in time. The GW emission frequency gradually scales as $f \sim r_{12}^{-3/2}$, and amplitude scales as $h \sim r_{12}^{-1}$, where r_{12} is the binary separation, producing a distinctive “chirp” where both frequency and amplitude sweep up over time. GWs are emitted in two polarizations, h_+ and h_\times , as predicted

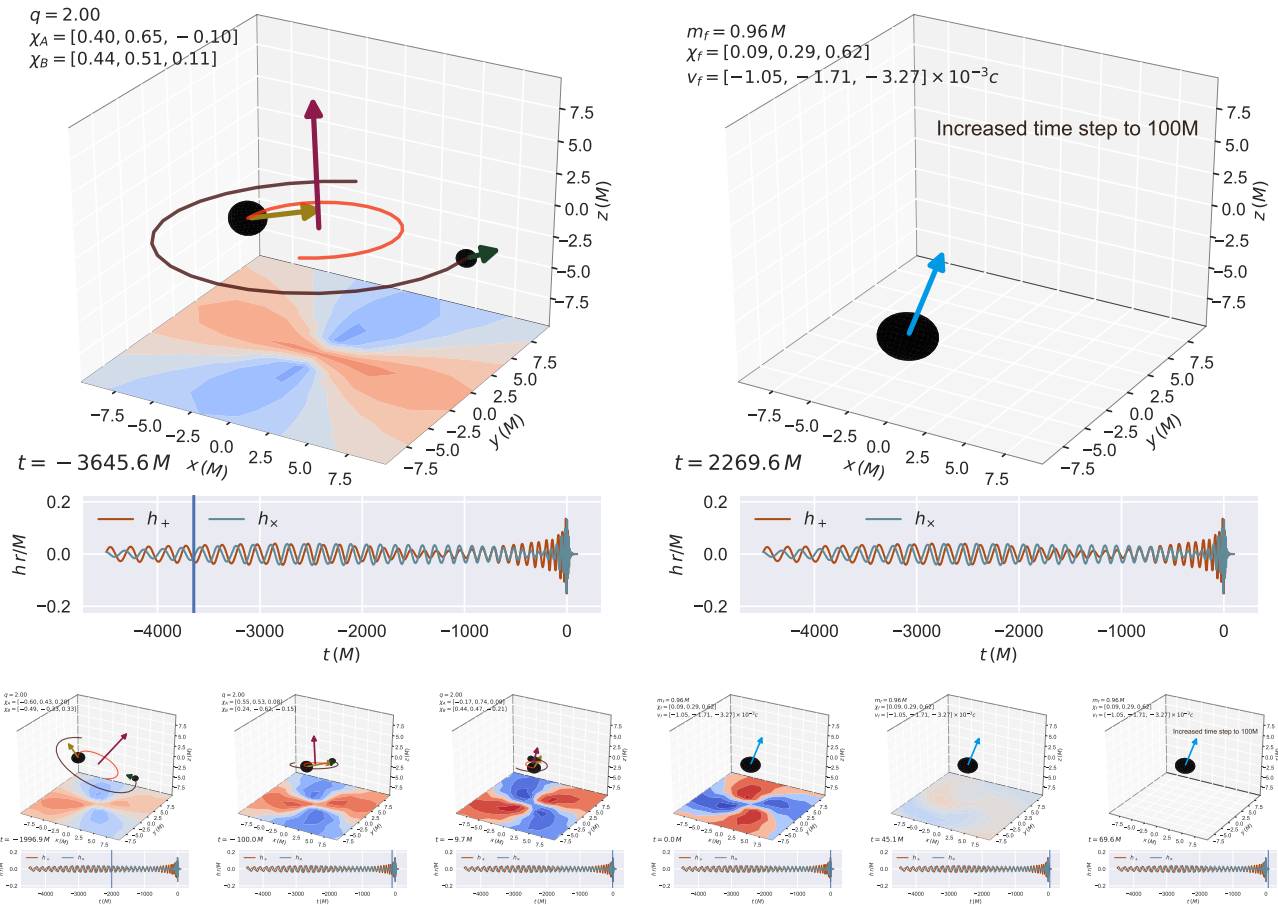


Figure 8.3.1: Snapshots during the inspiral (top-left), post-ringdown (top-right), and intermediate (bottom) stages of a precessing binary BH evolution. Each BH horizon is represented by an oblate spheroid. The arrows on the BHs indicate the spin vectors; the larger the spin the longer the arrow. The arrow centered at the origin indicates the orbital angular momentum. On the bottom plane, we show the plus polarization of GWs, as seen by an observer at each point. Red (blue) colors indicate positive (negative) values. Notice the quadrupolar nature of the emitted waves. The subplots at the bottom of each panel show GW plus and cross polarizations, as seen by a far-away observer viewing from the camera viewing angle. The time to the peak of the waveform amplitude is indicated in the figure text as well as the slider in the bottom subplots. This animation is available at vijayvarma392.github.io/binaryBHexp/#prec_bbh.

by Einstein's GR. As explored later, the relative amplitude of the two polarizations crucially depends on orientation of the observer with respect to the binary. Spin precession causes amplitude modulations during the inspiral phase, which are also dependent on the observer orientation. After merger, the component BHs are replaced by a remnant BH, whose properties are determined by conservation laws, as mentioned above. The merger process emits copious gravitational radiation, and corresponds to the peak amplitude of the waveform.

The rest of the paper is organized as follows. Sec. 8.4 describes methods and approximations employed to generate visualizations such as Fig. 8.3.1. In Sec. 8.5, we demonstrate the power of this tool with several examples aimed at exploring known phenomenology in BH dynamics. Sec. 8.6 describes code implementation and usage. Finally, we provide concluding remarks in Sec. 8.7.

8.4 Methods

Preliminaries

We start with some definitions, referring the reader to standard GR and GW textbooks for more details [13–18]. Throughout this paper, we use geometric units with $G = c = 1$.

An isolated astrophysical BH is characterized entirely by its mass m and spin angular momentum $\mathbf{S} = \chi m^2$. χ is the dimensionless spin, with magnitude $\chi \leq 1$, and $\mathbf{a} = \chi m$ is the Kerr parameter.

A quasicircular precessing binary BH system is characterized by seven intrinsic parameters: mass ratio $q = m_1/m_2$, and two spin vectors χ_1, χ_2 . Here, subscript 1 (2) corresponds to the heavier (lighter) of the two BHs. The total mass of the system $M = m_1 + m_2$ can be scaled out. Therefore, throughout this paper, all length and time quantities are in units of M . Similarly, all frequency quantities are in units of $1/M$. After the merger takes place, the remnant BH is characterized by its mass m_f , spin χ_f and recoil velocity \mathbf{v}_f .

If the BH spins are (anti-)aligned with respect to the orbital angular momentum \mathbf{L} , the emitted GWs have monotonically increasing amplitude and frequency. Instead, if the component spins are misaligned with respect to \mathbf{L} , couplings between the momenta \mathbf{L}, \mathbf{S}_1 , and \mathbf{S}_2 cause them to precess about the direction of the total angular momentum $\mathbf{J} = \mathbf{L} + \mathbf{S}_1 + \mathbf{S}_2$. GW amplitude and frequency are not monotonic, and their modulations strongly depend on the viewing angle [4]. This complexity can

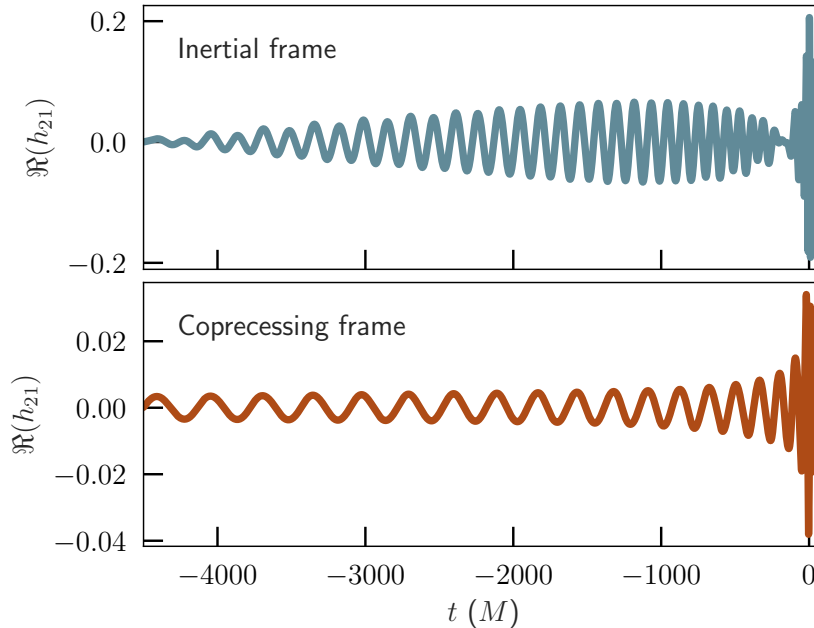


Figure 8.4.1: Example of the real part of the ($\ell = 2, m = 1$) spin-weighted spherical harmonic mode (see Sec. 8.4) of the GW for a precessing black hole binary, in the inertial (top) and coprecessing (bottom) frames. $t = 0$ corresponds to the peak of the waveform amplitude.

be in part removed by moving into a non-inertial reference frame which tracks the direction of L [19–21]. In this *coprecessing* frame, the waveform looks nearly as simple as that of a nonprecessing source (cf. bottom panel of Fig. 8.4.1), and can be modeled with methods developed to study nonprecessing systems.

Surrogate models

NR surrogate models provide a fast-but-accurate method to model GW signals. We use a model developed by Blackman et al. [11] named NRSur7dq2 to predict both the waveform and the BH spin dynamics. NRSur7dq2 was trained against 886 NR simulations in the 7-dimensional parameter space of mass ratios $q \leq 2$, and dimensionless spin magnitudes $\chi_1, \chi_2 \leq 0.8$. NRSur7dq2 predicts both the emitted GWs and the associated BH spin dynamics. In particular, it models four important quantities that we make use of in this work: (i) the waveform modes $h_{\ell m}$ expanded in spin-weighted spherical harmonics (cf. Sec. 8.4); (ii) the unit quaternions $\hat{Q}(t)$ describing the rotation between the coprecessing frame and a specified inertial frame; (iii) the orbital phase in the coprecessing frame ϕ_{orb} ; and (iv) the precession of component spins χ_1, χ_2 over time.

Modeling the BH remnant's properties is performed with the surrogate surfinBH7dq2 [12], which was also trained on the same set of NR simulations. This model takes in mass ratio q and component spin vectors χ_1, χ_2 at a given orbital frequency, and models the remnant mass m_f , spin vector χ_f , and kick vector \mathbf{v}_f .

Black-hole shapes

In our visualizations, we represent BH horizons with ellipsoids of revolution. The axis of symmetry is along the instantaneous spin of the BH. The polar (along the axis) and the equatorial (orthogonal to the axis) horizon radii are set to

$$r_{\text{pol}} = r_+, \quad r_{\text{equi}} = \sqrt{r_+^2 + a^2}, \quad (8.1)$$

where $r_+ = m + \sqrt{m^2 - a^2}$. r_{pol} and r_{equi} correspond to the Kerr-Schild [18, 22] coordinate distances from the BH center to the pole/equator of the horizon. Note that numerical simulations use a different coordinate system, meaning the BH shapes would be different even for an isolated BH. However, this captures the azimuthal symmetry and oblate nature seen in most coordinate systems.

This approximation, however, neglects much of the interesting phenomenology of event horizons (EHs) of BHs in binaries [15, 23, 24]. Event horizons are defined globally, so the locations of EHs cannot be determined without knowing the entire future development of a spacetime. Most NR simulations track the location of apparent horizons (AHs) [15], which *can* be defined locally. Both EHs and AHs of orbiting BHs are deformed by the tidal field of the other BH. This distortion becomes very strong close to merger, where the shape of the two event horizons do not resemble, even vaguely, that of ellipsoids (see e.g. [25]). Improving our representation of EH shapes requires building surrogate models for the morphology of the EH/AH, which is an interesting avenue for future work.

In addition, we assume the masses of the BHs are constant during the evolution. While the masses in an NR simulation can change due to in-falling energy through GWs, this is a very small effect (4PN (Post Newtonian) higher than leading orbital energy loss [26–28]) that is safely ignored in current waveform models including NRSur7dq2.

Component black-hole spin evolution

The two spins χ_1, χ_2 are modeled using NRSur7dq2. These are known to agree well with NR simulations and are crucial for the accuracy of that waveform model [11].

Note, however, that the spins modeled by NRSur7dq2 have had an additional smoothing filter applied to remove short-timescale oscillations [11]. This approximation propagates to our visualizations. Similarly to the masses of the BHs, we assume the spin magnitudes are constant during the evolution. In-falling angular momentum in the form of GWs can alter the spin magnitudes, but this is also a very small effect (4PN higher than leading angular-momentum loss [27, 28]) that is ignored by current waveform models including NRSur7dq2.

Spins are represented as arrows centered at the BH centers, that are proportional to the Kerr parameter \mathbf{a} of each BH. More specifically, the length is set to $10a$, and the direction is along $\hat{\mathbf{a}}$. The exaggeration of the magnitude is necessary to make the spin vectors clearly visible during the evolution; more on this in the next section.

Orbital angular momentum

NRSur7dq2 only predicts the unit rotation quaternion $\hat{Q}(t)$ and not the magnitude L . The (time dependent) direction of orbital plane is inferred from $\hat{Q}(t)$ and is orthogonal to the z-axis of the coprecessing frame. For the magnitude L , we implement the Newtonian expression

$$L = M^2 \frac{q}{(1+q)^2} (M\omega_{\text{orb}})^{-1/3}, \quad (8.2)$$

where ω_{orb} is the orbital frequency, as derived from the orbital phase in the coprecessing frame modeled by NRSur7dq2,

$$\omega_{\text{orb}} = \frac{d\phi_{\text{orb}}}{dt}. \quad (8.3)$$

In our visualizations, the angular momentum is indicated by an arrow at the origin. Its magnitude is rescaled to $12L$. This factor is arbitrary and it is chosen to make the arrow clearly visible.

Note that it is not appropriate to compare an arrow for orbital angular momentum $L \propto M^2$ to those representing the Kerr parameters $a_1, a_2 \propto M$ because they have different dimensions. The choice of representing a , rather than the $S \propto M^2$ was made to allow all arrows to be clearly visible throughout the inspiral for generic locations in the parameter space (i.e. different mass ratios). However, we provide an option to represent S for the spin arrows (cf. Sec. 8.6), in which case the arrow magnitudes are set to $12S$. This makes the arrow on the smaller BH barely visible in some cases, but allows direct comparison of the spin arrows to the orbital angular

momentum arrow. This could be informative for gaining intuition about peculiar spin phenomena like transitional precession [4, 29], spin orbit resonances [30], large nutations [31, 32] and precessional instabilities [33]. This phenomenology is currently beyond the scope of the surrogate we used, but is being actively researched with NR simulations [34, 35] and lies within the realm of future hybridized surrogate models (see e.g. [36]).

Component black-hole trajectories

The gauge symmetry of GR is broken in an NR simulation, since one necessarily has to specify a set of coordinates to represent the solution on a computer. The BH trajectories extracted from numerical simulations are, therefore, inherently gauge dependent.

In the construction of NRSur7dq2 [11] quantities like $\hat{Q}(t)$ and ϕ_{orb} are obtained from the GWs extrapolated to future null infinity, not from numerical simulations' BH coordinates.

In our visualizations, we reconstruct the trajectories of the BHs using the dynamics predicted by NRSur7dq2 and some PN arguments. In particular, one needs the separation between the BHs as a function of the orbital frequency, $r_{12}(\omega_{\text{orb}})$, with the orbital frequency defined as in Eq. (8.3). The separation $r_{12}(\omega_{\text{orb}})$ is modeled using the 3.5PN expressions reported in Eq. (4.3) of Ref. [37], along with the 2PN spin-spin term from Eq. (4.13) of Ref. [5].

Let us write the coprecessing frame coordinates as (x', y', z') . The trajectories in the coprecessing frame, where the orbital plane is orthogonal to the z' -axis, are given by

$$\begin{cases} x'_1 = r_1 \cos \phi_{\text{orb}} \\ y'_1 = r_1 \sin \phi_{\text{orb}} \\ z'_1 = 0 \end{cases} \quad \begin{cases} x'_2 = -r_2 \cos \phi_{\text{orb}} \\ y'_2 = -r_2 \sin \phi_{\text{orb}} \\ z'_2 = 0 \end{cases} \quad (8.4)$$

where r_1 (r_2) indicates the coordinate separation from the origin to the primary (secondary) BH center. We use the Newtonian relations

$$r_1 = \frac{m_2}{M} r_{12}, \quad r_2 = \frac{m_1}{M} r_{12}, \quad (8.5)$$

to enforce the Newtonian center-of-mass of the binary to be at the origin. This ignores the fact that true center of mass during inspiral and merger oscillates about

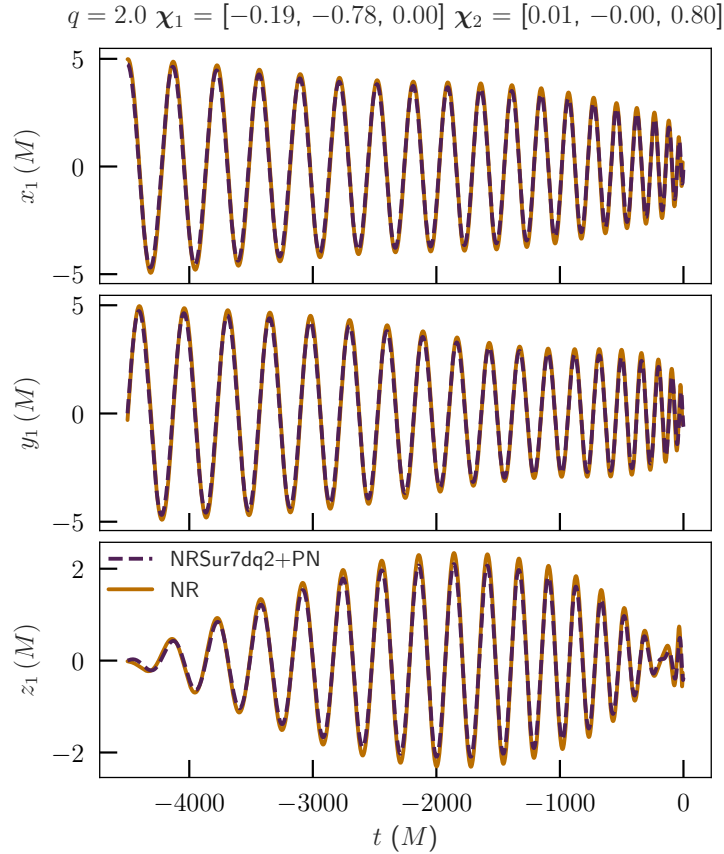


Figure 8.4.2: Comparison of the coordinate trajectories of the heavier BH for a precessing binary BH, between NR, and our approximation using NRSur7dq2 and PN. $t = 0$ corresponds to the peak of the waveform amplitude. The mass ratio, and spins at $t = -4500M$ are shown at the top of the plot.

the origin due to linear momentum carried away in GW. However, this correction would be too small to be noticeable on the scale of our visualizations (see e.g. Fig. 2 of [38]).

Given the trajectories in the coprecessing frame, the trajectories in the inertial frame are obtained by a quaternion transformation with the time-dependent rotation (unit) quaternions $\hat{Q}(t)$ (for a brief introduction to quaternions in this context, see e.g. App. A of [39]). Treating the Euclidean positions as purely imaginary quaternions, the transformation is

$$\mathbf{x}_i = \hat{Q}(t) \mathbf{x}'_i \hat{Q}^{-1}(t). \quad (8.6)$$

Figure 8.4.2 compares the trajectories predicted by our method to the gauge-dependent ones extracted from an NR simulation. Our approximate trajectories

turn out to be remarkably close to the NR trajectories. The dominant deviations are due to the PN formulae being in harmonic gauge, whereas the NR simulations use the damped harmonic gauge [40].

Gravitational waves

NR simulations predict the entire spacetime metric of a binary BH evolution. However, the full metric is usually discarded because most applications (notably GW observations) only require the gravitational waves as seen by an observer far away.

Indeed, splitting the metric into GWs and a non-oscillatory part can only be well defined in the *wave zone*, which is at distances r much larger than the gravitational wavelength λ . Let us suppose we are in a spacetime that is approximately Minkowski space, with a metric perturbation h_{ab} , in the transverse-tracefree (TT) gauge [41]. We define a spherical polar coordinate system (t, r, θ, ϕ) with the binary center-of-mass at the origin. The z axis ($\theta = 0$) of this coordinate system is parallel to \mathbf{L} at some reference time/frequency. The x axis lies along the line of separation from the lighter BH to the heavier BH at this time/frequency, and the y axis completes the triad.

The spherically outgoing gravitational wave is typically converted into a spin-weight -2 complex scalar by contracting $h \equiv h_{ab} \bar{m}^a m^b$, where $m^a = (\hat{e}_\theta^a + i\hat{e}_\phi^a)/\sqrt{2}$ is an element of a complex null dyad [18] along with its conjugate \bar{m}^a ; and where $\hat{e}_\theta^a, \hat{e}_\phi^a$ are the standard unit vectors in the θ and ϕ directions, respectively. The gravitational-wave strain h is then decomposed as

$$h(t, r, \theta, \phi) = \sum_{\ell=2}^{\infty} \sum_{m=-\ell}^{\ell} {}_{-2}Y_{\ell m}(\theta, \phi) h_{\ell m}(t, r), \quad (8.7)$$

where ${}_{-2}Y_{\ell m}$ are the $s = -2$ spin-weighted spherical harmonics [42]. The functions $h_{\ell m}$ are referred to as the *modes* of the GWs.

From the structure of the flat-space d'Alembertian operator, we can see that at large distances, h is dominated by a piece decaying as $\sim 1/r$ along lines of constant retarded time $t_{ret} \equiv t - r$ [43]. This motivates how waves are extracted from NR. First, $(r h_{\ell m})$ is evaluated on spheres of various radii in the computational domain. This is then extrapolated to future null infinity, defining

$$(r h_{\ell m})^\infty(t) \equiv \lim_{r \rightarrow \infty} r h_{\ell m}(t - r, r). \quad (8.8)$$

NRSur7dq2 only models these extrapolated GW modes, $(rh_{\ell m})^\infty$.

One can evaluate the GWs at any particular orientation in the source frame at $r \rightarrow \infty$ by applying Eq. (8.7) to $(rh_{\ell m})^\infty(t)$. This is used to generate the waveform time series in the bottom subplots of our animations (cf. Fig. 8.3.1), where we show the plus $h_+ = \Re(h)$ and cross $h_\times = -\Im(h)$ polarizations. We use all the spin-weighted spherical harmonic modes provided by NRSur7dq2, i.e. $2 \leq \ell \leq 4$ and $|m| \leq \ell$.

Since the full metric is not available in the bulk, we approximate it from $(rh)^\infty$. When showing GWs on the bottom plane of our visualizations (cf. Fig. 8.3.1), we approximate the strain as

$$h(t, r, \theta, \phi) \approx \frac{(rh)^\infty(t_{ret}, \theta, \phi)}{r}. \quad (8.9)$$

This neglects curved-background effects such as tails, and higher order $1/r$ corrections, so this approximation is only valid at large r . More work would be needed to recover the higher powers of $1/r$, but it is technically possible (see Eq. (2.53a) of [43]). The default position of the bottom-plane is quite close to the binary; moving it farther out improves this approximation.

Post merger phase

In NR simulations, a common apparent horizon typically forms at a retarded time close to the peak of the waveform $\mathcal{A}^2 = \sum_{\ell, m} |h_{\ell m}|^2$. This is taken to be the definition of the time of merger. We therefore shift the time variable t such that $t = 0$ corresponds to $\max_t \mathcal{A}$. At $t \geq 0$, the two component BHs are replaced by a single remnant. The final mass, spin, and kick of the remnant are predicted using surfinBH7dq2 [12].

Mass and spins of the remnant are used to draw a horizon ellipsoid and spin arrow as specified in Sec. 8.4 and Sec. 8.4. The remnant BH horizon is expected to be highly distorted at the common horizon formation time. We ignore this effect and simply represent the remnant BH by an ellipsoid of constant shape from $t = 0$ onwards.

During a BH inspiral and merger, linear momentum emitted in GWs causes motion of the binary's center of mass (cf. e.g. Ref. [38] and references therein). In practice, however, linear momentum flux is negligible at early times and the “kick” is only accumulated over the last few cycles before merger. Here we make the additional simplification of neglecting this effect, and assume that the remnant is formed at the origin and receives all of its kick velocity instantaneously. However, as mentioned

before, this correction would be at a scale that is not noticeable in our visualizations (cf. Fig. 2 of [38]).

Time steps and displayed text

To better highlight different phases of the evolution, we use a non-uniform time step. The time step between frames at $t \lesssim 75M$ is chosen to obtain 30 frames for each orbit. The animation, therefore, is artificially slowed down close to merger, so that the entire dynamics is easier to observe. After the ringdown stage, the animation is sped up to better illustrate the final kick. The current time is displayed in the figure text, as well as indicated by the blue vertical slider in the bottom waveform subplot (cf. Fig. 8.3.1).

The figure text at the top-left of the main visualization panel shows the parameters of the binary (remnant). At times $t < 0$, these are the mass ratio and instantaneous spin components. Mass, spin and kick of the remnant BH are shown after merger.

8.5 Explorations

We now provide additional examples that demonstrate the power and utility of our visualizations.

Waveform projection

Figure 8.4.3 shows a visualization of a precessing binary BH, when we also vary the camera viewing angle during the evolution. The polarization content and the morphology of the waveform therefore strongly depend on the direction of the line of sight, which can be understood as follows. From Eq. (8.7), the observer viewing angles (θ, ϕ) affect the relative weights with which the waveform modes $h_{\ell m}$ are combined into the strain h . Note that the standard quadrupole formula for GW emission only contains the dominant $\ell = |m| = 2$ modes, while here we use all modes with $\ell \leq 4$.

The GW amplitude is strongest along the direction of \mathbf{L} . This is evident from the bottom panel of Fig. 8.4.3, where the direction of \mathbf{L} aligns with the observer's viewing angle (i.e., the binary is *face-on*). On the other hand (top-left panel of Fig. 8.4.3) the GW amplitude is at its least when the observer viewing angle is orthogonal to \mathbf{L} (*edge-on*). The contribution of higher harmonics $\ell > 2$ to Eq. (8.7) also depends on observer viewing angle. For face-on binaries, the GWs are strongly dominated

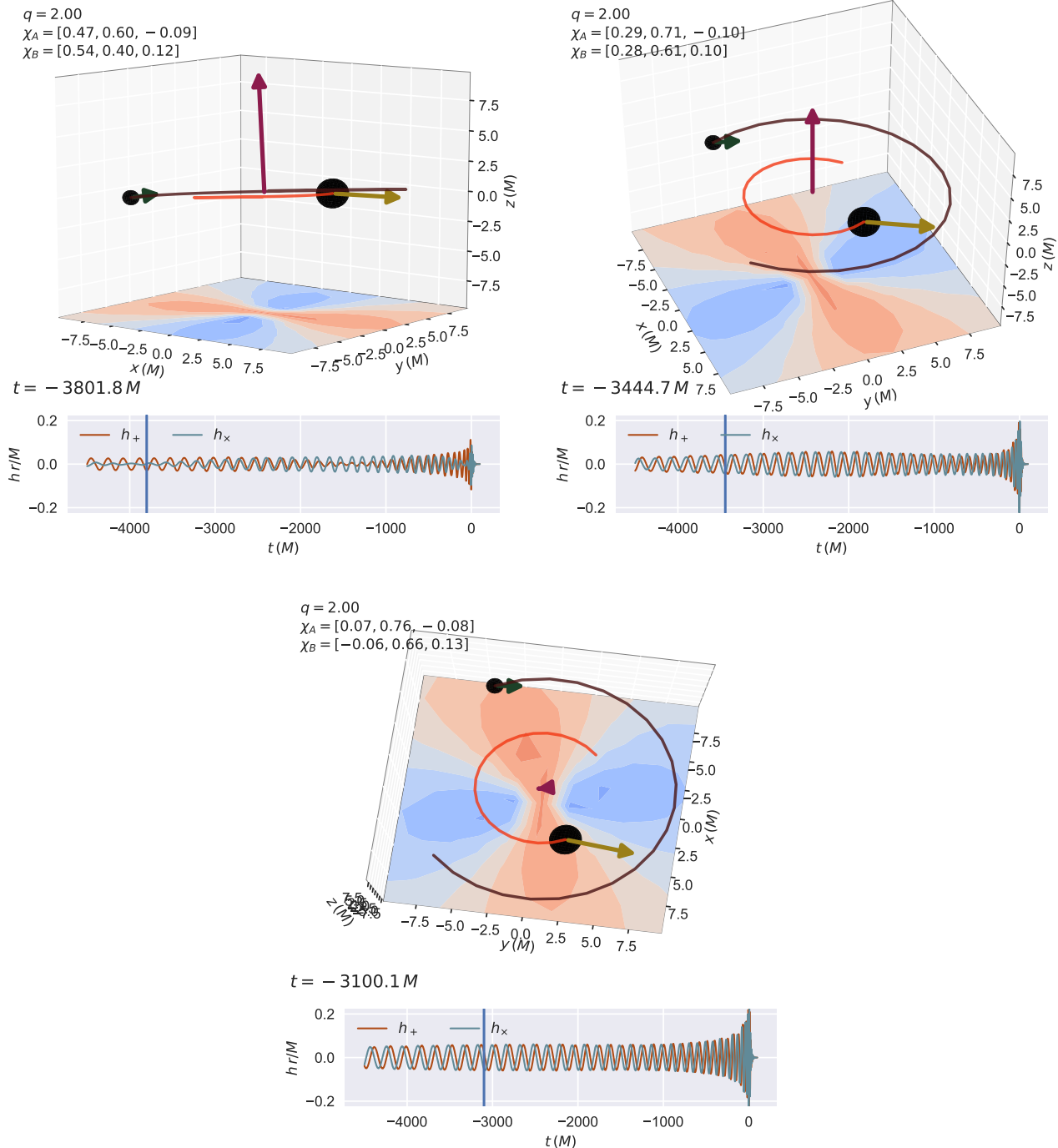


Figure 8.4.3: Visualization of a precessing binary black hole system where we also vary the camera viewing angle during the inspiral. Notice how the waveform structure in the bottom subplots changes based on whether the viewing angle is edge-on (top-left), intermediate (top-right), or face-on (bottom). This animation is available at [vijayvarma392.github.io/binaryBHexp/#prec_bbh_rotating_camera](https://github.com/vijayvarma392/binaryBHexp/#prec_bbh_rotating_camera).

by the quadrupolar modes. Going from face-on to edge-on, the contribution of the quadrupolar modes decreases and that of the nonquadrupolar modes increases.

One can also infer the polarization content of the GWs from the waveform panel. If there is a $\pm 90^\circ$ phase shift between $h_+ = \Re(h)$ and $h_\times = -\Im(h)$, the GWs are circularly polarized. The bottom panel of Fig. 8.4.3, which is mostly face-on, shows almost perfect circular polarization, deviating due to precession of the orbital plane. For comparison, when h_+ and h_\times are proportional with a real constant of proportionality, the GW has a linear polarization (this includes the simpler case where one of the two polarizations vanishes). The top-left panel of Fig. 8.4.3, where the system is (almost) edge-on, exhibits (almost) linear polarization at many times throughout the inspiral. Again the deviations are due to precession of the orbital plane. The modulation is more noticeable for nearly edge-on precessing systems, since one of the polarizations can temporarily vanish as the system precesses through perfectly edge-on configurations.

Orbital hang-up effect

Apart from precession, the BH spins have other important effects on the evolution of binaries. One such effect is the so called *orbital hang-up* effect [44–46] which delays or prompts the merger of the BHs based on the sign of the BH spin component along the orbital angular momentum, $\mathbf{S} \cdot \mathbf{L}$, where \mathbf{S} is one of \mathbf{S}_1 or \mathbf{S}_2 . This spin-orbit coupling is a 1.5 PN effect that effectively acts as an additional repulsion (attraction) when the sign of $\mathbf{S} \cdot \mathbf{L}$ is positive (negative). This means that binaries that have spins that are aligned (anti-aligned) with \mathbf{L} will merge slower (faster) than nonspinning binaries, when starting from the same orbital frequency. This is analogous to the location of the innermost stable circular orbits of Kerr BHs, which is at a smaller (larger) radius for co-(counter-)rotating particles.

This is demonstrated in Fig. 8.5.1, which shows an aligned, nonspinning and an anti-aligned binary, starting at the same orbital frequency. Unlike the rest of the animations discussed in this paper, here we use a constant time step between the frames of the movie (rather than a fixed 30 frames per orbit), and set $t = 0$ at the start of the waveform (rather than at the peak). Due to the orbital hang-up effect, the anti-aligned binary merges first, followed by the nonspinning system, and finally the aligned system. In addition, the aligned (anti-aligned) binary radiates more (less) energy due to its prolonged (shortened) evolution, and the final mass is therefore smaller (larger) than the nonspinning case. The interaction between spin

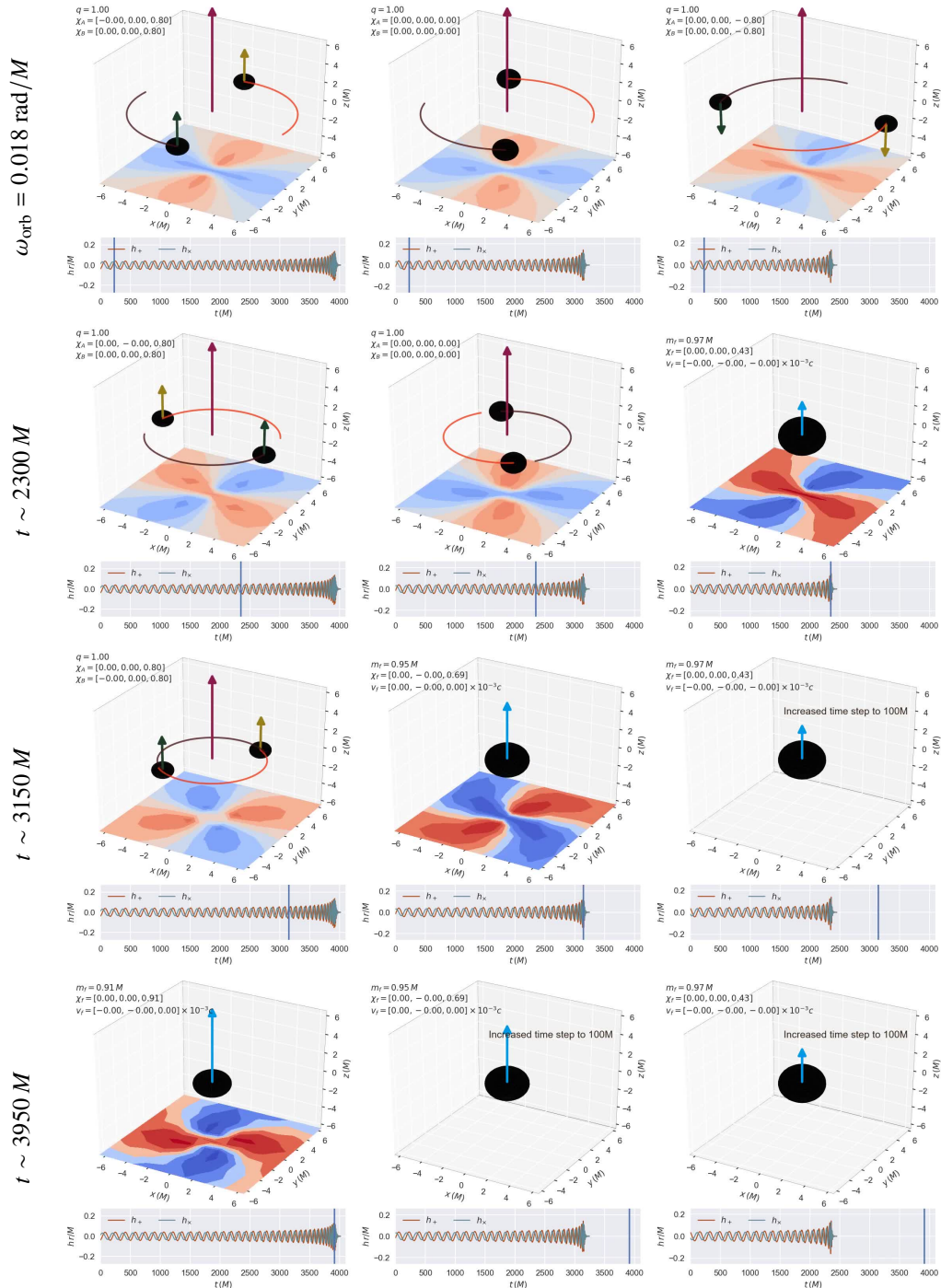


Figure 8.5.1: Visualization of the orbital hang-up effect. We show three nonprecessing systems with equal masses, and equal spins. In the left (right) column, both spins are aligned (anti-aligned) with L , with magnitude 0.8. The middle column shows a nonspinning binary. All three systems start at an orbital frequency of $0.018 \text{ rad}/M$. Due to orbital hang-up effect, the length of the waveform is longer (shorter) for the aligned case compared to the nonspinning case (see the bottom subplots showing the waveform). Time flows downwards (labeled at the left), and each row corresponds to a fixed time since the start of the animation. This animation is available at [vijayvarma392.github.io/binaryBHexp/#hangup](https://github.com/vijayvarma392/binaryBHexp/#hangup).

and orbital angular momentum also determines the remnant spin in a non-trivial way: the aligned (anti-aligned) case results in the largest (smallest) remnant spin magnitude.

The orbital hang-up effect can also be explained heuristically using the cosmic censorship conjecture. For the aligned-spin binary in Fig. 8.5.1, the initial magnitude of total angular momentum is given by $J = L + m_1^2 \chi_1 + m_2^2 \chi_2$. Using L from Eq. (8.2) with $\omega_{\text{orb}} = 0.018 \text{ rad}/M$, we get $J \sim 1.35M^2$. This is larger than the maximum allowed spin angular momentum for a Kerr BH, M^2 . On the other hand, for the anti-aligned case we have $J = L - m_1^2 \chi_1 - m_2^2 \chi_2 \sim 0.55M^2$, which is well within the limit. So, the aligned binary must radiate at least $0.35M^2$ of its total angular momentum in the form of GWs before it can merge, in order to not violate cosmic censorship. The anti-aligned case can therefore merge faster.

Super-kick

Next, we consider a binary BH in the so-called *super-kick* configuration. Anisotropic emission of GWs causes a net flux of linear momentum, which imparts a kick to the remnant BH. Some degree of asymmetry is necessary for a nonzero kick [47]. For instance the kick vanishes by symmetry during the merger of an equal-mass, nonspinning binary BH system. Strongly precessing binary BHs have been found to generate the highest kicks [48–50]. Some of these systems have kicks large enough to escape from even the most massive galaxies in the Universe [51, 52].

In particular, a very large kick (up to $\sim 3000 \text{ km/s}$) is imparted to BHs merging with spins lying in the orbital plane and anti-parallel to each other. These are the so-called *super-kicks* first discovered in 2007 [48, 49], by means of NR simulations. The largest kicks observed in numerical simulations to date are the so-called *hangup-kicks* [50], where the spins have non-zero components perpendicular to the orbital plane, but the in plane spins are anti-parallel. We will refer to all configurations where the spins near merger are coplanar, and their orbital plane projections are anti-parallel, as super-kick configurations. Crucially, large kicks are only found if the spins are in these fine-tuned configurations “near merger.”

For this reason, generating visualizations of BH super-kicks from simulations can be challenging. The spins are usually specified at the start of the simulations and several attempts are necessary to find the specific initial conditions that will result in co-planar spins near merger. With our tool, on the other hand, one can specify the spins at any time/frequency, including close to merger. Generating a visualization of

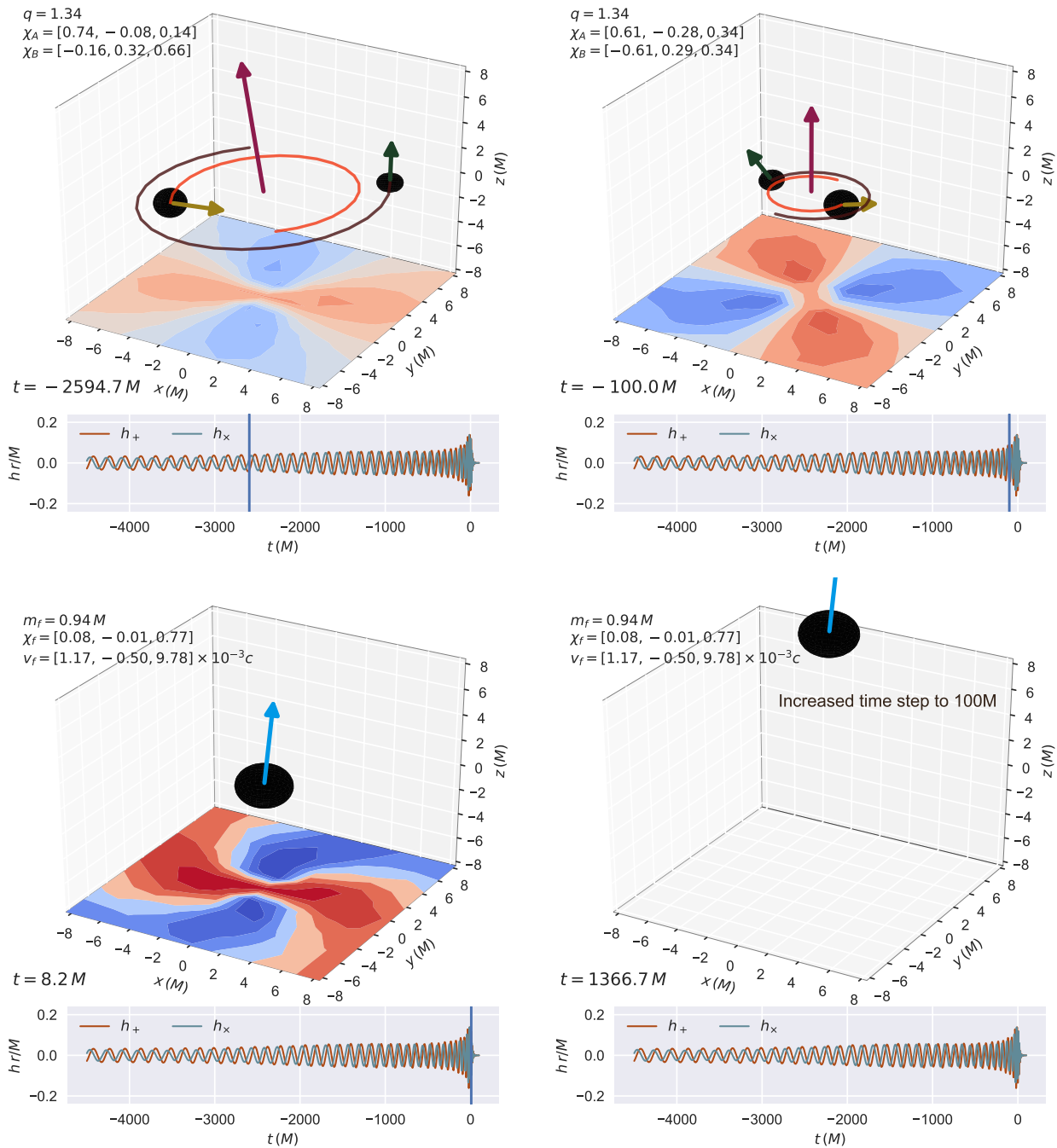


Figure 8.5.2: Evolution of a super-kick configuration. Time flows from left to right and from top to bottom, as shown at the bottom left of each panel. The top-left panel shows a snapshot taken in the early inspiral. In the top-right panel, the two BHs are about to merge and the spins are seen to be in a super-kick configuration. The bottom-left snapshot is taken at the time at which the peak of the waveform hits the bottom plane where the GW pattern is shown. After merger (bottom-right panel), the final BH is imparted a kick of ~ 3000 km/s (note that we speed up the animation after the ringdown by increasing the time steps to $100M$). This animation is available at vjayvarma392.github.io/binaryBHexp/#super_kick.

a system in a super-kick configuration is as easy as any other location in parameter space. This is shown in Fig. 8.5.2. The remnant reaches a final velocity of $\sim 10^{-2}c$ ($\sim 3000\text{km/s}$), in agreement with [48–50].

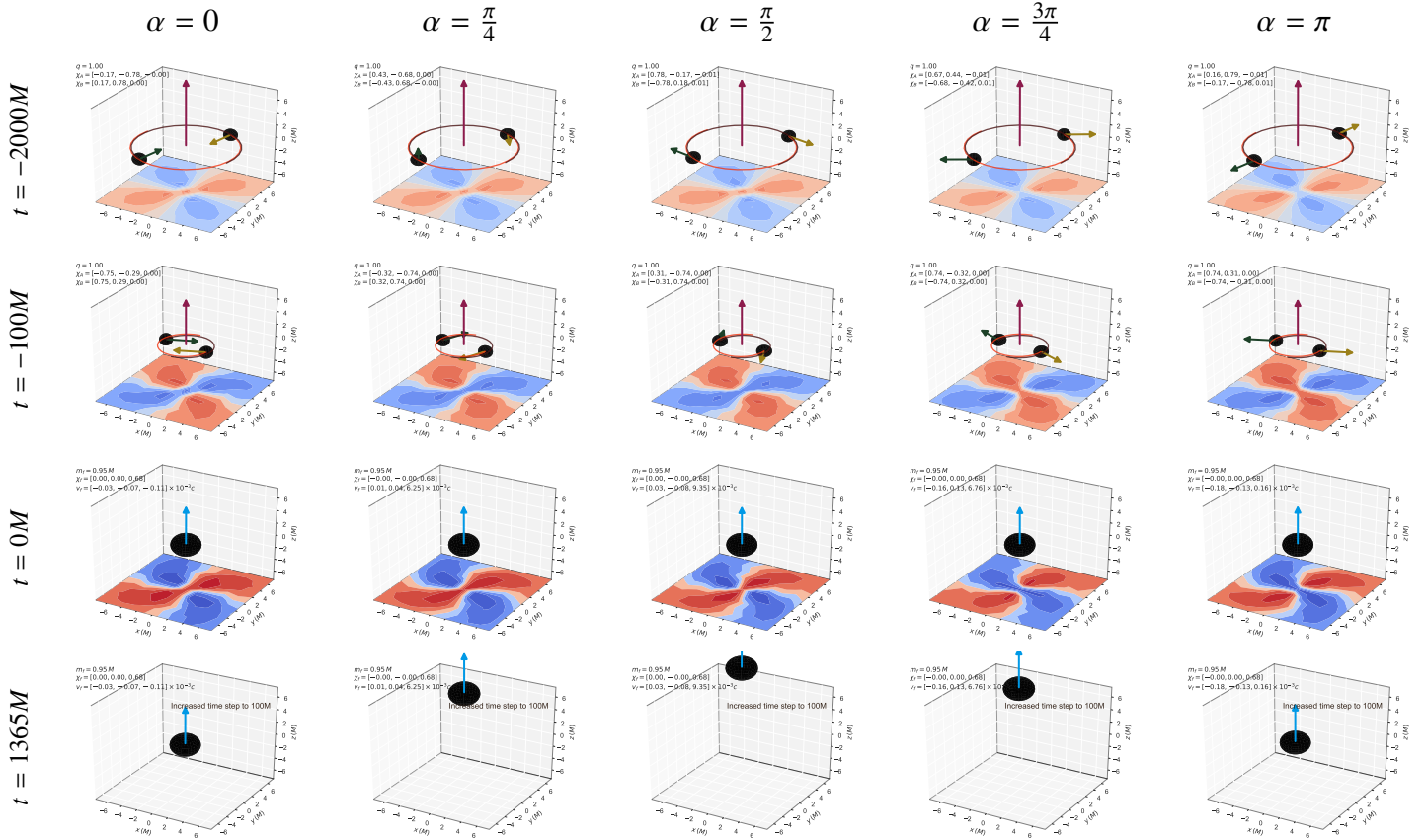


Figure 8.5.3: Sinusoidal dependence of the kick magnitude on the angle between spins close to merger. Five different cases are shown (left to right), with equal masses and equal spins. Both spins are confined to the orbital plane, and are anti-parallel to each other, but with a different angle in the plane α (labeled at top), specified at $t = -100M$. Time flows downwards (labeled at left). The bottom panels show the sinusoidal dependence of the final kick magnitude on the initial orbital phase. This animation is available at vijayvarma392.github.io/binaryBHexp/#sine_kicks.

Sinusoidal kick dependence

As suggested above, the remnant kick is quite sensitive to the angle between the spins close to merger. In particular, the component of the kick parallel to the orbital angular momentum has been found to depend sinusoidally on the orbital phase [38, 53]. Fig. 8.5.3 demonstrates this effect. All five different cases have equal-mass BHs, with anti-parallel spins lying in the orbital plane at $t = -100M$. Each evolution

is initialized with a different orbital phase or, equivalently, performing an overall rotation of the spins about the z -axis.

As expected, the final BH kick changes dramatically with the initial orbital phase. Even visually, the kick dependence appears to be sinusoidal. This example demonstrates the potential of *surfinBH* as a tool to perform detailed, but at the same time accessible, exploration of the phenomenology of precessing BH mergers.

8.6 Public Python implementation

Our package is made publicly available through the easy-to-install-and-use Python package, *surfinBH* [54]. Our code is compatible with both Python 2 and Python 3. The latest release can be installed from the Python Package Index using

```
pip install binaryBHexp
```

This adds a shell command called *surfinBH*, which can be used to generate visualizations with invocation as simple as

```
binaryBHexp --q 2 --chiA 0.2 0.7 -0.1 --chiB 0.2 0.6 0.1
```

Such an invocation yields a running movie that the user can interact with. By clicking and dragging on the movie as it plays, the user can change the viewing angle and the waveform time-series will update in real time as the viewing angle is manipulated. The full documentation for command-line arguments is available with the `--help` flag.

As mentioned in Sec. 8.4, the default setting for the spin arrows is to be proportional to the Kerr parameter of the BH, a . By passing the optional argument `--use_spin_angular_momentum_for_arrows` to the above command, the spin arrows can be made proportional to the spin angular momentum of the BH instead.

Python packages *NRSur7dq2* [55] and *surfinBH* [56] are specified as dependencies and are automatically installed by `pip` if missing. *surfinBH* is hosted on GitHub at github.com/vijayvarma392/binaryBHexp, from which development versions can be installed. Continuous integration is provided by *Travis* [57]. More details about the Python implementation, as well as animations corresponding to the examples discussed in this paper are available at vijayvarma392.github.io/binaryBHexp.

8.7 Conclusion

We present a tool for visualizing mergers of precessing binary black holes. Rather than rely on expensive numerical simulations, we base our animations on surrogate models of numerical simulations. These are inexpensive but very accurately reproduce numerical simulations. Therefore, we can generate visualizations anywhere in the parameter space of the underlying surrogate models, within a few seconds.

We make our code available through an easy-to-install-and-use python package *surfinBH* [54]. We demonstrate the power of this tool by generating visualizations of several well known phenomena such as: spin and waveform modulations due to precession, orbital-hangup effect, super kicks, sinusoidal behavior of the remnant kick, etc. This tool can be used by researchers and students alike, to gain valuable insights into the highly complex dynamics of precessing binary black holes.

8.8 Acknowledgments

We thank Harald Pfeiffer for useful comments. V.V. is supported by the Sherman Fairchild Foundation and NSF grants PHY–1404569, PHY–170212, and PHY–1708213 at Caltech. D.G. is supported by NASA through Einstein Postdoctoral Fellowship Grant No. PF6–170152 awarded by the Chandra X-ray Center, which is operated by the Smithsonian Astrophysical Observatory for NASA under Contract NAS8–03060.

References

- [1] B. P. Abbott et al. “Observation of Gravitational Waves from a Binary Black Hole Merger”. In: *Phys. Rev. Lett.* 116 (6 Feb. 2016), p. 061102. DOI: [10.1103/PhysRevLett.116.061102](https://doi.org/10.1103/PhysRevLett.116.061102). arXiv: [1602.03837 \[gr-qc\]](https://arxiv.org/abs/1602.03837). URL: <http://link.aps.org/doi/10.1103/PhysRevLett.116.061102>.
- [2] J. Aasi et al. “Advanced LIGO”. In: 32 (2015), p. 074001. DOI: [10.1088/0264-9381/32/7/074001](https://doi.org/10.1088/0264-9381/32/7/074001). arXiv: [1411.4547 \[gr-qc\]](https://arxiv.org/abs/1411.4547).
- [3] nobelprize.org/prizes/physics/2017.
- [4] Theocharis A. Apostolatos et al. “Spin induced orbital precession and its modulation of the gravitational wave forms from merging binaries”. In: *Phys. Rev. D* 49 (1994), pp. 6274–6297. DOI: [10.1103/PhysRevD.49.6274](https://doi.org/10.1103/PhysRevD.49.6274).
- [5] Lawrence E. Kidder. “Coalescing binary systems of compact objects to post-Newtonian 5/2 order. 5. Spin effects”. In: *Phys. Rev. D* 52 (1995), pp. 821–847. DOI: [10.1103/PhysRevD.52.821](https://doi.org/10.1103/PhysRevD.52.821). arXiv: [gr-qc/9506022](https://arxiv.org/abs/gr-qc/9506022).

- [6] Etienne Racine. “Analysis of spin precession in binary black hole systems including quadrupole-monopole interaction”. In: *Phys. Rev. D* 78 (2008), p. 044021. DOI: [10.1103/PhysRevD.78.044021](https://doi.org/10.1103/PhysRevD.78.044021). arXiv: [0803.1820](https://arxiv.org/abs/0803.1820) [gr-qc].
- [7] D. Gerosa et al. “Multi-timescale analysis of phase transitions in precessing black-hole binaries”. In: *Phys. Rev. D* 92 (2015), p. 064016. DOI: [10.1103/PhysRevD.92.064016](https://doi.org/10.1103/PhysRevD.92.064016). arXiv: [1506.03492](https://arxiv.org/abs/1506.03492) [gr-qc].
- [8] F Acernese et al. “Advanced Virgo: a second-generation interferometric gravitational wave detector”. In: *Classical and Quantum Gravity* 32.2 (2015), p. 024001. DOI: [10.1088/0264-9381/32/2/024001](https://doi.org/10.1088/0264-9381/32/2/024001). arXiv: [1408.3978](https://arxiv.org/abs/1408.3978) [gr-qc].
- [9] Luis Lehner and Frans Pretorius. “Numerical Relativity and Astrophysics”. In: *Ann. Rev. Astron. Astrophys.* 52 (2014), pp. 661–694. DOI: [10.1146/annurev-astro-081913-040031](https://doi.org/10.1146/annurev-astro-081913-040031). arXiv: [1405.4840](https://arxiv.org/abs/1405.4840) [astro-ph.HE].
- [10] SXS: youtube.com/user/SXSCollaboration,
LIGO Lab: youtube.com/channel/UC4oFISYpDywInX0lxiBPwA,
AEI: youtube.com/channel/UCw6knnFFBhdnwyIMohte45A,
LIGO/Virgo: youtube.com/channel/UCMATJmzibndbcdY8s9Prhjj.
- [11] Jonathan Blackman et al. “Numerical relativity waveform surrogate model for generically precessing binary black hole mergers”. In: *Phys. Rev. D* 96.2 (2017), p. 024058. DOI: [10.1103/PhysRevD.96.024058](https://doi.org/10.1103/PhysRevD.96.024058). arXiv: [1705.07089](https://arxiv.org/abs/1705.07089) [gr-qc].
- [12] Vijay Varma et al. “High-accuracy mass, spin, and recoil predictions of generic black-hole merger remnants”. In: *Phys. Rev. Lett.* 122 (2019), p. 011101. DOI: [10.1103/PhysRevLett.122.011101](https://doi.org/10.1103/PhysRevLett.122.011101). arXiv: [1809.09125](https://arxiv.org/abs/1809.09125) [gr-qc].
- [13] Bernard F. Schutz. *A First Course in General Relativity*. 2nd. New York: Cambridge University Press, 2009.
- [14] M Maggiore. *Gravitational Waves - Volume 1*. First. New York, NY: Oxford University Press, 2008.
- [15] Thomas W. Baumgarte and Stuart L. Shapiro. *Numerical Relativity: Solving Einstein's Equations on the Computer*. New York: Cambridge University Press, 2010. DOI: [10.1080/00107514.2011.586052](https://doi.org/10.1080/00107514.2011.586052).
- [16] James B. Hartle. *Gravity: An Introduction to Einstein's General Relativity*. New York: Addison-Wesley, 2003.
- [17] Sean Carroll. *Spacetime and Geometry: An Introduction to General Relativity*. New York: Addison Wesley, 2003.
- [18] Charles W. Misner, Kip S. Thorne, and John Archibald Wheeler. *Gravitation*. New York, New York: Freeman, 1973. DOI: [10.1002/asna.19752960110](https://doi.org/10.1002/asna.19752960110).

- [19] Michael Boyle, Robert Owen, and Harald P. Pfeiffer. “A geometric approach to the precession of compact binaries”. In: 84 (2011), p. 124011. doi: [10.1103/PhysRevD.84.124011](https://doi.org/10.1103/PhysRevD.84.124011). eprint: [arXiv:1110.2965](https://arxiv.org/abs/1110.2965) [gr-qc].
- [20] Patricia Schmidt et al. “Tracking the precession of compact binaries from their gravitational-wave signal”. In: *Phys. Rev. D* 84 (2011), p. 024046. doi: [10.1103/PhysRevD.84.024046](https://doi.org/10.1103/PhysRevD.84.024046). arXiv: [1012.2879](https://arxiv.org/abs/1012.2879) [gr-qc].
- [21] R. O’Shaughnessy et al. “Efficient asymptotic frame selection for binary black hole spacetimes using asymptotic radiation”. In: *Phys. Rev. D* 84 (2011), p. 124002. doi: [10.1103/PhysRevD.84.124002](https://doi.org/10.1103/PhysRevD.84.124002). arXiv: [1109.5224](https://arxiv.org/abs/1109.5224) [gr-qc].
- [22] Matt Visser. “The Kerr spacetime: A Brief introduction”. In: *Kerr Fest: Black Holes in Astrophysics, General Relativity and Quantum Gravity Christchurch, New Zealand, August 26-28, 2004*. 2007. arXiv: [0706.0622](https://arxiv.org/abs/0706.0622) [gr-qc]. URL: <https://inspirehep.net/record/752316/files/arXiv:0706.0622.pdf>.
- [23] Andy Bohn, Lawrence E. Kidder, and Saul A. Teukolsky. “Parallel adaptive event horizon finder for numerical relativity”. In: *Phys. Rev. D* 94.6 (2016), p. 064008. doi: [10.1103/PhysRevD.94.064008](https://doi.org/10.1103/PhysRevD.94.064008). arXiv: [1606.00437](https://arxiv.org/abs/1606.00437) [gr-qc].
- [24] Andy Bohn, Lawrence E. Kidder, and Saul A. Teukolsky. “Toroidal Horizons in Binary Black Hole Mergers”. In: *Phys. Rev. D* 94.6 (2016), p. 064009. doi: [10.1103/PhysRevD.94.064009](https://doi.org/10.1103/PhysRevD.94.064009). arXiv: [1606.00436](https://arxiv.org/abs/1606.00436) [gr-qc].
- [25] [youtube.com/watch?v=Tr1zDVbSjTM](https://www.youtube.com/watch?v=Tr1zDVbSjTM),
[youtube.com/watch?v=9HKh4ADvMoA](https://www.youtube.com/watch?v=9HKh4ADvMoA),
[youtube.com/watch?v=CeNP5NyW0z4](https://www.youtube.com/watch?v=CeNP5NyW0z4).
- [26] Eric Poisson and Misao Sasaki. “Gravitational radiation from a particle in circular orbit around a black hole. 5: Black hole absorption and tail corrections”. In: *Phys. Rev. D* 51 (1995), pp. 5753–5767. doi: [10.1103/PhysRevD.51.5753](https://doi.org/10.1103/PhysRevD.51.5753). arXiv: [gr-qc/9412027](https://arxiv.org/abs/gr-qc/9412027) [gr-qc].
- [27] Kashif Alvi. “Energy and angular momentum flow into a black hole in a binary”. In: *Phys. Rev. D* 64 (2001), p. 104020. doi: [10.1103/PhysRevD.64.104020](https://doi.org/10.1103/PhysRevD.64.104020). arXiv: [gr-qc/0107080](https://arxiv.org/abs/gr-qc/0107080) [gr-qc].
- [28] Eric Poisson. “Absorption of mass and angular momentum by a black hole: Time-domain formalisms for gravitational perturbations, and the small-hole / slow-motion approximation”. In: *Phys. Rev. D* 70 (2004), p. 084044. doi: [10.1103/PhysRevD.70.084044](https://doi.org/10.1103/PhysRevD.70.084044). arXiv: [gr-qc/0407050](https://arxiv.org/abs/gr-qc/0407050) [gr-qc].
- [29] Xinyu Zhao, Michael Kesden, and Davide Gerosa. “Nutational resonances, transitional precession, and precession-averaged evolution in binary black-hole systems”. In: *Phys. Rev. D* 96.2 (2017), p. 024007. doi: [10.1103/PhysRevD.96.024007](https://doi.org/10.1103/PhysRevD.96.024007). arXiv: [1705.02369](https://arxiv.org/abs/1705.02369) [gr-qc].

- [30] J. D. Schnittman. “Spin-orbit resonance and the evolution of compact binary systems”. In: *PRD* 70.12, 124020 (Dec. 2004), p. 124020. doi: [10.1103/PhysRevD.70.124020](https://doi.org/10.1103/PhysRevD.70.124020). eprint: [astro-ph/0409174](https://arxiv.org/abs/astro-ph/0409174).
- [31] C. O. Lousto and J. Healy. “Flip-Flopping Binary Black Holes”. In: *Physical Review Letters* 114.14, 141101 (Apr. 2015), p. 141101. doi: [10.1103/PhysRevLett.114.141101](https://doi.org/10.1103/PhysRevLett.114.141101). arXiv: [1410.3830 \[gr-qc\]](https://arxiv.org/abs/1410.3830).
- [32] D. Gerosa et al. “Wide precession: binary black-hole spins repeatedly oscillating from full alignment to full anti-alignment”. In: *arXiv e-prints* (Nov. 2018). arXiv: [1811.05979 \[gr-qc\]](https://arxiv.org/abs/1811.05979).
- [33] D. Gerosa et al. “Precessional Instability in Binary Black Holes with Aligned Spins”. In: *Physical Review Letters* 115.14, 141102 (Oct. 2015), p. 141102. doi: [10.1103/PhysRevLett.115.141102](https://doi.org/10.1103/PhysRevLett.115.141102). arXiv: [1506.09116 \[gr-qc\]](https://arxiv.org/abs/1506.09116).
- [34] C. Afle et al. “Detection and characterization of spin-orbit resonances in the advanced gravitational wave detectors era”. In: *PRD* 98.8, 083014 (Oct. 2018), p. 083014. doi: [10.1103/PhysRevD.98.083014](https://doi.org/10.1103/PhysRevD.98.083014). arXiv: [1803.07695 \[gr-qc\]](https://arxiv.org/abs/1803.07695).
- [35] Serguei Ossokine et al. “Transitional precession in numerical relativity simulations.” In: (2019). in preparation.
- [36] Vijay Varma et al. “Surrogate model of hybridized numerical relativity binary black hole waveforms”. In: *Phys. Rev. D* 99.6 (2019), p. 064045. doi: [10.1103/PhysRevD.99.064045](https://doi.org/10.1103/PhysRevD.99.064045). arXiv: [1812.07865 \[gr-qc\]](https://arxiv.org/abs/1812.07865).
- [37] Alejandro Bohe et al. “Next-to-next-to-leading order spin-orbit effects in the near-zone metric and precession equations of compact binaries”. In: 30 (2013), p. 075017. doi: [10.1088/0264-9381/30/7/075017](https://doi.org/10.1088/0264-9381/30/7/075017). arXiv: [1212.5520](https://arxiv.org/abs/1212.5520).
- [38] Davide Gerosa, François Hébert, and Leo C. Stein. “Black-hole kicks from numerical-relativity surrogate models”. In: *Phys. Rev. D* 97.10 (2018), p. 104049. doi: [10.1103/PhysRevD.97.104049](https://doi.org/10.1103/PhysRevD.97.104049). arXiv: [1802.04276 \[gr-qc\]](https://arxiv.org/abs/1802.04276).
- [39] Michael Boyle. “Angular velocity of gravitational radiation from precessing binaries and the corotating frame”. In: *Phys. Rev. D* 87.10 (2013), p. 104006. doi: [10.1103/PhysRevD.87.104006](https://doi.org/10.1103/PhysRevD.87.104006). arXiv: [1302.2919 \[gr-qc\]](https://arxiv.org/abs/1302.2919).
- [40] Bela Szilagyi, Lee Lindblom, and Mark A. Scheel. “Simulations of Binary Black Hole Mergers Using Spectral Methods”. In: *Phys. Rev. D* 80 (2009), p. 124010. doi: [10.1103/PhysRevD.80.124010](https://doi.org/10.1103/PhysRevD.80.124010). arXiv: [0909.3557 \[gr-qc\]](https://arxiv.org/abs/0909.3557).
- [41] Eanna E. Flanagan and Scott A. Hughes. “The Basics of gravitational wave theory”. In: *New J. Phys.* 7 (2005), p. 204. doi: [10.1088/1367-2630/7/1/204](https://doi.org/10.1088/1367-2630/7/1/204). arXiv: [gr-qc/0501041 \[gr-qc\]](https://arxiv.org/abs/gr-qc/0501041).

- [42] J. N. Goldberg et al. “Spin- s Spherical Harmonics and δ ”. In: *Journal of Mathematical Physics* 8.11 (1967), pp. 2155–2161. DOI: [10.1063/1.1705135](https://doi.org/10.1063/1.1705135). URL: <http://link.aip.org/link/?JMP/8/2155/1>.
- [43] Kip S. Thorne. “Multipole expansions of gravitational radiation”. In: *Rev. Mod. Phys.* 52.2 (Apr. 1980), pp. 299–339. DOI: [10.1103/RevModPhys.52.299](https://doi.org/10.1103/RevModPhys.52.299).
- [44] Thibault Damour. “Coalescence of two spinning black holes: an effective one-body approach”. In: *Phys. Rev. D* 64 (2001), p. 124013. DOI: [10.1103/PhysRevD.64.124013](https://doi.org/10.1103/PhysRevD.64.124013). arXiv: [gr-qc/0103018](https://arxiv.org/abs/gr-qc/0103018) [gr-qc].
- [45] Manuela Campanelli, C. O. Lousto, and Y. Zlochower. “Spinning-black-hole binaries: The orbital hang up”. In: *Phys. Rev. D* 74 (2006), p. 041501. DOI: [10.1103/PhysRevD.74.041501](https://doi.org/10.1103/PhysRevD.74.041501). arXiv: [gr-qc/0604012](https://arxiv.org/abs/gr-qc/0604012) [gr-qc].
- [46] Mark A. Scheel et al. “Improved methods for simulating nearly extremal binary black holes”. In: *Class. Quant. Grav.* 32.10 (2015), p. 105009. DOI: [10.1088/0264-9381/32/10/105009](https://doi.org/10.1088/0264-9381/32/10/105009). arXiv: [1412.1803](https://arxiv.org/abs/1412.1803) [gr-qc].
- [47] Latham Boyle, Michael Kesden, and Samaya Nissanke. “Binary black hole merger: Symmetry and the spin expansion”. In: *Phys. Rev. Lett.* 100 (2008), p. 151101. DOI: [10.1103/PhysRevLett.100.151101](https://doi.org/10.1103/PhysRevLett.100.151101). arXiv: [0709.0299](https://arxiv.org/abs/0709.0299) [gr-qc].
- [48] Manuela Campanelli et al. “Large merger recoils and spin flips from generic black-hole binaries”. In: *Astrophys. J.* 659 (2007), pp. L5–L8. DOI: [10.1086/516712](https://doi.org/10.1086/516712). arXiv: [gr-qc/0701164](https://arxiv.org/abs/gr-qc/0701164) [gr-qc].
- [49] J. A. Gonzalez et al. “Supermassive recoil velocities for binary black-hole mergers with antialigned spins”. In: *Phys. Rev. Lett.* 98 (2007), p. 231101. DOI: [10.1103/PhysRevLett.98.231101](https://doi.org/10.1103/PhysRevLett.98.231101). arXiv: [gr-qc/0702052](https://arxiv.org/abs/gr-qc/0702052) [GR-QC].
- [50] Carlos O. Lousto and Yosef Zlochower. “Hangup Kicks: Still Larger Recoils by Partial Spin/Orbit Alignment of Black-Hole Binaries”. In: *Phys. Rev. Lett.* 107 (2011), p. 231102. DOI: [10.1103/PhysRevLett.107.231102](https://doi.org/10.1103/PhysRevLett.107.231102). arXiv: [1108.2009](https://arxiv.org/abs/1108.2009) [gr-qc].
- [51] David Merritt et al. “Consequences of gravitational radiation recoil”. In: *Astrophys. J.* 607 (2004), pp. L9–L12. DOI: [10.1086/421551](https://doi.org/10.1086/421551). arXiv: [astro-ph/0402057](https://arxiv.org/abs/astro-ph/0402057) [astro-ph].
- [52] Davide Gerosa and Alberto Sesana. “Missing black holes in brightest cluster galaxies as evidence for the occurrence of superkicks in nature”. In: *Mon. Not. Roy. Astron. Soc.* 446 (2015), pp. 38–55. DOI: [10.1093/mnras/stu2049](https://doi.org/10.1093/mnras/stu2049). arXiv: [1405.2072](https://arxiv.org/abs/1405.2072) [astro-ph.GA].
- [53] Bernd Brügmann et al. “Exploring black hole superkicks”. In: 77.12, 124047 (2008), p. 124047. DOI: [10.1103/PhysRevD.77.124047](https://doi.org/10.1103/PhysRevD.77.124047). arXiv: [arXiv: 0707.0135](https://arxiv.org/abs/0707.0135) [gr-qc].

- [54] binaryBHexp. Website: vijayvarma392.github.io/binaryBHexp,
Python package: pypi.org/project/binaryBHexp,
Code repository: github.com/vijayvarma392/binaryBHexp.
- [55] J. Blackman et al. “NRSur7dq2”. In: (). pypi.org/project/NRSur7dq2.
- [56] V. Varma et al. “surfinBH”. In: (). pypi.org/project/surfinBH, doi.org/10.5281/zenodo.1418525.
- [57] Travis Continuous Integration. In: (). travis-ci.org.